DETERMINING THE EFFECTIVE SYSTEM DAMPING OF HIGHWAY BRIDGES

By

Maria Q. Feng, Professor

and

Sung Chil Lee, Post-doctoral Researcher

Department of Civil & Environmental Engineering

University of California, Irvine

CA-UCI-2009-001

June 2009

DETERMINING THE EFFECTIVE SYSTEM DAMPING OF HIGHWAY BRIDGES

Final Report Submitted to the Caltrans under
Contract No: RTA59A0495

By

Maria Q. Feng, Professor

and

Sung Chil Lee, Post-doctoral Researcher

Department of Civil & Environmental Engineering

University of California, Irvine

CA-UCI-2009-001

June 2009

TECHNICAL REPORT DOCUMENTAION PAGE

TR0003 (REV. 9/99)

1. REPORT NUMBER CA-UCI-2009-001	2. GOVERNMENT ASSOCIATION NUMBER	3. RECIPIENT'S CATALOG NUMBER
4. TITLE AND SUBTITLE DETERMINING THE EFFECTIVE SYSTEM DAMPING OF HIGHWAY BRIDGES		5. REPORT DATE June, 2009
		6. PERFORMING ORGANIZATION CODE UC Irvine
7. AUTHOR Maria Q. Feng, and Sungchil Lee		8. PERFORMING ORGANIZATION REPORT NO.
9. PERFORMING ORGANIZATION NAME AND ADDRESS Civil and Environmental Engineering E4120 Engineering Gateway University of California, Irvine Irvine, CA 92697-2175		10. WORK UNIT NUMBER
		11. CONTRACT OR GRANT NUMBER RTA59A0495
12. SPONSORING AGENCY AND ADDRESS California Department of Transportation (Caltrans) Sacramento, CA		13. TYPE OF REPORT AND PERIOD COVERED Final Report
		14. SPONSORING AGENT CODE

15. SUPPLEMENTARY NOTES

16. ABSTRACT

This project investigates four methods for modeling modal damping ratios of short-span and isolated concrete bridges subjected to strong ground motion, which can be used for bridge seismic analysis and design based on the response spectrum method. The seismic demand computation of highway bridges relies mainly on the design spectrum method, which requires effective modal damping. However, high damping components, such as embankments of short-span bridges under strong ground motion and isolation bearings make bridges non-proportionally damped systems for which modal damping cannot be calculated using the conventional modal analysis. In this project four methods are investigated for estimating the effective system modal damping, including complex modal analysis (CMA), neglecting off-diagonal elements in damping matrix method (NODE), composite damping rule (CDR), and optimization in time domain and frequency domain (OPT) and applied to a short-span bridge and an isolated bridge.

The results show that among the four damping estimating methods, the NODE method is the most efficient and the conventional assumption of 5% modal damping ratio is too conservative for short-span bridges when energy dissipation is significant at the bridge boundaries. From the analysis of isolated bridge case, the effective system damping is very close to the damping ratio of isolation bearing.

17. KEYWORDS Effective Damping, Concrete Bridge, Response Spectrum Method	18. DISTRIBUTION STATEMENT No restrictions.	
19. SECURITY CLASSIFICATION (of this report) Unclassified	20. NUMBER OF PAGES 288	21. COST OF REPORT CHARGED

DISCLAIMER: The contents of this report reflect the views of the authors who are responsible for the facts and the accuracy of the data presented herein. The contents do not necessarily reflect the official views or policies of the State of California or the Federal Highway Administration. This report does not constitute a standard, specification or regulation.

The United States Government does not endorse products or manufacturers. Trade and manufacturers' names appear in this report only because they are considered essential to the object of the document.

SUMMARY

The overall objective of this project is to study the fundamental issue of damping in bridge structural systems involving significantly different damping components and to develop a more rational method to determine the approximation of seismic demand of isolated bridges and short bridge. Within the framework of the current response spectrum method, on which the design of highway bridges primarily relies, four damping estimation methods including the complex modal analysis method, neglecting off-diagonal elements method, optimization method, and composite damping rule method, are explored to compute the equivalent modal damping ratio of short-span bridges and isolated bridges.

From the application to a real short-span bridge utilizing earthquake data recorded at the bridge site, the effective system damping ratio of the bridge was determined to be as large as 25% under strong ground motions, which is much higher than the conventional damping ratio used for design of such bridges. Meanwhile, the simulation with the 5% damping ratio produced nearly two times the demand of the measured data, which implies that the 5% value used in practice may be too low for the design of short-span bridges considering the strong ground motions which should be sustained.

The four damping estimating methods are also applied to an isolated bridge. By approximating non-linear isolation bearings with equivalent viscoelastic elements, an equivalent linear analysis is carried out. The estimation of the seismic demand based on the response spectrum method using the effective system damping computed by the four methods is verified by comparing the response with that from the non-linear time history analysis. Equivalent damping ratio of isolation bearing varies from 10% to 28% under

ground motions. For isolated bridges, majority of the energy dissipation takes place in isolation bearings, but contribution from the bridge structural damping should also be considered. A simplified way of determining the effective system damping of the isolated bridge is suggested as the summation of equivalent damping ratio of isolation bearing and the half of the damping ratio of bridge structure. Also, from the relation between the effective system damping ratio and ground motion characteristics, a simple approximation to predict the effective system damping of isolated bridges is suggested.

Table of Contents

List of Figures

List of Tables

Acknowledgement

Chapter 1

INTRODUCTION

This chapter first describes the motivations of this research for the determination of the effective damping of highway bridges then summarizes the objectives and overall scope of the research followed by the organization of this report.

1.1 Background

For the seismic design of ordinary bridges, current design specifications require the use of the modal-superposition-response-spectrum approach. It involves the following steps: (1) A three-dimensional space frame model of the bridge is developed with mass and stiffness matrices assembled. (2) Eigen analysis of this model is performed, usually using finite element analysis software, to obtain the undamped frequencies and mode shapes of the structure. A minimum of three times the number of spans or 12 modes are selected. (3) Assuming classical (i.e. proportional) Rayleigh's viscous damping, the equations of motion are reduced into individual decoupled modal equations, each of which can be envisioned as the motion equation for a corresponding single-degree-of-freedom (SDOF). (4) The seismic response for each of the selected modes to the design earthquake is evaluated using the specified SDOF acceleration response spectrum curve. (5) Combine the peak responses of all selected modes using the square-root-of-sum-of-

squares (SRSS) or complete-quadratic-combination (CQC) rule resulting in maximum demands that the structure is designed to sustain.

The response spectrum method is based on the assumption of proportional damping characteristics in the structure with a 5% modal damping ratio for all the selected modes. However, if a bridge has some components that are expected to have significant damping, the conventional 5% damping ratio is not likely to be a reasonable assumption. Therefore, in the cases of short-span bridges under strong ground motion and fully- or partially-isolated bridges which have isolators with extremely high damping, an appropriate damping ratio should be determined for each mode to provide a more economic and accurate design or seismic retrofit plan.

Resulting from several previous seismic observations and studies by other researchers, it was found that the concrete structure of short-span bridges behaves within the elastic range and sustains no damage, even under strong earthquakes, which can be attributed to the significant restraint and energy dissipation at the boundaries of these bridges. Through the analysis of valuable earthquake response data recorded at several bridge sites, the energy dissipation capacity of abutment-embankment and column boundaries of short-span bridges has been highlighted. In many previous studies, damping ratios much greater than 5% had to be used so that simulated responses would match well with the recorded ones. Therefore, when short-span brides are designed to sustain strong ground motion, a rational damping ratio for each mode should be found considering the damping effects of the bridge boundaries.

A seismically isolated bridge is another type of bridge with high damping components. In order to prevent damage resulting from seismic hazards, isolation bearing devices have

been commonly adopted in highway bridges. The isolation bearings alleviate seismic damage by shifting the first mode natural period of the original, un-isolated bridge into the region of lesser spectral acceleration and through the high dissipation of energy in the isolation bearings. Even for the seismic design of isolated bridges, many design guides such as the American Association of State Highway and Transportation Officials (AASHTO) Guide (2000), Japan Public Works Research Institute, and California Department of Transportation (Caltrans) adopt an equivalent linear analysis procedure utilizing an equivalent linear system for the isolation bearings and providing appropriate linear methods for estimating seismic response.

To develop a rational and systematic approach for evaluating modal damping in a structural system comprised of components with drastically different damping ratios, there arise a problems of fundamental theoretical interest. It has been well-established that only when a system is viscously damped with a damping matrix that conforms to the form identified by Caughey and O'Kelly (1965) can the damping matrix be diagonalized by the mode shape matrix. This system is said to be classically (or proportionally) damped for which the classical uncoupled modal superposition method applies. Unfortunately, the damping matrix of a system consisting of components with significantly different damping ratios is non-classical, such as the cases of short-span bridges and seismically isolated bridges. Usually, the embankments of short-span bridges and the base-isolation devices have equivalent damping ratios as high as 20-30% under strong ground motion, while the equivalent damping ratio of the rest of the concrete structural system can usually be reasonably approximated as 5%. Though the nonlinear behavior and damping of bridge boundaries and isolation bearings can be approximated by an equivalent linear system which is composed of effective stiffnesses and effective

damping coefficients, the damping matrix of the entire bridge system as described will be non-classical having important off-diagonal terms that cannot be diagonalized by the mode shape matrix. Therefore, the response spectrum method cannot be rigorously applied to non-classically damped systems.

1.2 Effective Modal Damping

To keep the design procedure within the framework of the modal superposition method, which is the current dynamic design procedure favored by engineers/designers, compromise has to be made to approximate the non-classical damping by a classical damping matrix. A usual approach for this purpose is as follows. Let $\overline{C} = \phi^T C \phi$, where C is the non-classical damping matrix of the system, ϕ is the mode shape matrix associated with the undamped system, and ϕ^T is the transposed mode shape matrix. $\overline{C}$ can have substantial off-diagonal terms that produce coupling of the normal modes. Ignoring the off-diagonal terms results in a classical damping matrix, C', whose elements c'_{ij} relate to the elements of $\overline{C}$, by $c'_{ii} = \overline{c}_{ii}$ and $c'_{ij} = 0$ when $i \neq j$. This approximation, which is defined as the neglecting off-diagonal elements (NODE) method, has been widely used in many studies.

Veletsos and Ventura (1986) proposed a critical and exact approach to generalize the modal superposition method for evaluating the dynamic response of non-classically damped linear systems. This approach begins by first rewriting the second order equation of motion into a first order equation in state space, and then by carrying out a complex-valued eigen analysis giving complex-valued characteristic values and characteristic vectors for the system. Examining carefully the physical meaning of each

pair of conjugated characteristic values and associated characteristic vectors, the authors were able to interpret each of these pairs as a mode similar to a SDOF system, except that the mode shape has different configurations at different times, varying periodically. A damping ratio was obtained for each of these 'modes', and the dynamic response of the system was represented in terms of modal superposition. This method is defined as the complex modal analysis (CMA) method in this study. A variety of system configurations were investigated through this method and the results were compared to those from the NODE method described above. It was concluded that while the agreement between these two methods is generally reasonable, there can be significant differences in the damping ratios and dynamic responses, particularly when much higher damping ratios are present in some components of the complete system.

A semi-empirical and semi-theoretical approach, referred to as the composite damping rule (CDR) was suggested by Raggett (1975). In this approach, energy dissipation in different components is estimated empirically under the assumption that the mode shapes and frequencies of a damped system remain the same as those of the undamped system. Energy dissipation in different components of a certain mode can be summed up to reach an estimate of the total energy dissipation of the system in this mode, such that an effective modal damping ratio (EMDR) for this mode may be obtained. This method has been adopted by many other studies (Lee et al, 2004; Chang et al, 1993; Johnson and Kienholz, 1982).

1.3 Objectives and Scope

Various methods have been studied in the literature for evaluating damping in a complex structural system, but they have never been compared and evaluated in a systematic way based on available seismic records. Therefore, the overall objective of this research is to study the fundamental issue of damping in complex bridge structural systems involving significantly different damping components (such as short bridges and fully isolated bridges) and to develop a more rational damping estimation method for improving dynamic analysis results and the seismic design of such bridges. Another objective is to relate the effective system damping with ground motion intensity.

In order to achieve these objectives, selected methods are investigated for their ability to compute the effective system damping of short-span and seismically isolated bridges. The detailed explanation of each method is given in Chapter 3 following the literature review on the damping of such bridges in Chapter 2.

The application of the damping estimating methods to a short-span bridge is investigated in Chapter 4. The Painter Street Overcrossing (PSO) was chosen as an example bridge due to the fact that this bridge has invaluable earthquake response data recorded during strong earthquakes. Utilizing the measured data, the equivalent linear systems of the bridge boundaries were identified and then each damping estimating method was applied to compute the effective system damping of the bridge. The validation of the damping estimating methods was carried out by comparing the modal combination results with the recorded bridge response data.

In Chapter 5, the application of the methods to a seismically isolated bridge is demonstrated. Because of the scarcity of measured data from isolated bridges, an

example bridge is assumed in this study. Under many earthquake ground motions, the bi-linear hysteretic behavior of each isolation bearing is approximated with an equivalent linear viscoelastic element. Afterwards, the damping estimating methods are applied to compute the effective system damping of the bridge. These methods are verified by comparing the results found through the standard response spectrum method with the results obtained from a non-linear seismic analysis. Also, the effective system damping is related with the characteristics of ground motions.

Finally, conclusions of this research are presented in Chapter 6 along with recommended future research.

Chapter 2

LITERATURE REVIEW

In this chapter, previous studies to understand the impact of the significant energy dissipation in short-span bridges and isolated bridges on the dynamic response of the bridges are reviewed. Also, many attempts to find the effective system damping of such bridges are also described. From the literature review, several important conclusions are derived to guide this research.

2.1 Energy Dissipation and EMDR of Short-span Bridges

A short-span bridge has a superstructure constructed to be connected directly to wing-walls and an abutment at one or each end of the bridge. It has a relatively long embankment compared with bridge length. In the 1970s, investigating the influence of the embankment on the dynamic response of such bridges started (Tseng and Penzien, 1973; Chen and Penzien, 1975, 1977). It was found that the monolithic type of abutment and embankment typical of short-span bridges has drastic effects on the bridge behavior under strong ground motions. Because of a long embankment and relatively small size of the bridge, most of the input energy is dissipated through the embankment soil during earthquakes and the bridge behaves essentially as a rigid body in the elastic range of the

structure. In modern earthquake engineering, appropriate modeling of bridge boundaries has become one of the important factors in seismic analysis and many efforts have been focused on identification of a damping ratio for the soil boundary during strong earthquakes. However, it is essential that any reasonable estimate of this damping should be based on recorded earthquake data from similar structures.

One of the most valuable data sets available is from the vibration measurements at the Meloland Road Overpass (MRO) during the 1979 Imperial Valley earthquake. Analyzing the data Werner et al. (1987) found that this 2-span RC box-girder, single-columned short bridge with monolithic abutments exhibited two primary modes: the vertical mode mainly involved the vertical vibration of the superstructure, having a damping ratio of 6.5%; the transverse mode mainly involved the horizontal translation of the abutments and the superstructure, inducing bending in the single-column pier, coincidently having a damping ratio of 6.5%. These modal damping ratios are slightly higher than the 5% used in design. However, these modes, especially the transverse mode, involve substantial movement of the abutments. This further implies that the soil disturbance and friction between the abutments and the soil most likely may have contributed a large portion of the energy dissipation, leading to a higher damping ratio.

Another set of important earthquake data was recorded at the Painter Street Overpass (PSO) from which McCallen and Romstad (1994) tried to determine the effective system damping of the PSO. The authors built, as well as a stick model, a full three dimensional model of the bridge including abutment, pile foundation, and boundary soil using solid elements. Based on the CALTRANS method, the effective stiffness for the embankment soil and pile foundation was computed for their stick model and they tried to simulate the measured bridge response by updating the EMDR of the entire bridge model. Through

extensive trial and error, it was found that the EMDR was 20% and 30% for the transverse and longitudinal modes, respectively.

Utilizing the same measured data at the PSO, the spring force and damping force of the abutment of the PSO were identified by Goel and Chopra (1995). In their study the spring force and damping force of the abutment were combined as one force. By drawing the slope line on the force-displacement diagram acquired through the force identification procedure, the authors could compute the time variant abutment stiffness. Also, they found that under the less intense earthquakes the force-displacement diagram showed an elliptical shape which implies linear viscoelastic behavior of the abutment system, however, it showed significant nonlinearity of the system under stronger ground motion. Though the damping effect of the abutment system could be obtained from the force-displacement diagram, the effective system damping of the entire bridge system was not studied.

The quantification of the EMDR based on the deformation of the abutment system during an earthquake was attempted by Goel (1997). After observing the relation between the EMDR and the abutment flexibility, he suggested a simple formula by which the EMDR could be computed. Using this proposed formula and six earthquake ground motions, he identified the EMDR of the PSO as ranging from 5 to 12%. However, the upper bound of the EMDR was limited to 15% in his equation.

Though there have been many studies on the identification of the effective system damping of short-span bridges under strong ground motions, few studies have been done on the formulation to compute the effective stiffness and damping of the bridge boundary. However, Wilson and Tan (1990) developed simple explicit formulae to represent the

embankment of short- or medium-span bridges with linear springs based on the plane strain analysis of embankment soil. The spring stiffness per unit length of embankment was expressed as a function of embankment geometry (i.e. width, height, and slope) and the shear modulus of the embankment soil. The total spring stiffness was obtained by multiplying the embedded length of the wing wall by the unit spring stiffness. The authors applied the method to the MRO. Utilizing the recorded data, the damping ratio of the embankment soil was found as 20-40%, however, the damping ratio of the entire bridge system was determined to range from 3 to 12%. It should be noted that while an equivalent spring stiffness was developed to model the embankment only, they used it for the combined abutment-embankment system.

A comprehensive study on the approximation of an equivalent linear system for an abutment-embankment system of short-span bridges was done by Zhang and Makris (2002). Based on previous research, they suggested a systematic approach to compute the frequency-independent spring and viscous damping coefficient of embankment and pile groups at the abutments and bridge bents. In their derivation, the embankment was represented by a one-dimensional shear beam and the solution of the shear beam model under harmonic loading was used to compute the spring stiffness and damping coefficient of the embankment. Applying their method to the PSO and MRO, they found the equivalent linear system of the bridge boundaries. From the complex modal analysis, the EMDR was found as 9% (transverse), and 46% (longitudinal) for the PSO and 19% (transverse), and 57% (longitudinal) for the MRO, respectively.

Kotsoglou and Pantazopoulou (2007) established an analytical procedure to evaluate the dynamic characteristics and dynamic response of an embankment under earthquake excitation. Instead of using the one dimensional shear beam model used by Zhang and

11

Makris (2002), the author developed a two dimensional equation of motion for the embankment and solved it to investigate the dynamic characteristics of the embankment. From the application of their method to the PSO embankment, the modal damping ratio of the embankment was found to be 25% in the transverse direction.

Based on bridge damping data base, Tsai et al. (1993) investigated appropriate damping ratio for design of short-span bridges in Caltrans. Though the data base was composed of 53 bridges including steel and concrete bridges, as indicated by the authors, the identified damping ratios cannot be adopted for seismic design because most of the data base were from free or forced vibration excitation with well below 0.1g, except two earthquake excitation data. The authors recommended to use damping ratio of 7.5% for seismic design when a SSI parameter satisfies a criterion and to investigate the composite damping rule method for computing effective system damping ratio of short-span bridges.

2.2 Energy Dissipation and EMDR of Isolated Bridge

The prevention of seismic hazards in highway bridges by installing isolation bearings is increasingly adopted now days in construction of new bridges and in seismic retrofit of old bridges (Mutobe and Cooper, 1999; Robson et al., 2001; Imbsen, 2001; Dicleli, 2002; Dicleli et al., 2005). The isolation bearing has relatively smaller stiffness than the bridge column and decouples the superstructure from the substructure such that the substructure can be protected from the transfer of inertial force from the massive superstructure. From the viewpoint of response spectrum analysis, the isolation bearings elongate the natural period of an isolated bridge so that the spectral acceleration which the isolated bridge

should sustain becomes less than that of the un-isolated bridge. Among many types of isolation bearing devices such as rubber bearing, lead rubber bearing, high damping rubber bearing, friction pendulum bearing, rolling type bearing, and so on, the most commonly used isolation bearing is the lead rubber bearing (LRB). In North America, 154 bridges out of the 208 isolated bridges are installed with LRBs (Buckle et al., 2006).

To approximate the mechanical behavior of an isolation bearing, the Bouc-Wen model (Wen, 1976; Baber and Wen, 1981; Wong et al., 1994a, 1994b, Marano and Sgobba, 2007) and the bi-linear model (Stehmeyer and Rizos, 2007; Lin et al., 1992; Roussie et al., 2003; Jangid, 2007; Katsaras et al., 2008; Warn and Whittaker, 2006) have been most commonly used. In contrast to the bi-linear model, the Bouc-Wen model can simulate the smooth transition from elastic to plastic behavior and many kinds of hysteretic loops can be generated using different combinations of model parameters. While the bi-linear model can be thought of as one special case of the Bouc-Wen model, it can easily model any type of isolation bearing (Naeim and Kelly, 1999).

Turkington et al. (1989) suggested a design procedure for isolated bridges. In their procedure, the EMDR of an isolated bridge is computed by simply adding together the damping ratios of the isolation bearing and the concrete structure. The damping ratio of the isolation bearing is found using the bi-linear model and 5% is assigned for the concrete structure.

Hwang and Sheng (1993) suggested an empirical formulation to compute the effective period and effective damping ratio of individual isolation bearings represented by the bi-linear model. Their method is based on the work of Iwan and Gates (1979) which indicates that the maximum inelastic displacement response spectrum can be

approximated by using the elastic response spectrum and adopting an effective period shift and effective damping ratio of the inelastic SDOF system. The work of the authors was extended to compute the effective linear stiffness and effective system damping ratio of an isolator-bridge column system (Hwang et al., 1994). To compute the EMDR of the isolator-bridge column system, they applied the composite damping rule method. However, the original work of Iwan and Gates was developed for ductility ratios of 2, 4, and 8 which is too small for isolated bridges under strong earthquakes.

Considering the large ductility ratio of isolation bearings, Hwang et al. (1996) proposed a semi-empirical formula to approximate the equivalent linear system of isolation bearings. The suggested equations, which were modified from the AASHTO method, were found by optimizing the effective stiffness and damping ratio under 20 ground motions using the same algorithm by Iwan and Gates.

A comprehensive study for the equivalent linear approximation of hysteretic materials was done by Kwan and Billington (2003). The authors considered six types of hysteretic loops and proposed a formula to compute the effective linear system based on Iwan's approach (Iwan, 1980). In their study, the effective period shift was assumed to be related to the ductility ratio, and the effective damping ratio to both the effective period shift and ductility ratio. However, since only a small range of ductility ratios (i.e. from 2 to 8) was considered, which is too low for isolated bridges, it should be verified that this method is applicable to isolation bearings. The important finding from this study was that the effective damping ratio of a hysteretic material increases with increase of the ductility ratio, even in the case of no hysteretic loop. This observation shows that the direct summation of the damping ratios of the isolation bearing and concrete structure might be incorrect.

Dall'Asta and Ragni (2008) approximated a non-linear, high damping rubber with an effective linear system during both stationary and transient excitation. The effective stiffness of the linear system was estimated from the secant stiffness at the maximum displacement of the force-displacement plot and the effective damping ratio was found by equating the dissipated energy from the non-linear system and the effective linear system.

Regarding soil-structure interaction in isolated bridges, there is relatively little literature; however, several published papers have investigated this effect. Tongaonkar and Jangid (2003) studied the influence of the SSI on the seismic response of three-span isolated bridges considering four different soil types (soft, medium, hard, and rigid). In their simulation, the soil-pile foundation was modeled with a frequency independent spring-viscous damping-mass system. The authors concluded that the SSI increases the displacement of the isolation bearing located at the abutments only, while it decreases other responses such as deck acceleration, pier base shear, and isolation bearing displacement at the piers.

Ucak and Tsopelas (2008) investigated the effect of the SSI on two types of isolated bridges, one being a typical stiff freeway overcrossing and the other a typical flexible multispan highway bridge, under near fault and far field ground motions. From their results, the consideration of the SSI does not have much affect on either isolator or pier response of the stiff freeway overcrossing except for isolator drift under far field ground motions. In the multispan highway bridge case, the consideration of the SSI was conservative for the design of the isolator system, but not for the pier design.

2.3 Summary

From the literature review on short-span bridges, summaries and conclusions are drawn as follows:

(1) From research based on recorded earthquake data, bridge boundary soil was found to have non-linearity during earthquakes. Though the soil non-linearity can be represented by a non-linear spring or a frequency-dependent spring and a damping model, these elements cannot be used directly in the current response-spectrum-based design method. To be applicable in this response spectrum method, these elements must be approximated in equivalent linear forms. Therefore, in this research the bridge boundary is modeled with an equivalent linear system composed of an elastic spring and viscous damping.

(2) The results of the EMDR of short-span bridges are quite dependent on how the bridge and boundaries are modeled and which system identification method is applied. All previous research was conducted utilizing not only its own bridge modeling technique but also its own system identification method. That is why the EMDR from previous studies is not consistent, even for the same bridge under the same earthquake. Thus, if the identified EMDR of short-span bridges is going to be used for new design or retrofit planning of such bridges, the modeling of bridges used in the identification of the EMDR should be consistent with the one used in the current design practice. In this study, the finite element modeling of a short-span bridge is established based on the current design practice.

(3) The inherent damping ratio of the concrete structure of bridges is assumed to be constant regardless of ground motion intensity but the boundary soil damping

16

changes depending ground motion characteristics. The shear modulus and damping characteristics of the boundary soil varies with the soil strain. Under relatively strong earthquakes, soil strain becomes large resulting in small shear modulus and large damping, and vice versa under weak earthquakes. Considering that the bridge boundary soil damping varies with the characteristics of the exciting ground motion, the EMDR is represented as being related with the ground motion intensity in this research.

From the literature review on isolated bridges, summaries and conclusions are drawn as follows:

(1) In many studies, the bi-linear hysteretic model has generally been used to represent the mechanical behavior of the isolation bearing. Although the Bouc-Wen model has greater capability than this, it is chosen in this study because it can be applied to any type of isolation bearing and, more importantly, because most design specifications (Guide, 2000; Manual, 1992; Hwang et al., 1994, 1996) make use of it.

(2) Two different levels of equivalent linearization are involved in isolated bridges: i) equivalent linearization of the isolation bearing unit, and ii) equivalent linearization of the entire isolated bridge. So far, most of the previous research has focused on the development of the equivalent linear system of the isolation bearing. When there has been a need to compute the EMDR of an entire bridge system, only the composite damping rule method was adopted. In this study, not only the composite damping rule method but also other methods are applied and verified in the framework of the response spectrum method.

(3) The enclosed area of a bi-linear hysteretic loop of the isolation bearing is the dissipated energy which depends on the maximum displacement of the bearing. Therefore, the effective damping of an isolation bearing varies depending on the characteristics of the exciting ground motion. Thus, as in the case of short-span bridges, the EMDR of an isolated bridge is related to the ground motion parameters.

<div align="right">

Chapter 3

</div>

EFFECTIVE SYSTEM DAMPING ESTIMATING METHODS

This chapter describes the basic principles of four effective system damping estimating methods (complex modal analysis method, neglecting off-diagonal element in damping matrix method, optimization method, composite damping rule method) for non-proportionally damped systems. At the end of this chapter, the pros and cons of each method are discussed.

3.1 Complex Modal Analysis (CMA) Method

Depending on the damping characteristics of a system, the mode shapes and natural frequencies of the system are determined as having either real or complex values. If the damping is classical (i.e. proportional), the modal properties are real-valued, otherwise they are complex-valued. In this method the EMDR is directly computed from the complex-valued eigenvalue of each mode.

3.1.1 Normal Modal Analysis

The equation of motion of a viscously damped multi-degree-of-freedom (MDOF) system excited by ground motion is represented by the equation

$$[m]\{\ddot{x}(t)\} + [c]\{\dot{x}(t)\} + [k]\{x(t)\} = -[m]\{i\}\ddot{x}_g(t) \tag{3-1}$$

in which $[m], [c]$ and $[k]$ are the mass, damping, and stiffness matrices of the MDOF system; $\{x(t)\}$ is the column vector of the displacement of nodes relative to ground motion; the dots denote differentiation with respect to time, t; $\{i\}$ is the influence vector ; and $\ddot{x}_g(t)$ is the acceleration ground motion.

The damping of a MDOF system is defined as proportional damping if and only if it satisfies the following Caughey criterion (Caughey and O'Kelley, 1965).

$$[c][m]^{-1}[k] = [k][m]^{-1}[c] \tag{3-2}$$

For a proportionally damped system, the coupled Eq. (3-1) can be decoupled into single-degree-of-freedom (SDOF) systems using normal modal analysis. The solution of each decoupled SDOF system is computed in modal coordinates and the total solution is obtained by combining all the individual responses, which is known as the modal superposition method.

The solution of Eq. (3-1) has the form of $\{x(t)\} = [\Phi]\{q(t)\}$ where $[\Phi]$ is mass normalized mode shape matrix. Substituting this form into Eq. (3-1) and pre-multiplying both sides by $[\Phi]^T$ goes

$$[\Phi]^T[m][\Phi]\{\ddot{q}\} + [\Phi]^T[c][\Phi]\{\dot{q}\} + [\Phi]^T[k][\Phi]\{q\} = -[\Phi]^T[m]\{i\}\ddot{x}_g(t) \tag{3-3}$$

Using modal orthoonality relation, Eq. (3-3) can be rewritten for the nth SDOF equation as

$$\ddot{q}_n(t) + 2\xi_n\omega_n\dot{q}_n(t) + \omega_n^2 q_n(t) = f_n(t) \qquad n = 1, 2, \dots \qquad (3\text{-}4)$$

in which ω_n is the natural frequency of the nth mode; ξ_n is the modal damping ratio of

the nth mode; and $f_n(t)$ is modal force $(f_n(t) = \{\phi_n\}^T[m]\{i\}\ddot{x}_g(t)/\{\phi_n\}^T[m]\{\phi_n\})$.

Thus, the nth mode frequency and damping ratio are

$$\omega_n = \frac{\{\phi_n\}^T[k]\{\phi_n\}}{\{\phi_n\}^T[m]\{\phi_n\}} \qquad (3\text{-}5)$$

$$\xi_n = \frac{\{\phi_n\}^T[c]\{\phi_n\}}{2\omega_n\{\phi_n\}^T[m]\{\phi_n\}} \qquad (3\text{-}6)$$

3.1.2 Complex Modal Analysis and EMDR Estimation

For the proportionally damped system the modal analysis and identification of the damping ratio is straightforward as illustrated above. However, a non-proportionally damped system which does not satisfy Eq. (3-2) has complex-valued eigenvectors and eigenvalues. Because the eigenvectors have different phase at each node of the system, the maximum amplitude at each node does not occur simultaneously.

Modal analysis is still applicable to the non-proportionally damped system; however, it is in the modal domain with complex numbers. Veletsos and Ventura (1986) generalized the modal analysis which is applicable to both proportionally and non-proportionally damped system. In the case of the non-proportionally damped system, Eq. (3-1) can be decoupled using the complex modal analysis by introducing the state space variables $\{z\} = \begin{Bmatrix} \{\dot{x}\} \\ \{x\} \end{Bmatrix}$. Equation (3-1) can be transformed to

21

$$[A]\{\dot{z}\}+[B]\{z\} = \{Y(t)\} \tag{3-7}$$

in which $[A]$ and $[B]$ are $2n$ by $2n$ real matrices as shown below and $\{Y(t)\}$ is a $2n$ component vector.

$$[A] = \begin{bmatrix} [0] & [m] \\ [m] & [c] \end{bmatrix}, \quad [B] = \begin{bmatrix} -[m] & [0] \\ [0] & [k] \end{bmatrix}, \quad \{Y(t)\} = \begin{Bmatrix} \{0\} \\ -[m]\{i\}\ddot{x}_g(t) \end{Bmatrix}$$

The homogeneous solution of Eq. (3-7) is $\{x\} = \{\varphi\}e^{st}$ and its characteristic equation becomes

$$s([A]+[B])\{z\} = \{0\} \tag{3-8}$$

The eigenvalues and eigenvectors of Eq. (3-8) are complex conjugate pairs as given by Eq. (3-9) and (3-10), respectively.

$$\begin{Bmatrix} s_n \\ \bar{s}_n \end{Bmatrix} = -\sigma \pm i\omega_D = -\omega_n \xi_n \pm i\omega_n \sqrt{1-\xi_n^2} \tag{3-9}$$

$$\begin{Bmatrix} \{\psi_n\} \\ \{\bar{\psi}_n\} \end{Bmatrix} = \{\varphi_n\} \pm i\{\chi_n\} \tag{3-10}$$

Finally, the natural frequency and EMDR of a non-proportionally damped system is obtained from Eq. (3-9) as

$$\omega_n = \sqrt{(\operatorname{Re}(s_n))^2 + (\operatorname{Im}(s_n))^2} \tag{3-11}$$

$$\xi_n = \frac{\operatorname{Re}(s_n)}{\omega_n} \tag{3-12}$$

where, $\text{Re}(s_n)$ and $\text{Im}(s_n)$ are the real and imaginary parts of s_n.

3.1.3 Procedure of CMA Method

The steps of applying the CMA method are as follows:

Step 1. Establish mass, stiffness, and damping matrix of a bridge system.

Step 2. Compute $[A]$ and $[B]$ matrix from Eq. (3-7).

Step 3. Obtain eigenvalues of the characteristic equation shown in Eq.(3-8).

Step 4. Compute natural frequency of each mode from corresponding eigenvalue using Eq. (3-11).

Step 5. Compute effective damping ratio of each mode from real part of eigenvalue and natural frequency of corresponding mode using Eq. (3-12).

3.2 Neglecting Off-Diagonal Elements (NODE) Method

In the modal superposition method, the equation of motion of a MDOF system is transformed into modal coordinates so that the coupled equation may be decoupled allowing the solution of the MDOF system to be reduced to the solution of many SDOF systems. However, if the damping matrix is non-proportional, the equation of motion cannot be decoupled by pre- and post-multiplication by undamped normal mode shapes. If the off-diagonal elements in this damping matrix are neglected, the MDOF equation of motion becomes uncoupled allowing the EMDR to be computed from the diagonal elements.

3.2.1 Basic Principles

The coupled matrix equation of motion, Eq. (3-1), is decoupled by transforming the original equation into modal coordinates. If the damping of a system is proportional, pre- and post-multiplication by the mode shape matrix decomposes the damping matrix as shown in Eq. (3-13)

$$[\Phi]^T[c][\Phi] = \begin{bmatrix} \ddots & & 0 \\ & \{\phi_i\}^T[c]\{\phi_i\} & \\ 0 & & \ddots \end{bmatrix} = \begin{bmatrix} \ddots & & 0 \\ & 2\omega_i\xi_i & \\ 0 & & \ddots \end{bmatrix} \tag{3-13}$$

in which $[\Phi]$ is the normal mode shape matrix. From Eq. (3-13) the EMDR for each mode can be calculated as shown in Eq. (3-6).

However, if the damping matrix consists of proportional damping from structure and local damping from the system boundaries or other damping components, as shown in Fig. 3.2.1, the overall damping matrix becomes non-proportional and the MDOF equation cannot be decoupled.

$$[c] = [c_{str}] + [c_{local}]$$
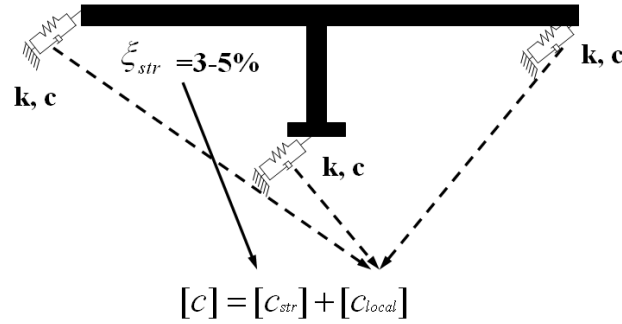
Figure 3.2.1 Non-proportional damping of short-span bridge

As shown in Eq. (3-14), the proportional damping matrix of structure is diagonalized, but the damping matrix composed of boundary damping can not be diagonalized.

$$[\Phi]^T[c][\Phi] = [\Phi]^T[c_{str}][\Phi] + [\Phi]^T[c_{local}][\Phi] = \begin{bmatrix} \ddots & & 0 \\ & c_{i,i}^* & \\ 0 & & \ddots \end{bmatrix} + \begin{bmatrix} c_{1,1} & \cdots & c_{1,n} \\ \vdots & c_{i,i} & \vdots \\ c_{n,1} & \cdots & c_{n,n} \end{bmatrix} \quad (3\text{-}14)$$

If the damping effect from the off-diagonal elements in Eq. (3-14) on overall dynamic response is small, the off-diagonal elements can be neglected and Eq. (3-14) is reduced to Eq. (3-15). From Eq. (3-15), the EMDR of each mode can be computed as Eq. (3-16).

$$[\Phi]^T[c][\Phi] = \begin{bmatrix} \ddots & & 0 \\ & c_{i,i}^* + c_{i,i} & \\ 0 & & \ddots \end{bmatrix} \quad (3\text{-}15)$$

25

$$\xi_i = \frac{c^*_{i,i} + c_{i,i}}{2\{\phi_i\}^T [m]\{\phi_i\}\omega_i}$$ (3-16)

where ξ_i is the i th EMDR.

3.2.2 Error Criteria of NODE Method

The accuracy of the NODE method depends on the significance of the neglected elements on overall dynamic response. Equation (3-17) shows the generalized damping matrix having off-diagonal terms.

$$[\Phi]^T [c][\Phi] = \begin{bmatrix} \{\phi_1\}^T [c]\{\phi_1\} & \cdots & \{\phi_1\}^T [c]\{\phi_n\} \\ \vdots & \ddots & \vdots \\ \{\phi_n\}^T [c]\{\phi_1\} & \cdots & \{\phi_n\}^T [c]\{\phi_n\} \end{bmatrix}$$ (3-17)

Warburton and Soni (1977) proposed a parameter $e_{i,j}$ to quantify the modal coupling for the NODE method as shown below ;

$$e_{i,j} = \frac{\{\phi_i\}^T [c]\{\phi_j\}\omega_i}{\left|\omega_i^2 - \omega_j^2\right|}$$ (3-18)

A small $e_{i,j}$, less than 1, indicates little modal coupling of the ith and j[th] modes. If $e_{i,j}$ is small enough relative to unity for all pairs of modes, the NODE method is thought to yield accurate results.

3.2.3 Procedure of NODE Method

The steps of applying the NODE method are as follows:

Step 1. Establish mass, stiffness, and damping matrix of a bridge system.

Step 2. Compute undamped mode shape and natural frequency of each mode from mass and stiffness matrix.

Step 3. Obtain modal damping matrix by pre- and post-multiplying mode shape matrix to damping matrix as shown in Eq.(3-15).

Step 4. Compute effective damping ratio of each mode from Eq. (3-16) ignoring off-diagonal elements of modal damping matrix.

Step 5. Check error criteria using Eq. (3-18). If a parameter from Eq. (3-18) of any two modes is greater than unity, change to other methods.

3.3 Optimization (OPT) Method

The optimization method in both time domain and frequency domain is used to compute the EMDR. In this method, the damping of a non-proportionally damped model (NP-Model) is approximated by the EMDR for an equivalent proportionally damped model (P-Model) to produce the same damping effect through model iterations.

3.3.1 Basic Principle

In the OPT method, the damping ratio of equivalent P-Model is searched through iteration so that the dynamic responses from P-Model and NP-Model close to each other. The damping matrix of the NP-Model shown in Eq.(3-19) is composed of the damping matrix of concrete structure $[c_{str}]$, which is assumed as the Rayleigh damping, and the damping matrix from other damping components $[c_{local}]$. The damping matrix of the equivalent P-Model shown in Eq. (3-20) is assumed as the Rayleigh damping with coefficients α and β to have the same damping effect of the NP-Model.

$$[c] = [c_{str.}] + [c_{local}] \qquad \text{NP-Model} \qquad (3\text{-}19)$$

$$[c] = \alpha\,[m] + \beta\,[k] \qquad \text{Equivalent P-Model} \qquad (3\text{-}20)$$

The coefficients α and β can be computed from specified damping ratios ξ_i and ξ_j for the ith and jth modes, respectively, as shown in Eq. (3-21)

$$\alpha = \frac{2\omega_i\omega_j}{\omega_i^2 - \omega_j^2}\left(\omega_i\xi_j - \omega_j\xi_i\right)$$

$$\beta = \frac{2}{\omega_i^2 - \omega_j^2}\left(\omega_i\xi_i - \omega_j\xi_j\right)$$

(3-21)

where ω_i and ω_j are natural frequency of the i th and j th modes, respectively.

The damping ratio of n th mode can be determined by Eq. (3-22).

$$\xi_n = \frac{1}{2\omega_n}\alpha + \frac{\omega_n}{2}\beta$$

(3-22)

The optimization method is conducted in both time domain and frequency domain. In the time domain, a time history response from the equivalent P-Model is compared with that of the original NP-Model, while in the frequency domain the frequency response functions of both systems are used in the optimization algorithm.

3.3.2 Time Domain

Figure 3.3.1 (a) shows the flow chart of the optimization method in time domain. The procedures are explained as follows: (1) the initial EMDR of the equivalent proportionally damped system is assumed, (2) time history analysis of both models under a ground motion is performed, (3) an objective function is made by mean-square-error of results from the NP-Model and P-Model as shown in Eq. (3-23), (4) check criterion, (5) if the criterion is not satisfied, the EMDR is updated to minimize the objective function, (6) repeat procedure (2) to (5) until the criteria is satisfied.

$$F = \min\left[\sum_{i=1}^{N}\frac{1}{N}\left(x_i^{np} - x_i^{p}\right)^2\right]$$

(3-23)

29

where the superscript np and p represent the NP-Model and P-Model, respectively, N is total number of analysis time step, and x_i^{np} and x_i^p are the response at the ith time step of the NP-Model and P-Model, respectively.

3.3.3 Frequency Domain

The optimization method in time domain requires the application of a direct numerical integration method such as the Newmark method to compute the dynamic response from both the non-proportionally and proportionally damped models. However, the time history analysis can be avoided in frequency domain by establishing the objective function as being composed of the frequency response function of both models.

The optimization method in the frequency domain, shown in Fig. 3.3.1 (b), is almost the same as that in time domain. However, instead of computing the response time history, the frequency response functions of both models are utilized in this method. The frequency response function is defined by Eq. (3-24) where $X(j\omega)$ is the Fourier Transform of the response; $F(j\omega)$ is the Fourier Transform of the input force.

$$H(j\omega) = \frac{X(j\omega)}{F(j\omega)} \qquad (3\text{-}24)$$

The equation of motion of a MDOF system subject to ground motion is shown in Eq. (3-25). The Fourier Transform of the second-order equation of motion reduces the original problem into a linear algebraic problem as shown in Eq. (3-26) where j is $\sqrt{-1}$; $X(j\omega)$ and $X_G(j\omega)$ are the Fourier Transforms of the response and ground motion accelerations, respectively; and ω is circular frequency in rad/sec.

$$[m]\{\ddot{x}(t)\}+[c]\{\dot{x}(t)\}+[k]\{x(t)\}=-[m]\{i\}\ddot{x}_g(t) \tag{3-25}$$

$$\left[[k]-\omega^2[m]+j\omega[c]\right]\{X(j\omega)\}=-[m]\{i\}X_G(j\omega) \tag{3-26}$$

The frequency response function is expressed by Eq. (3-27)

$$[H(j\omega)]=\frac{X(j\omega)}{F(j\omega)}=\frac{1}{[k]-\omega^2[m]+j\omega[c]} \tag{3-27}$$

where $F(j\omega)$ is $-[m]\{i\}X_G(j\omega)$.

The mass and stiffness matrices of the frequency response function of both models are the same but the damping matrix of both models is different. The damping matrix of the non-proportionally damped and the proportionally damped model in Eq. (3-27) are expressed as Eq. (3-19) and (3-20).

The objective function in the frequency domain is composed of frequency response functions of both P-Model and NP-Model shown in Eq. (3-28).

$$F=\min\left[\sum_{i=1}^{M}\frac{1}{M}\left[H^{np}(j\omega_i)-H^{p}(j\omega_i)\right]^2\right] \tag{3-28}$$

where $H^{np}(j\omega_i)$ and $H^{p}(j\omega_i)$ are the frequency response functions of the non-proportionally and equivalent proportionally damped systems at ω_i, respectively, and M is total number of frequencies considered.

If the damping of the non-proportionally damped system is hysteretic, the frequency response function in Eq. (3-27) changes to

31

$$H(j\omega) = \frac{1}{[k] - \omega^2 [m] + j[\hat{k}]}$$

(3-29)

where, $[\hat{k}]$ is a stiffness matrix for the entire system obtained by assembling individual

finite-element stiffness matrices $[\hat{k}^{(m)}]$ of the form (superscript m denotes element m)

$$[\hat{k}^{(m)}] = 2\xi^{(m)}[k^{(m)}]$$

(3-30)

in which $[k^{(m)}]$ denotes the individual elastic stiffness matrix for an element m as used in

the assembly process to obtain the stiffness matrix $[k]$ for the entire system; and $\xi^{(m)}$ is a

damping ratio selected to be appropriate for the material used in element m .

The frequency response function of a proportionally damped system is shown in Fig.
3.3.2 for several different values of the EMDR. The peaks of the frequency response
function correspond to the natural frequencies of the system. As seen in these figures,
the overlapping of frequency response function with adjacent modes increases as the
EMDR increases. However, the natural frequencies (i.e. peaks) do not move by
increasing the EMDR but they change in the non-proportionally damped system with
increases in the damping of local damping components. Thus, if the undamped and
damped natural frequencies of a non-proportionally damped system are not close to each
other, the accuracy of the frequency domain optimization is not guaranteed.

3.3.4 Procedure of OPT Method

The steps of applying the OPT method in time domain are as follows:

Step 1. Establish mass, stiffness, and damping matrix of a bridge system.

Step 2. Compute undamped natural frequencies.

Step 3. Specify damping ratios of two modes of P-Model as Rayleigh damping and compute α and β using Eq. (3-21).

Step 4. Compute damping matrix of P-Model as shown in Eq. (3-20).

Step 5. Compute seismic responses of both NP-Model and P-Model through time history analysis.

Step 6. Evaluate objective function of Eq. (3-23). If a value from objective function is smaller than criterion, go to step 8.

Step 7. Repeat from step 3 to step 6.

Step 8. Compute damping ratios of other modes using Eq. (3-22).

The procedure of the OPT method in frequency domain is as follows:

Step 1 to step 4 are the same as those in time domain method above.

Step 5. Compute frequency response function of both NP-Model and P-Model using Eq. (3-27)

Step 6. Evaluate objective function of Eq. (3-28). If a value from objective function is smaller than criterion, go to step 8.

Step 7. Repeat from step 3 to step 6.

Step 8. Compute damping ratios of other modes using Eq. (3-22).
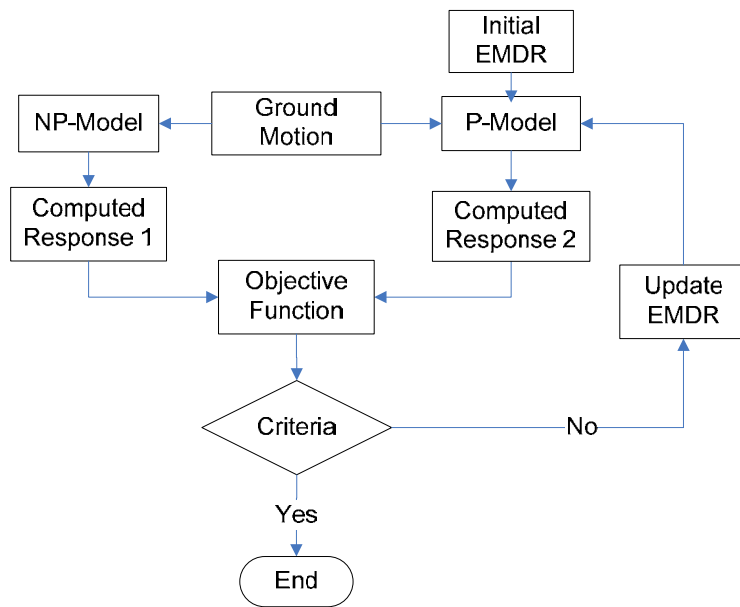
(a) Time domain
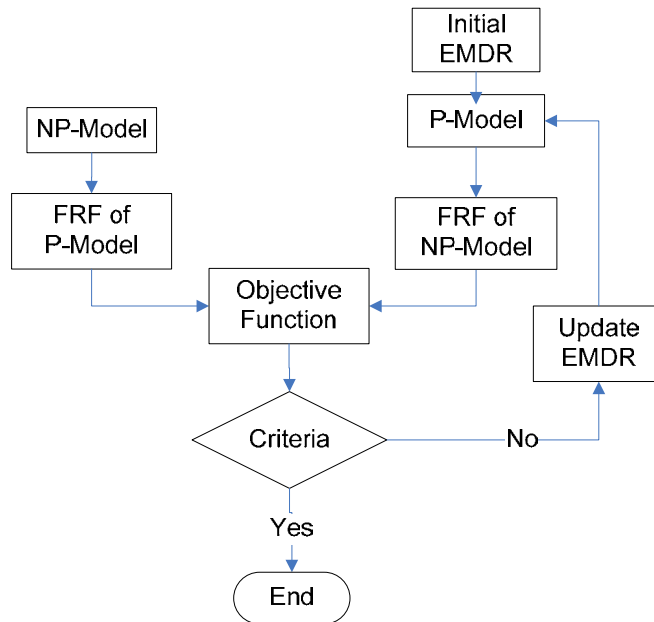
(b) Frequency domain

Figure 3.3.1 Flow chart of optimization method
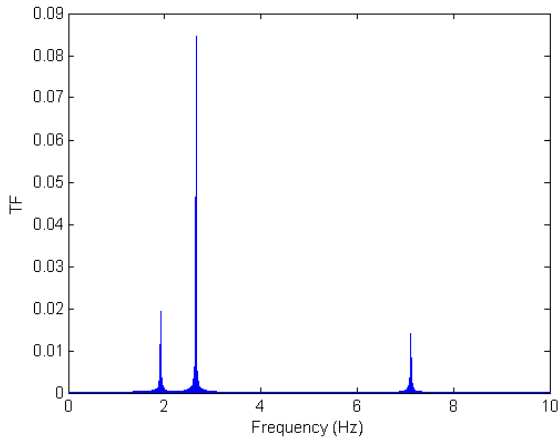
(a) EMDR=0%
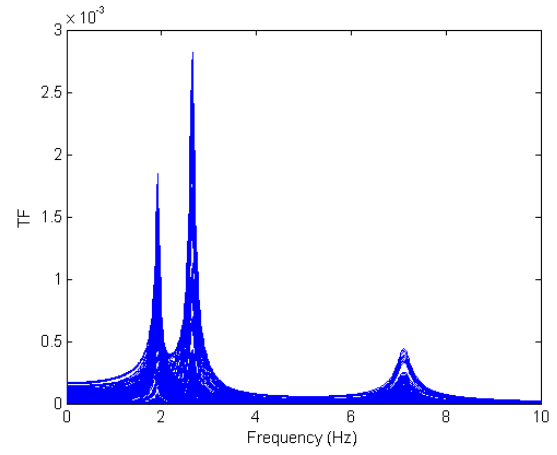
(a) EMDR=2%
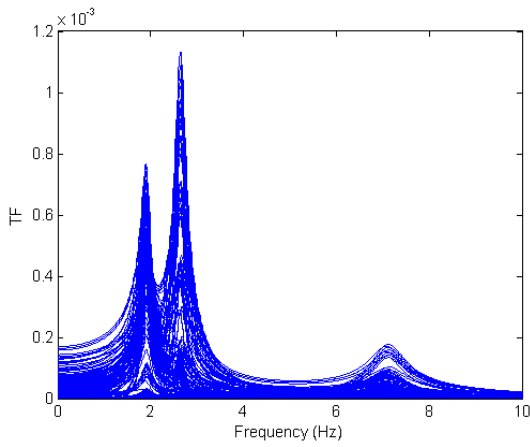
(c) EMDR=5%
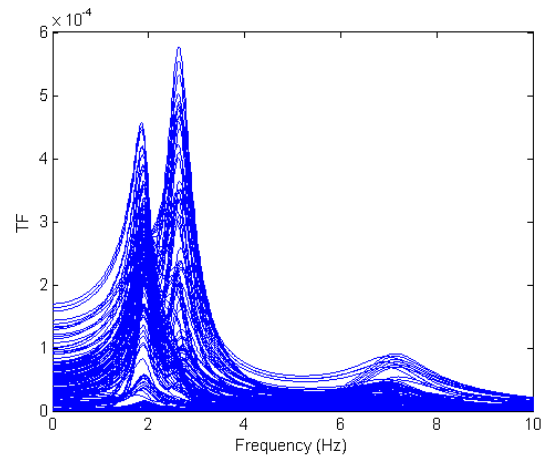
(d) EMDR=10%

Figure 3.3.2 Frequency response function for different EMDR

3.4 Composite Damping Rule (CDR) Method

The composite damping rule was suggested by Raggett (1975) for calculation of the EMDR of building structures with different damping components. This method is based on the assumption of viscous damping of the components. Hwang and Tseng (2005) applied this method to compute the EMDR for the design of viscous dampers to reduce the seismic hazard of highway bridges. The basic principle of this method is described here.

3.4.1 Basic Principle

The total dissipated energy of a linear system with different damping components is the sum of the dissipated energy of each component as shown in Eq. (3-31).

$$E_t = \sum_i E_i \tag{3-31}$$

If equivalent viscous damping is assumed for each component, the dissipated energy from each component is

$$E_i = 4\pi \, \xi_i \, U_i \tag{3-32}$$

where, ξ_i is the component energy dissipation ratio; U_i is the peak component energy per cycle of motion.

From Eqs. (3-31) and (3-32), the total dissipated energy is

$$E_t = 4\pi \sum_i \xi_i \, U_i = 4\pi \, \xi_t \, U_t \tag{3-33}$$

where, ξ_t is the total modal viscous damping ratio (EMDR); U_t is the total peak potential energy per cycle of motion. From Eq. (3-33), the EMDR is

$$\xi_t = \sum_i \xi_i \frac{U_i}{U_t} \tag{3-34}$$

Equation (3-34) shows that the EMDR is equal to the sum of the damping ratios of each component weighted by the ratio of the components potential energy to the total potential energy. The potential energy of the total system and of each component are computed by Eq. (3-35) and after substituting $\{x\} = \{\phi\}q(t)$ into the potential energy ratio (U_i/U_t) is given by (3-36).

$$U_t = \frac{1}{2}\left|\{x\}^T[k_t]\{x\}\right|$$

$$\tag{3-35}$$

$$U_i = \frac{1}{2}\left|\{x\}^T[k_i]\{x\}\right|$$

$$\frac{U_i}{U_t} = \frac{\left|\{\phi\}^T[k_i]\{\phi\}\right|}{\left|\{\phi\}^T[k_t]\{\phi\}\right|} \tag{3-36}$$

where $\{\phi\}$ is the mode shape; $[k_t]$ is the system stiffness matrix of the entire system; $[k_i]$ is the system stiffness matrix having all zero elements except for the stiffness of the ith component.

Another method which is conceptually very similar to the composite damping rule method is the modal strain energy method. This method was developed by Johnson and

Kienhholz (1982). Though it was first developed for aerospace structures with viscoelastic material, this method has been applied to concrete and steel frames with viscoelastic dampers (Shen and Soong, 1995; Chang et al, 1995).

The dissipated energy per cycle through viscous damping is proportional to response frequency. However, many tests indicate that the energy loss is essentially independent of frequency (Clough and Penzien, 1993). Therefore, hysteretic damping, in which the damping force is proportional to the displacement amplitude and in phase with velocity, is used in the modal strain energy method.

The damping force of hysteretic damping is expressed as

$$f_d(t) = i\eta\,k\,x(t) \qquad (3\text{-}37)$$

where i is $\sqrt{-1}$ which puts the damping force in phase with the velocity; η is the hysteretic damping coefficient; k is the elastic stiffness of a component; and $x(t)$ is the displacement of the component.

Considering the complex damping force combined with the elastic force, the equation of motion of free vibration is expressed as

$$[m]\{\ddot{x}\} + [k + i\eta\,k]\{x\} = \{0\} \qquad (3\text{-}38)$$

If a system has different damping components such as an embankment at short-span bridges or isolation bearings at isolated bridges, the complex-stiffness in Eq. (3-38) is comprised of two parts as shown in Eq. (3-39).

$$[k + i\eta k] = [k_1] + [k_2] + i(\eta_1[k_1] + \eta_2[k_2]) \tag{3-39}$$

where, $[k_1]$ is the elastic stiffness matrix of the structures concrete components; $[k_2]$ is the elastic stiffness matrix of the soil boundary components; η_1 and η_2 are the hysteretic damping coefficients corresponding to $[k_1]$ and $[k_2]$, respectively.

The total hysteretic damping energy of the system is the sum of the hysteretic damping energies of all components.

$$\eta_{i,eq}\{\phi_i\}^T ([k_1] + [k_2])\{\phi_i\} = \eta_1 \{\phi_i\}^T [k_1]\{\phi_i\} + \eta_2 \{\phi_i\}^T [k_2]\{\phi_i\} \tag{3-40}$$

where, $\eta_{i,eq}$ is the EMDR of the ith mode; $\{\phi_i\}$ is the ith mode shape.

Therefore, the EMDR of the ith mode is

$$\eta_{i,eq} = \frac{\eta_1 \{\phi_i\}^T [k_1]\{\phi_i\} + \eta_2 \{\phi_i\}^T [k_2]\{\phi_i\}}{\{\phi_i\}^T ([k_1] + [k_2])\{\phi_i\}} \tag{3-41}$$

Replacing $[k_2]$ in Eq. (3-41) with $[k_2] = [k_1] + [k_2] - [k_1]$, Eq. (3-41) becomes

$$\eta_{i,eq} = \frac{\eta_1 \{\phi_i\}^T [k_1]\{\phi_i\}}{\{\phi_i\}^T ([k_1] + [k_2])\{\phi_i\}} + \eta_2\left(1 - \frac{\{\phi_i\}^T [k_1]\{\phi_i\}}{\{\phi_i\}^T ([k_1] + [k_2])\{\phi_i\}}\right) \tag{3-42}$$

Finally, the EMDR of the ith mode of the modal strain energy method is

$$\eta_{i,eq} = \eta_2 - (\eta_2 - \eta_1)\frac{\{\phi_i\}^T [k_1]\{\phi_i\}}{\{\phi_i\}^T ([k_1] + [k_2])\{\phi_i\}} \tag{3-43}$$

Or, applying the relation $\{\phi_i\}^T([k_1]+[k_2])\{\phi_i\} = \omega_i^2$, Eq. (3-43) can be simplified to Eq. (3-44).

$$\eta_{i,eq} = \eta_2 - (\eta_2 - \eta_1)\frac{\{\phi_i\}^T[k_1]\{\phi_i\}}{\omega_i^2} \qquad (3\text{-}44)$$

In the modal strain energy method, the true damped mode shapes are approximated by undamped normal mode shapes. From Eq. (3-44), the EMDR of a bridge system $(\eta_{i,eq})$ is always lower than the highest damping ratio of components (η_2).

3.4.2 Procedure of CDR Method

The steps of the CDR method are as follows:

Step 1. Establish mass and stiffness matrix of a bridge system.

Step 2. Obtain undamped mode shapes.

Step 3. Compute potential energy ratio of each component for each mode using Eq. (3-36).

Step 4. Compute EMDR using Eq. (3-34).

3.5 Summary

The four damping estimating methods (CMA, NODE, OPT, and CDR) used to approximate the EMDR of non-proportionally damped systems are discussed above. Each method has pros and cons. Some important features of each when they are applied to compute the EMDR are described here.

The CMA method is thought to be an exact solution of the EMDR. This method involves establishing the mass, stiffness, and damping matrices of a system and carrying out a complex modal analysis to determine the eigenvalues of the system.   However, the EMDR of each mode is determined easily once the eigenvalue of each mode is attained.

In the NODE method, the damping coefficient values are needed as in the CMA method for the computation of the EMDR. The mode shapes from an undamped system should be computed from normal modal analysis to get the generalized damping matrix. This method is very easy to implement, however, the accuracy depends on the significance of modal coupling between the modes (Warburton and Soni, 1977) and also the location of the different damping components as shown in Veletsos and Ventura (1986).

The OPT method in the time domain is the only method which requires response time history analysis to compute the EMDR among the proposed methods. As applied in the frequency domain, a frequency response function is utilized to establish the objective function. The unique advantage of the frequency domain method is that the complex frequency-dependent stiffness can be accommodated easily, which is very difficult in the other methods. Damping coefficients are required to compute the EMDR in both the time and frequency domain methods .

Instead of damping coefficient values, the CDR method needs the damping ratio of the individual structural components. For the computation of the EMDR, the potential energy of an entire system and each component of the system should be computed. This process also requires mode shapes of the system.

Chapter 4

APPLICATION TO SHORT-SPAN BRIDGE

In this chapter, the four methods described for estimating the damping in the previous chapter are applied to a short-span bridge. The Painter Street Overcrossing (PSO), which has strong earthquake recordings, is chosen as an example bridge. The whole analysis procedure is explained first and then the description of the bridge and the finite element modeling of the bridge are presented, followed by the application and results of each method.

4.1 Analysis Procedure

The application and verification of the four damping estimating methods is summarized in Fig. 4.1.1. The finite element model of the PSO was established first. The damping of the finite element model is composed of two components: i) damping from the concrete structure part which is assumed as Rayleigh damping, and ii) damping from the bridge boundary which is assumed as viscous damping. The boundary condition of the bridge under strong earthquake was modeled with a viscoelastic element. The linear elastic stiffness and viscous damping coefficient of the element were determined by utilizing the recorded data through optimization. Because of the viscous damping at the boundary, the

finite element model of the bridge is a non-proportionally damped model which is denoted as NP-Model in Fig. 4.1.1.

After establishing the NP-Model, the damping of the NP-Model is approximated with the EMDR for each mode, applying each damping estimating method. Therefore, the EMDR is thought to have the same damping effect as the NP-Model. The NP-Model is changed to an equivalent proportionally damped model (P-Model) with the previously determined EMDR. The mass and stiffness matrices of the NP-Model and P-Model are the same but only the damping of the NP-Model is approximated with the EMDR. Now, based on the P-Model, the mode shapes and undamped natural frequencies which will be used in the modal combination can be computed. The computed responses from the NP-Model and P-Model under a strong ground motion are termed 'Computed response 1' and 'Computed response 2', respectively, in Fig. 4.1.1. The time history response of the NP-Model was computed by the Newmark integration method; however, that of the P-Model was calculated by the modal superposition method using the EMDR of each mode.

With the mode shapes, natural frequencies, and the EMDR of each mode, the response spectrum method can be applied to compute the seismic demand on the bridge. The modal combination results are termed 'Computed response 3' in Fig. 4.1.1. Instead of using a constant modal damping ratio for all modes considered, different modal damping ratios from the EMDR estimation methods are used for the modal combination results.

The finite element modeling of the bridge with the boundary elements is validated by comparing the 'Measured response' and 'Computed response 1' and the accuracy of the EMDR by each method is verified by comparing the 'Computed response 1' and 'Computed response 2'. Finally, the application of the response spectrum method with

the approximated mode shapes, natural frequencies, and EMDR to compute the seismic demand of the NP-Model is verified by comparing the peak value of the 'Measured response' and 'Computed response 3'. The validation lists and comparable responses are summarized in Table 4.1.1.

Table 4.1.1 Summary of validation check

Validation	Comparable responses
FE modeling and boundary condition	Measured & Computed response 1
Estimation of EMDR	Computed response 1 & 2
Response spectrum method for NP-Model	Computed response 1 & 3
Overall performance	Measured & Computed response 3
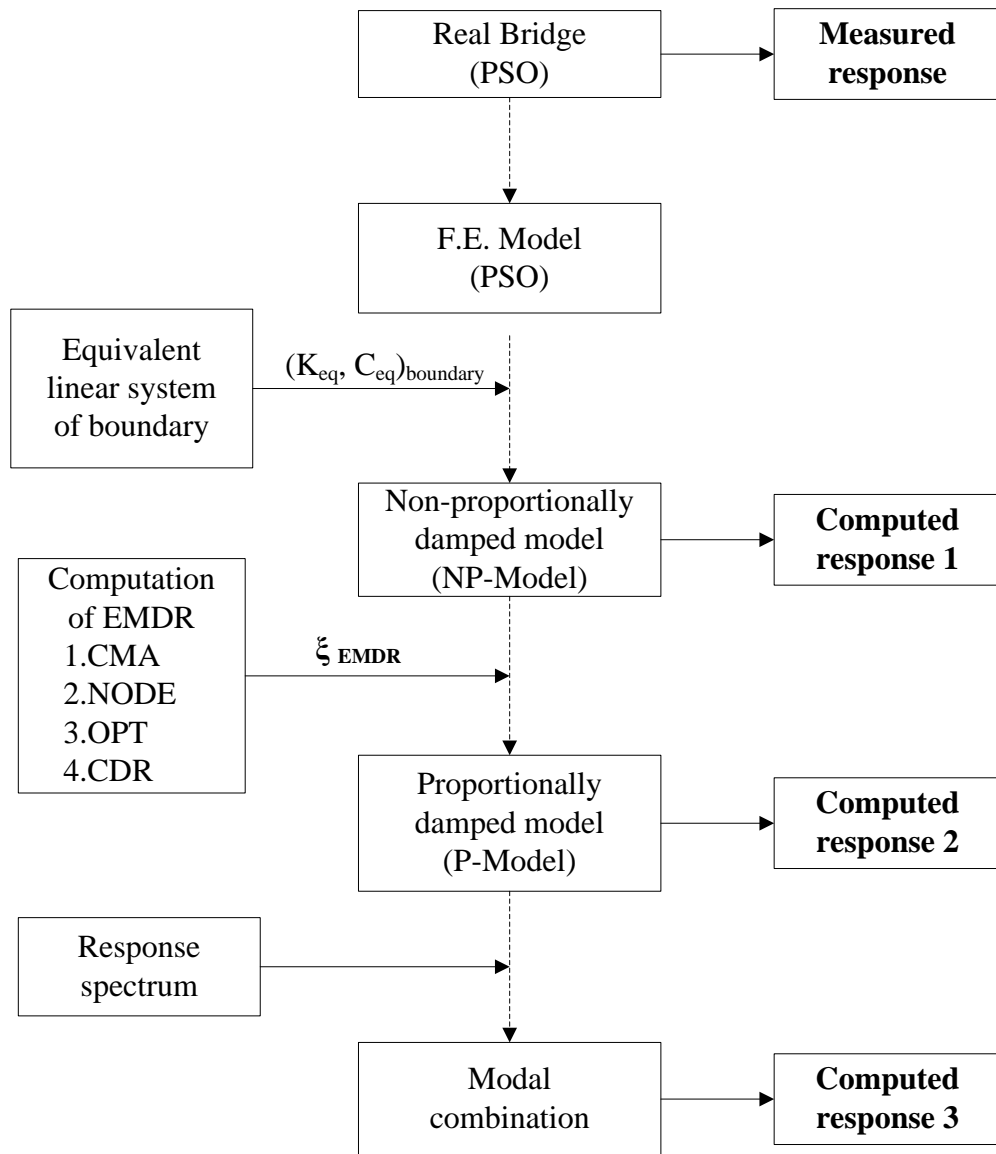
Figure 4.1.1 Analysis procedure

4.2 Example Bridge and Earthquake Recordings

The description of the PSO and the sensor locations of the monitoring system are presented in this section. In addition, the recorded free field ground motions are shown.

4.2.1 Description of Painter St. Overpass

The PSO, shown in Fig. 4.2.1, is located in Rio Dell, California. The bridge consists of a continuous reinforced concrete, multi-cell, box-girder deck and is supported on integral abutments at both ends and a two-column center bent. It has two unequal spans of 119 and 146 ft. Both abutments are skewed at an angle of $38.9°$. The east abutment is monolithically connected to the deck, but the west abutment contains a thermal expansion joint between the abutment diaphragm and the pile cap of the abutment.

4.2.2 Recorded Earthquakes and Dynamic Responses

To date, the monitoring system installed at the PSO has recorded 9 sets of earthquake data. Among them, 6 earthquakes were selected for use in this study based on the availability of all channel data. The peak ground acceleration (PGA) and bridge response are summarized in Table 4.2.1. The free field ground motion acceleration, velocity, and displacement time histories of the six earthquakes are shown in Appendix A. The recorded PGA varied from 0.06g to 0.54g in the transverse direction. In this chapter, the results of the analysis under only the Cape Mendocino/Petrolina Earthquake in 1992, which is the strongest earthquake, are presented.
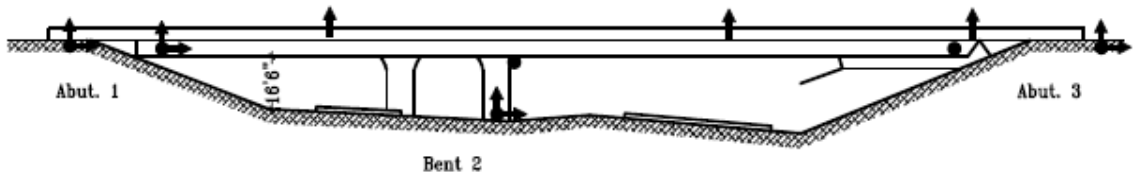
(a) Elevation view
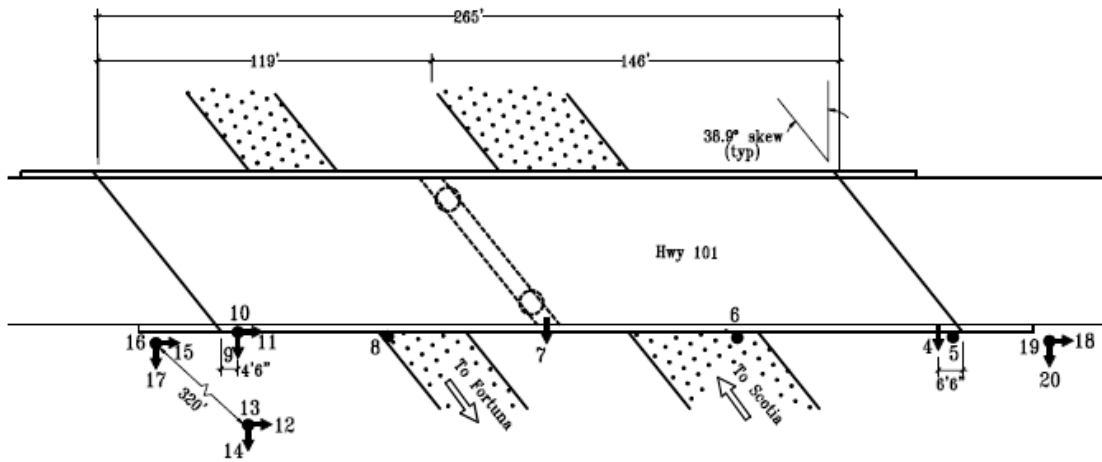
(b) Plan view
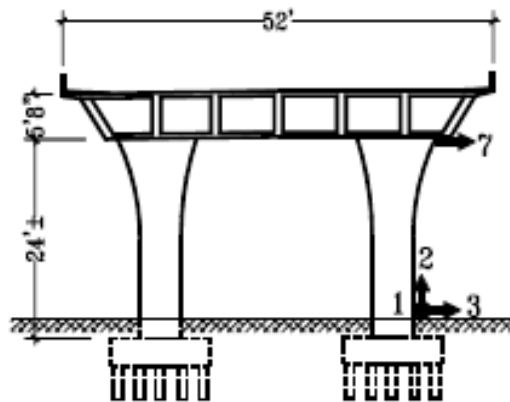
(c) Section at bent 2

Figure 4.2.1 Description of PSO and sensor locations

Figure 4.2.2 shows the free field ground motion of the Cape/Mendocino Earthquake in the transverse direction. The PGA was 0.54g and the dominant frequency of the ground motion was found as 2-2.5Hz as shown in Fig. 4.2.2. The acceleration response at the top of both embankments are displayed in Fig. 4.2.3 along with the free field ground motion. The PGA of 0.54g was amplified to 1.34g and 0.78g at the West and East embankments, respectively. The different amplification effect is attributed to the different conditions of the abutment-deck connection. The deck of the East side is monolithic with the pile foundation cap, however, the deck is resting on a neoprene pad on the West side. The effect of the different boundary conditions on the acceleration response at both ends of the deck is shown in Fig. 4.2.4.
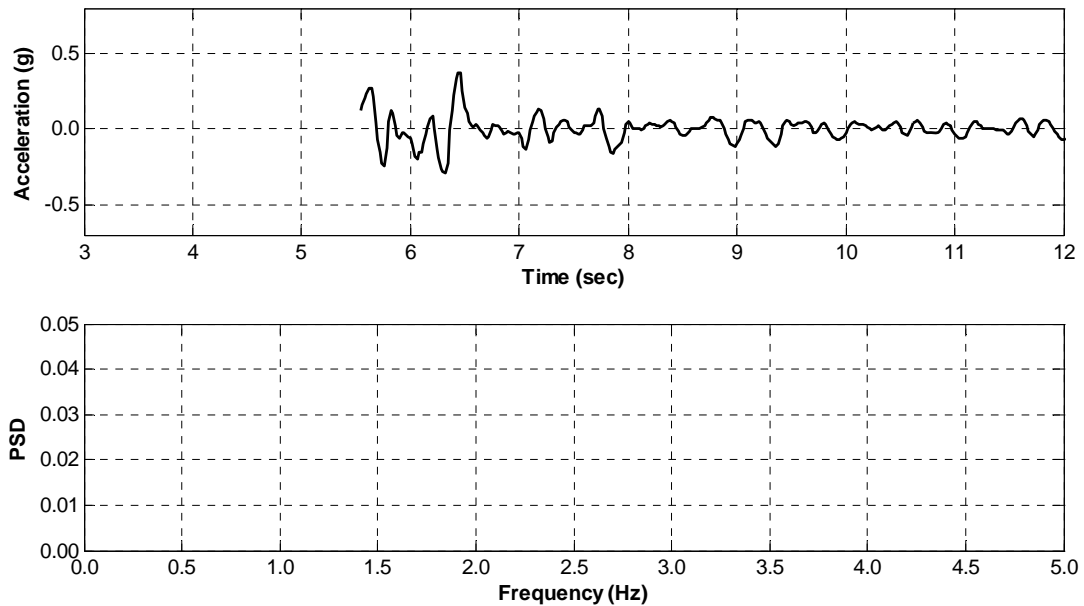
Figure 4.2.2 Cape Mendocino/Petrolina Earthquake in 1992
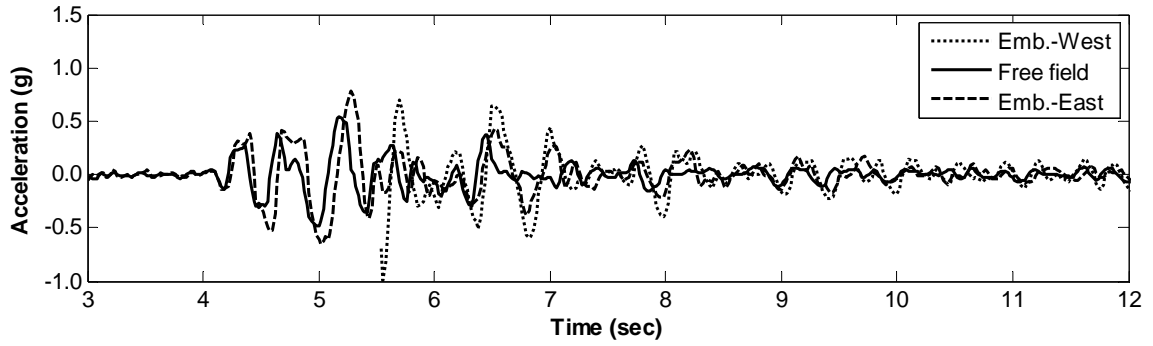
Figure 4.2.3 Acceleration response at embankment of PSO
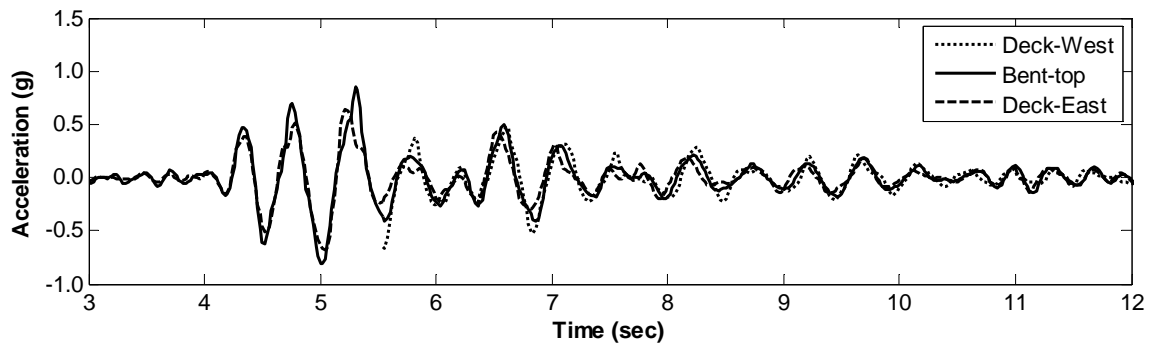
Figure 4.2.4 Acceleration response at deck of PSO

Table 4.2.1 Peak acceleration of earthquake recording

| Earthquake | Maximum acceleration (g) in transverse direction | | | | | |
| | Free field | Deck | | | Embankment | |
		East	West	Center	East	West
Cape Mendocino (1986)	0.15	0.22	0.16	0.25	0.22	0.30
Aftershock	0.12	0.30	0.21	0.35	0.22	0.22
Cape Mendocino (1987)	0.09	0.24	0.17	0.33	0.15	0.23
Cape Mendocino/Petrolina (1992)	0.54	0.69	1.09	0.86	0.78	1.34
Aftershock 1	0.52	0.60	0.76	0.62	0.72	0.83
Aftershock 2	0.20	0.26	0.31	0.30	0.31	0.32

4.3 Seismic Response from NP-Model

In order to include the energy dissipation from boundary soil, the bridge boundaries were modeled with equivalent viscoelastic elements. The effective elastic stiffness and damping of the elements were estimated to minimize the error between the simulated and measured response.

4.3.1 Modeling of Concrete Structure

Figure 4.3.1 shows the finite element model of the PSO. The deck and bent are composed of 10 and 4 elements, respectively. Each node was assumed to have 2 degrees-of-freedom, i.e. displacement in the Y direction and rotation about the Z-axis for deck elements and displacement in the Y direction and rotation about the X-axis for column elements. In totality, the finite element model has 30 degrees-of-freedom. The original two columns of the center bent of the bridge were combined as one equivalent member in the finite element model for simplification. The effective viscoelastic elements at the bridge boundaries were assumed to act only in the transverse direction. The rotational degree-of-freedom at the bottom of the bent was assumed to be fixed.

Table 4.3.1 shows the element properties used in the finite element model. The Young's modulus of concrete was assumed to be 80% of its initial value after considering the ageing effect (Zhang and Makris, 2002). The damping ratio of the concrete structure part of the system was assigned 5% Rayleigh damping. The mass of the deck and bent was lumped at each node and rotational mass was not considered.
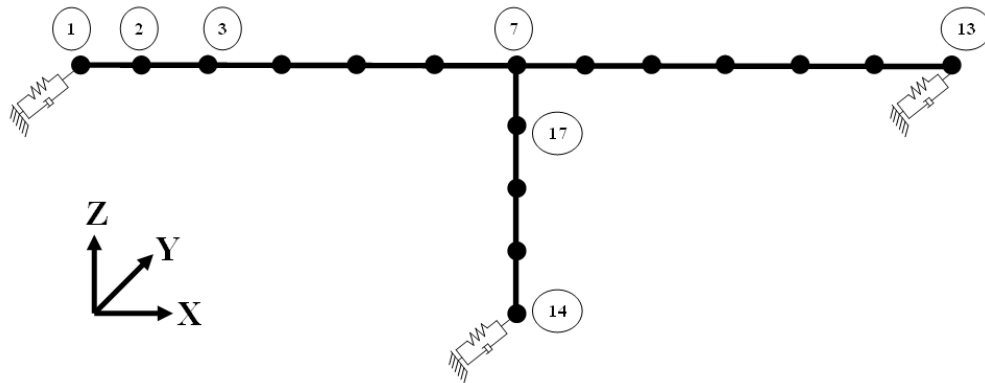
Figure 4.3.1 Finite element model of PSO

Table 4.3.1 Element properties of finite element model of PSO

Properties	Deck	Column
Mass density (ρ)	2,400kg/m^3	2,400kg/m^3
Young's modulus (E_c)	22GPa	22GPa
Sectional area (A)	8.29m^2	1.92m^2
Moment of inertia (I)	153.90m^4	0.29m^4

4.3.2 Estimation of Boundary Condition and Response from NP-Model

The shear modulus and damping characteristics of the boundary soils change depending on soil properties (Seed and Idriss, 1970). In the previous study (Goel, 1997), the natural frequency of the PSO was observed to vary according to the ground motion intensity during the Cape Mendocino/Petrolina earthquake, which indicates the nonlinearity of the boundary soils. However, instead of a non-linear model, an equivalent viscoelastic

model composed of linear elastic stiffness and viscous damping was adopted to represent the bridge boundaries for application of the damping estimating methods.

The effective stiffness and the damping coefficients were estimated by minimizing the square error between the measured and computed response. The optimization procedure is shown in Fig. 4.3.2. The free field ground motion in the transverse direction was used as an input ground motion and the response at the top of the bent was chosen for comparison. The objective function was constituted by the sum of squares of the difference between the measured and computed response and the power spectral density as shown in Eq. (4-1) (Li and Mau, 1991).

$$F = \frac{\sum_i \left(x_i^{meas} - x_i^{comp}\right)^2}{\sum_i \left(x_i^{meas}\right)^2} \;+\; \frac{\sum_j \left\{p(\omega_j)^{meas} - p(\omega_j)^{comp}\right\}^2}{\sum_j \left\{p(\omega_j)^{meas}\right\}^2} \tag{4-1}$$

where, F is the objective function; x_i is the response at the ith time step; $p(\omega_j)$ is the power spectral density of response at frequency ω_j; superscript *meas* and *comp* means 'Measured response' and 'Computed response', respectively.

Table 4.3.2 shows the final identified results for the equivalent viscoelastic model of the bridge boundaries. Figures 4.3.3 and 4.3.4 show the response time histories and power spectral densities of the PSO at the top of the bent obatained from both measurement and simulation under the Cape Mendocino/Petrolina Earthquake in 1992. From the figures, both in time domain and frequency domain, the computed response shows good agreement with the measured response.
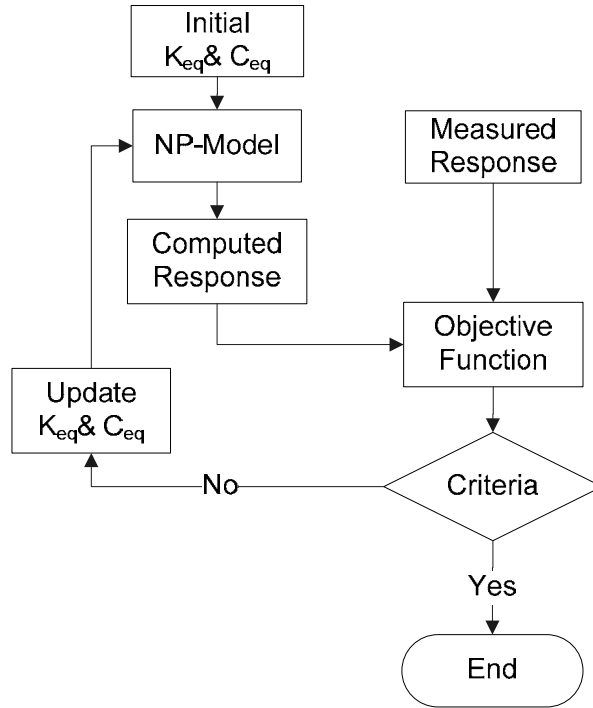
Figure 4.3.2 Optimization algorithm for estimating boundary condition

Table 4.3.2 Effective stiffness and damping coefficient of PSO boundary

Boundary		Identified
Spring stiffness **(MN/m)**	East Abutment	78
	West Abutment	78
	Bent	642
Damping coefficient **(MN·sec/m)**	East Abutment	5
	West Abutment	5
	Bent	5
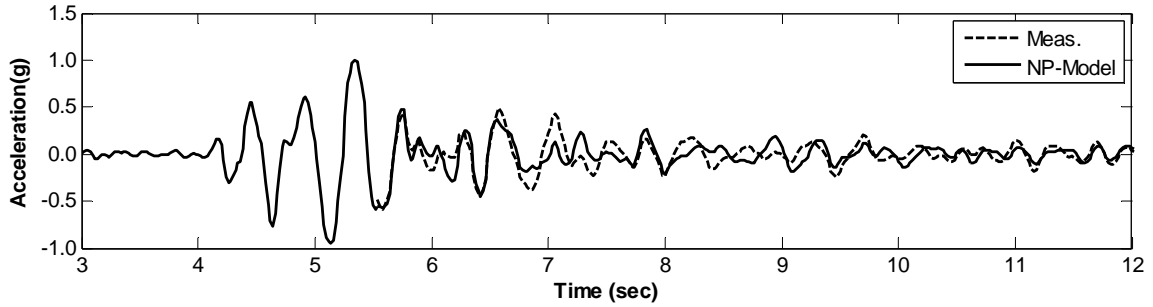
Figure 4.3.3 Comparison of response time history
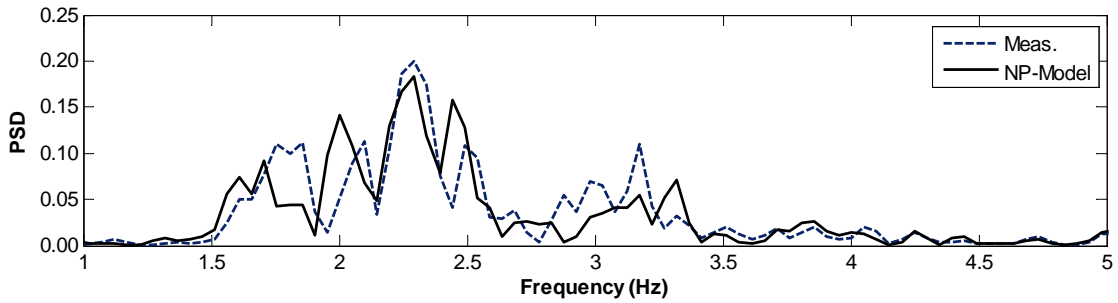
Figure 4.3.4 Comparison of power spectral density

4.3.3 Natural Frequencies and Mode Shapes

The natural frequencies and mode shapes obtained from the eigen analysis of the undamped model of the PSO are given in Table 4.3.3 and Fig. 4.3.5. The mode shapes in Fig. 4.3.5 are the mass normalized mode shapes. The first and second mode frequencies were computed as 1.696 and 2.643 Hz, respectively, which are in the dominant frequency range of the earthquake as shown in Fig. 4.2.2.

The boundary springs at both ends of the deck deform in the same direction as the bent in the first mode, but they deform in opposite directions in the third mode. In the second mode, the bent does not deform much, but the boundary springs at both ends of the deck exhibit large deformations in opposite directions to each other.

Table 4.3.3 Natural frequency and period of PSO

No. of mode	Painter St. Overpassing	
	Frequency (Hz)	Period (sec)
1	1.648	0.606
2	2.643	0.378
3	7.329	0.136
4	18.832	0.053
5	23.762	0.042
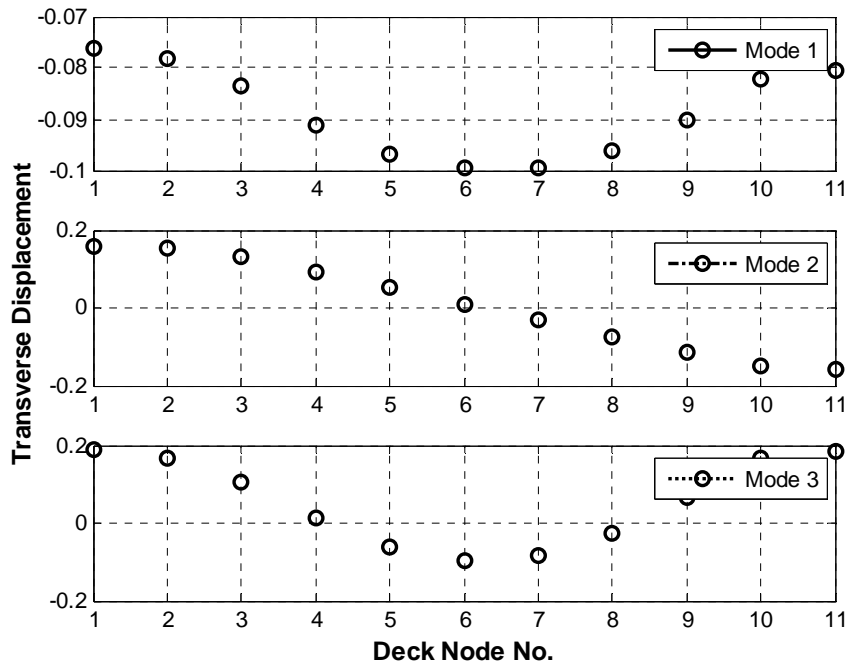
(a) Deck
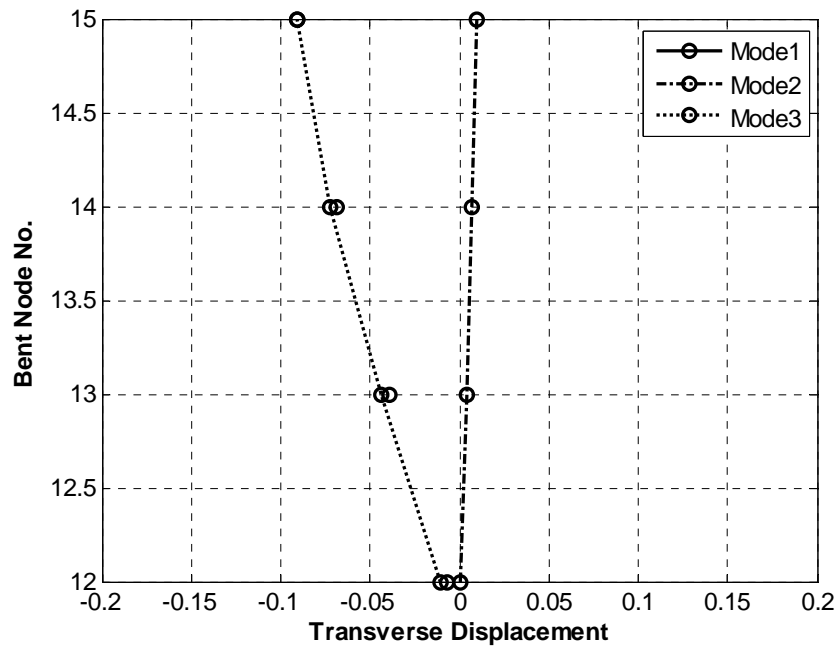
(b) Bent

Figure 4.3.5 Mode shape of PSO

4.4 EMDR Estimation

Based on the NP-Model of the PSO, each damping estimating method is applied to determine the EMDR of each mode. The responses from the NP-Model, P-Model, and the measured response at the top of the bent are compared to verify each method. The results of the EMDR from each method is summarized in Table 4.4.10, and the comparison of the peak response values from each method is given in Table 4.4.11 and 4.4.12.

4.4.1 Complex Modal Analysis (CMA) Method

The NP-Model of the PSO is analyzed using the CMA method to obtain the EMDR. The procedure of the CMA method is explained as follows:

Step 1. Establish mass, stiffness, and damping matrix of a bridge system.

- The element used for deck and bent of the PSO is shown in Fig. 4.4.1. The lumped mass matrix $[m^e]$ of the element which has 2 degrees-of-freedom is represented as Eq. (4-2). The matrix has half of the element mass at each translational nodal degree-of-freedom. In Eq. (4-2), ρ is the mass density of concrete, A is the area of element section, and l is element length. The global mass matrix of whole bridge system is obtained by assembling each element mass matrix.

$$[m^e] = \frac{\rho A l}{2} \begin{bmatrix} 1 & 0 & 0 & 0 \\ 0 & 0 & 0 & 0 \\ 0 & 0 & 1 & 0 \\ 0 & 0 & 0 & 0 \end{bmatrix} \tag{4-2}$$

- The stiffness matrix of the element shown in Fig. 4.4.1 is shown in Eq. (4-3)

$$[k^e] = \frac{EI}{l^3} \begin{bmatrix} 12 & 6l & -12 & 6l \\ 6l & 4l^2 & -6l & 2l^2 \\ -12 & -6l & 12 & -6l \\ 6l & 2l^2 & -6l & 4l^2 \end{bmatrix}$$

(4-3)

where E is Young's modulus of element and I is the moment of inertia. Global stiffness matrix is obtained by assembling each element stiffness matrix. The boundary spring stiffnesses found in section 4.3.2 are directly added to corresponding degree-of-freedom elements in the global stiffness matrix.
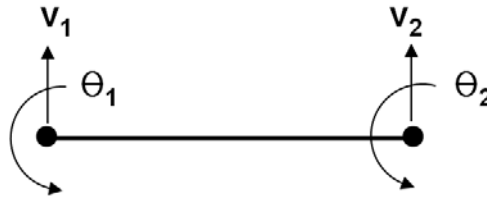
Figure 4.4.1 Element degree-of-freedom

- The damping of concrete structure of the PSO is assumed as 5% Rayleigh damping. The damping coefficient α and β can be found by specifying 5% damping ratio to any two modes. In this research, it was assigned to the first and third mode. So, the damping matrix of the concrete structure is $[c_{str}] = \alpha[m] + \beta[k]$. The damping matrix of the bridge boundary $[c_{local}]$ has zero elements except the corresponding degree-of-freedom elements of boundary damping found in section 4.3.2. The global damping matrix is obtained by adding $[c_{str}]$ and $[c_{local}]$

Step 2. Obtain $[A]$ and $[B]$ matrix using Eq. (3-7).

Step 3. Compute eigenvalues of the characteristic equation shown in Eq.(3-8).

- The dimension of the matrix $[A]$ and $[B]$ is $2n \times 2n$ (n is the total number of degree-of-freedom), and $2n$ conjugate eigenvalues are obtained from eigen analysis. The second column of Table 4.4.1 shows the eigenvalues of the NP-Model of the PSO from the complex modal analysis.

Table 4.4.1 Eigenvalues and natural frequencies of NP-Model of PSO

Mode	Eigenvalues	Natural frequency (rad/sec)
1	2.674 –10.291i	$\sqrt{2.674^2 + 10.291^2} = 10.633$
2	9.288 – 14.054i	$\sqrt{9.288^2 + 14.054^2} = 16.845$
3	13.930 – 42.939i	$\sqrt{13.930^2 + 42.939^2} = 45.142$
4	22.866 – 114.754i	$\sqrt{22.866^2 + 114.754^2} = 117.010$
5	50.547 – 161.112i	$\sqrt{50.547^2 + 161.112^2} = 168.855$

Step 4. Compute natural frequency of each mode from corresponding eigenvalue using Eq. (3-11).

- The third column of Table 4.4.1 shows the natural frequency computed using the eigenvalues of the second column of Table 4.4.1.

Step 5. Compute effective damping ratio of each mode from real part of eigenvalue and natural frequency of corresponding mode using Eq. (3-12).

61

- Table 4.4.2 shows the final results of EMDR from the CMA method. The first and second modal damping ratios are found as 25% and 55%, respectively. Table 4.4.3 compares the undamped natural frequency of NP-Model and P-Model of the PSO.

Table 4.4.2 EMDR of PSO by CMA method

Mode	EMDR
1	$2.674/10.633 = 0.251$
2	$9.288/16.845 = 0.551$
3	$13.930/45.142 = 0.324$
4	$22.866/117.010 = 0.195$
5	$50.547/168.855 = 0.299$

The acceleration and displacement time history from the NP-Model and P-Model at the top of the bent are drawn along with the measured time history in Fig. 4.4.2. The response of the P-Model shows good agreement with the NP-Model response as well as the measured response. The summary of peak response values from the measurement, NP-Model, and P-Model are presented in Table 4.4.11 and 4.4.12. The relative error of the P-Model with the NP-Model and measurement is within 10% and 2%, respectively.

Table 4.4.3 Undamped natural frequency and EMDR from CMA method

| Mode | Undamped Natural Frequency (Hz) | | EMDR |
	NP-Model	P-Model	
1	1.742	1.648	0.251
2	2.681	2.643	0.551
3	7.194	7.329	0.324
4	18.624	18.832	0.195
5	27.166	23.762	0.299
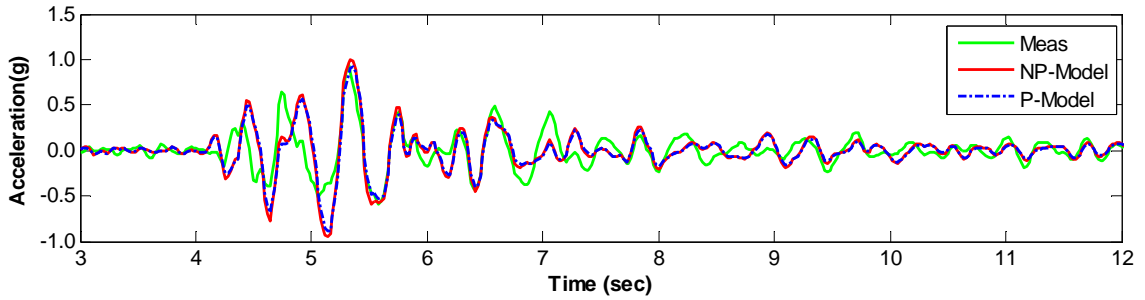
(a) Acceleration
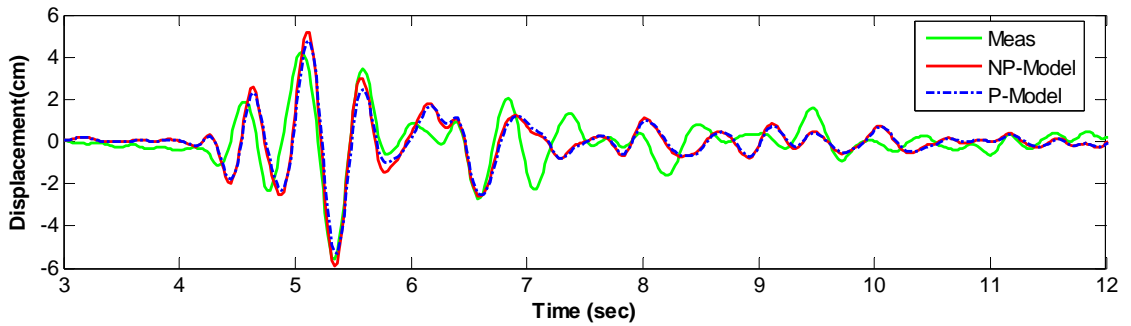
(b) Displacement

Figure 4.4.2 Response time history from CMA method

63

4.4.2 Neglecting Off-Diagonal Elements (NODE) Method

The step 1 of the NODE method is the same as in the CMA method.

Step 2. Compute undamped mode shape and natural frequency of each mode from mass and stiffness matrix.

- The undamped mode shapes and natural frequencies are obtained in Table 4.3.3 and Fig. 4.3.5.

Step 3. Obtain modal damping matrix by pre- and post-multiplying mode shape matrix to damping matrix as shown in Eq.(3-15).

- Table 4.4.4 shows the results of pre- and post-multiplication of the normal mode shapes to the damping matrix of the NP-Model up to the fifth mode.

Table 4.4.4 Modal damping matrix ($[\phi]^T [c][\phi]$)

Mode	1	2	3	4	5
1	5.141	0.196	-9.722	0.484	2.294
2	0.196	18.068	0.200	18.390	1.692
3	-9.722	0.200	27.708	-0.255	1.938
4	0.484	-18.394	-0.255	46.057	1.566
5	2.294	1.692	1.938	1.566	107.145

Step 4. Compute effective damping ratio of each mode from Eq. (3-16) ignoring off-diagonal elements of modal damping matrix.

- If the mode shapes are mass normalized ones, the term $\{\phi_i\}^T[m]\{\phi_i\}$ in the denominator of Eq. (3-16) is unity and the EMDR of i th mode becomes

$$\xi_i = \frac{c_{i,i}}{2(2\pi f_i)} \tag{4-4}$$

where f_i is undamped natural frequency (Hz) of i th mode. Table 4.4.5 shows the EMDR of each mode computed by Eq. (4-4).

Step 5. Check error criteria using Eq. (3-18). If a parameter from Eq. (3-18) of any two modes is greater than unity, change to other methods.

- The accuracy of the NODE method can be assessed by modal coupling parameters which are shown in Table 4.4.6. Though the shaded off-diagonal elements in Table 4.4.4 are significant compared with the elements in the diagonal line, the modal coupling parameters of the off-diagonal elements in Table 4.4.6 are much less than unity.

Table 4.4.5 EMDR from NODE method

Mode	EMDR
1	$5.141/(2\times 2\pi \times 1.648) = 0.248$
2	$18.068/(2\times 2\pi \times 2.643) = 0.544$
3	$27.708/(2\times 2\pi \times 7.329) = 0.301$
4	$46.057/(2\times 2\pi \times 18.832) = 0.195$
5	$107.145/(2\times 2\pi \times 23.762) = 0.359$

Table 4.4.6 Modal coupling parameter

65

Mode	1	2	3	4	5
1	-	0.012	-0.050	0.000	0.001
2	0.019	-	0.002	0.022	0.001
3	-0.222	0.005	-	-0.001	0.004
4	0.004	0.158	-0.002	-	0.022
5	-0.015	0.011	0.014	-0.028	-

The computed responses from the NP-Model and P-Model are shown in Fig. 4.4.3 along with the measured response. In Table 4.4.10 the EMDR from this method is very close to the result from the complex modal analysis method in all modes. The relative error of the P-Model with NP-Model and measurement is less than 10% and 3%, respectively, in Table 4.4.11 and 4.4.12.
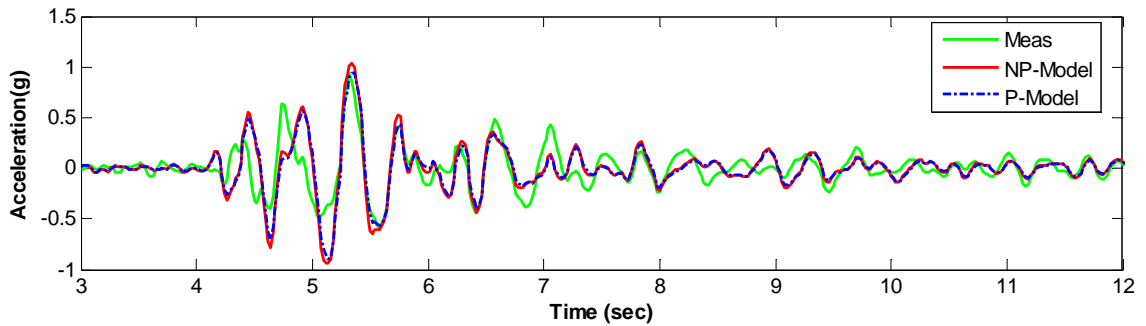
(a) Acceleration
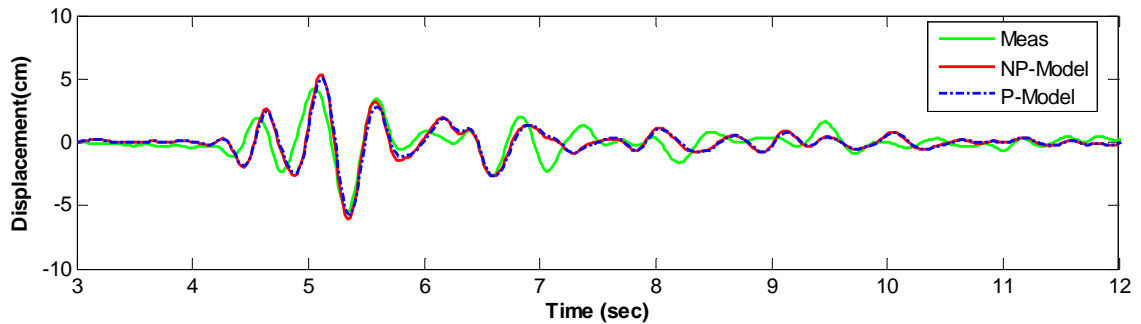
(b) Displacement

Figure 4.4.3 Response time history from NODE method

4.4.3 Composite Damping Rule (CDR) Method

To apply the CDR method, the PSO was divided into two components: i) concrete structure component which includes deck and bent, and ii) bridge boundary component. The damping ratios were assumed as 25% and 5% for the boundary component (Kotsoglou and Pantazopoulou, 2007) and the concrete structure component, respectively. The procedure of the CDR method is as follows:

Step 1. Establish mass and stiffness matrix of a bridge system. This step is the same as in the CMA method.

Step 2. Obtain undamped mode shapes. Based on the mass and stiffness matrix of the NP-Model of the PSO, undamped mode shapes are computed as shown in Fig. 4.3.5.

Step 3. Compute potential energy ratio of each component for each mode using Eq. (3-36).

- The computed potential energy of each component is given in Table 4.4.7. In the table the potential energy ratio of the boundary component is 72% and 97% for the first and second mode, respectively, and it becomes smaller at the third mode. Considering that the first two modes are in the dominant frequency range of the earthquake, the potential energy ratio implies that most of the input energy will be dissipated from the boundary component rather than the concrete structure component.

Step 4. Compute EMDR using Eq. (3-34).

- Based on Eq. (3-34), the EMDR of each mode is computed as in Table 4.4.8.

Table 4.4.7 Potential energy ratio in CDR method

Mode	Potential energy			Energy ratio	
	Total (U_{total})	Structure (U_{str})	Boundary (U_{bnd})	U_{str}/U_{total}	U_{bnd}/U_{total}
1	0.54E2	0.16E2	0.38E2	0.293	0.707
2	1.38E2	0.04E2	1.34E2	0.026	0.974
3	10.60E2	8.69E2	1.92E2	0.819	0.181
4	70.00E2	68.23E2	1.77E2	0.975	0.025
5	111.46E2	55.52E2	55.93E2	0.498	0.502

Table 4.4.8 EMDR from CDR method

Mode	EMDR
1	$(0.05)(0.293) + (0.25)(0.707) = 0.191$
2	$(0.05)(0.026) + (0.25)(0.974) = 0.245$
3	$(0.05)(0.819) + (0.25)(0.181) = 0.086$
4	$(0.05)(0.975) + (0.25)(0.025) = 0.055$
5	$(0.05)(0.498) + (0.25)(0.502) = 0.150$

The EMDR from the composite damping rule was computed as 19% and 24% for the first and second mode, respectively. As the modal potential energy ratio of the concrete structure component increases after the third mode, the EMDR decreases consequently.

Figure 4.4.4 shows the response time history of the P-Model compared with the NP-Model and with measured response. The relative error from the composite damping rule method was computed as less than 6% and 14% when compared with the NP-Model and with measured response, respectively, as shown in Tables 4.4.11 and 4.4.12.

(a) Acceleration

(b) Displacement
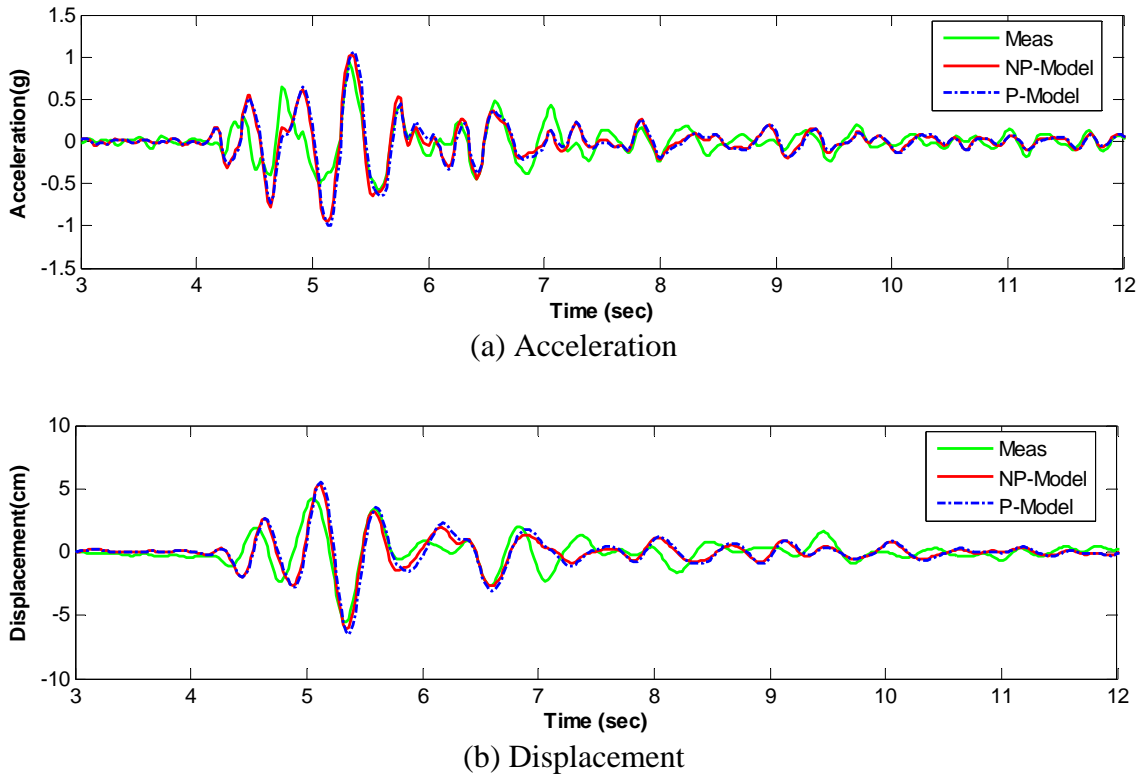
Figure 4.4.4 Response time from CDR method

4.4.4 Optimization (OPT) Method

Using the optimization algorithm shown in Fig. 3.3.1, the EMDR of the NP-Model was estimated. The procedure of the OPT method is explained below.

OPT method in time domain

Step 1 is the same as in the CMA method.

Step 2. Compute undamped natural frequencies.

- The undamped natural frequencies were computed based on the mass and stiffness matrix of the NP-Model of the PSO.

Step 3. Specify damping ratios of two modes of P-Model as Rayleigh damping and compute α and β using Eq. (3-21).

- Initial damping ratio of 5% is assumed for the first and third modes to compute Rayleigh damping coefficient α and β. From Eq. (3-21), α and β are computed as

$$\alpha = (0.05)\frac{2(2\pi)(1.648)(7.329)}{1.648 + 7.329} = 0.845$$

$$\beta = (0.05)\frac{2}{(2\pi)(1.648 + 7.329)} = 0.002$$

- From the next iteration, damping ratio is searched by optimization algorithm. After damping ratio is determined, new α and β values are computed.

Step 4. Compute damping matrix of P-Model as shown in Eq. (3-20).

- Using α and β values, the damping matrix of the P-Model is constructed as

$$[c] = 0.865[m] + 0.002[k]$$

Step 5. Compute seismic responses of both NP-Model and P-Model through time history analysis.

- For time history analysis, any ground motion can be used. In this research, Cape Mendocino/Petrolina earthquake (1992) was used and Newmark direct integration method was adopted.

Step 6. Evaluate objective function of Eq. (3-23). If a value from objective function is smaller than criterion, go to step 8.

Step 7. Repeat from step 3 to step 6.

Step 8. Compute damping ratios of other modes using Eq. (3-22).

- From optimization, the damping ratio was obtained as 0.255. α and β values corresponding to the damping ratio are

$$\alpha = (0.255)\frac{2(2\pi)(1.648)(7.329)}{1.648 + 7.329} = 4.311$$

$$\beta = (0.255)\frac{2}{(2\pi)(1.648 + 7.329)} = 0.009$$

- Damping ratios of other modes are computed using Eq. (3-22) and shown in Table 4.4.9.

Table 4.4.9 EMDR from OPT method in time domain

Mode	EMDR
1	$\dfrac{1}{2(2\pi)(1.648)}(4.311)+\dfrac{(2\pi)(1.648)}{2}(0.009)=0.255$
2	$\dfrac{1}{2(2\pi)(2.643)}(4.311)+\dfrac{(2\pi)(2.643)}{2}(0.009)=0.205$
3	$\dfrac{1}{2(2\pi)(7.329)}(4.311)+\dfrac{(2\pi)(7.329)}{2}(0.009)=0.255$
4	$\dfrac{1}{2(2\pi)(18.823)}(4.311)+\dfrac{(2\pi)(18.823)}{2}(0.009)=0.553$
5	$\dfrac{1}{2(2\pi)(23.762)}(4.311)+\dfrac{(2\pi)(23.762)}{2}(0.009)=0.689$

OPT method in frequency domain

Step 1 to step 4 are the same as those in time domain method above.

Step 5. Compute frequency response function of both NP-Model and P-Model using Eq. (3-27).

- The frequency response function at the top of the bent ($H_{6,i}$) was chosen for objective function of optimization. The only difference of frequency response function of the NP-Model and P-Model is damping matrix of both models. The damping matrix of the NP-Model is $[c_{NP}]=[c_{str}]+[c_{local}]$, while that of the P-Model is $[c_P]=\alpha[m]+\beta[k]$. α and β values are updated for every iteration.

Step 6. Evaluate objective function of Eq. (3-28). If a value from objective function is smaller than criterion, go to step 8.

Step 7. Repeat from step 3 to step 6.

Step 8. Compute damping ratios of other modes using Eq. (3-22).

Figure 4.4.5 shows the frequency response function of the NP-Model and P-Model after optimization. The frequency response function of the P-Model shows a good agreement with that of the NP-Model.

The EMDR from the optimization method in time domain and frequency domain are summarized in Table 4.4.10. From Table 4.4.10 it can be seen that the EMDR from the optimization method is very close to the results from the CMA method. It should be noted in Table 4.4.10 that the large EMDR after the fourth mode from the optimization method is attributed to the assumption of Rayleigh damping for the P-Model. However, because of little contribution from the higher modes, the overall time history responses are very similar to the results from the complex modal analysis method.

Figure 4.4.6 and 4.4.7 show the time history response of the P-Model with the NP-Model and measurement. The comparison of the peak values of the measured and computed response is given in Tables 4.4.11 and 4.4.12. The relative error of the P-Model with the NP-Model and measurement is less than 10% and 4% for acceleration and displacement, respectively.
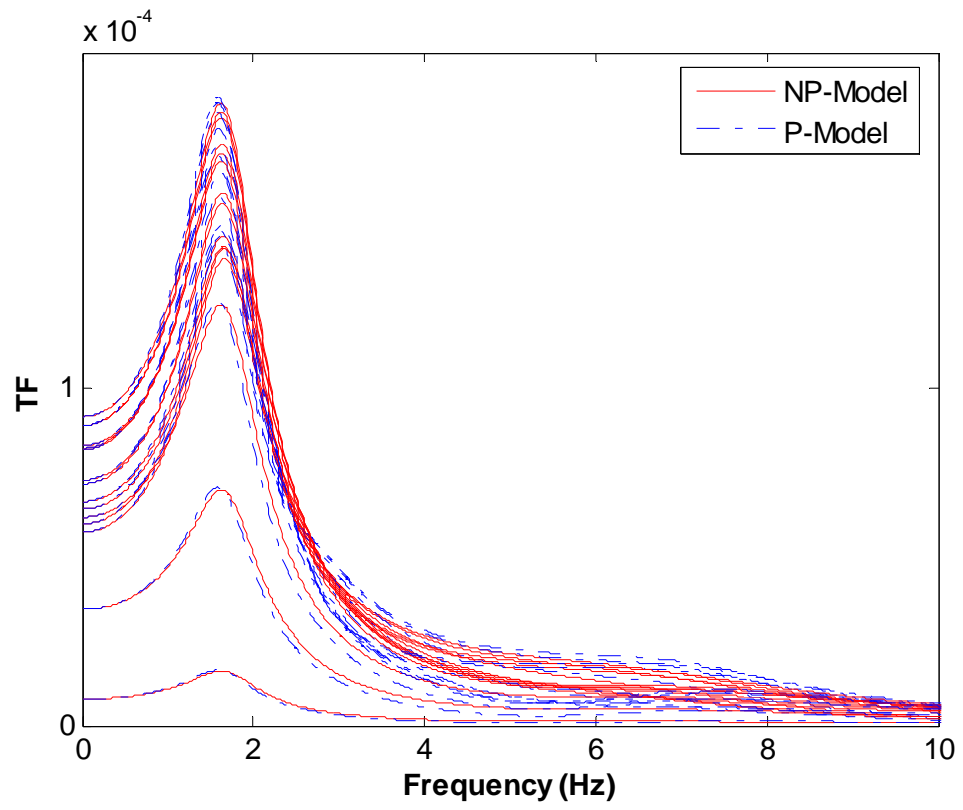
Figure 4.4.5 FRF of NP-Model and P-Model after optimization
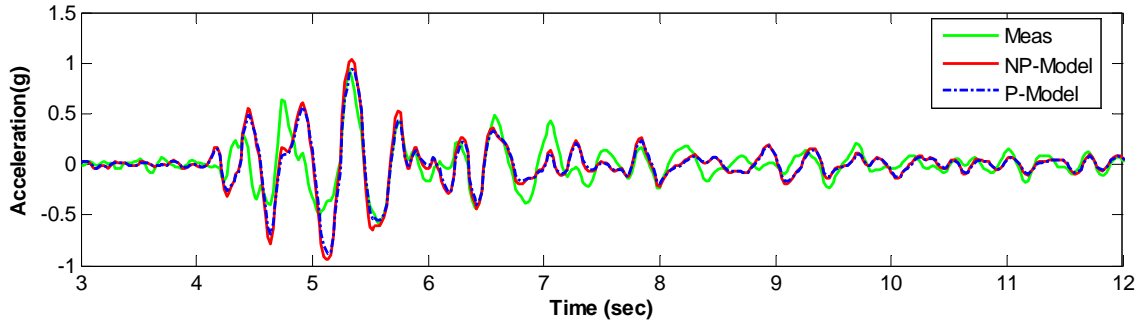
(a) Acceleration
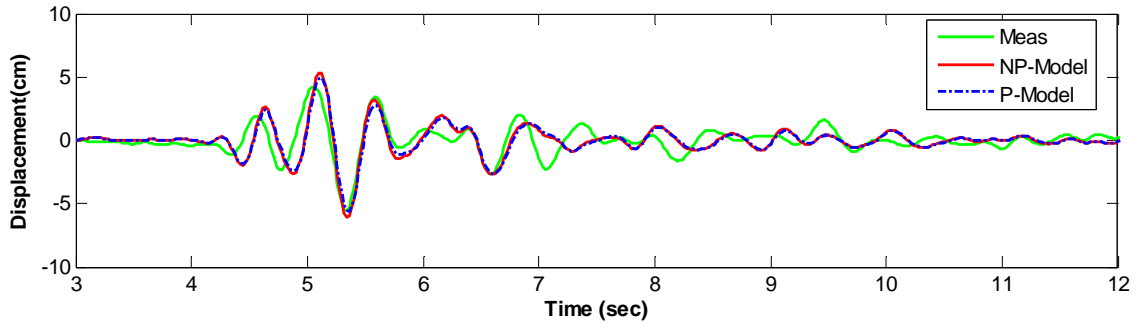
(b) Displacement

Figure 4.4.6 Response time history from OPT method in time domain
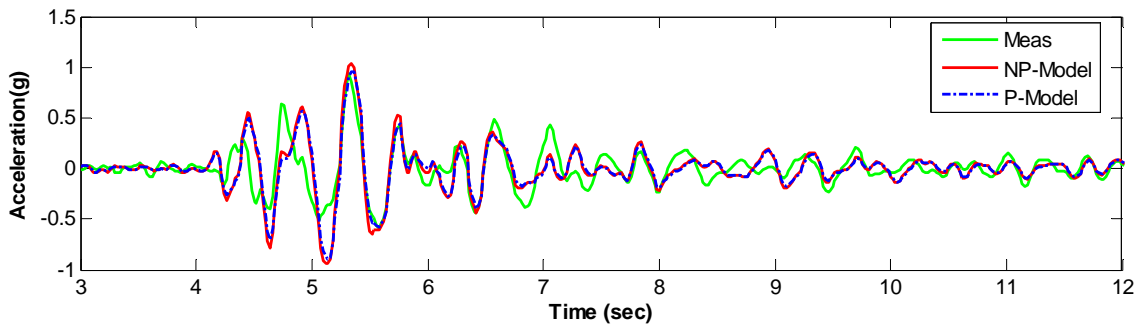
(a) Acceleration
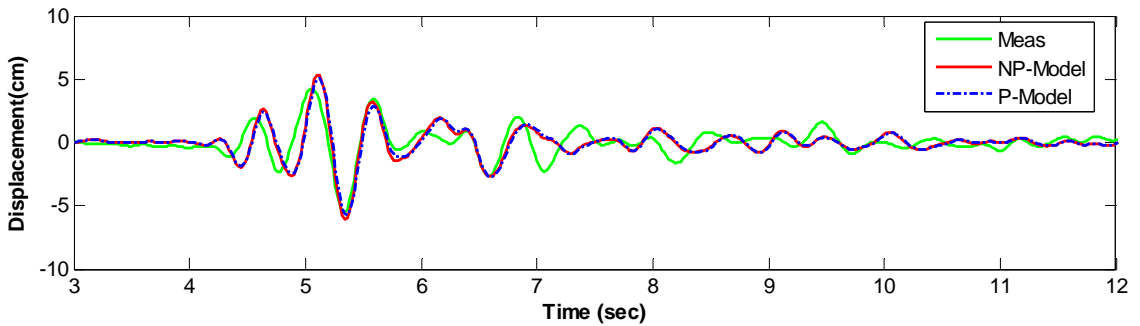
(b) Displacement

Figure 4.4.7 Response time history from OPT method in frequency domain

Table 4.4.10 Summary of EMDR identified by each method

Mode	CMA	NODE	OPT Time Domain	OPT Frequency Domain	CDR
1	0.251	0.248	0.255	0.242	0.191
2	0.551	0.544	0.205	0.197	0.245
3	0.308	0.301	0.255	0.242	0.086
4	0.195	0.195	0.553	0.522	0.055
5	0.299	0.359	0.689	0.651	0.150

Table 4.4.11 Summary of peak acceleration from each method

Method	Measured (g)	Computed (g) Response 1 (NP-Model)	Computed (g) Response 2 (P-Model)	Relative Error $(P-NP)/P$	Relative Error $(P-Meas)/P$
CMA	0.942	1.031	0.941	-9%	-1%
NODE			0.947	-9%	1%
OPT[*]			0.937	-10%	-1%
OPT[**]			0.954	-8%	1%
CDR			1.068	4%	11%

OPT[*] & OPT[**] : optimization method in time domain and frequency domain, respectively
Meas : Measured response, *NP* : results from NP-Model, *P* : results from P-Model

Table 4.4.12 Summary of peak displacement from each method

Method	Measured (cm)	Computed (cm) Response 1 (NP-Model)	Computed (cm) Response 2 (P-Model)	Relative Error $(P-NP)/P$	Relative Error $(P-Meas)/P$
CMA	5.553	6.098	5.662	-8%	2%
NODE			5.706	-7%	3%
OPT[*]			5.622	-8%	1%
OPT[**]			5.758	-6%	4%
CDR			6.478	6%	14%

OPT[*] & OPT[**] : optimization method in time domain and frequency domain, respectively
Meas : Measured response, *NP* : results from NP-Model, *P* : results from P-Model

4.5 Comparison with Current Design Method

Seismic response of the PSO was computed based on the response spectrum method. The normal mode shapes and natural periods from the P-Model, and the EMDR of each mode in Table 4.4.10 were used for the computation. The three modal combination rules such as the absolute sum (ABSSUM), square-root-of-sum-of-squares (SRSS), and complete quadratic combination (CQC) methods were applied in the response spectrum method.

Tables 4.5.1 and 4.5.2 summarize the response spectrum analysis results for each damping estimating method. The last row of Tables 4.5.1 and 4.5.2 show the modal combination results when the conventional 5% damping ratio was used for all the modes. The computed response with the 5% damping ratio is nearly twice that of the measured response. From the tables it is concluded that the conventional 5% damping ratio is too conservative for the seismic design of short-span bridges under strong earthquakes. Also, in these tables it can be seen that the result from each modal combination rule is very similar to each other, which is attributed to the well-separated modes of the P-Model.

Figure 4.5.1 shows the relative error of the results from the response spectrum method with the peak values of measured response at the top of bent. Except for the composite damping rule method, the relative error of each damping estimating method is less than 5% and 10% for acceleration and displacement, respectively. The high error of the composite damping rule method is attributed to the low EMDR of the first mode. In general, among the damping estimating methods, the complex modal analysis method and the neglecting off-diagonal elements method are more accurate than other methods.

Also, among the modal combination rules, the CQC method produces more accurate estimation than the other two modal combination methods.

Table 4.5.1 Acceleration from response spectrum method (unit : g)

Method	ABSSUM	SRSS	CQC
CMA	0.957	0.925	0.942
NODE	0.944	0.918	0.928
OPT*	0.980	0.939	0.957
OPT**	0.967	0.951	0.952
CDR	1.196	1.148	1.164
EMDR=5%	1.960	1.876	1.911
NP-Model	1.087		
Meas.	0.942		

OPT* & OPT** : optimization method in time domain and frequency domain, respectively

Table 4.5.2 Displacement from response spectrum method (unit : cm)

Method	ABSSUM	SRSS	CQC
CMA	5.201	5.089	5.157
NODE	5.126	5.053	5.095
OPT*	5.298	5.053	5.095
OPT**	5.771	5.745	5.745
CDR	6.615	6.497	6.559
EMDR=5%	10.962	10.750	10.886
NP-Model	5.725		
Meas.	5.553		

OPT* & OPT** : optimization method in time domain and frequency domain, respectively
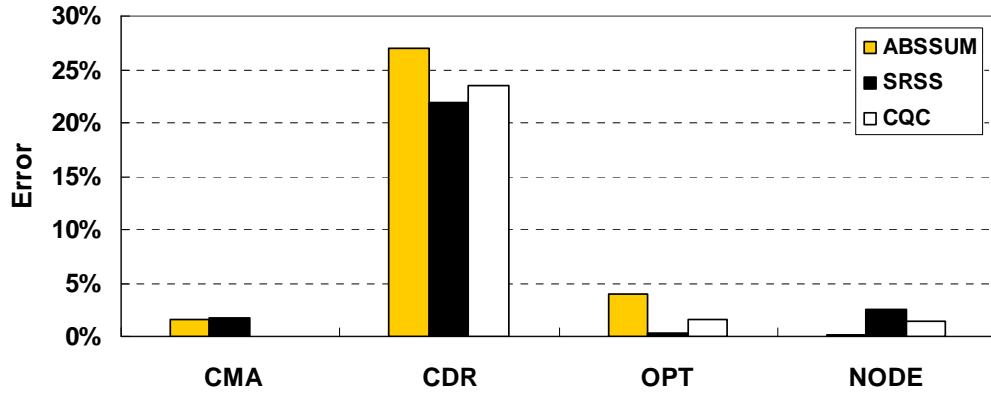
(a) Acceleration
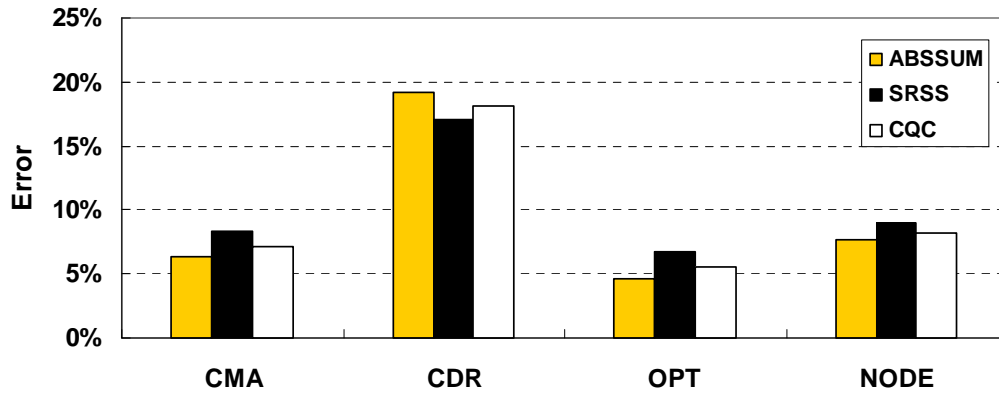
(b) Displacement

Figure 4.5.1 Relative error of response spectrum method with measured response

4.6 EMDR and Ground Motion Characteristics

Since the shear modulus and damping of a soil depend on soil strain, the effective stiffness and damping of the equivalent viscoelastic element representing the bridge boundary will change if the intensity of exciting ground motion is different. Applying the measured data recorded at the PSO site during six earthquakes, the EMDR of the bridge under each ground motion was computed by the optimization in time domain method and the equivalent damping ratio of the first mode was related with the ground motion characteristics to investigate any relationship with ground motion parameters.

4.6.1 Ground Motion Parameters

Many parameters have been proposed to characterize the ground motion in a simple quantitative form. Table 4.6.1 summarizes the parameters which were investigated in this research to be correlated with the EMDR. The detail of the parameters can be found in references (Werner, 1976; Sucuoglu and Nurtug, 1995; Kramer, 1996).

4.6.2 Relationship of EMDR with Ground Motion Parameters

The EMDR of the PSO under other ground motions was found by applying the same procedure described in previous sections and the results are given in Table 4.6.2. In this table, the EMDR under each earthquake was computed by the complex modal analysis method. Figures A.2.1 to A.2.4 in Appendix A show the relation between the EMDR and ground motion parameters.

Among many ground motion parameters, the root-mean-square (RMS) intensity and an average intensity (Avg.) defined as the square of the RMS intensity, as well as the

response spectrum intensity (RSI) show good correlations with the EMDR, as shown in Fig. 4.6.1. Based on Fig. 4.6.1 it is possible to predict the EMDR roughly, as shown in Table 4.6.3, according to the ground motion parameters though it is apparent that more data points are needed for more accurate estimation of the EMDR.

Table 4.6.1 List of ground motion parameters

Main characteristic	Parameter
Amplitude	**-PGA** **-PGV** **-PGV/PGA**
Time duration	**-Bracketed duration** **-Trifunac & Brady duration**
Intensity based on ground motion acceleration	**-Total intensity** **-Average intensity (Avg)** **-Arias intensity (Arias)** **-RMS intensity (RMS)** **-Characteristic intensity (CI)** **-Cumulative absolute velocity (CAV)**
Intensity based on response spectrum	**-Response spectrum intensity (RSI)** **-EPA & EPV** **-Acceleration spectrum intensity (ASI)**
Other	**-Energy dissipation index (EDI)**

Table 4.6.2 Peak acceleration of earthquake and EMDR

Earthquake	PGA (g)	EMDR
Cape Mendocino (1986)	0.15	0.17
Aftershock	0.12	0.03
Cape Mendocino (1987)	0.09	0.09
Cape Mendocino/Petrolina (1992)	0.54	0.25
Aftershock 1	0.52	0.31
Aftershock 2	0.20	0.15

Table 4.6.3 Prediction of EMDR by ground motion parameters

RMS, Avg., RSI	EMDR
0.5 > Intensity	0.05
0.5< Intensity < 1.2	0.10
Intensity > 1.2	0.20
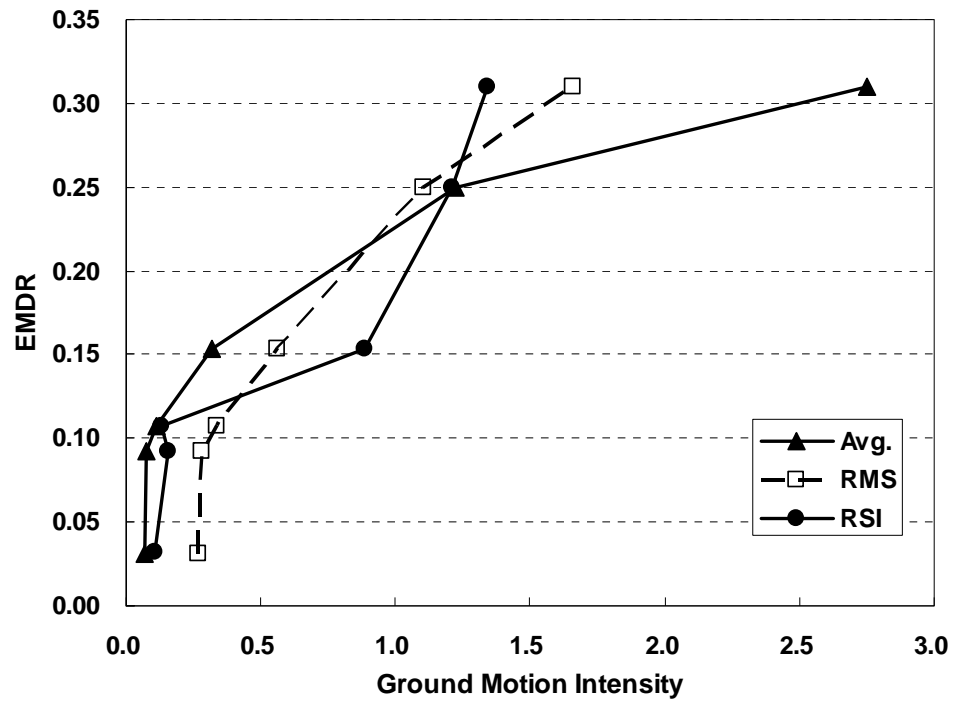
Figure 4.6.1 Relationship between ground motion intensity and EMDR

4.7 Summary

The simplified finite element model of the PSO was established using the equivalent viscoelastic model for the bridge boundaries. The properties of the equivalent viscoelastic model were estimated utilizing the recorded response. The verification of the NP-Model was conducted by comparing the simulated response with the measured response in both time domain and frequency domain and it was found to be satisfactory.

Each damping estimating method was applied to the NP-Model of the PSO to compute the EMDR for each mode. The EMDR of the first mode was found as nearly 25%, which is very close to the boundary damping computed by Kotsoglou and Pantazopoulou (2007). However, it was estimated to be a little bit lower than this value obtained by the CDR method. It should be mentioned that the EMDR from the CDR method is always lower than the highest damping ratio among those for the individual components.

With the EMDR for each mode, the time history response of the P-Model was computed based on the modal superposition method. From the comparison of the peak values of the P-Model with the NP-Model and measurement, the application of the each method to compute the EMDR of non-proportionally damped system was verified.

Also, from the comparison of the seismic response based on the response spectrum method with the measured response, the whole procedure used in this research was verified to be applicable for estimating the EMDR for each mode and predicting the seismic demand of a non-proportionally damped short-span bridge by approximating it with an equivalent proportionally damped system.

The modal combination results from current design practice which uses 5% damping ratio for all modes were nearly twice the measured responses. So the assumption of 5% damping ratio of all modes is thought to be too conservative for the design of short-span bridges which have significant energy dissipation at bridge boundaries under strong motion.

The first modal damping ratio of the PSO was computed for six recorded earthquakes. Among many ground motion parameters, average intensity, root mean square intensity, response spectrum intensity show good correlation with the first modal damping ratio. A simple EMDR estimation method, though it is very limited, was suggested based on the observation between the ground motion parameters and the first modal damping ratio of the PSO.

Chapter 5

APPLICATION TO ISOLATED BRIDGE

Isolation devices are widely used to protect highway bridges from seismic hazards. The damping of these devices makes such bridges non-proportionally damped. For an equivalent linear analysis, it is necessary to estimate the EMDR of such bridges. In this chapter, application of the proposed methods to an isolated bridge is investigated under 27 ground motions.

First, the equivalent linearization of the isolation bearing and the estimation of the EMDR applying each damping estimating method are depicted. Then, seismic response of the non-proportionally damped bridge is approximated using the response spectrum method. The proposed method is verified by comparing the peak seismic response obtained by the response spectrum method with that obtained by non-linear analysis. In addition, the EMDR of the isolated bridge is related to certain ground motion characteristics.

5.1 Analysis Procedure

To verify the applicability of the damping estimating methods, an example isolated bridge was selected from a paper by Hwang et al. (1996). The detail of the bridge is described in Section 5.3. The finite element model of the example bridge, which is referred to as 'Bi-linear model' in Fig. 5.1.1 was first established. For this model, the mechanical behavior of each isolation bearing was represented by a bi-linear hysteretic model. The deck and column of the example bridge was assumed to be linear elastic, which is a reasonable assumption considering that most of the earthquake energy is dissipated by the isolation bearings and the deformation of the bridge is concentrated at the locations of the these bearings.

After establishing the finite element model of the bridge, the bi-linear hysteretic model of each isolation bearing was approximated by an equivalent linear system so that the equivalent linear analysis could be applied. The elastic stiffness and viscous damping of the equivalent linear system were estimated by three different methods (AASHTO, Caltrans 94, and Caltrans 96) utilizing the maximum relative displacement of the isolation bearing. The finite element model with the equivalent linear system of the isolation bearing is the linear non-proportionally damped system which is designated as 'NP-Model' in Fig. 5.1.1.

Based on the NP-Model, the EMDRs of the NP-Model were estimated by applying the damping estimating methods. The damping of the concrete structure components and isolation bearing components was approximated with the EMDR of the entire bridge system. With the EMDRs, the NP-Model is reduced to the proportionally damped model

which is defined as the 'P-Model' in Fig. 5.1.1. Normal mode shapes and modal frequencies can be computed from this model.

The time history responses of the Bi-linear Model and the NP-Model designated as 'Computed response 1' and 'Computed response 2', respectively, in Fig. 5.1.1 were computed by the direct Newmark integration method. The 'Computed response 3', which is a modal combination result, was computed by the response spectrum method using the mode shapes, modal frequencies, and the EMDRs.

The accuracy of the equivalent linearization of the isolation bearings can be verified by comparing the Computed responses 1 and 2. The proposed method to approximate the non-proportionally damped isolated bridge response using the response spectrum method can be validated by comparing the Computed responses 1 and 3.

```
┌─────────────────┐
│     Example     │
│ Isolated bridge │
└─────────────────┘
         ┊
         ▼
┌─────────────────┐                      ┌─────────────────┐
│  Bi-linear Model │ ───────────────────▶ │    Computed     │
│                 │                      │   Response 1    │
└─────────────────┘                      └─────────────────┘
         ┊                                        ┊
         ┊                                        ▼
         ┊                               ┌─────────────────────┐
         ┊          ┌──────────────┐     │ Equivalent linear   │
         ┊ ◀─────── │ (Keff, Ceff) │◀─── │ system of isolator  │
         ┊          │    isolator  │     │ 1)  AASHTO          │
         ┊          └──────────────┘     │ 2) Caltrans 94      │
         ┊                               │ 3) Caltrans 96      │
         ┊                               └─────────────────────┘
         ▼
┌─────────────────┐                      ┌─────────────────┐
│  Linear Model   │ ───────────────────▶ │    Computed     │
│   (NP-Model)    │                      │   Response 2    │
└─────────────────┘                      └─────────────────┘
         ┊
┌─────────────────┐
│ Computation     │
│ of EMDR         │     ξ EMDR
│ 1. CMA          │ ───────────▶
│ 2. NODE         │
│ 3. CDR          │
│ 4. OPT          │
└─────────────────┘
         ▼
┌─────────────────┐
│ Proportionally  │
│ damped Model    │
│   (P-Model)     │
└─────────────────┘
         ┊
┌─────────────────┐
│   Response      │ ──────────▶
│   spectrum      │
└─────────────────┘
         ▼
┌─────────────────┐                      ┌─────────────────┐
│     Modal       │ ───────────────────▶ │    Computed     │
│  combination    │                      │   Response 3    │
└─────────────────┘                      └─────────────────┘
```
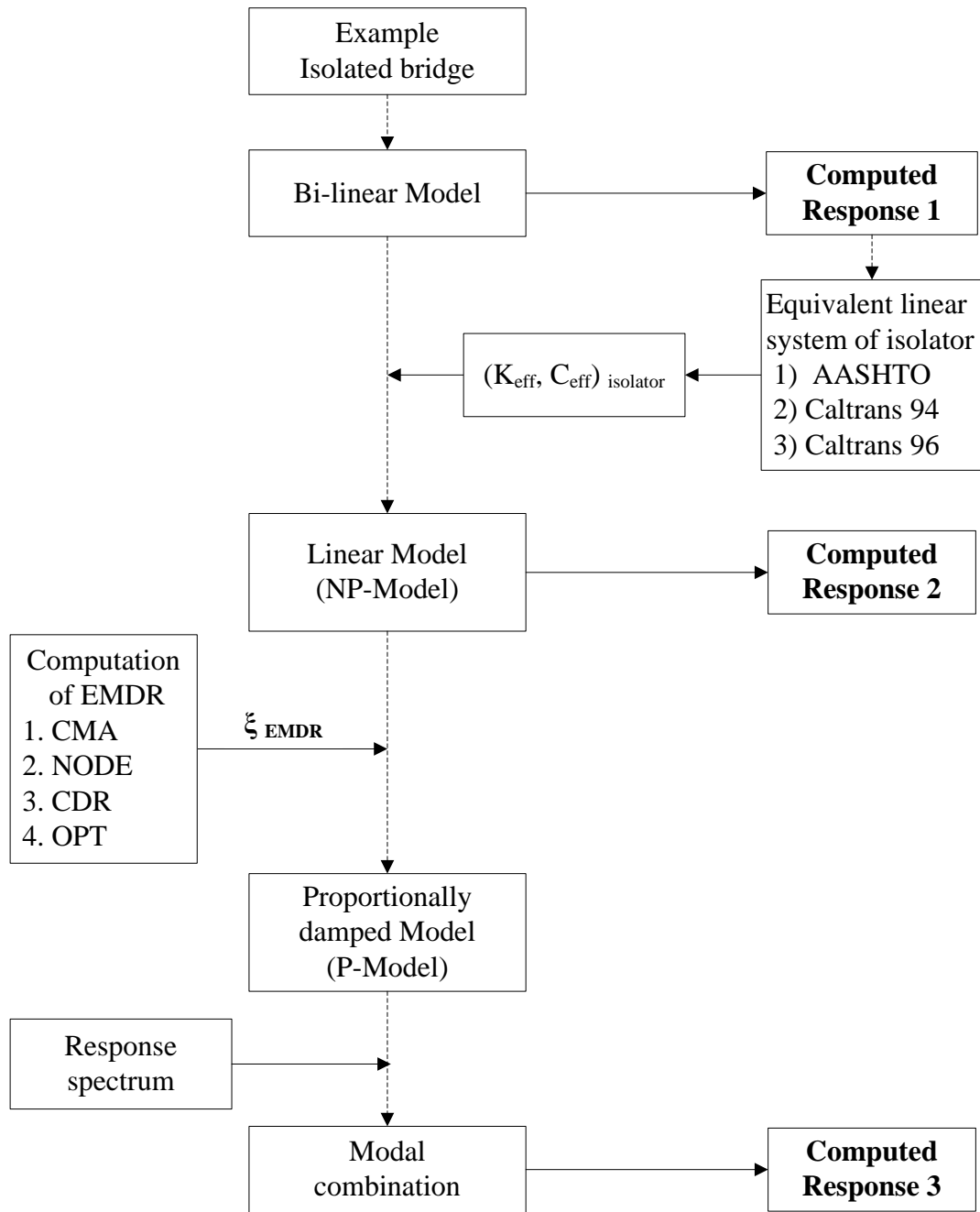
Figure 5.1.1 Analysis procedure diagram

5.2 Equivalent Linearization of Isolation Bearing

The mechanical behavior of any type of isolation bearing can be represented by a bi-linear hysteretic model. However, it is approximated with an equivalent linear system when using the equivalent linear analysis adopted in many bridge specifications. The bi-linear hysteretic model and equivalent linearization of the isolation bearing are discussed in this section.

5.2.1 Bi-linear Model of Isolation Bearing

The bi-linear model, shown in Fig. 5.2.1, can be defined by three parameters: initial stiffness (K_1), post-yielding stiffness (K_2), and characteristic strength (Q), which is the intercept of the hysteresis loop and the force axis. In many design specifications, the seismic analysis of isolated bridges relies primarily on the equivalent linear analysis rather than the inelastic analysis. Thus, the bi-linear model should be approximated with an equivalent linear system composed of an effective stiffness and effective damping. The effective stiffness of the bi-linear model is defined on the basis of peak-to-peak loads as shown in Fig. 5.2.1. Thus, the effective stiffness depends on the maximum displacement of the isolation bearing.

The effective stiffness can be expressed using the maximum displacement (D_{max}) and the maximum shear force at the maximum displacement (F_D) as in Eqs. (5-1) or (5-2) using the basic parameters K_1, K_2, and Q. In the design phase, the design displacement of the isolation bearing is used as the maximum displacement to compute the effective stiffness.

$$K_{eff} = \frac{F_D}{D_{max}} \qquad (5\text{-}1)$$

$$K_{eff} = K_2 + \frac{Q}{D_{max}} \qquad (5\text{-}2)$$

The effective damping ratio is defined by Eq. (5-3) for one cycle of hysteresis loop.

$$\xi_{eff} = \frac{4Q(D_{max} - D_y)}{2\pi K_{eff} D_{max}^2} \qquad (5\text{-}3)$$

where $4Q(D_{max} - D_y)$ is the area of the hysteresis loop.
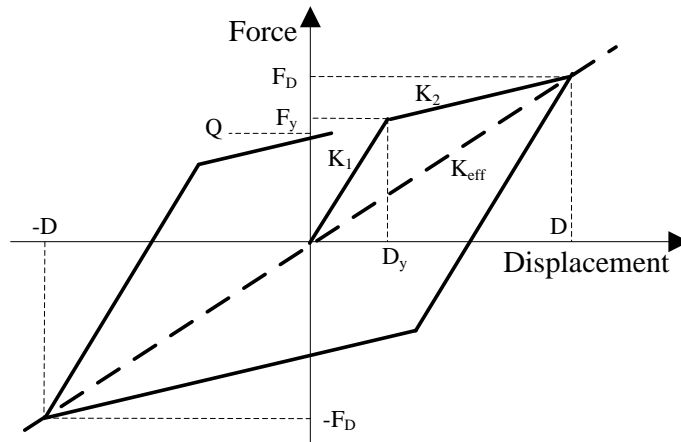
Figure 5.2.1 Bi-linear hysteretic force-displacement model of isolator

5.2.2 Equivalent Linearization of Isolation Bearing

The AASHTO provisions specify an equivalent linearization of the isolation bearing based on the bi-linear model (Guide, 2000). For this method, the effective stiffness and damping ratio of an isolation bearing is obtained using Eqs. (5-1) and (5-3). Using a

ductility ratio (μ), and a strain hardening ratio (α) of the isolation bearing, as defined by $\alpha = K_2 / K_1$ and $\mu = D_{max} / D_y$, the effective stiffness and damping ratio can be expressed as shown by Eqs. (5-4) and (5-5), respectively (Hwang et al., 1996).

$$K_{eff} = \frac{1 + \alpha(\mu - 1)}{\mu} K_1 \tag{5-4}$$

$$\xi_{eff} = \frac{2(1-\alpha)\left(1 - \dfrac{1}{\mu}\right)}{\pi \left[1 + \alpha(\mu - 1)\right]} \tag{5-5}$$

Hwang et al. (1994) suggested a method, designated as the Caltrans 94 method herein, in which K_{eff} and ξ_{eff} are obtained using Eqs. (5-6) and (5-7). This method was derived from curve fitting of the system identification results for inelastic response spectra with constant ductility ratios reported by Iwan and Gates (1979) and Iwan (1980). This method, as stated by the authors, was established without consideration of any physical or mechanical significance of isolation bearings and was developed based on the results of Iwan's study with the constant displacement ductility ratio up to 8, which are much less than the ductility ratios of isolation bearings under strong ground motions.

$$K_{eff} = \frac{K_1}{\left\{1 + \ln\left[1 + 0.13(\mu - 1)^{1.137}\right]\right\}^2} \tag{5-6}$$

$$\xi_{eff} = 0.0587(\mu - 1)^{0.371} \tag{5-7}$$

Because of the limitations of the previous Caltrans 94 method, a refined method, designated as the Caltrans 96 method herein, was suggested by Hwang et al. (1996). Based on the concept that the inelastic displacement spectrum can be approximated by

the equivalent elastic displacement spectrum by modifying the period shift and damping ratio, an equivalent linear model was developed to consider the various ductility ratios of isolation bearings having mechanical behavior as defined by the bi-linear hysteretic model. In this case, the equations for effective stiffness and damping ratio are as follows:

$$K_{eff} = \frac{1+\alpha(\mu-1)}{\mu}\left(1-0.737\frac{\mu-1}{\mu^2}\right)^{-2} \tag{5-8}$$

$$\xi_{eff} = \frac{2(1-\alpha)\left(1-\dfrac{1}{\mu}\right)}{\pi\left[1+\alpha(\mu-1)\right]}\left(\frac{\mu^{0.58}}{6-10\mu}\right) \tag{5-9}$$

It can be seen that Eqs (5-8) and (5-9) are modified equations of the AASHTO Eqs. (5-4) and (5-5).

5.3 Example Bridge and Ground Motions

An example bridge and its finite element model are depicted in this section. Effective stiffnesses and damping ratios from each equivalent linearization method are evaluated and. Finally, the characteristics of the 27 ground motions used as seismic input are described.

5.3.1 Description of Example Bridge

The bridge model analyzed by Hwang et al. (1996), as shown in Fig. 5.3.1, was chosen as an example bridge for this research. It has five spans with total length of 204.2m (39.62m + 39.62m + 45.72m + 39.62m + 39.62m). The bridge is symmetric and the height of the piers is the same for P2, P5 and P3, P4, respectively. The boundary conditions of both abutments (A1 and A6) and the bottom of the piers were assumed to be fixed. The geometry and material properties of the deck and pier are shown in Table 5.3.1. In the finite element model of the bridge, each span and each pier were composed of 6 and 4 elements, respectively.

The example bridge has isolation bearings installed at the top of the piers and abutments. The initial elastic stiffness, post-yielding stiffness, and yield strength of the isolation bearings are shown in Table 5.3.2. Though the stiffness of the isolation bearing at each abutment is somewhat lower than the stiffness at each pier, the hardening ratios of all isolation bearings are nearly the same.
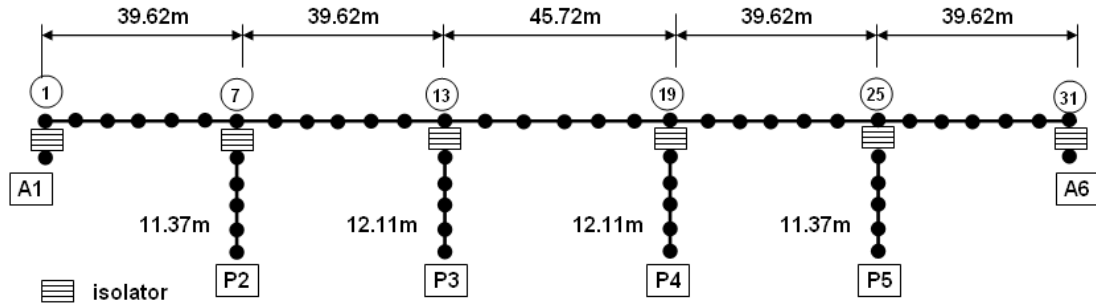
Figure 5.3.1 Isolated bridge model

Table 5.3.1 Element properties of example bridge

Properties		Deck	Pier
Mass density (ρ)		2,400kg/m^3	2,400kg/m^3
Young's Modulus (E$_c$)		22GPa	22GPa
Area (A)		6.87m^2	2.71m^2
Moment of Inertia	I$_y$	2.50m^4	0.59m^4
	I$_z$	105.77 m^4	0.59m^4

Table 5.3.2 Characteristic values of isolator

Location	Initial stiffness (K$_1$)	Post yielding stiffness (K$_2$)	Yield strength (F$_y$)	Hardening Ratio(=K$_2$/K$_1$)
Abutment	12,686 kN/m	1,954 kN/m	146 kN	0.1541
Pier	32,510 kN/m	5,002 kN/m	292 kN	0.1538

It can be seen in Eqs. (5-4) to (5-9) that the effective stiffness and damping ratio of an isolation bearing is a function of the hardening ratio and ductility ratio. Figures 5.3.2 and 5.3.3 show the effective stiffness and damping ratio of the isolation bearing with varying

shear ductility ratios for the hardening ratio of the example bridge (α =0.154). From Fig. 5.3.2, the effective stiffness, which is normalized to the initial stiffness, decreases significantly up to the ductility ratio of 10 in each method. So, the effective stiffness is very sensitive to small changes of the ductility ratio when the ductility ratio is smaller than 10. However, it is not so sensitive after the ductility ratio exceeds 10. The effective stiffness of the isolation bearing is only about 20% of the initial stiffness when the ductility ratio is larger than 15. Also, it is seen in Fig. 5.3.2 that in the range of small ductility ratios (less than 15) the AASHTO method estimates the smallest effective stiffness, while the Caltrans 94 method estimates the smallest effective stiffness in the range of large ductility ratios (greater than 15).

The effective damping ratios computed by each method show very different trends when compared to each other, as shown in Fig. 5.3.3. The effective damping ratio obtained by from the AASHTO method reaches its highest value (28%) at the ductility ratio of 4 and then decreases with increase of ductility ratio. The effective damping ratio obtained by the Caltrans 94 method keeps increasing gradually as the ductility ratio increases, while for the Caltrans 96 method, it remains around 15% for ductility ratios over 10. It should be noted that under the ductility ratio of 50, the effective damping ratios of the isolation bearings of the example bridge are always less than 28%, 25%, and 18% based on the AASHTO, Caltrans 94, Caltrans 96 methods, respectively.
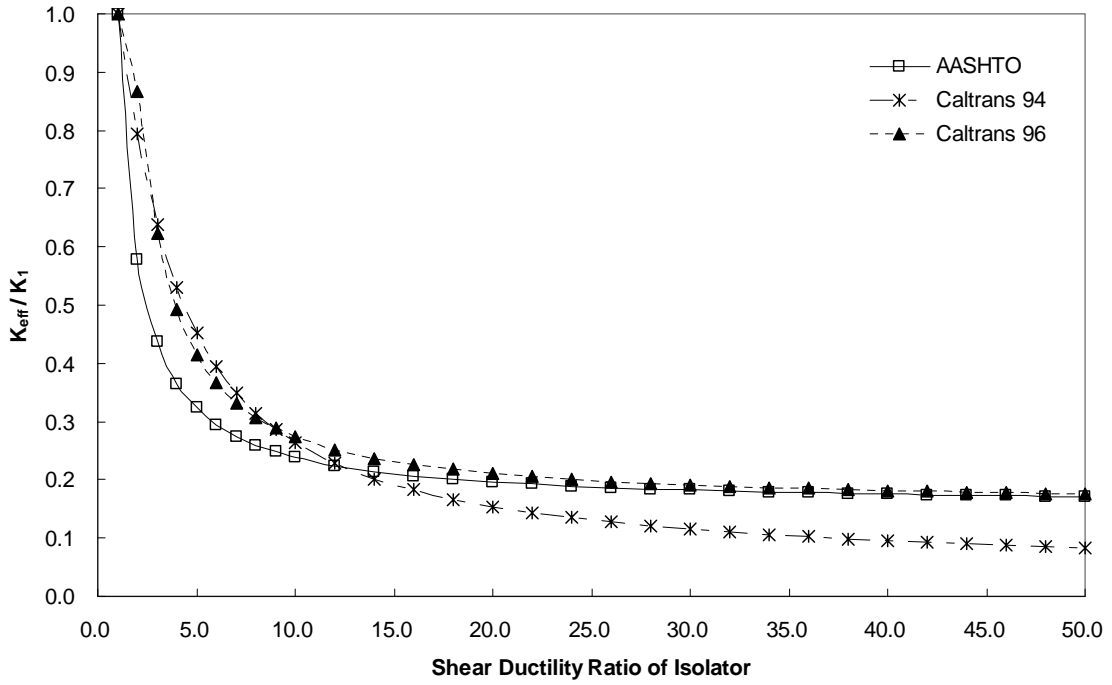
Figure 5.3.2 Effective stiffness of isolation bearing (α =0.154)
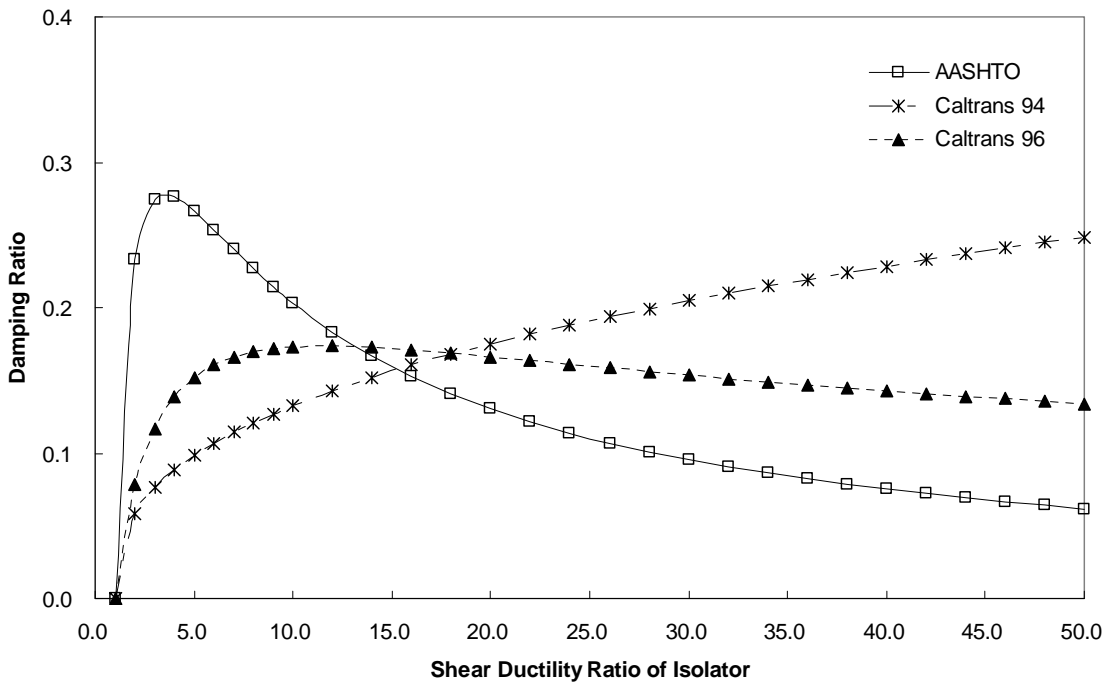
Figure 5.3.3 Effective damping ratio of isolation bearing (α =0.154)

5.3.2 Modal Analysis Results

A preliminary modal analysis was conducted for an un-isolated bridge case and an isolated bridge case of the example bridge. In the un-isolated bridge case, all the isolators were excluded from the bridge model and a rigid element at each pier top was directly connected to the deck. In the isolated bridge case, two different stiffness values were used as an effective stiffness of the isolation bearings: the initial elastic stiffness (K_1) and the post-yielding stiffness (K_2). Those two values can be thought of as the upper and lower bounds of the effective stiffness of the isolation bearings.

A comparison of the natural frequencies of the un-isolated and isolated bridge cases is shown in Table 5.3.3. The first mode of the un-isolated bridge case is a transverse directional mode with natural frequency of 1.803Hz, which is in the dominant frequency range of most of the earthquake motion used. However, as can be seen in Table 5.3.3, by installing the isolation bearings the fundamental frequency of the bridge was shifted from 1.80Hz to 1.01Hz (or 0.49Hz when K_2 was used as the effective stiffness of the isolation bearings) which is out of the dominant frequency range of the earthquake motions used. Figure 5.3.4 shows the first and third mode shapes of the isolated bridge case.

Table 5.3.3 Preliminary modal analysis of example bridge

Mode	Natural frequency (Hz)		
	Un-isolated case	Isolated case	
		Effective stiffness= K_1	Effective stiffness= K_2
1	1.80[†]	1.01[†]	0.49[†]
2	2.56[*]	1.15[‡]	0.51[‡]
3	3.44[*]	1.26[†]	0.75[†]
4	3.78[†]	2.26[*]	2.19[*]

† : Transverse mode, ‡ : Longitudinal mode, * : Vertical mode
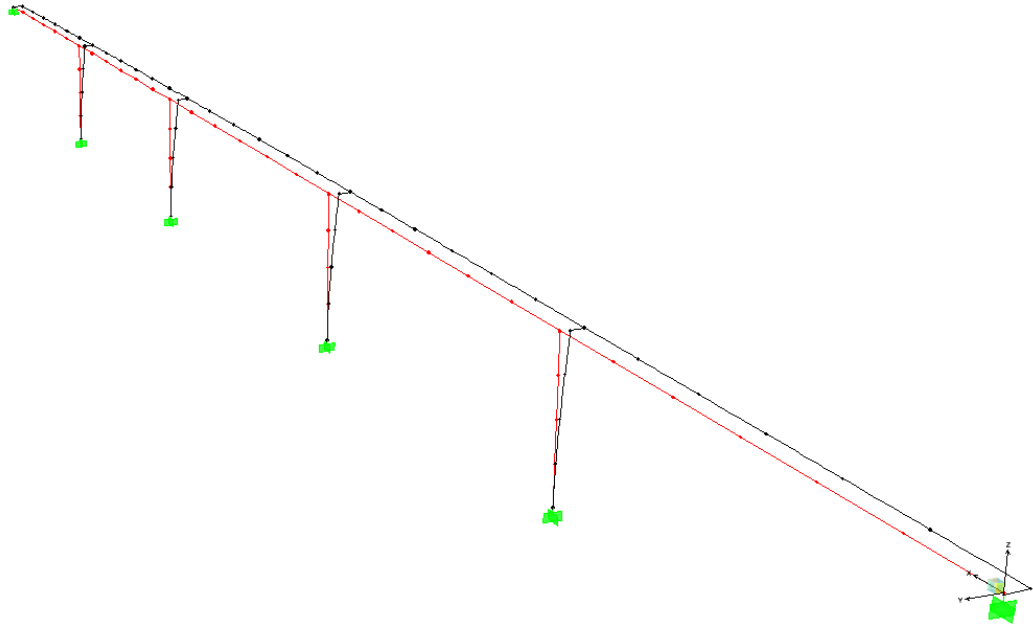
(b) 1st mode of transverse direction
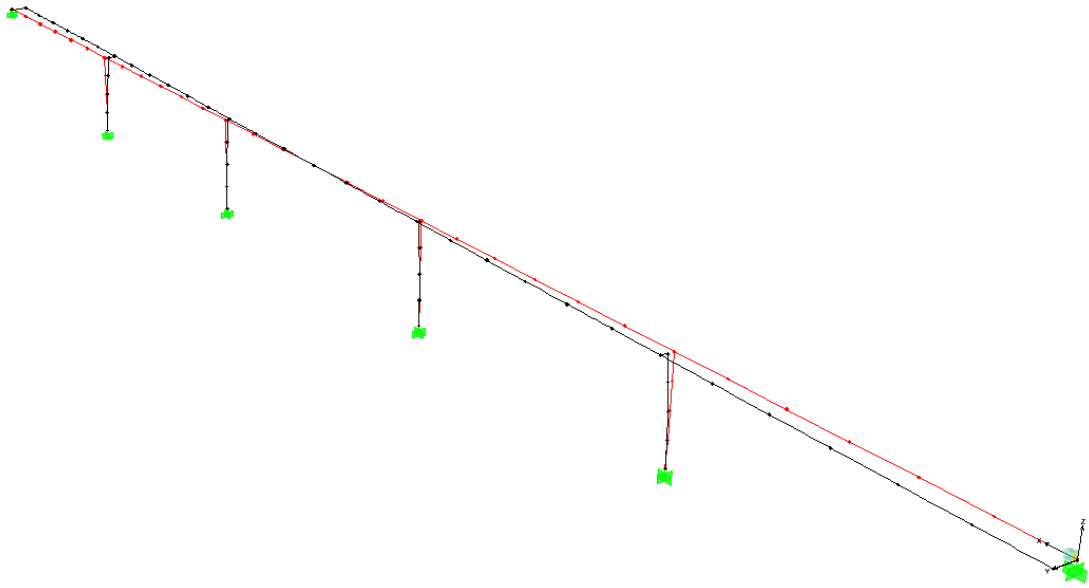
(b) 3rd mode of transverse direction

Figure 5.3.4 Mode shape of isolated bridge case

99

5.3.3 Ground Motions

The example bridge was subjected to the 27 earthquake motions suggested by Naeim and Kelly (1999). Though each pair of the ground motions were recorded in two perpendicular directions, each component of a pair of ground motion was applied to the example bridge only in transverse direction to investigate the applicability of the damping estimating method and the procedure proposed in this research.

The ground motions are divided into 3 groups according to their characteristics, as shown in Table 5.3.4. The ground motions in Group 1 have been suggested by the California Division of Mines and Geology for the design of seismically isolated structures.

Table 5.3.4 Description of ground motion group

Group	Characteristics
1	Near-fault effects, large ground velocities -1979 Imperial Valley EQ, the El Centro Array #6 station -1989 Loma Prieta EQ, the Hollister and Lexington dam station -1992 Petrolina EQ, the Petrolina station -1992 Landers EQ, the Lucerne Valley and Yermo station -1994 Northridge EQ, the Sylmar (County Hospital building parking lot) and the Newhall Fire Station
2	High-frequency, large ground accelerations with less significant long period content -1989 Loma Prieta EQ, the Corralitos station -1994 Northridge EQ, the Santa Monica City Hall grounds
3	More moderate ground shaking at various site conditions. -1989 Loma Prieta EQ, the Oakland Outer Harbor Wharf station -1990 Upland EQ, the Pomona (4th and Locust) station -1991 Sierra Madre EQ, the Altadena (Eaton Canyon Park) station -1994 Northridge EQ, the Century City station

5.4 Seismic Response from Bi-linear Model

The displacements of the deck and pier top of the example bridge at the locations of the isolation bearings were computed from the Bi-linear model giving results are summarized in Table 5.4.1. Since the bridge is symmetric, only the results of half of the bridge are presented. Figure 5.4.1 shows designated displacements for the deck and pier tops. The deck displacement (D_{deck}) is the summation of the pier top displacement (D_{pier}) and the relative displacement of the isolation bearing (D_{iso}).

Figure 5.4.2 shows ratios of maximum to minimum displacements along the deck and at the pier tops (i.e. $D_{deck}^{\max}/D_{deck}^{\min}$ and $D_{pier}^{\max}/D_{pier}^{\min}$) for the 27 earthquake motion used. It can be seen that this displacement ratio for the deck is nearly unity for all earthquake inputs; whereas, the same ratio for the pier tops is between 1.3 and 1.4 indicating that the relative displacements of the isolation bearings were quite different. From observation, the response results show the deck to behave essentially as a rigid body; while the isolation bearings experienced different maximum shear deformations and shear forces.

Table 5.4.1 Seismic displacement from Bi-linear model

Group	No.	Ground Motion	PGA (g)	D_{deck}			D_{pier}	
				A-1	P-2	P-3	P-2	P-3
Group 1	1	Array#6 140˚	0.376	35.70	35.73	35.83	4.41	6.04
	2	Array#6 230˚	0.437	40.89	40.90	40.98	4.97	6.80
	3	Holliste 0˚	0.369	21.70	21.73	21.82	2.89	3.97
	4	Holliste 90˚	0.178	7.02	7.01	7.00	1.26	1.73
	5	Lexingt 0˚	0.442	23.48	23.51	23.62	2.94	4.02
	6	Lexingt 90˚	0.410	27.55	27.61	27.75	3.45	4.73
	7	Petrolia 0˚	0.590	11.33	11.30	11.28	1.71	2.37
	8	Petrolia 90˚	0.663	29.98	30.03	30.15	3.54	4.83
	9	Lucerne Long.	0.704	4.59	4.58	4.57	1.09	1.46
	10	Lucerne Tran.	0.665	24.95	25.03	25.19	3.22	4.41
	11	Yermo 270˚	0.245	17.01	17.06	17.16	2.32	3.18
	12	Yermo 360˚	0.152	7.79	7.84	7.93	1.38	1.90
	13	Sylmarff 90˚	0.605	26.73	26.82	27.02	3.45	4.75
	14	Sylmarff 360˚	0.844	45.45	45.51	45.68	5.45	7.46
	15	Newhall 90˚	0.583	14.98	15.00	15.06	2.18	2.99
	16	Newhall 360˚	0.590	31.29	31.32	31.44	3.69	5.06
Group 2	17	Corralit 0˚	0.630	8.65	8.73	8.89	1.27	1.80
	18	Corralit 90˚	0.479	13.12	13.13	13.17	1.88	2.58
	19	S. Monica 90˚	0.884	12.01	12.06	12.16	1.85	2.53
	20	S. Monica 360˚	0.753	5.39	5.43	5.49	1.11	1.53
Group 3	21	Oak Whaf 35˚	0.287	12.33	12.36	12.46	1.80	2.48
	22	Oak Whaf 305˚	0.271	12.38	12.39	12.42	1.83	2.51
	23	Pomona 0˚	0.186	2.47	2.50	2.57	0.79	1.07
	24	Pomona 90˚	0.207	2.34	2.39	2.48	0.78	1.12
	25	Altadena 0˚	0.448	5.01	5.04	5.10	0.97	1.32
	26	Lacc. North 90˚	0.256	5.08	5.07	5.07	1.11	1.52
	27	Lacc. North 360˚	0.222	6.64	6.64	6.67	1.23	1.69
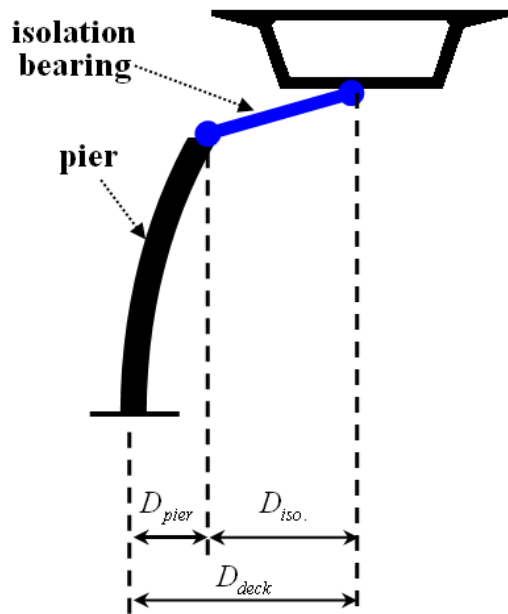
Figure 5.4.1 Definition of deck and pier top displacement
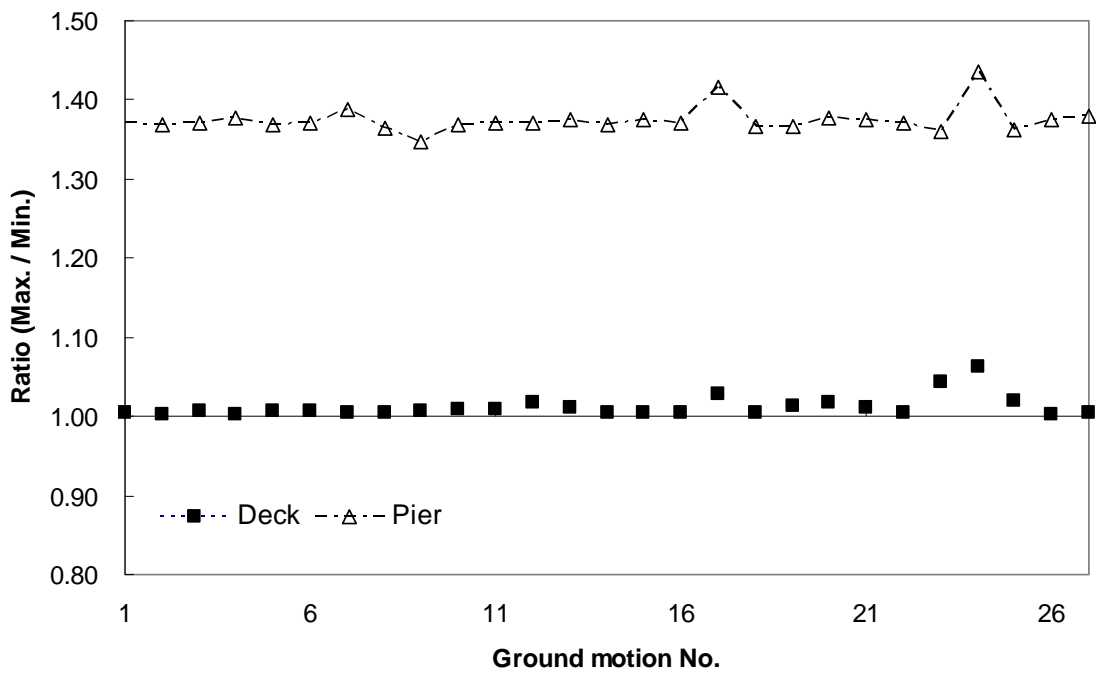
Figure 5.4.2 Ratio of maximum to minimum response of deck and pier top

5.5 Seismic Response from NP-Model

For the equivalent linear analysis of the isolated bridge, the isolation bearings were approximated by the equivalent linear model consisting of an elastic stiffness and a viscous damping ratio for each of the three linearization methods. Comparing the responses obtained respectively using the Bi-linear Model and the NP-Model, the accuracies of the different linearization methods were examined.

5.5.1 Results of Equivalent Linearization of Isolation Bearing

Using the maximum displacement from the seismic analysis of the Bi-linear Model, the isolation bearings were approximated as equivalent linear systems based on the AASHTO, Caltrans 94, and Caltrans 96 method. As seen in Eqs. (5-4) to (5-9), the estimation of the equivalent linear system depends on the hardening ratio and ductility ratio of isolation bearings.

Effective stiffness

Under each ground motion, the effective stiffness of the isolation bearings of the bridge was computed based on Eq. (5-4), (5-6), and (5-8) for each linearization method. The effective stiffness of the isolation bearing P-3 when the bridge is subjected to the first ground motion is shown below.

- Maximum relative displacement of isolation bearing

    From the seismic analysis of the Bi-linear Model, the maximum relative displacement of the isolation bearing P-3 was 29.793 cm.

- Yielding displacement and ductility ratio

104

$$D_y = \frac{F_y}{K_1} = \frac{292kN}{32,510 \times 10^{-2} \, kN/cm} = 0.898cm$$

$$\mu = \frac{D_{max}}{D_y} = \frac{29.793cm}{0.898cm} = 33.193$$

- AASHTO method

$$K_{eff} = \frac{1 + \alpha(\mu - 1)}{\mu} K_1 = \frac{1 + (0.154)(33.193 - 1)}{33.193}(32,510kN/m) = 5,830kN/m$$

- Caltrans 94 method

$$K_{eff} = \frac{K_1}{\left\{1 + \ln\left[1 + 0.13(\mu - 1)^{1.137}\right]\right\}^2} = \frac{32,510kN/m}{\left\{1 + \ln\left[1 + 0.13(33.193 - 1)^{1.137}\right]\right\}^2} = 3,505kN/m$$

- Caltrans 96 method

$$K_{eff} = \frac{1 + \alpha(\mu - 1)}{\mu}\left(1 - 0.737\frac{\mu - 1}{\mu^2}\right)^{-2}$$

$$= \frac{1 + (0.154)(33.193 - 1)}{33.193}\left(1 - (0.737)\frac{33.193 - 1}{33.193^2}\right)^{-2}$$

$$= 6,090kN/m$$

Tables B.1.1 to B.1.3 of Appendix B show the effective stiffness from the three linearization methods. Figure 5.5.1 plots the effective stiffness of the isolation bearing P-3 normalized to the elastic stiffness (K_1) for each earthquake and for the different linearization methods. Figure 5.5.2 shows the same normalized effective stiffness plotted as a function of shear ductility ratio of the isolation bearing.
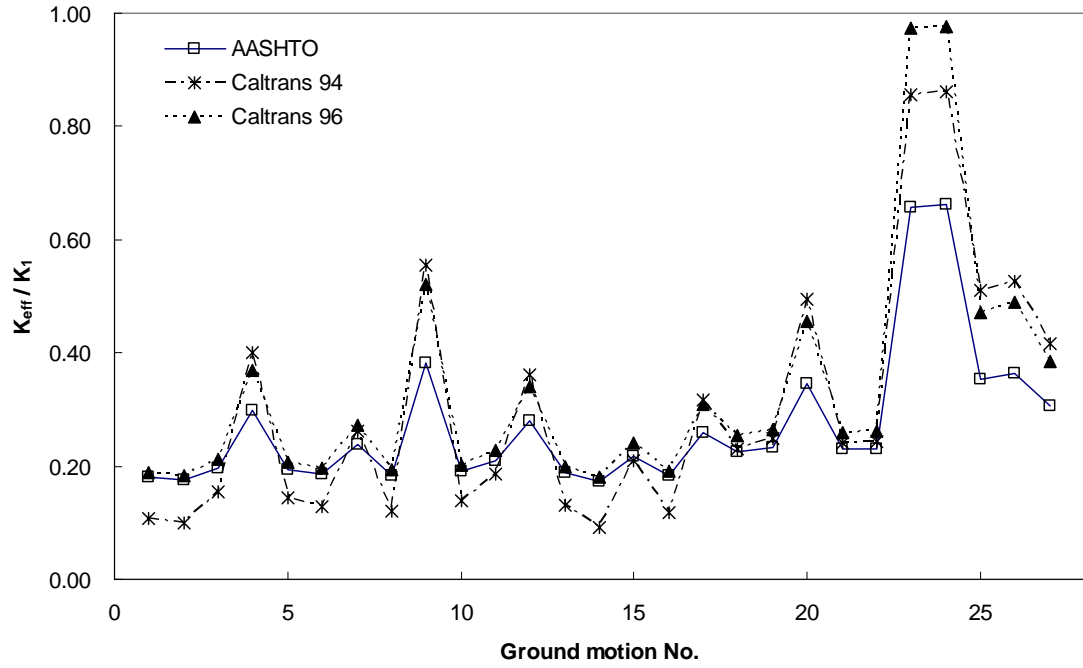
Figure 5.5.1 Effective stiffness of isolation bearing P-3
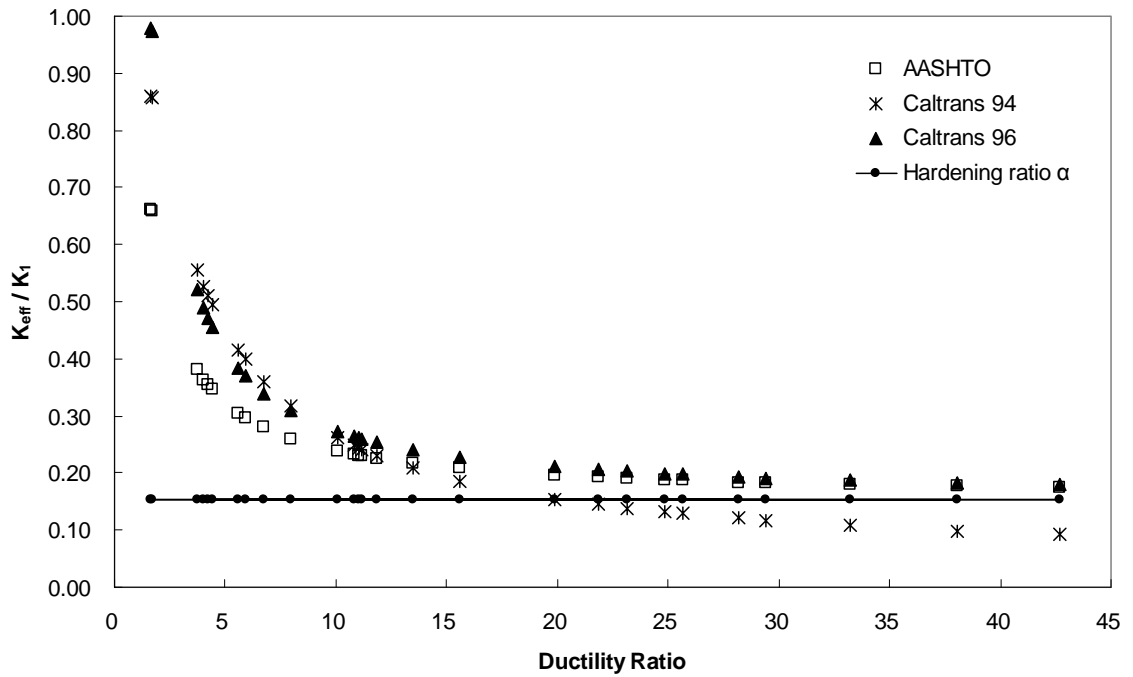
Figure 5.5.2 Effective stiffness of isolation bearing P-3 with ductility ratio

It can be seen from Fig. 5.5.1 that all the linearization methods show a similar trend with ground motion numbers. In Fig. 5.5.2, as the ductility ratio increases, the effective stiffness ratios from the AASHTO and Caltrans 96 methods converge to the hardening ratio; however, the effective stiffness ratios from the Caltrans 94 method are smaller than the hardening ratio of 0.154 for ductility ratios greater than 20, which indicates that the effective stiffness from the Caltrans 94 method is smaller than the post-yielding stiffness of the isolator (K_2).

Effective damping ratio

The effective damping ratios of the isolation bearings from each linearization method are given in Table B.1.1 to B.1.3. The effective damping ratio of the isolation bearing P-3 is computed below when the bridge is subjected to the first ground motion using Eq. (5-5), (5-7), and (5-9) for each linearization method.

- AASHTO method

$$\xi_{eff} = \frac{2(1-\alpha)(1-1/\mu)}{\pi\left[1+\alpha(\mu-1)\right]} = \frac{2(1-0.154)(1-1/33.193)}{\pi\left[1+(0.154)(33.193-1)\right]} = 0.088$$

- Caltrans 94 method

$$\xi_{eff} = 0.0587(\mu-1)^{0.371} = 0.0587(33.193-1)^{0.371} = 0.213$$

- Caltrans 96 method

$$\xi_{eff} = \frac{2(1-\alpha)(1-1/\mu)}{\pi\left[1+\alpha(\mu-1)\right]}\left(\frac{\mu^{0.58}}{6-10\mu}\right)$$

$$= \frac{2(1-0.154)(1-1/33.193)}{\pi\left[1+0.154(33.193-1)\right]}\left(\frac{33.193^{0.58}}{6-10(33.193)}\right) = 0.150$$

Effective damping coefficient

Since the damping coefficient, instead of the damping ratio, of the isolation bearing is needed for the linear time history analysis, it is computed from the assumption that the dissipated energy of the equivalent viscoelastic model and the bi-linear model of the isolation bearing is the same.

The enclosed areas in Fig. 5.5.3 (a) and (b) represent the dissipated energy of both models during one cycle. The dissipated energy of an equivalent viscoelastic model is as follows:

$$E_{vis.}^{D} = \pi c \omega D_{max}^{2} \tag{5-10}$$

where c is the effective damping coefficient; ω is the frequency of vibration; D_{max} is the maximum amplitude.

Meanwhile, the hysteretic dissipated energy of the bi-linear model is

$$E_{bilinear}^{D} = 4 Q_{d} (D_{max} - D_{y}) \tag{5-11}$$

Equation (5-11) can be expressed using the effective damping ratio and the strain energy of the bi-linear model as

$$E_{bilinear}^{D} = 4\pi E_{S} \xi_{eff} \tag{5-12}$$

where E_{S} is the strain energy and ξ_{eff} is the effective damping ratio.

Substituting $E_{S} = \dfrac{1}{2} K_{eff} D_{max}^{2}$, Eq. (5-12) is represented as

$$E_{bilinear}^{D} = 2\pi K_{eff} D_{max}^{2} \xi_{eff} \tag{5-13}$$

where K_{eff} is the effective stiffness of the bi-linear model.

Equating (5-10) and (5-13), the damping coefficient can be derived as

$$c = \frac{2 K_{eff} \xi_{eff}}{\omega} \tag{5-14}$$

The first natural frequency of the undamped bridge model was used as the vibration frequency ω in Eq. (5-14), assuming that the first mode is the dominant vibration mode of the isolated bridge. Viscous damping coefficient of the isolation bearing P-3 from each linearization method is

- AASHTO method

$$c = \frac{2 K_{eff} \xi_{eff}}{\omega} = \frac{2 (5,830)(0.088)}{3.302} = 310 kN \cdot \sec/m$$

- Caltrans 94 method

$$c = \frac{2 K_{eff} \xi_{eff}}{\omega} = \frac{2 (3,505)(0.213)}{2.618} = 570 kN \cdot \sec/m$$

- Caltrans 96 method

$$c = \frac{2 K_{eff} \xi_{eff}}{\omega} = \frac{2 (6,090)(0.150)}{3.365} = 543 kN \cdot \sec/m$$

The first modal frequency of the bridge varies because the effective stiffness of the isolation bearings are different from each linearization method. Figures 5.5.4 and 5.5.5 show the effective damping ratio and damping coefficient of the isolation bearing P-3 under the ground motions, respectively. In Fig. 5.5.4 the damping ratio from the Caltrans 94 method shows an opposite trend when compared to the results from the AASHTO method. The variance of the damping ratios from the AASHTO and Caltrans 94 methods are very large compared with the corresponding variance from the AASHTO and Caltrans 96 method. As shown in Fig. 5.5.5, the damping coefficients from the Caltrans 94 method are nearly the same for all ground motions.

The constant damping coefficients from the Caltrans 94 method can be explained considering the results in Figs. 5.5.1 and 5.5.4. The effective stiffness from the Caltrans 94 method in Fig. 5.5.1 shows an opposite trend to that of the effective damping ratio in Fig. 5.5.4 with increasing ground motion number. As a result, the two quantities in opposite trends compensate for each other in Eq. (5-14) to produce nearly the same damping coefficients for all ground motions. Figures 5.5.6 and 5.5.7 show the damping ratio and damping coefficient versus the ductility ratio for isolation bearing P-3 as obtained using the different linearization methods.

110
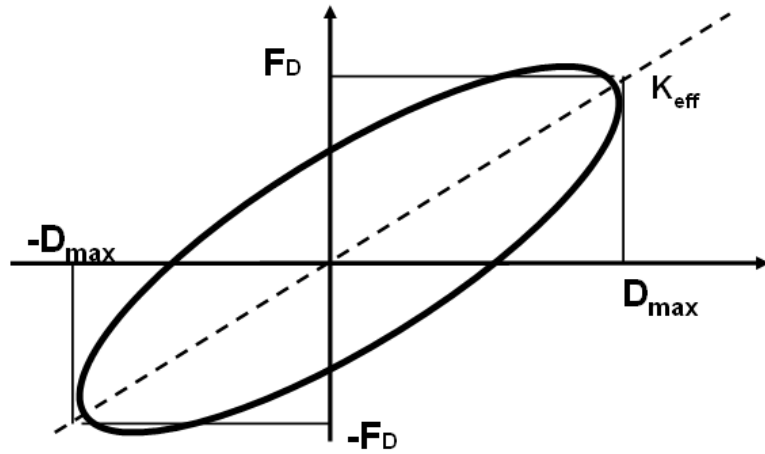
(a) Equivalent viscoelastic system
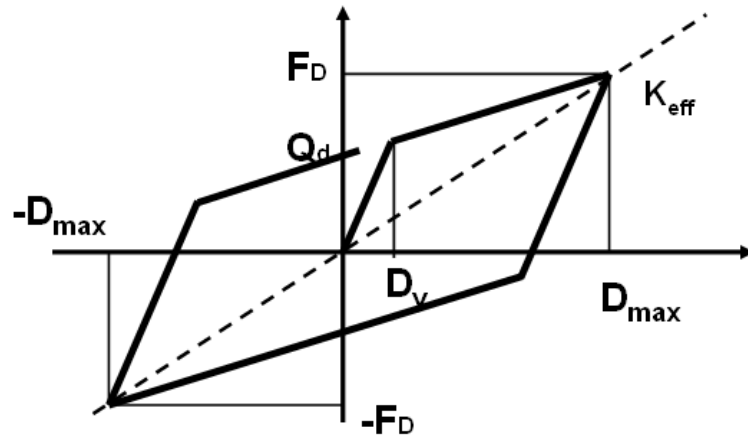
(b) Bilinear model

Figure 5.5.3 Dissipated energy of equivalent linear system and bilinear model
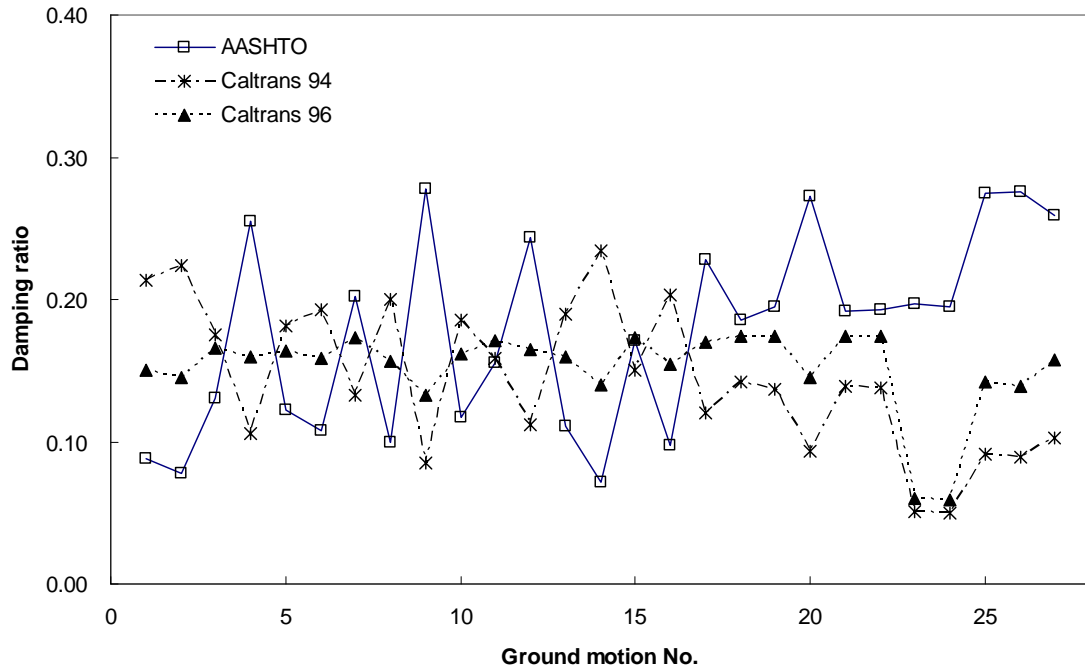
Figure 5.5.4 Damping ratio of isolator P-3
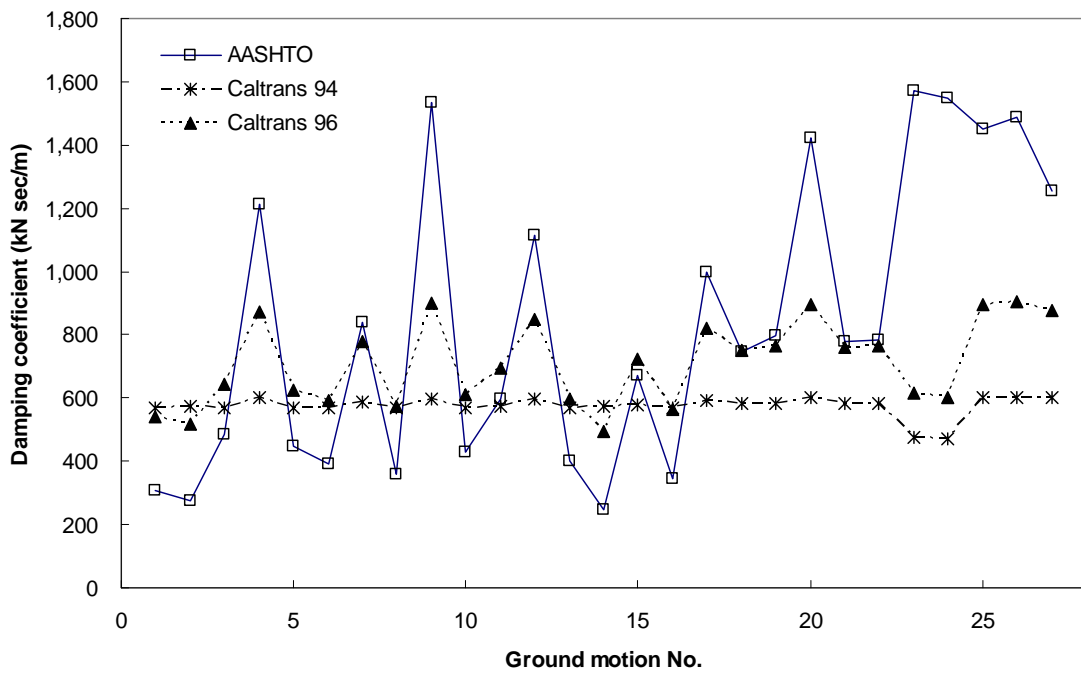
Figure 5.5.5 Damping coefficient of isolator P-3
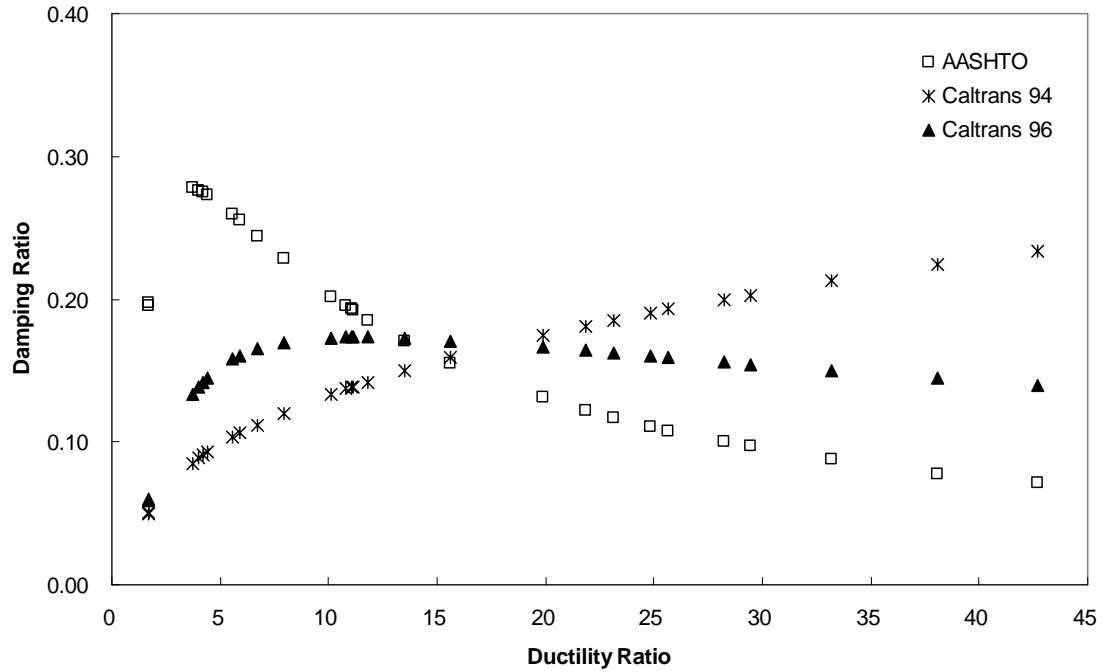
Figure 5.5.6 Damping ratio vs. ductility ratio of isolator P-3
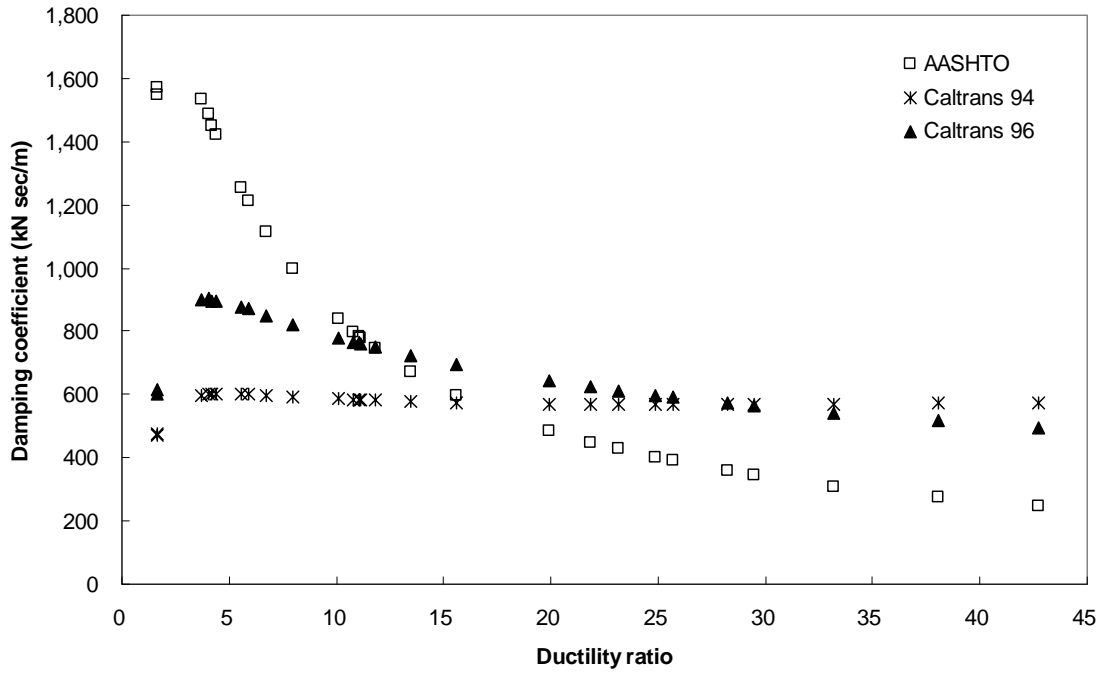
Figure 5.5.7 Damping coefficient vs. ductility ratio of isolation bearing P-3

113

5.5.2 Seismic Response from NP-Model

The finite element model of the bridge with equivalent viscoelastic elements for the isolation bearings is the NP-Model. Based on the NP-Model, the displacements of the deck and pier tops were computed by the Newmark integration method giving results as shown in Table B.2.1 to B.2.3 of Appendix B. The relative error of each maximum displacement obtained using the NP-Model and the Bi-linear Model is plotted in Fig's. 5.5.8 to 5.5.10 for each linearization method.

From Figs. 5.5.8 to 5.5.10, it can be seen that the relative error of the pier tops is greater than that of the deck for all linearization methods, which means that the three linearization methods are less accurate for the estimation of the pier top displacements. Among the three methods, the AASHTO method appears to be the most accurate method of all the methods evaluated, as seen when comparing the AASHTO method responses with corresponding NP-Model and Bi-linear Model responses. The relative error from the Caltrans 94 method is found to be very high for the pier tops. The accuracy of each linearization method is quantified by the root-mean-square-error (RMSE) which is defined in the following Eq. (5-15).

$$ RMSE = \sqrt{ \frac{1}{MN} \sum_{j=1}^{M} \sum_{i=1}^{N} \left(\frac{x_{i,j}^{li} - x_{i,j}^{bi}}{x_{i,j}^{bi}} \right)^2 } \qquad (5\text{-}15) $$

In this equation, N is the total number of displacement locations; M is the total number of ground motions; $x_{i,j}^{li}$ and $x_{i,j}^{bi}$ represent the separate displacements of the NP-Model and Bi-linear Model at location i under ground motion j.

114

Table 5.5.4 summarizes the RMSE of each linearization method. In this table, the RMSE values from the AASHTO method are the lowest and that from the Caltrans 94 is the highest. Also, it can be seen that the RMSE from all linearization methods is high for both the deck and pier tops under earthquake Groups 2 and 3.

Figures 5.5.11 to 5.5.13 show the relation between the ductility ratio of the isolation bearings and the accuracy of each linearization method. It is observed that as the ductility ratio becomes smaller, the relative error generally becomes larger, especially for the Caltrans 94 and 96 methods. So it can be concluded that the linearization methods tend to overestimate the response under ground motions which produce a low ductility ratios of the isolation bearings. That is why the relative errors under earthquake Groups 2 and 3 are higher than that of Group 1 in Table 5.5.1.

It should be noted that the relative error of the pier top from the Caltrans 94 is very large for both small and large ductility ratios. Especially, the displacement at the pier tops is underestimated for the large ductility ratio range from the Caltrans 94 method.

Table 5.5.1 RMSE of linearization method

Earthquake Group	AASHTO		Caltrans 94		Caltrans 96	
	Deck	Pier top	Deck	Pier top	Deck	Pier top
1	0.115	0.126	0.167	0.343	0.126	0.200
2	0.135	0.239	0.321	0.573	0.197	0.419
3	0.132	0.215	0.214	0.482	0.121	0.373
All	**0.123**	**0.172**	**0.209**	**0.423**	**0.138**	**0.293**
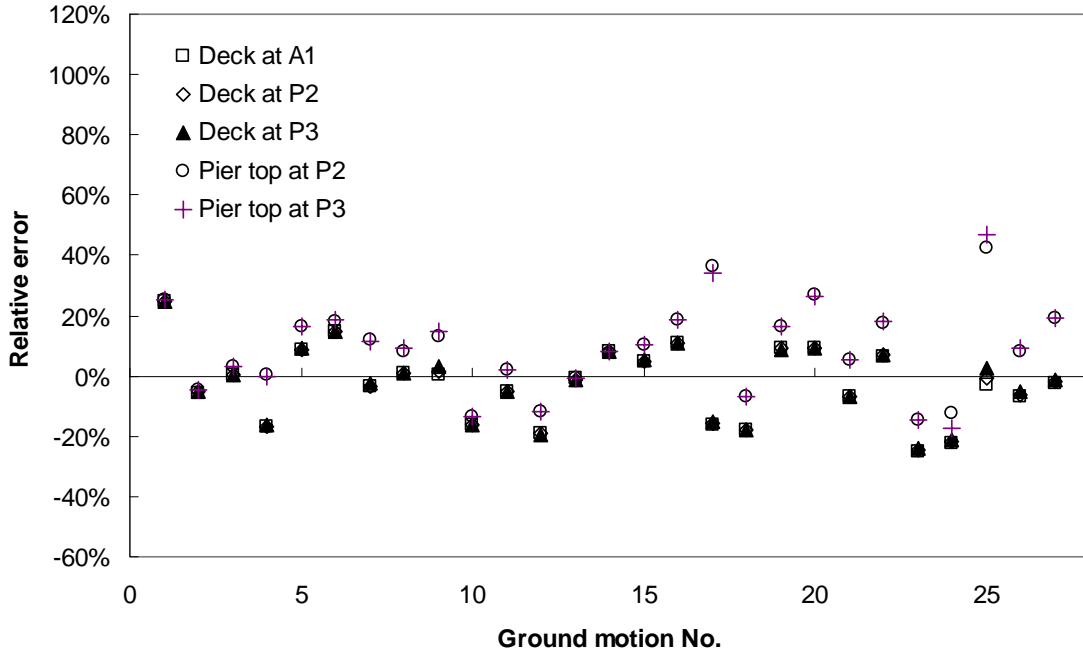
Figure 5.5.8 Relative error of AASHTO method
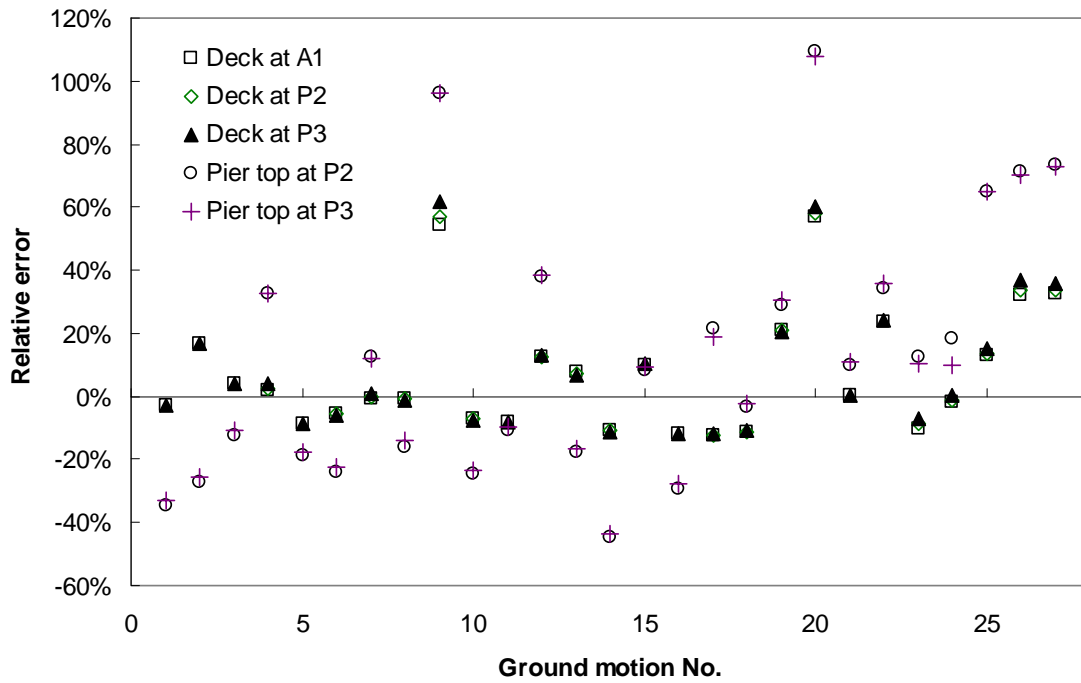
Figure 5.5.9 Relative error of Caltrans 94 method
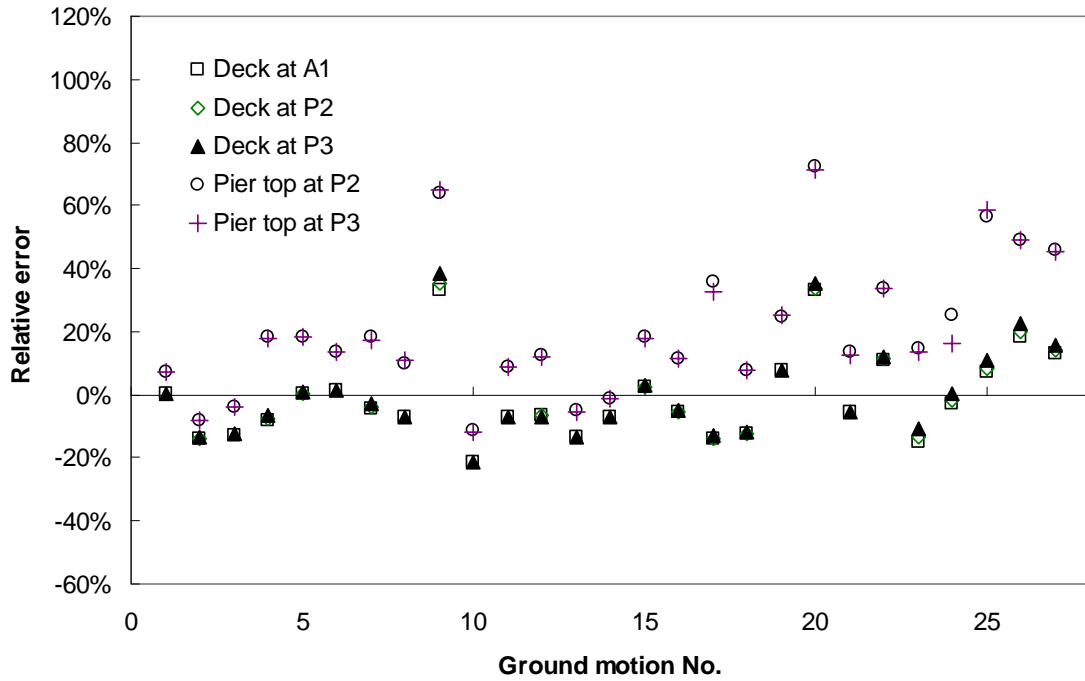
Figure 5.5.10 Relative error of Caltrans 96 method
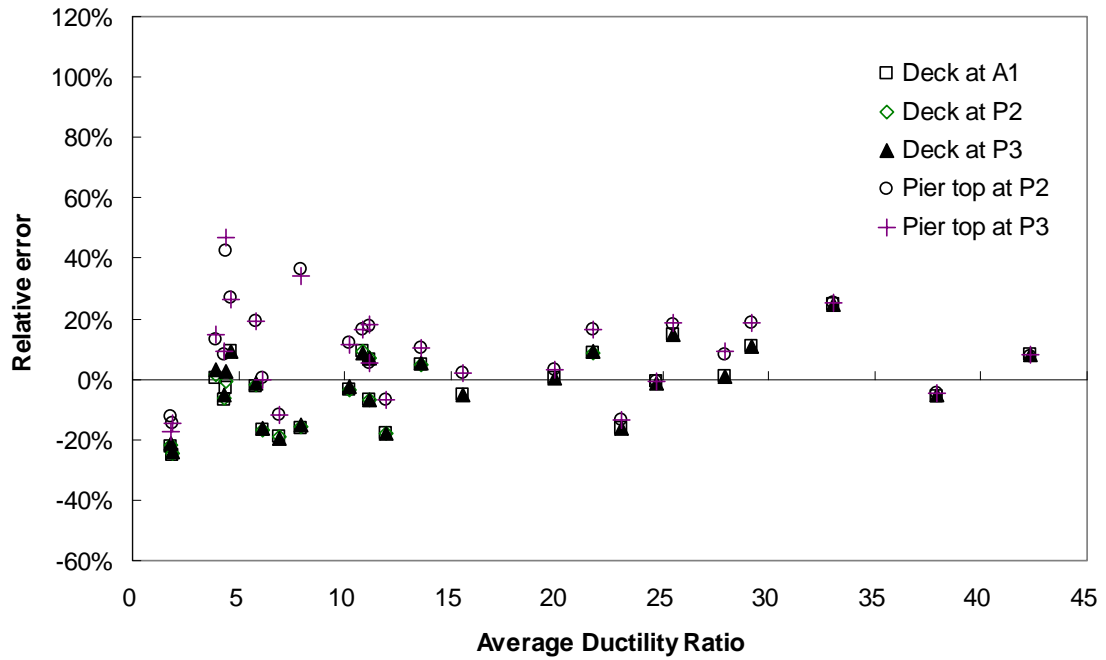
Figure 5.5.11 Relative error with average ductility ratio by AASHTO method

117
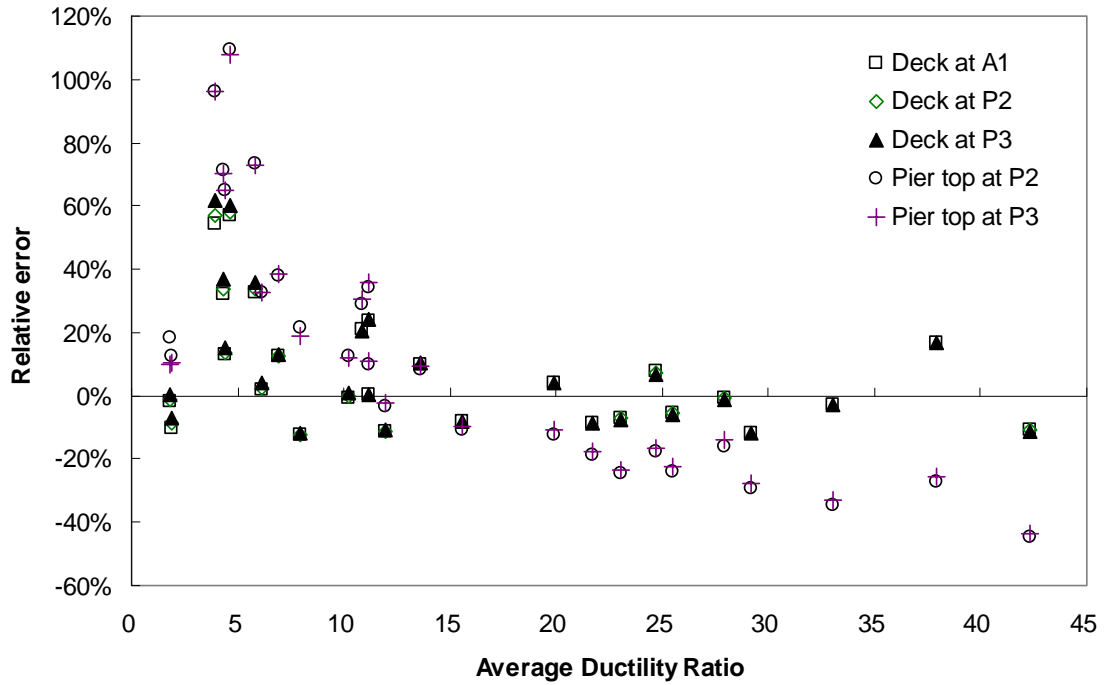
Figure 5.5.12 Relative error with average ductility ratio by Caltrans 94 method
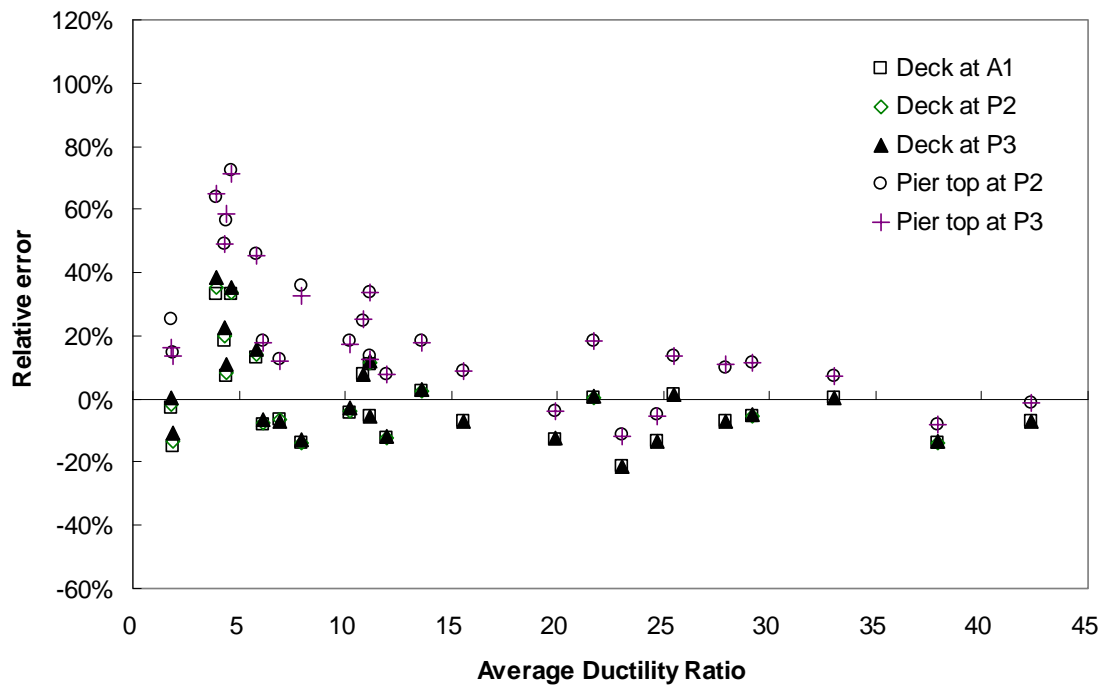
Figure 5.5.13 Relative error with average ductility ratio by Caltrans 96 method

5.6 EMDR Estimation

The four damping estimating methods are applied to the NP-Model of the bridge to compute the EMDR of each mode. The EMDR of the first mode obtained by each damping estimation method is presented in this section and it is compared with the effective damping ratio of the isolation bearings estimated by each linearization method. The procedure of each damping estimation method is described when AASHTO linearization method is used and the bridge is subjected to the first ground motion.

5.6.1 Complex Modal Analysis (CMA) Method

The procedure of the CMA method is explained as follows:

Step 1. Establish mass, stiffness, and damping matrix of ia bridge system.

- The element used for deck and bent of the bridge is shown in Fig. 5.6.1. The lumped mass matrix $[m^e]$ of the element which has 2 degrees-of-freedom is represented as Eq. (5-16). The matrix has half of the element mass at each translational nodal degree-of-freedom. In Eq. (5-16), ρ is mass density of concrete, A is area of element section, and l is element length. The global mass matrix of whole system is obtained by assembling each element mass matrix.

$$[m^e] = \frac{\rho\, A\, l}{2} \begin{bmatrix} 1 & 0 & 0 & 0 \\ 0 & 0 & 0 & 0 \\ 0 & 0 & 1 & 0 \\ 0 & 0 & 0 & 0 \end{bmatrix} \tag{5-16}$$

- The stiffness matrix of the element shown in Fig. 5.6.1 is shown in Eq. (5-17)

119

$$[k^e] = \frac{EI}{l^3} \begin{bmatrix} 12 & 6l & -12 & 6l \\ 6l & 4l^2 & -6l & 2l^2 \\ -12 & -6l & 12 & -6l \\ 6l & 2l^2 & -6l & 4l^2 \end{bmatrix}$$

(5-17)

where E and I are Young's modulus and moment of inertia of element. Global stiffness matrix is obtained by assembling each element stiffness matrix. The stiffness matrix of each isolation bearing is formulated as Eq. (5-18) using effective stiffness of the isolation bearing and is added to corresponding degree-of-freedom elements in the global stiffness matrix.

$$[k_{iso}^e] = k_{eff} \begin{bmatrix} 1 & 0 & -1 & 0 \\ 0 & 0 & 0 & 0 \\ -1 & 0 & 1 & 0 \\ 0 & 0 & 0 & 0 \end{bmatrix}$$

(5-18)
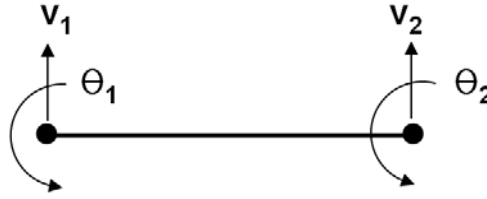
Node degree-of-freedom

- The damping of deck and pier of the bridge is assumed as 5% Rayleigh damping. The damping coefficient α and β can be found by specifying 5% damping ratio of any two modes. In this research, it was assigned to the first and third mode. So, the damping matrix of the concrete structure is $[c_{str}] = \alpha[m] + \beta[k]$. The damping matrix of each isolation bearing $[c_{iso}^e]$ is formulated as Eq. (5-19). The global damping matrix is obtained by adding $[c_{str}]$ and $[c_{iso}^e]$

$$[c_{iso}^e] = c_{eff} \begin{bmatrix} 1 & 0 & -1 & 0 \\ 0 & 0 & 0 & 0 \\ -1 & 0 & 1 & 0 \\ 0 & 0 & 0 & 0 \end{bmatrix} \tag{5-18}$$

Step 2. Obtain $[A]$ and $[B]$ matrix using Eq. (3-7).

Step 3. Compute eigenvalues of the characteristic equation shown in Eq.(3-8).

- The dimension of the matrix $[A]$ and $[B]$ is $2n \times 2n$ (n is the total number of degree-of-freedom), and $2n$ conjugate eigenvalues are obtained from eigen analysis. The second column of Table 5.6.1 shows the eigenvalues of the NP-Model of the bridge from the complex modal analysis.

Table 5.6.1 Eigenvalues and natural frequencies of NP-Model

Mode	Eigenvalues	Natural frequency (rad/sec)
1	0.392 –3.200i	$\sqrt{0.392^2 + 3.200^2} = 3.224$
2	0.451 – 3.363i	$\sqrt{0.451^2 + 3.363^2} = 3.393$
3	0.743 – 8.522i	$\sqrt{0.743^2 + 8.522^2} = 8.554$
4	2.465 –21.630i	$\sqrt{2.465^2 + 21.630^2} = 21.770$

Step 4. Compute natural frequency of each mode from corresponding eigenvalue using Eq. (3-11).

- The third column of Table 5.6.1 shows the natural frequency computed using the eigenvalues of the second column of Table 5.6.1.

Step 5. Compute effective damping ratio of each mode from real part of eigenvalue and natural frequency of corresponding mode using Eq. (3-12).

- Table 5.6.2 shows the final results of EMDR from the CMA method. The first and second modal damping ratios are found as 25% and 55%, respectively. Table 5.6.3 compares the undamped natural frequency of NP-Model and P-Model of the bridge. It is shown that they are very close to each other.

Table 5.6.2 EMDR of example bridge by CMA method

Mode	EMDR
1	$0.392/3.224 = 0.122$
2	$0.451/3.393 = 0.133$
3	$0.743/8.554 = 0.087$
4	$2.465/21.770 = 0.113$

Table 5.6.3 Undamped natural frequency and EMDR from CMA method

Mode	Undamped Natural Frequency (Hz)		EMDR
	NP-Model	P-Model	
1	0.512	0.513	0.122
2	0.539	0.540	0.133
3	1.360	1.362	0.087
4	3.460	3.465	0.113

Figure 5.6.1 shows the EMDR of the first mode from the complex modal analysis method. The EMDR in Fig. 5.6.1 shows nearly the same trend as the effective damping ratio of the isolation bearing shown in Fig. 5.5.4. As in the case of the effective damping ratio, the EMDR from the Caltrans 94 and AASHTO method show an opposite trend to each other and the EMDR from the Caltrans 96 method is between the two values. For all ground motions the EMDR ranges from 0.1 to 0.3.

5.6.2 Neglecting off-Diagonal Elements (NODE) Method

The step 1 of the NODE method is the same as in the CMA method.

Step 2. Compute undamped mode shape and natural frequency of each mode from mass and stiffness matrix. For the NODE method, the undamped mode shapes from the P-Model were used.

Step 3. Obtain modal damping matrix by pre- and post-multiplying mode shape matrix to damping matrix.

- Table 5.6.4 shows the results of pre- and post-multiplication of the normal mode shapes to the damping matrix of the NP-Model up to the fourth mode.

Table 5.6.4 Modal damping matrix ($[\phi]^{T}[c][\phi]$)

Mode	1	2	3	4
1	0.793	**0.009**	**-0.109**	**0.000**
2	**0.009**	0.900	**-0.003**	**0.195**
3	**-0.109**	**-0.003**	1.486	**0.004**
4	**0.000**	**0.195**	**0.004**	4.947

Step 4. Compute effective damping ratio of each mode from Eq. (3-16) ignoring off-diagonal elements of modal damping matrix.

- If the mode shapes are mass normalized ones, the term $\{\phi_i\}^T[m]\{\phi_i\}$ in the denominator of Eq. (3-16) is unity and the EMDR of i th mode becomes

$$\xi_i = \frac{c_{i,i}}{2\omega_i} \tag{5-19}$$

where ω_i is undamped natural frequency (rad/sec) of i th mode. Table 5.6.5 shows the EMDR of each mode computed by Eq. (5-19).

Table 5.6.5 EMDR from NODE method

Mode	EMDR
1	$0.793/(2 \times 3.224) = 0.123$
2	$0.900/(2 \times 3.393) = 0.133$
3	$1.486/(2 \times 8.554) = 0.087$
4	$4.947/(2 \times 21.770) = 0.114$

Step 5. Check error criteria using Eq. (3-18). If a parameter from Eq. (3-18) of any two modes is greater than unity, change to other methods.

- Table 5.6.6 shows the modal coupling parameters and it can be seen that all the parameters are less than unity.

Table 5.6.6 Modal coupling parameter

Mode	1	2	3	4
1	-	0.026	-0.005	0.000
2	0.027	-	0.000	0.001
3	-0.014	-0.000	-	0.000
4	0.000	0.009	0.000	-

Figure 5.6.2 shows the EMDR from the NODE method. In this figure, the EMDR ranges from 0.1 to 0.3 in most cases; however, it becomes unreasonably large under some ground motions, in some cases exceeding 0.7. The occurrences of the high EMDR do not coincide in each linearization method. For example, the high EMDR occurs under the ground motion numbers 6, 12, and 27 from the Caltrans 96 method, however, it occurs under the ground motion numbers 14, 16, and 25 from the Caltrans 94 method. The modal coupling parameters of the high EMDR cases were found to be greater than unity.
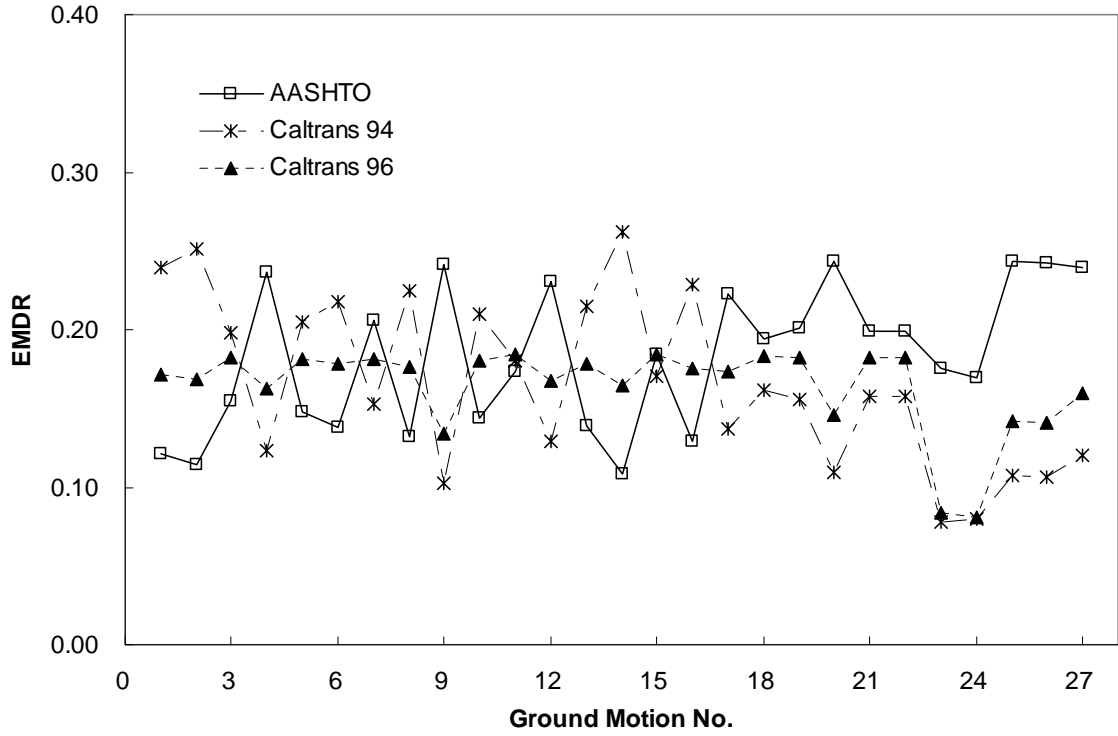
Figure 5.6.1 EMDR from CMA method
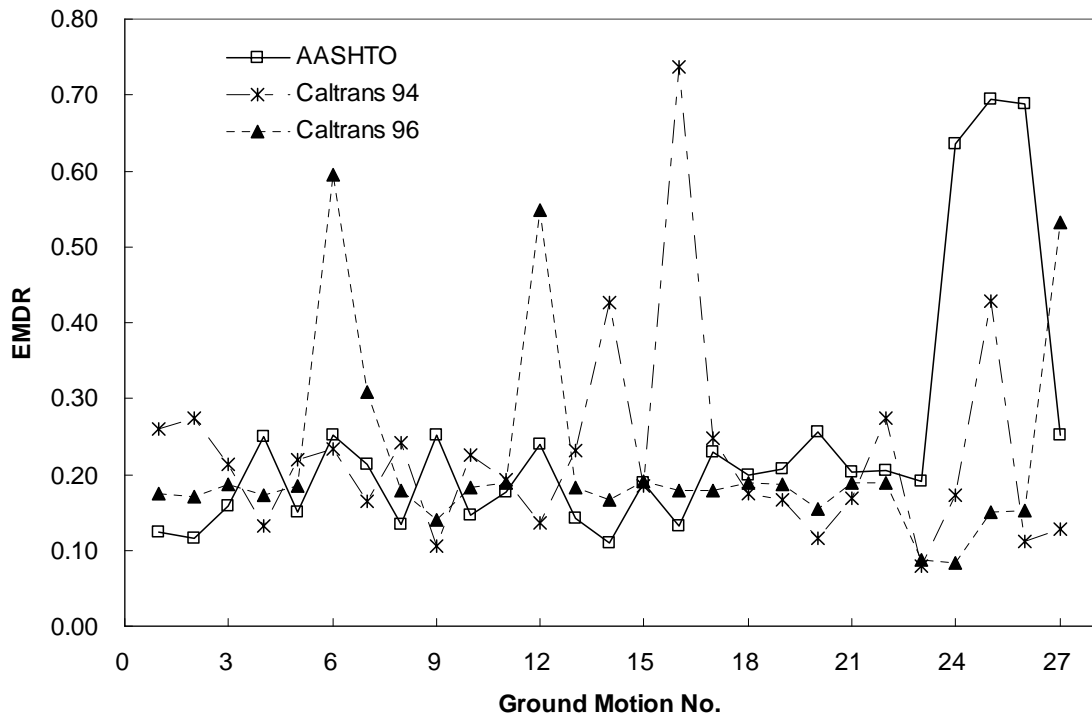
Figure 5.6.2 EMDR from NODE method

126

5.6.3 Composite Damping Rule (CDR) Method

To apply the composite damping rule method, the example bridge was divided into two components : i) concrete structure, and ii) isolation bearings. The damping ratio of the concrete structure components was assumed as 5% and the effective damping ratio from the linearization method was used as the damping ratio of the isolation bearing components. The procedure of the CDR method is shown as follows:

Step 1. Establish mass and stiffness matrix of a bridge system. This step is the same as the first step of the CMA method.

Step 2. Obtain undamped mode shapes based on the mass and stiffness matrix of step 1.

Step 3. Compute potential energy ratio of each component for each mode using Eq. (3-36).

- For the computation of the modal strain energy of the deck for the isolated modes, the relative mode shape, instead of the absolute mode shape, should be used because the deformation of the isolation bearing does not contribute to the modal strain energy of the deck. Therefore, in this study the relative mode shape of the bridge deck was calculated by subtracting the deformation of the isolation bearing ($d_{iso.}$) from the absolute mode shape amplitude ($\phi_{abs.}$) as illustrated in Fig. 5.6.3.

- The computed potential energy of each component is given in Table 5.6.7. In the table the potential energy ratio of isolation bearing component is 80% and 89% for the first and second mode, respectively. After the third mode, the ratio of isolation bearing component decreases.

127

Table 5.6.7 Potential energy ratio in CDR method

Mode	Potential energy			Energy ratio	
	Total (U_{total})	Structure (U_{str})	Isolator (U_{iso})	U_{str} / U_{total}	U_{bnd} / U_{total}
1	5.462	1.055	4.407	0.193	0.807
2	5.855	0.623	5.232	0.106	0.893
3	43.413	37.669	5.744	0.867	0.132
4	244.816	238.440	6.376	0.974	0.026

Step 4. Compute EMDR using Eq. (3-34).

- The damping ratio of isolation bearings were identified as 0.093, 0.084, and 0.088 for isolator A-1, P-2, and P-3, respectively, from the AASHTO linearization method. The average damping ratio of the isolation bearing is used as the damping ratio of isolation bearing component in estimation of the EMDR. Based on Eq. (3-34), the EMDR of each mode is computed as in Table 5.6.8.

Table 5.6.8 EMDR from CDR method

Mode	EMDR
1	$(0.050)(0.193) + (0.088)(0.807) = 0.081$
2	$(0.050)(0.106) + (0.088)(0.893) = 0.084$
3	$(0.050)(0.867) + (0.088)(0.132) = 0.055$
4	$(0.050)(0.974) + (0.088)(0.026) = 0.051$

The EMDR from the composite damping rule method is shown in Fig. 5.6.4. It ranges from 0.05 to 0.2, which is always smaller than the effective damping ratio of the isolation bearings.
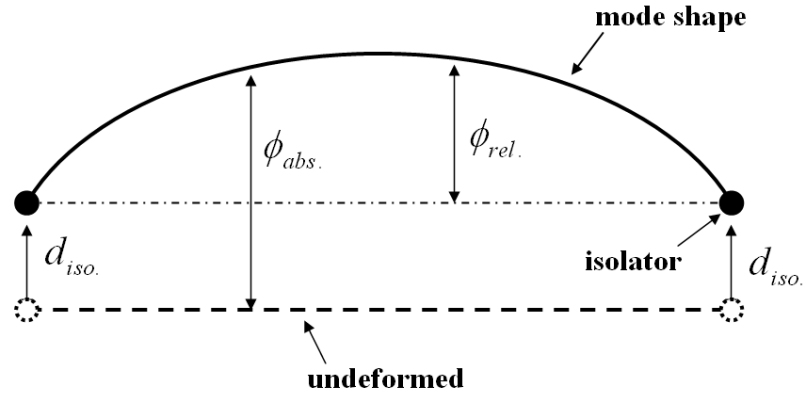
Figure 5.6.3 Relative mode shape amplitude of isolated bridge deck
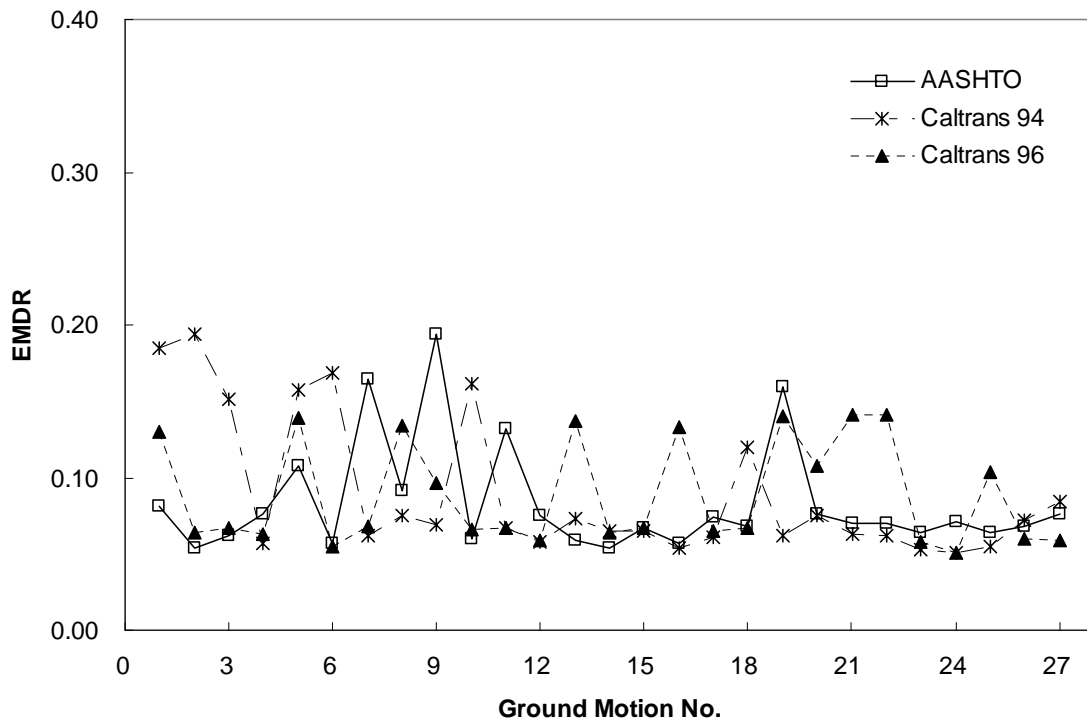
Figure 5.6.4 EMDR from composite damping rule method

5.6.4 Optimization (OPT) Method

The EMDR was found from optimization in the time domain by minimizing the response error from the NP-Model and P-Model of the example bridge. The procedure of the OPT method in time domain is as follows:

Step 1 is the same as in the CMA method.

Step 2. Compute undamped natural frequencies.

- The undamped natural frequencies were computed based on the mass and stiffness matrix of the bridge as shown in the third column of Table 5.6.3.

Step 3. Specify damping ratios of two modes of P-Model as Rayleigh damping and compute α and β using Eq. (3-21).

- Initial damping ratio of 5% is assumed for the first and third modes to compute Rayleigh damping coefficient α and β. From Eq. (3-21), α and β are computed as

$$\alpha = (0.05)\frac{2(3.224)(8.554)}{3.224+8.554} = 0.023$$

$$\beta = (0.05)\frac{2}{3.224+8.554} = 0.008$$

- From the next iteration, damping ratio is searched by optimization algorithm. After damping ratio is determined, new α and β values are computed.

Step 4. Compute damping matrix of P-Model as shown in Eq. (3-20).

- Using α and β values, the damping matrix of the P-Model is constructed as

$$[c] = 0.023[m] + 0.008[k]$$

Step 5. Compute seismic responses of both NP-Model and P-Model through time history analysis.

- For time history analysis, the first ground motion was used and Newmark direct integration method was adopted.

Step 6. Evaluate objective function of Eq. (3-23). If a value from objective function is smaller than criterion, go to step 8.

Step 7. Repeat from step 3 to step 6.

Step 8. Compute damping ratios of other modes using Eq. (3-22).

- From optimization, the damping ratio was obtained as 0.121. α and β values corresponding to the damping ratio are

$$\alpha = (0.121)\frac{2(3.224)(8.554)}{3.224+8.554} = 0.566$$

$$\beta = (0.121)\frac{2}{3.224+8.554} = 0.021$$

- Damping ratios of other modes are computed using Eq. (3-22) and shown in Table 5.6.9.

Figure 5.6.5 shows the EMDR from the time domain optimization method. As in the other previous methods, the EMDR ranges from 0.1 to 0.3.

Table 5.6.9 EMDR from OPT method in time domain

Mode	EMDR
1	$\dfrac{1}{(2)(3.224)}(0.566) + \dfrac{3.224}{2}(0.021) = 0.121$
2	$\dfrac{1}{(2)(3.393)}(0.566) + \dfrac{3.393}{2}(0.021) = 0.118$
3	$\dfrac{1}{(2)(8.554)}(0.566) + \dfrac{8.554}{2}(0.021) = 0.121$
4	$\dfrac{1}{(2)(21.770)}(0.566) + \dfrac{21.770}{2}(0.021) = 0.236$
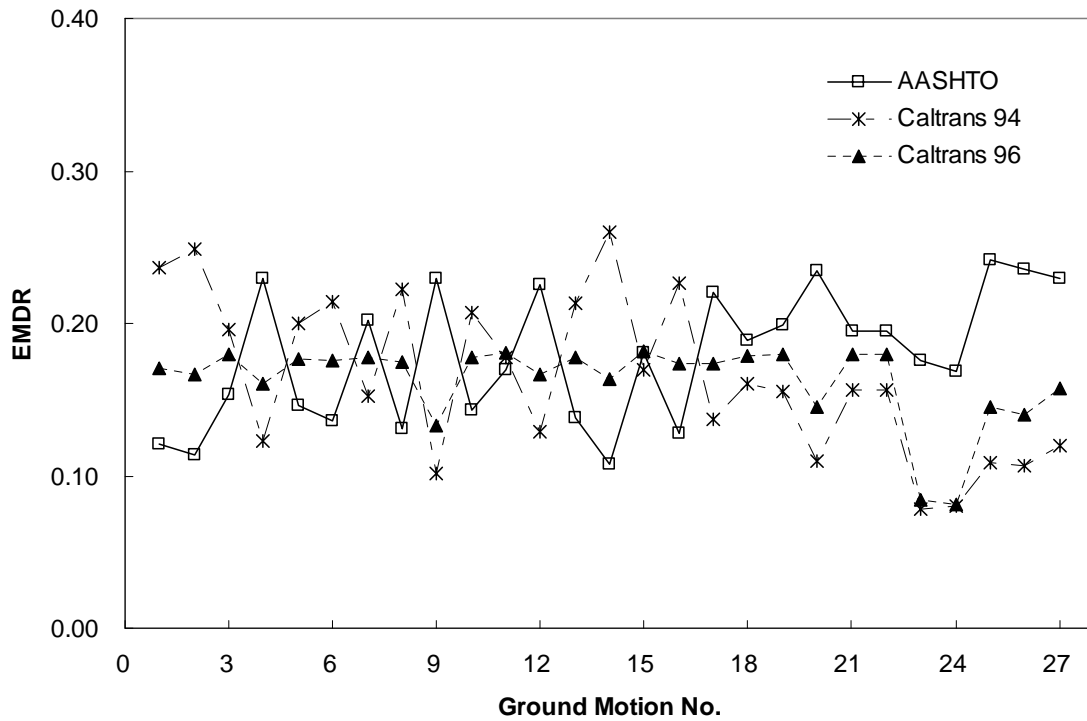
Figure 5.6.5 EMDR from time domain optimization method

5.6.5 Comparison of EMDR

The EMDR of the first mode computed by each damping estimating method is shown in Figs. 5.6.6 to 5.6.8 for each linearization method. From the figures, it is found that the EMDR from the composite damping rule (CDR) method is the lowest under all the ground motions. In many cases the EMDR from the CDR method was estimated as around 5% which is assumed as the damping ratio of the concrete structure components. Also, it can be seen that the EMDR results from the CDR method and several cases of the NODE method are much different than the results from the other methods.

The comparison of the EMDR with the effective damping ratio of the isolation bearing and the effective damping ratio plus the 5% damping ratio of the concrete structure, which is thought as the upper limit of the EMDR, is shown in Figs. 5.6.9 to 5.6.11. In these figures, EMDRs higher than 0.4 from the NODE method are not included. From the figures, it is seen that the EMDR by each linearization method is always smaller than the upper limit, whatever damping estimating method is applied.

In the AASHTO method shown in Fig. 5.6.9, the EMDR from each method is estimated to be lower than the effective damping ratio of the isolation bearing for the range of ductility ratios less than 10. From the Caltrans 94 method shown in Fig. 5.6.10, the EMDR from the NODE method is getting close to the upper limit as the ductility ratio increases, however, the EMDR from the other methods remains in the middle of the two lines. Regarding the Caltrans 96 method in Fig. 5.6.11, it is seen that the EMDR from each damping estimating method is nearly the same as the effective damping ratio of the isolation bearing when the ductility ratio is less than 10. However, it remains between

133

the two lines in the ductility ratio range greater than 10. Based on Figs. 5.6.9 to 5.6.11, the EMDR of the example bridge can be approximated as given in Table 5.6.10.

Table 5.6.10 Approximation of EMDR base on ductility ratio

AASHTO		Caltrans 94	Caltrans 96	
DR < 15	DR > 15	For all DR	DR < 15	DR > 15
ξ_{eff}	$\xi_{eff} + 0.5\,\xi_{str}$	$\xi_{eff} + 0.5\,\xi_{str}$	ξ_{eff}	$\xi_{eff} + 0.5\,\xi_{str}$

DR : ductility ratio; ξ_{eff} : effective damping ratio of isolation bearing

ξ_{str} : damping ratio of concrete structure of isolated bridge
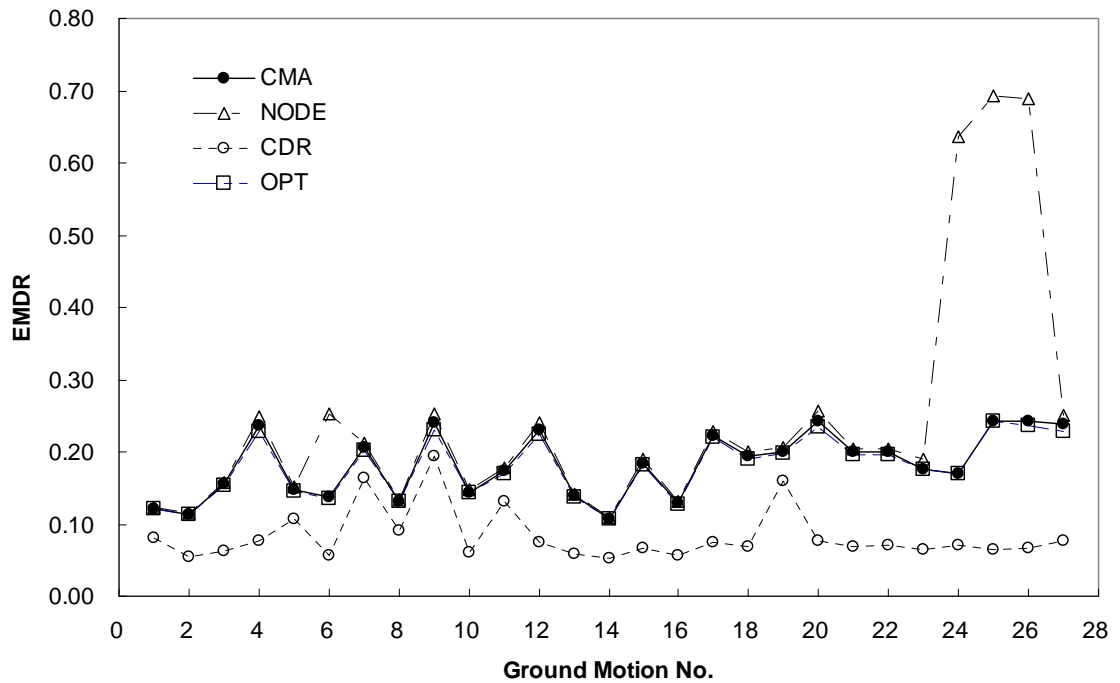
Figure 5.6.6 EMDR from AASHTO method

134
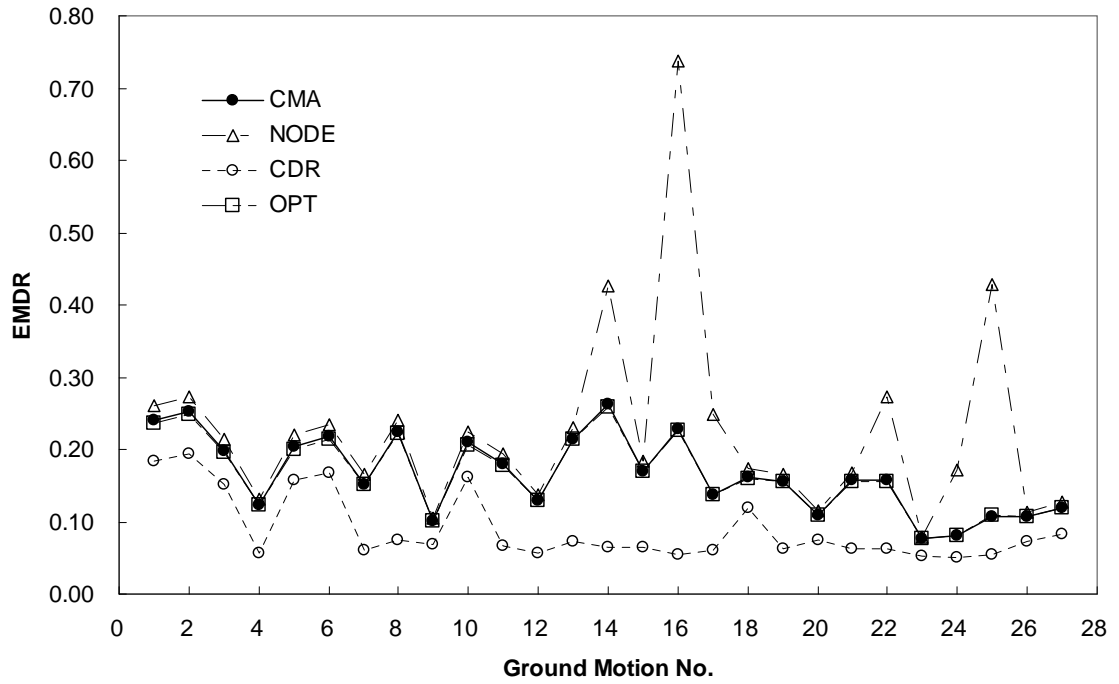
Figure 5.6.7 EMDR from Caltrans 94 method
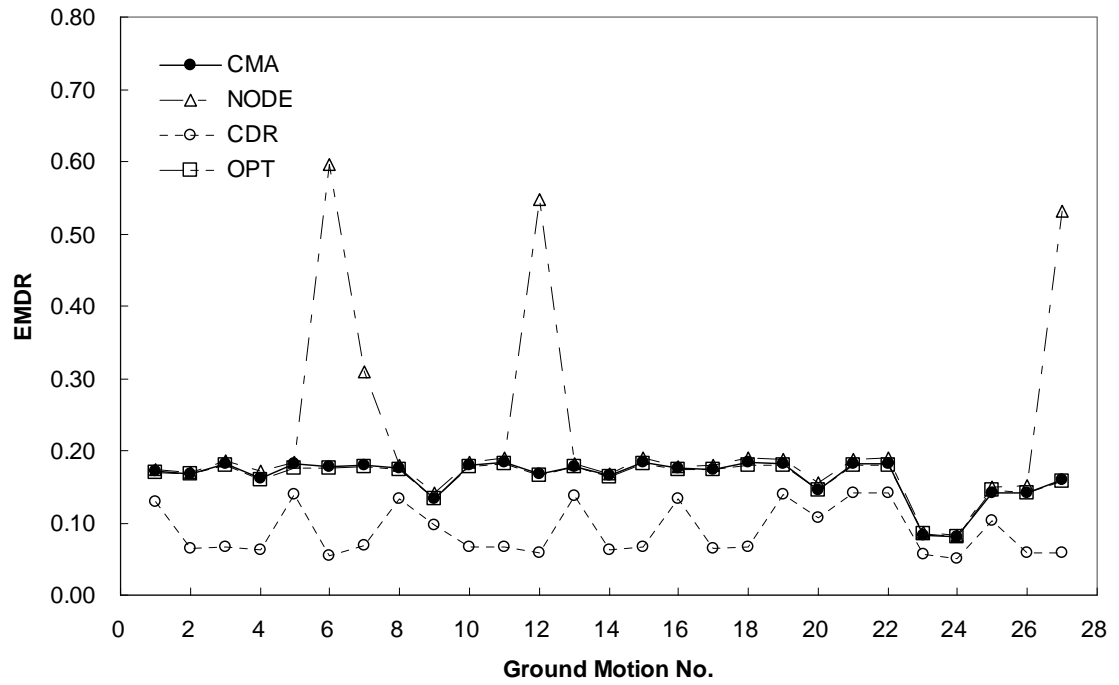
Figure 5.6.8 EMDR from Caltrans 96 method

135
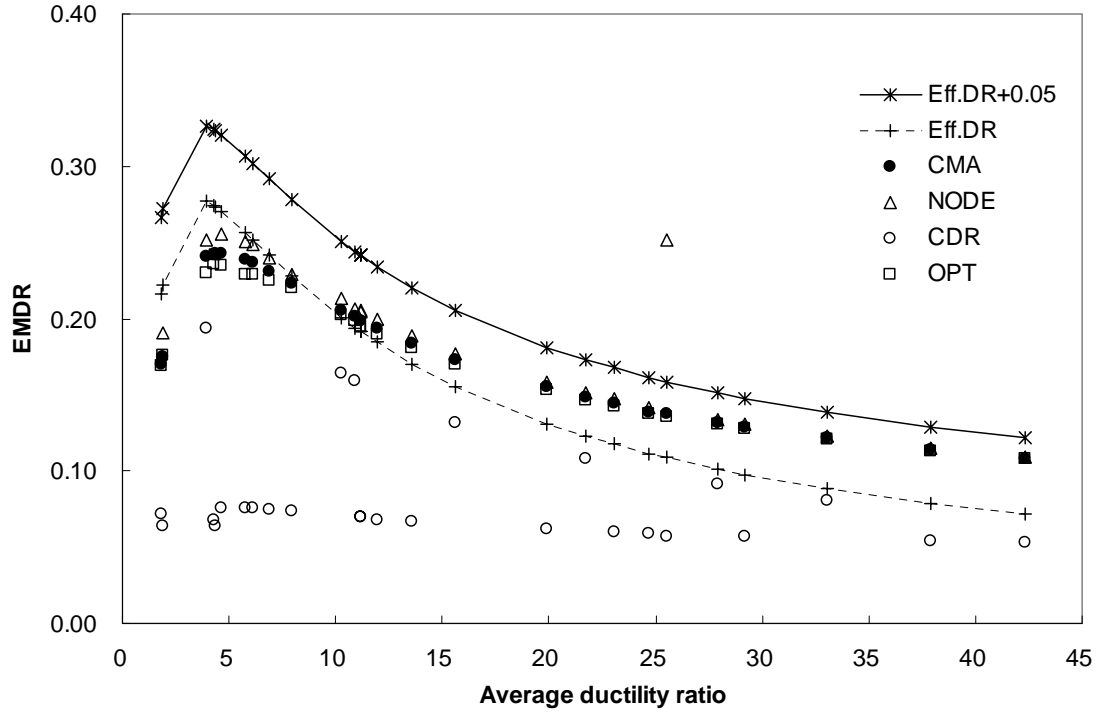
Figure 5.6.9 EMDR with ductility ratio from AASHTO method
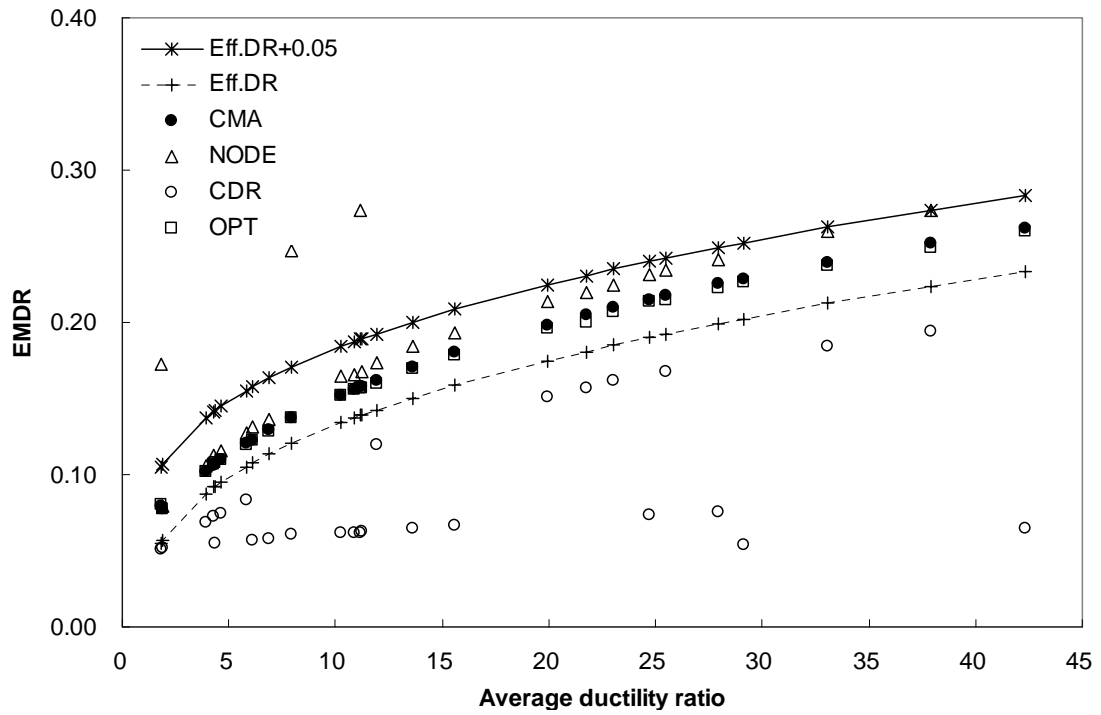
Figure 5.6.10 EMDR with ductility ratio from Caltrans 94 method
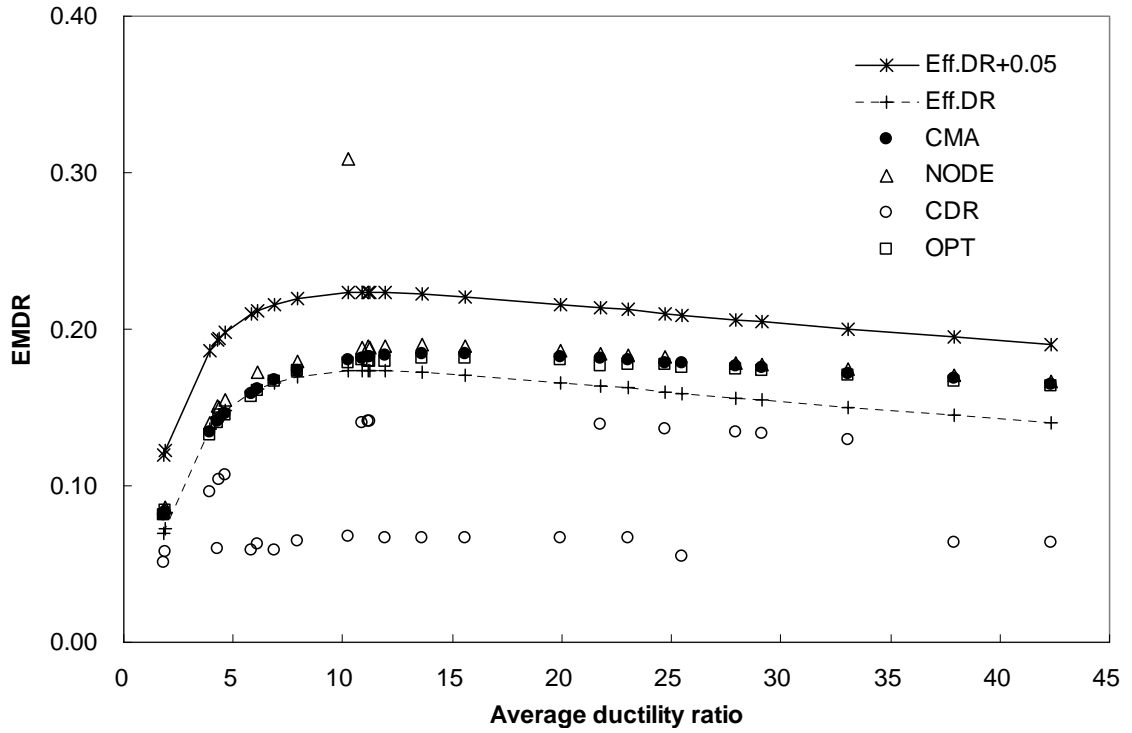
Figure 5.6.11 EMDR with ductility ratio from Caltrans 96 method

5.7 Seismic Response from Modal Combination

The displacement of the deck and pier tops was computed by the CQC modal combination method based on the response spectrum of each ground motion and it was compared with the result from the Bi-linear model to verify the applicability of the proposed method. Elastic response spectrum curves for each modal damping ratio, the undamped mode shapes, and natural periods from the P-Model were used in the modal combination results.

Figures 5.7.1 to 5.7.3 show the relative error of the modal combination results from the CMA and NODE methods with the results from the Bi-linear Model. From the figures, it is observed that as the ductility ratio increases, the relative error of the deck displacement decreases with all linearization methods.

Regarding the relative error of the pier top displacement in the AASHTO method, it does not seem to vary with the ductility ratio. However, it is strongly related to the ductility ratio in both Caltrans methods, especially the Caltrans 94 method. In the Caltrans 94 and 96 methods, the relative errors of the pier top displacements decreases significantly as the ductility ratios increase. In Fig. 5.7.2, the modal combination results from the Caltrans 94 method match well with the results from the Bi-linear Model for the range of ductility ratio greater than 15. Also, with the Caltrans 96 method shown in Fig. 5.7.3, the relative error of the pier top displacements are less than 50% for the ductility ratio range larger than 15. It should be noted that all of the relative errors of the deck and pier top displacements shown in the figures are positive values, which means that the modal

combination results from each linearization method and each damping estimating method overestimate the maximum seismic displacements of the deck and pier tops.

Table 5.7.1 summarizes the RMSE of the modal combination results with response from the Bi-linear Model for ductility ratios greater than 15. The values in parenthesis are relative errors for ductility ratios less than 15. In this table, it is noted that all damping estimating methods produce similar RMSE except for the CDR method. It can be seen in the table that the RMSE of all pier tops is much higher than that of the decks, especially for the ductility ratios less than 15, which implies that the linearization methods and damping estimating methods are less accurate in estimating the displacements of pier tops.

From the results, it is concluded that the proposed methods can be applied to compute the seismic displacement of isolated bridges under the condition that large ductility ratios of the isolation bearings are expected. It is apparent that the accuracy of the proposed methods is different depending on the average ductility ratio of the isolation bearing. As the average ductility ratio increases, the accuracy of the proposed method increases and this observation implies a certain relationship between the ground motion characteristics and the accuracy of the proposed method.

Table 5.7.1 RMSE of modal combination results with Bi-linear Model results

Method	AASHTO		Caltrans 94		Caltrans 96	
	Deck	Pier top	Deck	Pier top	Deck	Pier top
CMA	0.102 (0.314)	0.479 (0.615)	0.192 (0.450)	0.203 (1.221)	0.255 (0.364)	0.586 (0.976)
NODE	0.113 (0.243)	0.486 (0.523)	0.122 (0.483)	0.140 (1.215)	0.176 (0.295)	0.485 (0.887)
CDR	0.337 (0.683)	0.820 (1.215)	0.403 (0.698)	0.419 (1.659)	0.415 (0.657)	0.929 (1.480)
OPT	0.114 (0.362)	0.494 (0.679)	0.200 (0.469)	0.207 (1.250)	0.276 (0.406)	0.617 (1.034)

( ) : Relative error for ductility ratios of less than 15.
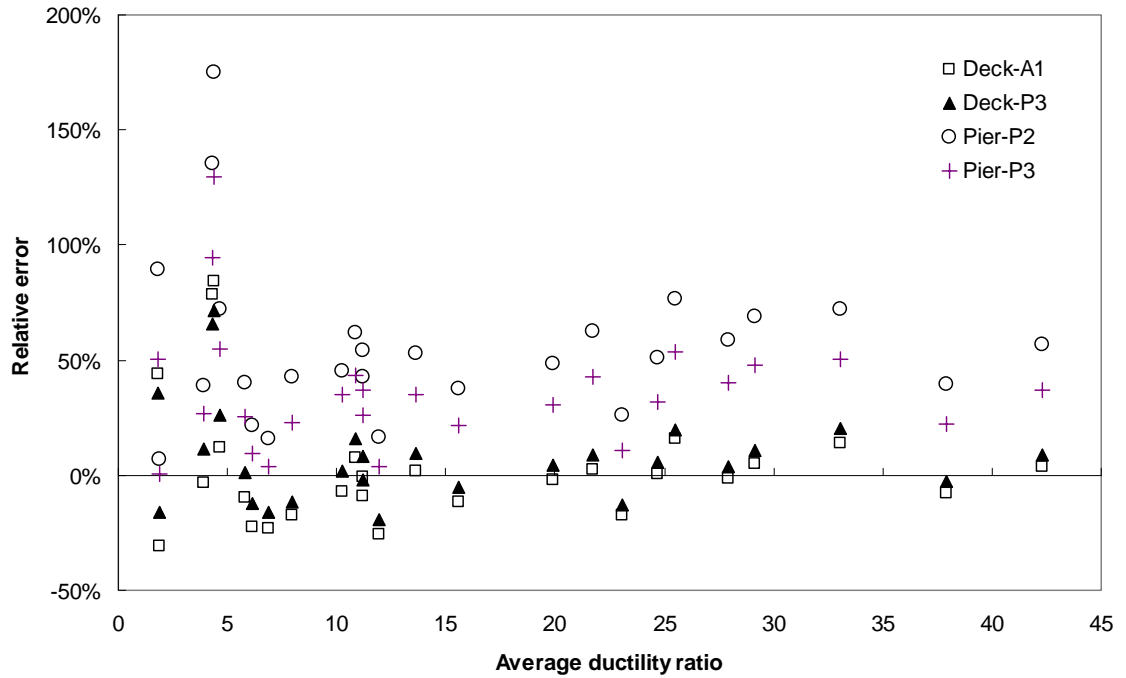
(a) CMA method
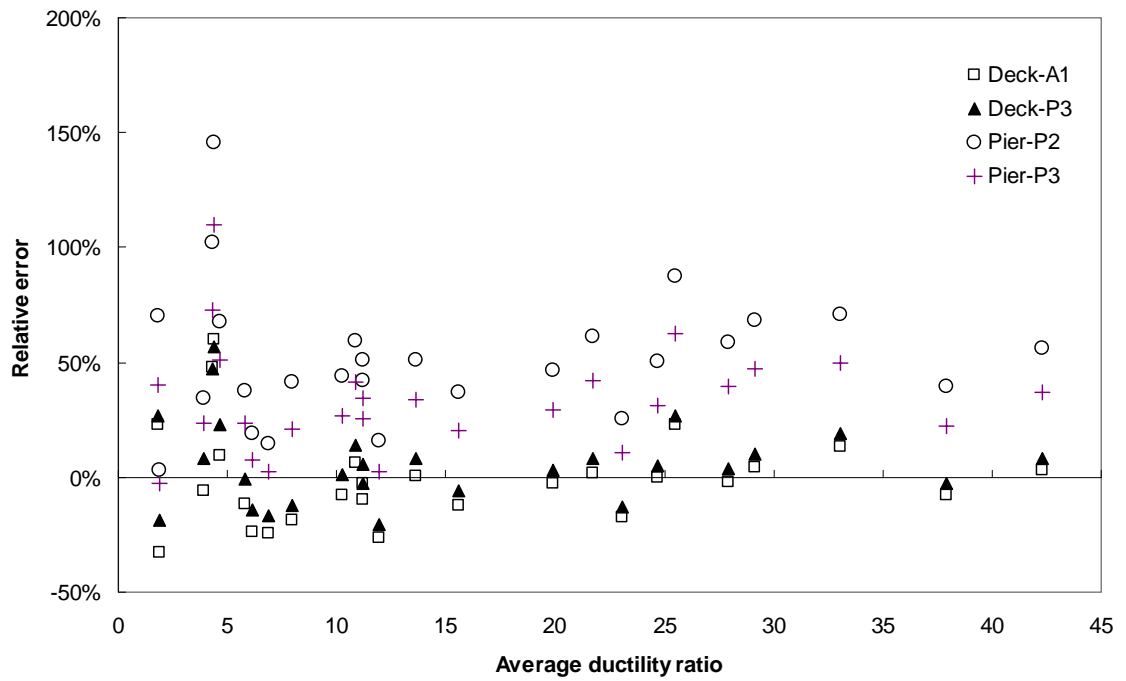
(b) NODE method

Figure 5.7.1 Relative error from AASHTO method
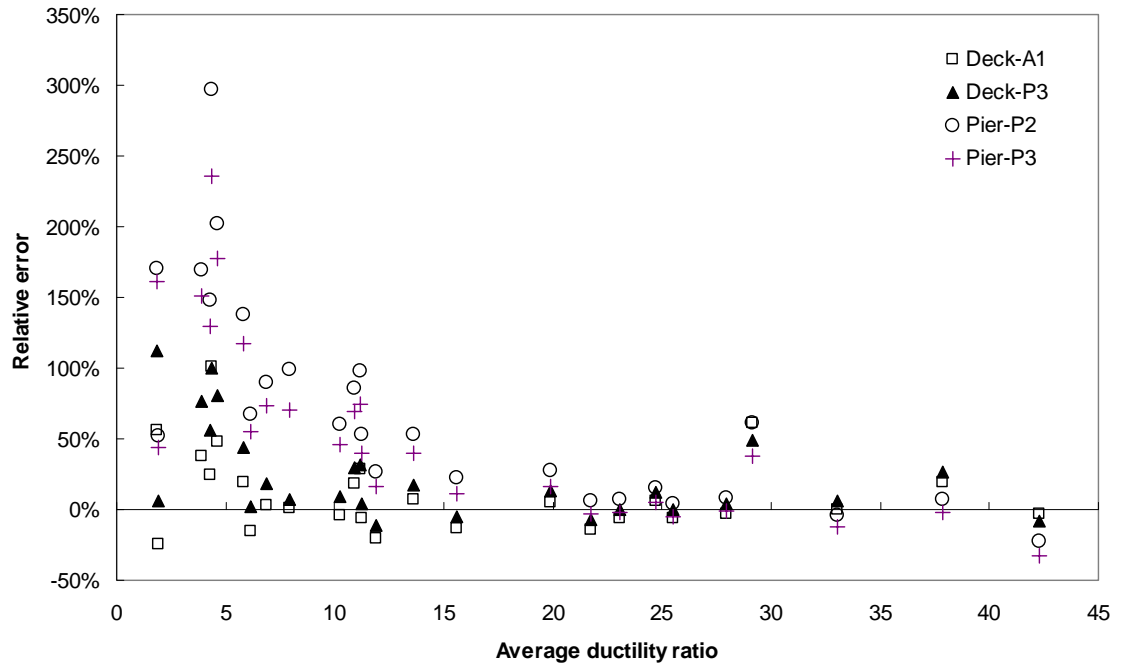
(a) CMA method
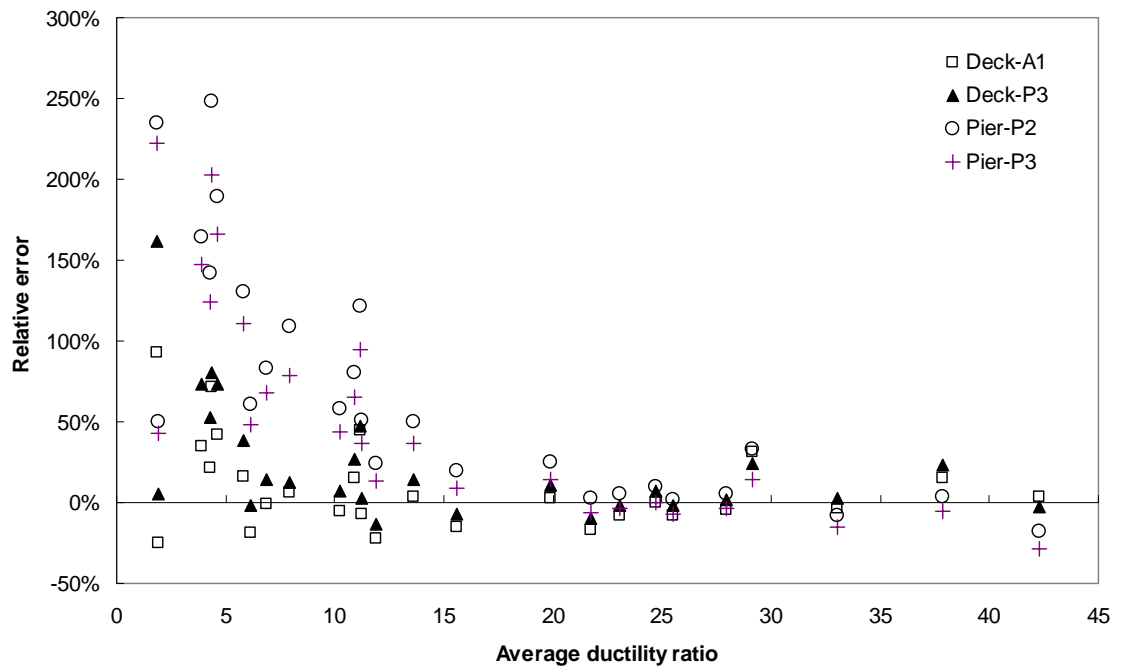
(b) NODE method

Figure 5.7.2 Relative error from Caltrans 94 method

142
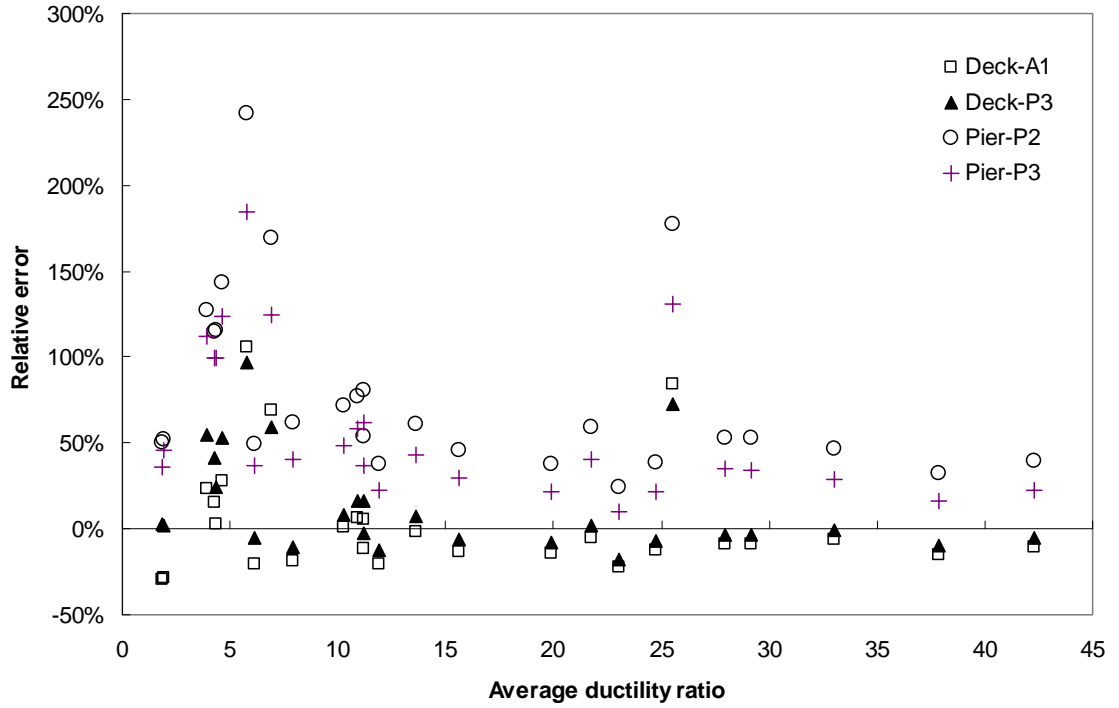
(a) CMA method
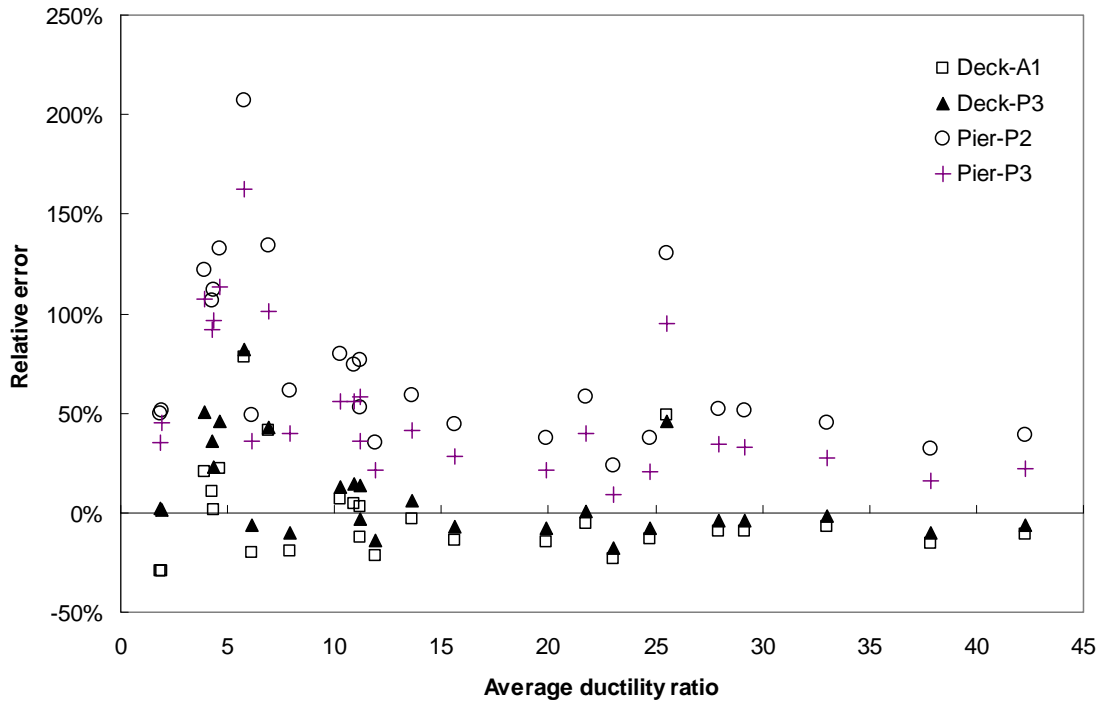
(b) NODE method

Figure 5.7.3 Relative error of Caltrans 96 method

143

5.8 Comparison with Current Design Method

In current design practice of isolated bridges and AASHTO Guide (1999), a constant damping ratio is used for all isolated modes in modal combination. Instead of using elastic Acceleration Response Spectra (ARS) curves for each modal damping ratio, the ARS curve of 5% damping ratio is divided by damping coefficient B determined by each modal damping ratio. Table 5.8.1 shows the damping coefficients specified in the AASHTO Guide (1999) along with damping ratio. In the AASHTO Guide the equivalent damping ratio of isolation bearing is assumed as effective damping ratio of whole bridge system and the damping from other bridge components such as pier and deck is neglected.

Table 5.8.1 Damping coefficient (AASHTO Guide, 1999)

Damping Ratio	≤ 0.02	0.05	0.10	0.20	0.30	0.40	0.50
Coefficient (B)	0.8	1.0	1.2	1.5	1.7	1.9	2.0

Figures 5.8.1 to 5.8.3 show the first four modal damping ratios by the CMA method from each linearization method. In these figures, the damping ratios are not close to each other and the second modal damping ratio is always greater than the first modal damping ratio. Also, as discussed in the section 5.6, the first modal damping ratio is not the same as the effective damping ratio of isolation bearing.

In this section, modal combination results from two cases: Case I) using the effective damping ratio of isolation bearing as the EMDR of the whole bridge, Case II) using

different modal damping ratios computed by the CMA method, are compared. In both cases, elastic response spectrum of 5% damping ratio is divided by corresponding damping coefficient B.

Figure 5.8.4 and 5.8.5 show the RMSE of deck and pier displacement results from modal combination regarding to the Bilinear Model results. In all linearization methods, the RMSE of the Case I is greater than that of the Case II for both deck and pier displacement. When the ductility ratio of isolation bearing is less than 15, the RMSE difference of two cases are much larger from the Caltrans 94 method rather than from the other two methods. The RMSE from the AASHTO method slightly increases when ductility ratio is greater than 15, however, the RMSE difference between two cases is not so significant, generally. It is attributed to a high effective damping ratio and high modal participation of the first mode. If damping ratio is very high, the small change of it does not incur much difference in dynamic response. From these figures, it can be concluded that though the current design practice most likely produces similar results with those from different modal damping ratios, it is recommended to use different effective modal damping ratios computed by the damping estimation methods and corresponding damping coefficients for these effective modal damping ratios.
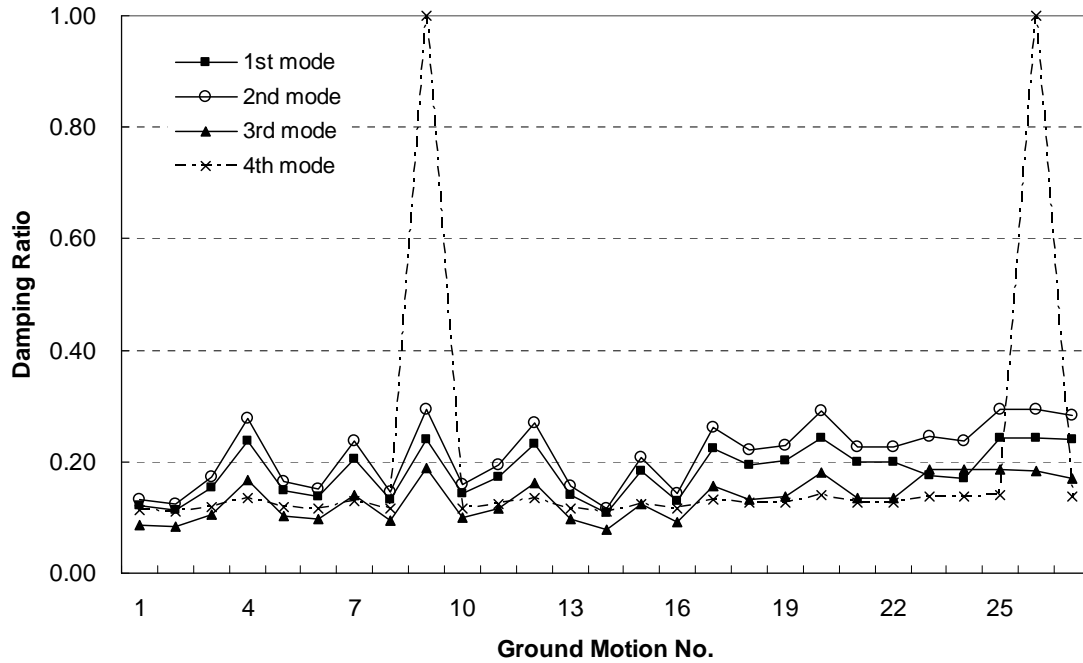
Figure 5.8.1 Damping ratio from AASHTO method (CMA)
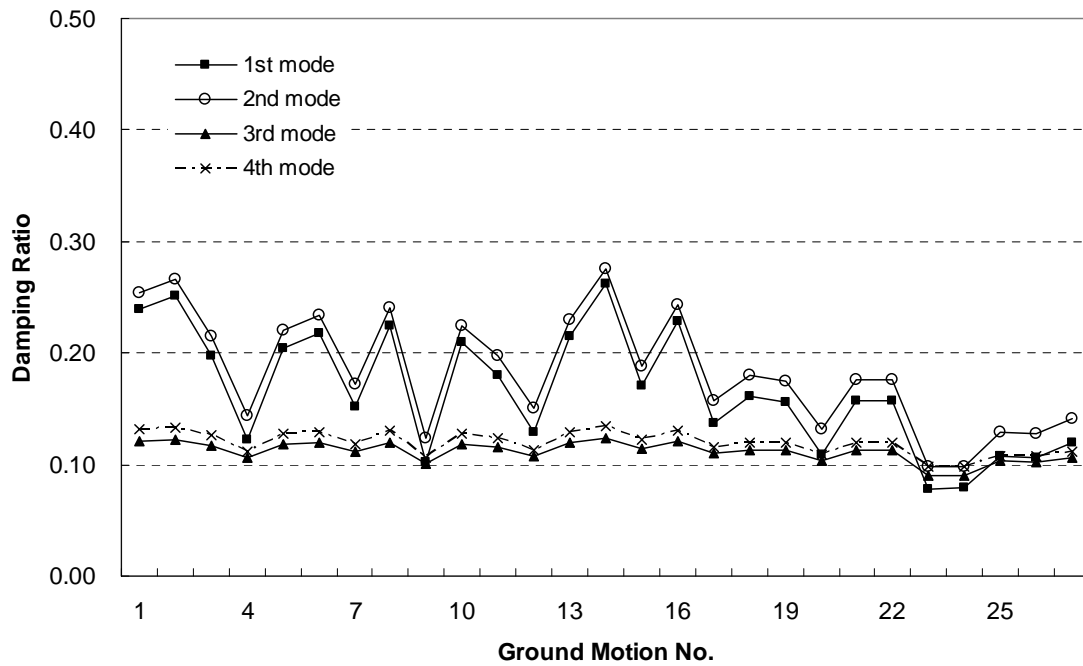
Figure 5.8.2 Damping ratio from Caltrans 94 method (CMA)

146
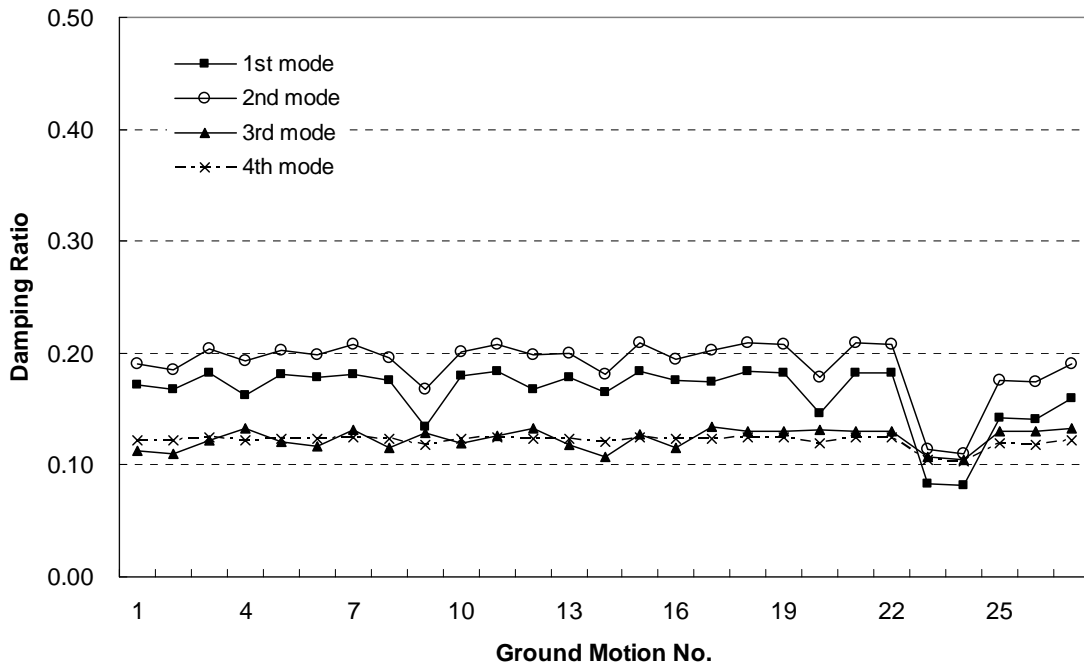
Figure 5.8.3 Damping ratio from Caltrans 96 method (CMA)
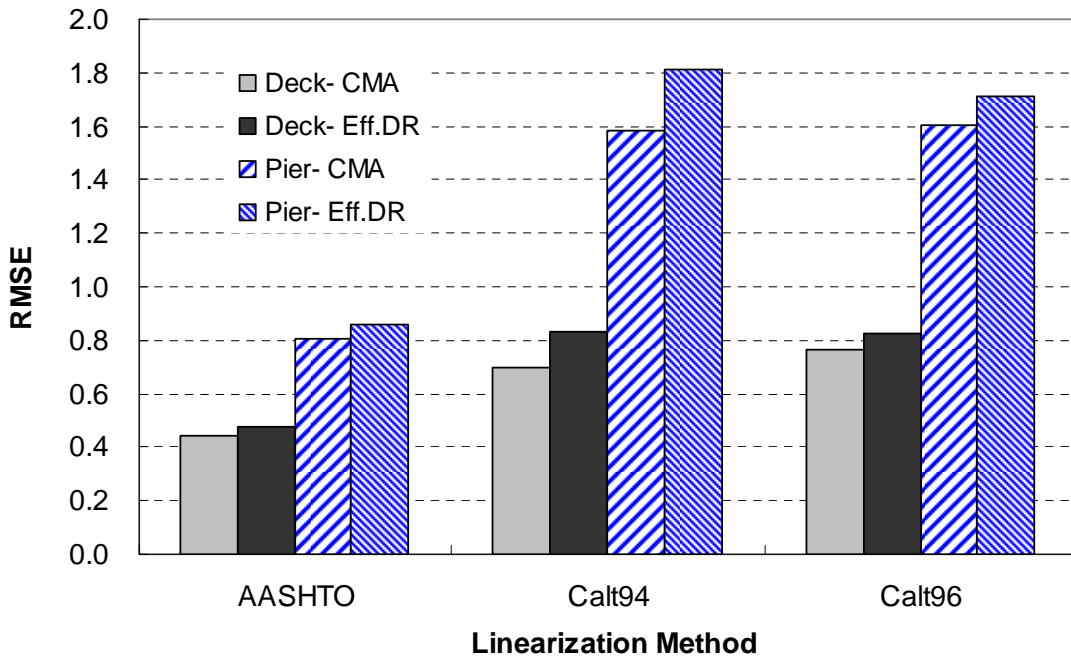
Figure 5.8.4 Comparison of RMSE (Ductility ratio <15)
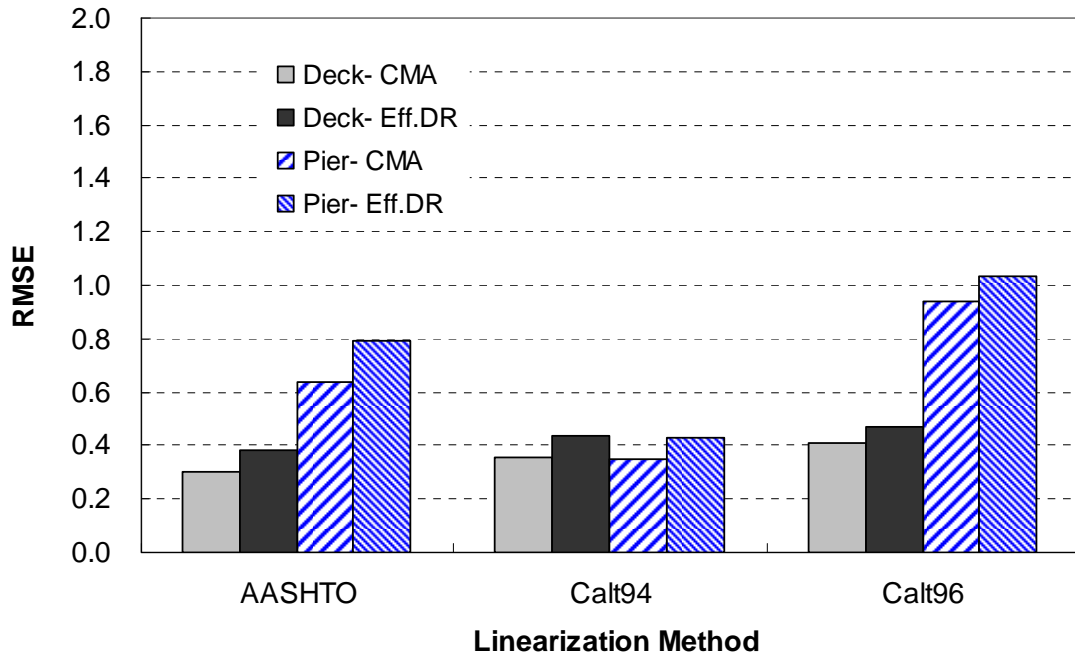
Figure 5.8.5 Comparison of RMSE (Ductility ratio >15)

5.9 Effects of Ground Motion Characteristics

As seen in previous sections, the accuracy of the seismic displacement of the isolated bridge using the response spectrum method is related to the ductility ratio of the isolation bearings, and the ductility ratio is related to the ground motion characteristics. In this section, the effects of the ground motions on the ductility ratio, the equivalent linearization of the isolation bearing, and the EMDR are investigated. From the results, the response spectrum intensity and energy dissipation index are found as the most appropriate ground motion parameters as they correlate well with the EMDR.

5.9.1 Effects on Ductility Ratio

The ductility ratio is defined as the ratio of the maximum displacement to the yielding displacement of the isolation bearing. Because the ductility ratio is the only factor in determining the equivalent linear model of the isolation bearing, any ground motion parameter which has an effect on the ductility ratio will have an effect on the EMDR.

Under each ground motion, the ductility ratios of the isolation bearings of the example bridge was computed and shown along with each ground motion parameter in Fig. C.1.1 to C.1.6 in Appendix C. For example, Fig. 5.9.1 shows the relation between PGA and the ductility ratio. Among many ground motion parameters, only the response spectrum intensity (RSI) and the energy dissipation index (EDI) show a good relations with the ductility ratio as shown in Fig. 5.9.2. It can be seen from this figure that both ground motion parameters have an almost linear relationship with ductility ratio.

The characteristics of each ground motion group can be described based on the results in Figs. 5.9.1 and 5.9.2 for the three ground motion groups. The motions in Group 1 show a wide range of PGA, RSI, and EDI but the ground motions in Group 2 and 3 have small values of the RSI and EDI, causing small ductility ratios less than 12. The distinct difference between Groups 2 and 3 is the PGA. The ground motions in Group 2 have a PGA larger than 0.5g, whereas that of Group 3 is less than 0.5g. Therefore, the RSI and EDI as well as the ductility ratio could be small earthquakes of high PGA.
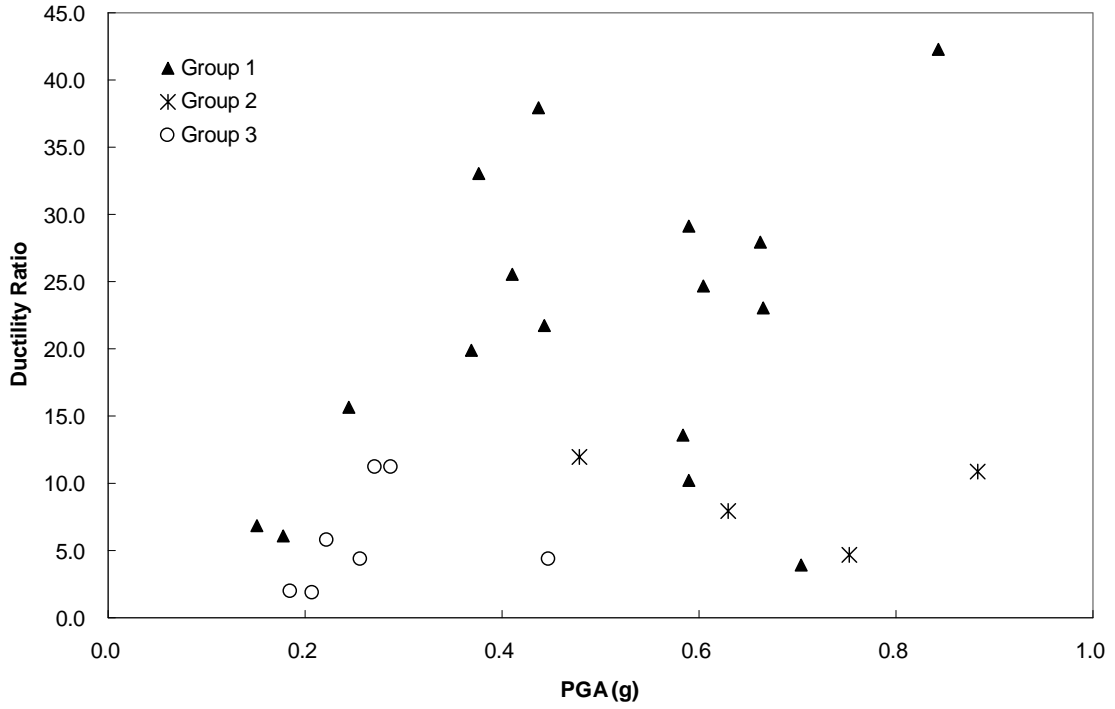
Figure 5.9.1 Ductility ratio and response spectrum intensity and energy dissipation index
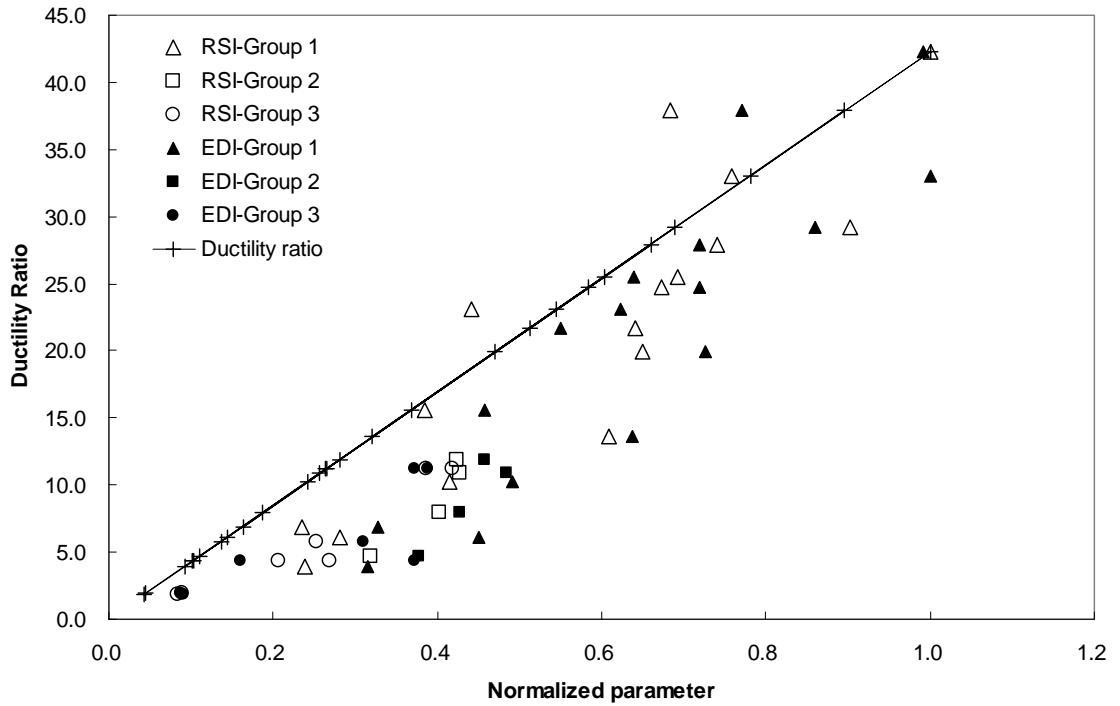
Figure 5.9.2 Ductility ratio and peak ground acceleration

151

5.9.2 Effects on Equivalent Linearization of Isolation Bearing

Figures 5.9.3 and 5.9.4 show the normalized effective stiffness of the isolation bearing with the response spectrum intensity and energy dissipation index, respectively. In these figures, each parameter is normalized with the maximum value of each parameter. As can be seen from the figures, the RSI and EDI show a good correlation with the effective stiffness in the ductility ratio range larger than 15.

A similar trend can be seen in the relation of the effective damping ratio with the ground motion parameters, shown in Fig's. 5.9.5 and 5.9.6. As the normalized ground motion parameters increase, the correlation of the ground motion parameters with the effective damping becomes better. In particular, for the Caltrans 96 method, the ground motion parameters in all ranges match well with the ductility ratio.

From the above observations, the effective stiffness and effective damping ratio of the isolation bearings under a ground motion can be approximated with the RSI or EDI value of the ground motion. The equivalent linear system of the isolation bearing can be estimated by using the values of Eq.(5-20) instead of the ductility ratio in each linearization method.

$$\mu = 10\,RSI \qquad \textbf{for } RSI > 2$$
$$\mu = 20\,EDI \qquad \textbf{for } EDI > 1$$

(5-20)

where, *RSI* and *EDI* are the response spectrum intensity and the energy dissipation index of a ground motion, respectively.
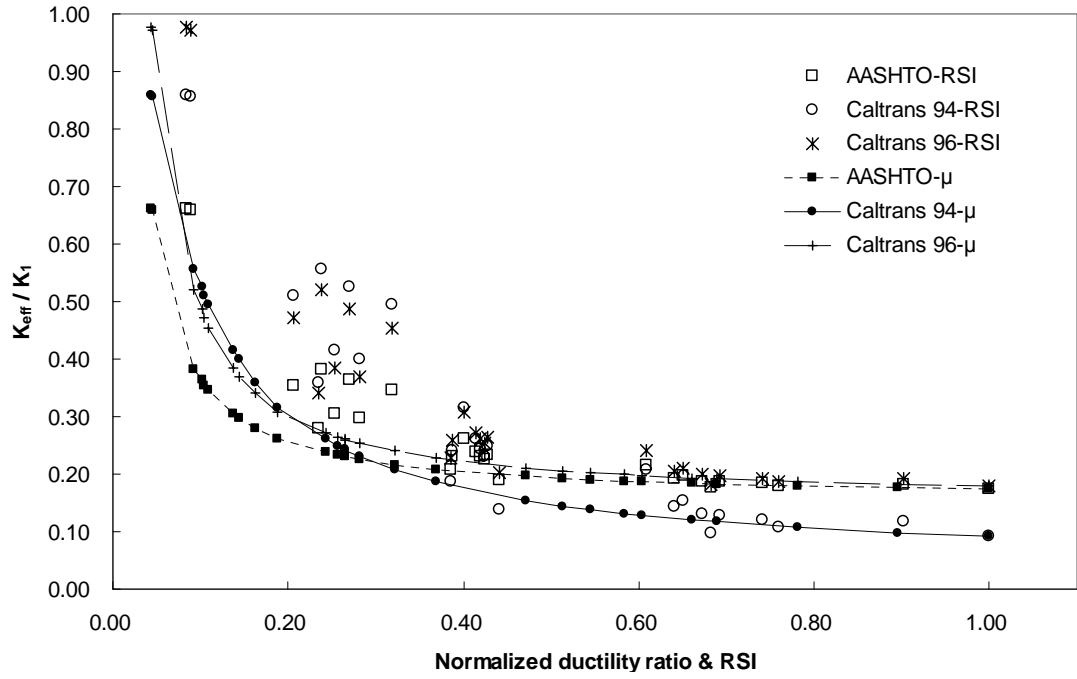
Figure 5.9.3 Effective stiffness and response spectrum intensity
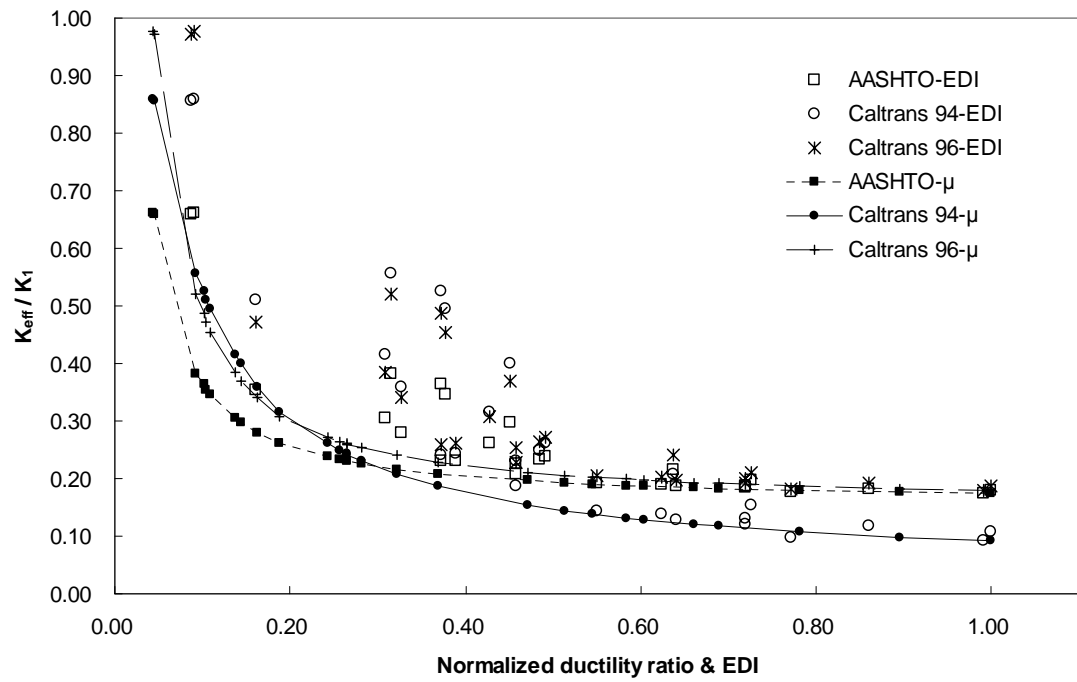
Figure 5.9.4 Effective stiffness and energy dissipation index

153
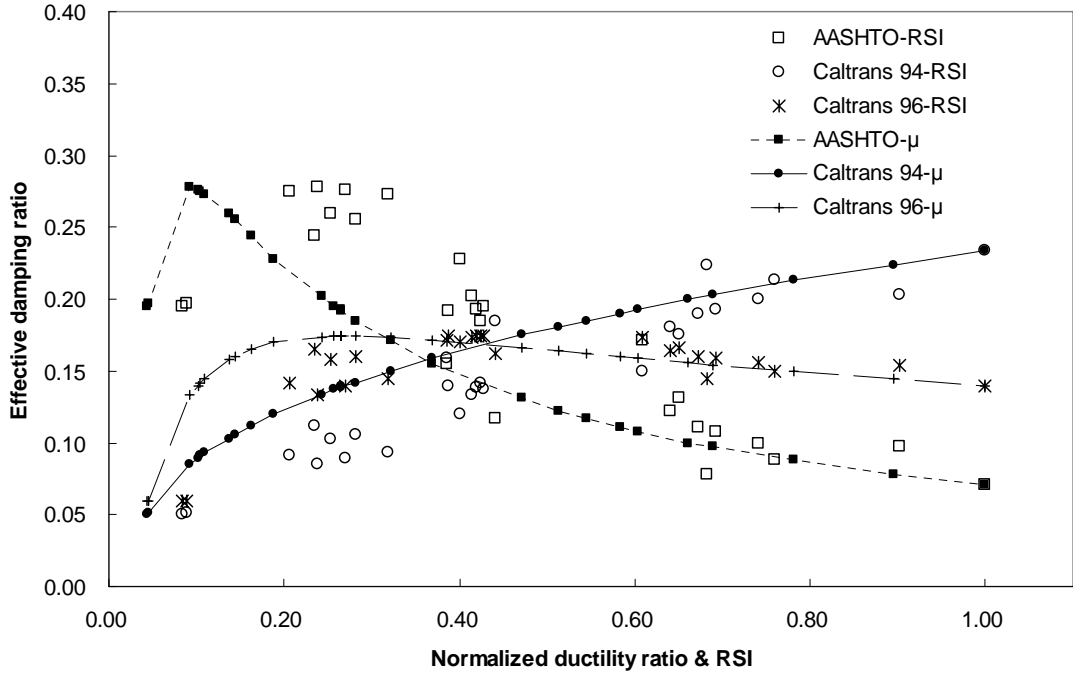
Figure 5.9.5 Effective damping ratio and response spectrum intensity
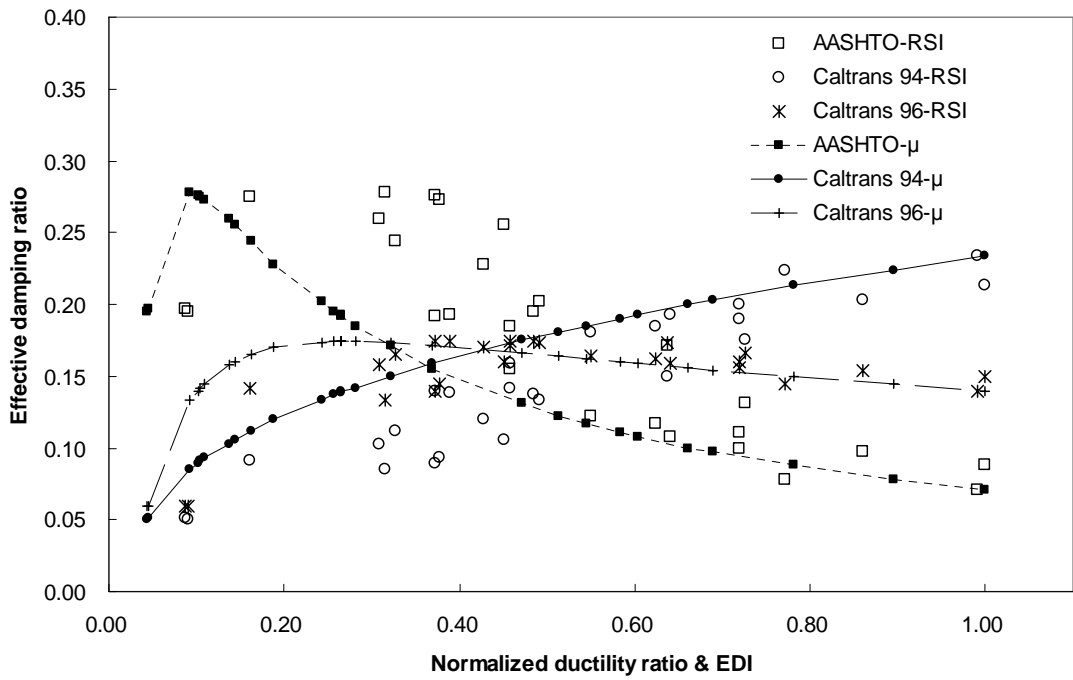
Figure 5.9.6 Effective damping ratio and energy dissipation index

154

5.9.3 Effects on EMDR

Figures 5.9.7 to 5.9.9 show the relation between the EMDR and the ground motion parameters. The EMDR shown in these figures is the result from the complex modal analysis method. The ground motion parameters are normalized to the maximum value of each parameter. Also, the ductility ratio is normalized to the maximum value.

In each figure, both ground motion parameters, RSI and EDI, show a good relation with the EMDR of each linearization method. Though the ground motion parameters are scattered in the low ductility ratio region, they gradually approach the EMDR-ductility ratio line. In the Caltrans 96 method in particular the ground motion parameters can be thought of as good indicators to predict the EMDR of isolated bridges for the ductility ratio range greater than 20.

Therefore, if the RSI or EDI of a ground motion is computed, the effective damping ratio of the isolation bearing can be approximated by using the value given by Eq. (5-20) in each linearization method and the EMDR of the example bridge can be approximated from Table 5.6.10.
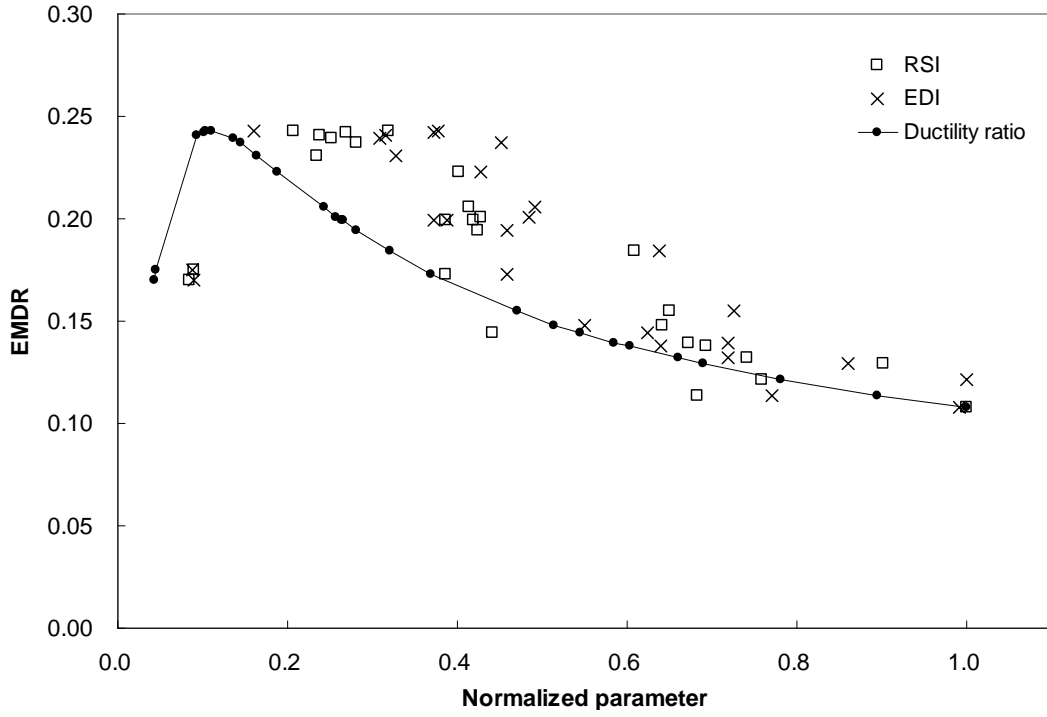
Figure 5.9.7 EMDR with ground motion parameters (AASHTO)
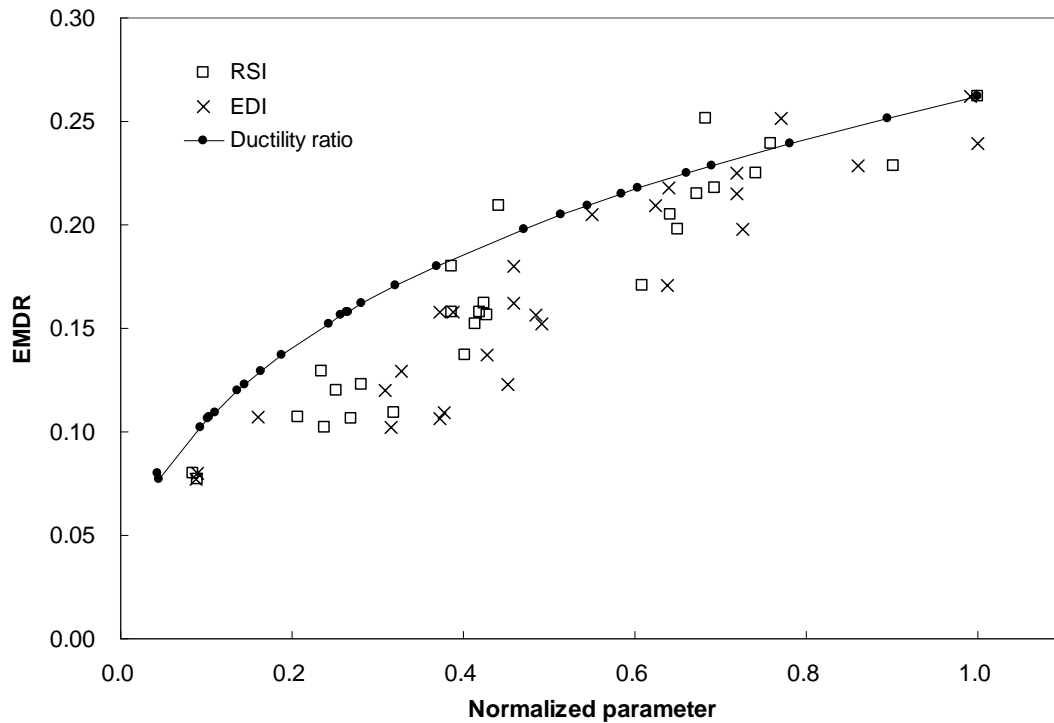
Figure 5.9.8 EMDR with ground motion parameters (Caltrans 94)

156
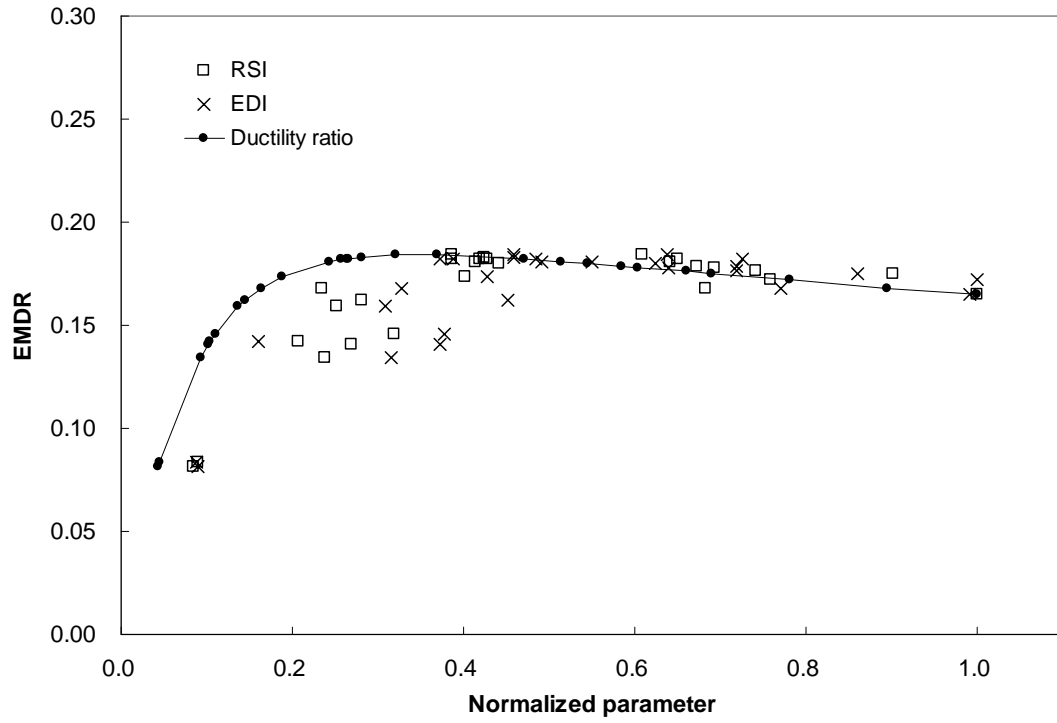
Figure 5.9.9 EMDR with ground motion parameters (Caltrans 96)

157

5.10 Summary

The seismic response of the isolated bridge which is a non-proportionally damped system was computed by equivalent linear analysis. For the equivalent linear model of the bridge, the bi-linear hysteretic model of the isolation bearing was approximated with the equivalent viscoelastic model applying the AASHTO, Caltrans 94, and Caltrans 96 methods. From the comparison of the responses from the bi-linear model and the equivalent linear model of the bridge under 27 ground motions, each linearization method was evaluated.

Among the three equivalent linearization methods, the AASHTO method produced the most accurate results in general; however, it was found that the accuracy of the equivalent linearization method varied according to the ductility ratio of the isolation bearing. As the ductility ratio increased, the equivalent linearization of the isolation bearing became more accurate.

After the equivalent linear model of the bridge was established, the EMDR was computed by applying the four damping estimating methods. In each equivalent linearization method, all damping estimating methods produced nearly the same EMDR values except for the composite damping rule method and in some cases for the neglecting off-diagonal element method. Based on the results of the computed EMDR, the rough estimation of the EMDR of the isolated bridge was suggested as the sum of the effective damping ratio of the isolation bearing and half of the damping ratio of the concrete structure, when the ductility ratio of the isolation bearing is greater than 15.

Using the EMDR, the seismic displacement of the isolated bridge was computed based on the response spectrum method. From the comparison of the results from the response spectrum method and the Bi-linear Model of the bridge, it was found that the deck and pier top displacement was predicted well by the proposed procedure for the ductility ratio range larger than 15 with relative errors less than 50%.

The current design practice in which the effective damping ratio of isolation bearing is used as a damping ratio of a whole isolated bridge is investigated. From the comparison of modal combination results, it is observed that the current method overestimates both pier and deck displacement for high shear ductility ratio ranges of isolation bearing.

From the investigation of the relation between the EMDR and ground motion parameters, the RSI and EDI were found to correlate well with the EMDR of the isolated bridge. The simple approximation method was proposed to estimate the EMDR of the bridge by using the RSI or EDI of a ground motion applied to the bridge.

CONCLUSIONS AND RECOMMENDED PROCEDURE

This research represents the first effort to systematically investigate the computation of the seismic demand of non-proportionally damped highway bridges utilizing the response spectrum method which assumes proportional damping of a structure. Conclusions and recommended EMDR estimating method are presented in this chapter.

6.1 Conclusions

In this research, because of the significant energy dissipation of the bridge boundary of short-span bridges and the isolation bearing devices of isolated bridges, short-span bridges and isolated bridges are considered as the typical non-proportionally damped bridges. The applicability of the four damping estimating methods was evaluated.

The PSO bridge was chosen as an example bridge for short-span bridges for analysis due to the availability of many earthquake recordings. The concrete structure of the bridge was modeled as linear elastic and assigned to have a 5% damping ratio. The bridge boundaries were modeled using equivalent viscoelastic elements. The effective stiffness and effective damping coefficient of the viscoelastic elements were identified utilizing the recorded data. The finite element model of the entire bridge, which is non-

proportionally damped, was validated by comparing the simulated and measured data in the time domain and the frequency domain.

The four damping estimating methods were applied to the non-proportionally damped bridge model to compute the effective system modal damping ratio of the bridge. The seismic demand of the bridge was computed based on the current response spectrum method utilizing the modal information, such as mode shapes and natural periods, of the undamped model of the bridge and the effective system modal damping ratio was found for each damping estimating method. The analysis of the PSO led to the following conclusions:

1. The simple equivalent viscoelastic model can be used to represent the boundary soil of the PSO under strong ground motions. The accuracy of the equivalent model was validated by comparing the simulated responses with recorded ones.

2. The EMDR of the bridge under a strong ground motion was found to be as high as 25% for the first transverse mode, which is much higher than the 5% value used in current practice. Also, the 25% value is the same value computed for the damping ratio of the embankment of the bridge by Kotsoglou and Pantazopoulou (2007). The simulated responses with the conventional 5% damping ratio produced nearly twice the measured response, which implies that the 5% damping ratio is too conservative for the design of short-span bridges subjected to strong ground motions.

3. Estimation of the seismic demand of the non-proportionally damped bridge by the response spectrum method using the effective system modal damping ratio is accurate with a relative error of less than 10%, except for the CDR method. Among

161

the four damping estimating methods, the NODE method is thought to be the most efficient method.

4. From the investigation of the relation between ground motion characteristics and the effective system modal damping ratio of the bridge, the simple EMDR estimation method is suggested based on the average intensity, root mean square intensity, and response spectrum intensity of ground motions. However, to ensure the suggested simple relation between the ground motion parameters and the EMDR, more earthquake data recorded under different ground motion intensities are needed.

To verify the applicability of the four damping estimating methods to an isolated bridge, a five-span example bridge was chosen and analyzed under 27 ground motions which were suggested by Naeim and Kelly (1999) for the design of isolated structures. The bi-linear model of the isolation bearings of the bridge was approximated with equivalent viscoelastic elements. The effective stiffness and effective damping ratio were estimated by three linearization methods, i.e. the AASHTO, Caltrans 94, and Caltrans 96 methods. Based on the equivalent linear model of the bridge, the four damping estimating methods were applied to compute the EMDR of the entire bridge system. Afterwards, the seismic demand was computed using the response spectrum method, the EMDR and the mode shapes and modal periods of the undamped model of the bridge. From the results obtained, the following conclusions are drawn:

1. The accuracy of all equivalent linearization methods varied depending on the ductility ratio of the isolation bearing. The larger the ductility ratio, the more accurate the equivalent linearization methods are. Thus, the equivalent linearization methods should be modified to enhance the accuracy in the low ductility ratio range.

162

2. In each linearization method, all damping estimating methods produced nearly the same EMDR, except for the CDR method and in some cases of the NODE method. In the Caltrans 94 method, the EMDR was observed to be nearly the sum of the effective damping ratio of the isolation bearing and half of the damping ratio assumed for the concrete structure of the bridge over for the full range of ductility ratio.

3. In the AASHTO and Caltrans 96 method, the effective damping ratio of the isolation bearing can be used as the EMDR when the ductility ratio is less than 15. For ductility ratios greater than 15, the sum of the effective damping ratio and half of the damping ratio of the concrete structure can be used to roughly approximate the EMDR.

4. The maximum seismic displacements based on the current response spectrum method using the EMDR match quite well with the results from the non-linear analysis for ductility ratios larger than 15, with errors less than 50%. Though the errors are high for low ductility ratios, such errors are attributed mainly to the inaccuracy of the equivalent linearization method, rather than to inaccuracies of the four damping estimating methods.

5. In all linearization methods, it is seen that prediction of deck displacement is more accurate than prediction of the pier top displacement, based on the response spectrum method. However, using the Caltrans 94 method, both displacements are found to be very accurate for ductility ratios range greater than 15.

6. The current design practice of assuming the effective damping ratio of isolation bearing as a damping ratio of isolated bridge system is found as little bit conservative

than using a different damping ratio for each mode computed by the suggested method in this research.

7. From the investigation of the relation between ground motion characteristics and the EMDR, the RSI and the EDI are found to have good correlations the EMDR. Based on the correlations obtained, if the bridge is subjected to ground motions of which the RSI values are larger than 2, or the EDI values are greater than 1, the corresponding ductility ratios can be estimated by $10 \times RSI$ or $20 \times EDI$. The effective damping ratio of isolation bearing can be approximated by substituting the ductility value for each equivalent linearization method and the EMDR of entire isolated bridge system can be evaluated using the four damping estimating methods.

6.2 Recommended Procedure

Among the four damping estimating methods, though the CMA method is considered as the most accurate method, the NODE method is recommended for computing EMDR because of its efficiency and high accuracy. The CMA method involves the complex modal analysis, while the NODE method uses mode shapes from normal modal analysis. When, however, applying the NODE method, the modal coupling parameters should be less than unity to ensure the accuracy of this method. In this research, a combined method of the NODE and the CMA method is recommended. The procedure for computing EMDR of bridge based on the combined method is as follows:

Step 1. Establish mass $[m]$, stiffness $[k]$, and damping matrix $[c]$ of a bridge

Step 2. Compute mode shapes and natural frequencies using the mass and stiffness matrix (normal modal analysis).

Step 3. Check modal coupling parameters for each pair of modes which are considered for modal combination as shown below:

$$e_{i,j} = \frac{\{\phi_i\}^T[c]\{\phi_j\}\omega_i}{\left|\omega_i^2 - \omega_j^2\right|} \tag{6-1}$$

where, $e_{i,j}$ is the modal coupling parameter of the ith and jth mode; ϕ_i is the ith normal mode shape; ω_i is the ith normal mode frequency.

Step 4. If the modal coupling parameters computed in **Step 3** are greater than unity, go to **Step 6**.

Pre- and post-multiply the mode shape matrix to the damping matrix.

$$\{\phi_1, \phi_2, \cdots, \phi_n\}^T[c]\{\phi_1, \phi_2, \cdots, \phi_n\} \tag{6-2}$$

where, n is the number of modes considered for modal combination; T denotes transpose of matrix.

Step 5. From diagonal elements only, compute the EMDR of each mode.

$$\xi_i = \frac{c_{i,i}}{2\{\phi_i\}^T[m]\{\phi_i\}\omega_i} \tag{6-3}$$

where, $c_{i,i}$ is the ith diagonal element in modal damping matrix of Eq.(6-2); ξ_i is the ith effective modal damping ratio.

Go to **Step 10**.

If any of the modal coupling parameters computed from Eq.(6-1) is greater than unity, apply the CMA method as follows:

Step 6. Obtain [A] and [B] matrix as below:

$$[A] = \begin{bmatrix} [0] & [m] \\ [m] & [c] \end{bmatrix}, \quad [B] = \begin{bmatrix} -[m] & [0] \\ [0] & [k] \end{bmatrix} \tag{6-4}$$

Step 7. Compute eigenvalues of $[A]^{-1}[B]$.

Step 8. Compute the natural frequency of each mode from real and imaginary part of the eigenvalue as shown in Eq. (6-5):

$$\omega_n = \sqrt{\left(\mathrm{Re}(s_n)\right)^2 + \left(\mathrm{Im}(s_n)\right)^2} \tag{6-5}$$

where, ω_n is the nth natural frequency; s_n is the eigenvalue of nth mode; $\mathrm{Re}(s_n)$ and $\mathrm{Im}(s_n)$ are real and imaginary part of s_n, respectively.

Step 9. Compute modal damping ratio of each mode from natural frequency and the real part of the eigenvalue.

$$\xi_n = \frac{\mathrm{Re}(s_n)}{\omega_n} \tag{6-6}$$

Step 10. For each modal damping ratio computed by equation (6-3) or (6-6), compute damping coefficient according to the AASHTO Guide (1999) shown below. A modal damping ratio between two values can be obtained by linear interpolation.

Damping Ratio	≤ 0.02	0.05	0.10	0.20	0.30	0.40	0.50
Coefficient (B)	0.8	1.0	1.2	1.5	1.7	1.9	2.0

Step 11. Divide response spectrum curve of 5% damping ratio by damping coefficient of corresponding mode to obtain modal response of that mode.

Step 12. Apply modal combination rule, such as CQC, to compute final seismic demand.
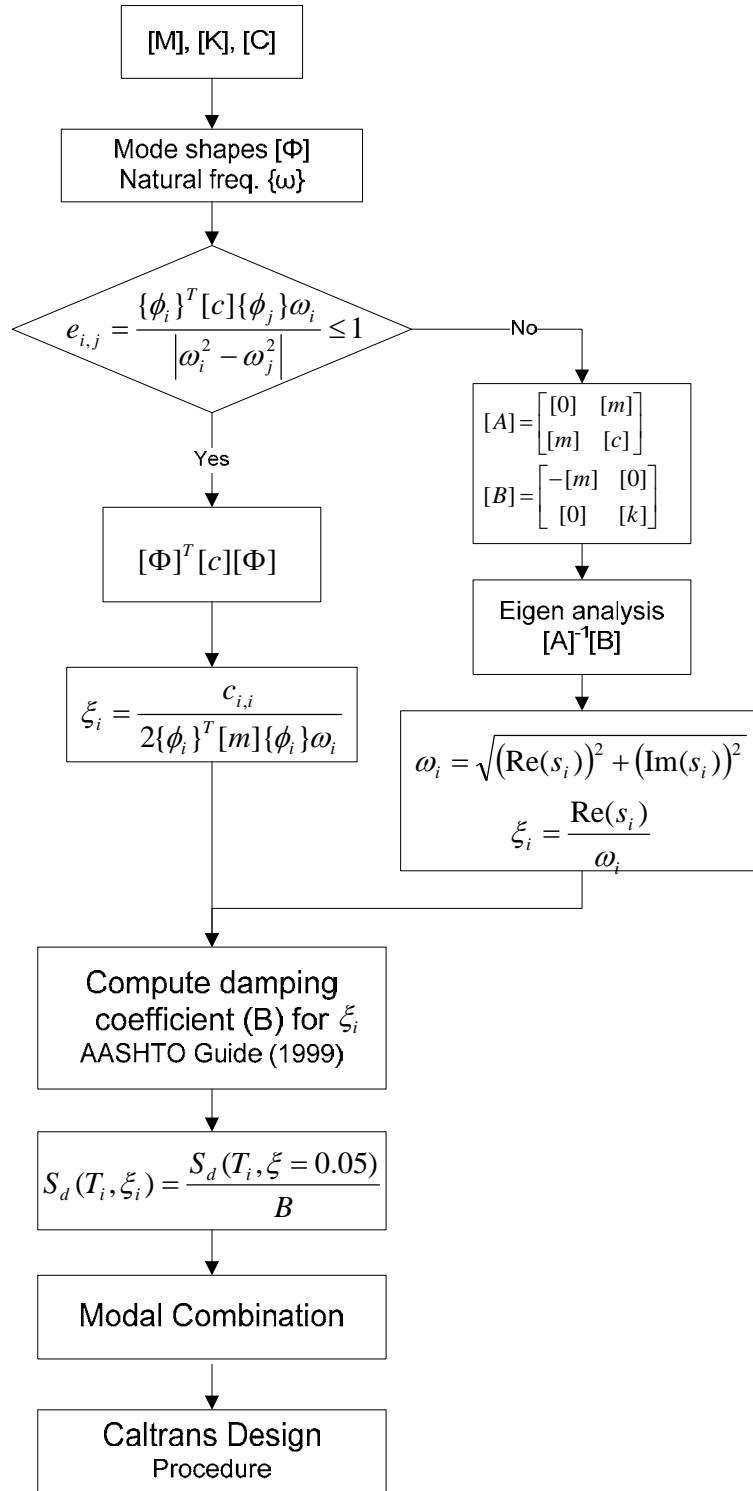
Figure 6.2.1 Recommended procedure for seismic demand

REFERENCES

AASHTO LRFD Bridge Design Specifications. (2007). American Association of State Highway and Transportation Officials, Wahsington, D.C.

Baber, T. T., and Wen, Y.-K. (1981). "Random vibration of hysteretic, degrading systems." Journal of Engineering Mechanics Division, Vol. 107, No. EM6, pp. 1069-1087.

Buckle, I., Constantinou, M., Dicleli, M., and Ghasemi, H. (2006). "Seismic isolation of highway bridges." Special Report MCEER-06-SP07, MCEER, SUNY at Buffalo.

Caughey, T. H., and O'Kelly, M. E. (1965). "Classical normal modes in damped linear dynamic systems." Journal of Applied Mechanics, ASME, Vol. 32, pp. 583-588.

Chang, K.C., Lai, M.L., Soong, T.T., Hao, D.S. and Yeh, Y.C. (1993). "Seismic behavior and design guidelines for steel frame structures with added viscoelastic dampers.", Technical Report NCEER-93-0009.

Chang, K.C., Soong, T.T., Oh, S-T., Lai, M.L. (1991). "Seismic response of a 2/5 scale steel structure with added viscoelastic dampers", Technical Report NCEER-91-0012.

Chang, K. C., Soong, T. T., Oh, S.–T., and Lai, M. L. (1995). "Seismic behavior of steel frame with added viscoelastic dampers." Journal of Structural Engineering, Vol. 24, pp. 1217-1227.

Chen, M. C., and Penzien J. (1975). "Analytical investigation of the seismic response of short single or multiple span highway bridges." Report No. EERC-75-4, Earthquake Engineering Research Center, University of California, Berkeley, California.

Chen, M. C., and Penzien J. (1977). "Nonlinear soil-structure interaction of skew highway bridges." Report No. EERC-77-24, Earthquake Engineering Research Center, University of California, Berkeley, California.

Clough, R. W., and Penzien, J. (1993). Dynamics of structures, 2nd ed., McGraw-Hill, New York.

Dall'Asta, A., and Ragni, L. (2008). "Dynamic systems with high damping rubber: Nonlinear behaviour and linear approximation." Earthquake Engineering and Structural Dynamics, DOI: 10.1002/eqe.825.

Dicleli, M. (2002). "Seismic design of lifeline bridge using hybrid seismic isolation." Journal of Bridge Engineering, Vol. 7, No. 2, pp. 94-103.

Dicleli, M., Mansour, M. Y., and Constantinou, M. C. (2005). "Efficiency of seismic isolation for seismic retrofitting of heavy substructured bridge." Journal of Bridge Engineering, Vol. 10, No. 4, pp. 429-441.

Elias, V. (2000). "Corrosion/Degradation of Soil Reinforcements for Mechanically Stabilized Earth Walls and Reinforced Soil Slopes," FHWA-NHI-00-044, Federal Highway Administration.

Elias, V. and Christopher, B.R. (1997), "Mechanically Stabilized Earth Walls and Reinforced Soil Slopes, Design and Construction Guidelines," FHWA Demo Project 82-1, Washington DC.

Elias, V., Christopher, B. R., and Berg, R. R. (2001). "Mechanically Stabilized Earth Walls and Reinforced Soil Slopes Design and Construction Guidelines," FHWA-NHI-00-043, Federal Highway Administration.

Goel, R. K. (1997). "Earthquake characteristics of bridges with integral abutments." Journal of Structural Engineering, Vol. 123, No. 11, pp. 1435-1443.

Goel, R. K., and Chopra, A. K. (1995). "Seismic response study of the HWY 101/Painter Street Overpass near Eureka using strong-motion records." Report CSMIP/95-01.

Goel, R.K. and Chopra, A.K. (1997), "Evaluation of bridge abutment capacity and stiffness during earthquakes," Earthquake Spectra, Vol. 13, No.1, pp. 1-22.

Guide specifications for seismic isolation design. (2000). American Association of State Highway and Transportation Officials, Wahsington, D.C.

Hwang, J. S., and Sheng, L. H. (1993). "Effective stiffness and equivalent damping ratio of base-isolated bridges." Journal of Structural Engineering, Vol. 119, No. 10, pp. 3094-3101.

Hwang, J. S., Sheng, L. H., and Gates, J. H. (1994). "Practical analysis of bridges on isolation bearings with bi-linear hysteresis characteristics." Earthquake Spectra, Vol. 10, No. 4, pp.705-727.

Hwang, J. S., Chiou, J. M., Sheng, L. H., and Gates, J. H. (1996). "A refined model for base-isolated bridges with bi-linear hysteretic bearings." Earthquake Spectra, Vol. 12, No. 2, pp.245-272.

Hwang, J. S., Sheng, L. H., and Tseng, Y. S. (2005). "Design formulations for supplemental viscous dampers to highway bridges." Earthquake Engineering and Structural Dynamics, Vol. 34, pp. 1627-1642.

Imbsen, R. A. (2001). "Use of isolation for seismic retrofitting bridges." Journal of Bridge Engineering, Vol. 6, No. 6, pp. 425-438.

Iwan, W. D. (1980). "Estimating inelastic response spectra from elastic spectra." Earthquake Engineering and Structural Dynamics, Vol. 8, No. 4, pp. 375-388.

Iwan, W. D., and Gates, N. C. (1979). "The effective period and damping of A class of hysteretic structures." Earthquake Engineering and Structural Dynamics, Vol. 7, pp. 199-211.

Jangid, R. S. (2007). "Equivalent linear stochastic seismic response of isolated bridges." Journal of Sound and Vibration, doi:10.1016/j.jsv.2007.07.071.

Johnson, C. D., and Kienhholz, D. A. (1982). "Finite element prediction of damping in structures." American Institute of Aeronautics and Astronautics Journal, Vol. (20), No. (9), pp. 1284-1290.

Katsaras, C. P., Panagiotakos, T. B., and Kolias, B. (2007). "Restoring capability of bilinear hysteretic seismic isolation systems." Earthquake Engineering and Structural Dynamics, Vol. 38, pp. 557-575.

Kotsoglou, A. and Pantazopoulou, S. (2007), "Bridge-embankment interaction under transverse ground excitation" Earthquake Engineering and Structural Dynamics, in press.

Kramer, S. L. (1996). Geotechnical earthquake engineering, Prentice-Hall, New Jersey.

Kwan, W-P., and Billington, S. L. (2003). "Influence of hysteretic behavior on equivalent period and damping of structural systems." Journal of Structural Engineering, Vol. 129, No. 5, pp. 576-585.

Lee, S.-H., Min, K.-W., Hwang, J.-S. and Kim, J. (2004), Evaluation of Equivalent Damping Ratio of a Structure with Added Dampers, Engineering Structures, Vol. 26, pp. 335–346

Lin, A. N. and Shenton, H. W. (1992). "Seismic performance of fixed-base and base-isolated steel frames." Journal of Engineering Mechanics, Vol. 118, No. 31, pp. 921-941.

Manual for menshin design of highway bridges. (1992). Japanese Public Works Research Institute (JPWRI), Tsukuba City, Japan.

Marano, G. C., and Sgobba, S. (2007). "Stochastic energy analysis of seismic isolated bridges." Soil Dynamics and Earthquake Engineering, Vol. 27, pp. 759-773.

McCallen, D. B., and Romstad, K. M. (1994). "Dynamic analyses of a skewed short-span, box-girder overpass." Earthquake Spectra. Vol. 10, No. 4, pp. 729-755.

Mutobe, R. M., and Cooper, T. R. (1999). "Nonlinear analysis of a large bridge with isolation bearings." Computers and Structures, Vol. 72, pp. 279-292.

Naeim, F., and Kelly, J. M. (1999). Design of seismic isolated structures : from theory to practice, John Wiley, New York.

Price, T.E. and Eberhard, M.O. (2005), "Factors contributing to bridge-embankment interaction" Journal of Structural Engineering, Vol. 131, No. 9, pp. 1345-1354.

Raggett, J.D. (1975), "Estimation of damping of real structures," Journal of Strcutural Division, Proceedings of the ASCE, Vol. 101, No. ST9, pp. 1823-1835.

Robson, B. N., Harik, I. E., and Gupta, V. (2001). "Effectiveness of seismic isolation of highly skewed P/C I-Girder bridge." Journal of Bridge Engineering, Vol. 6, No. 3, pp. 221-224.

Roussis, P. C., Constantinou, M. C., Erdik, M., Durukal, E., and Dicleli, M. (2003). "Assessment of performance of seismic isolation system of Bolu Viaduct." Journal of Bridge Engineering, Vol. 8, No. 4, pp. 182-190.

Seed, H. B. and Idriss, I. M. (1970). "Soil moduli and damping factors for dynamic response analysis." Report No. EERC 70-10. Berkeley, California, University of California.

Shen, K. L., and Soong, T. T. (1995). "Seismic behavior of reinforced concrete frame with added viscoelastic dampers." Engineering Structures, Vol. 17, No. 5, pp. 21-29.

Stehmeyer, E. H., and Rizos, D. C. (2007). "Considering dynamic soil structure interaction (SSI) effects on seismic isolation retrofit efficiency and the importance of natural frequency ratio." Soil Dynamics and Earthquake Engineering, doi:10.1016/j.soildyn.2007.07.008.

Sucuoglu H. and Nurtug A. (1995), "Earthquake ground motion characteristics and seismic energy dissipation," Earthquake Engineering and Structural Dynamics, Vol.24, pp. 1195-1213.

Tongaonkar, N. P., and Jangid, R. S. (2003). "Seismic response of isolated bridges with soil-structure interaction," Soil Dynamics and Earthquake Engineering, Vol. 23, pp. 287-302.

Tsai, N. C., Werner, S. D., Mahin, S. A. (1993). "Compilation and evaluation of current bridge damping data base," Report for Caltrans, Dames & Moore, Oakland, California.

Tseng, W. C., and Penzien J. (1973). "Analytical investigation of the seismic response of long multiple span highway bridges." Report No. EERC-73-12, Earthquake Engineering Research Center, University of California, Berkeley, California.

Turkington, D. H., Cooke, N., Moss, P. J., and Carr, A. J. (1989). "Development of a design procedure for bridges on lead-rubber bearings." Engineering Structures, Vol. 11, pp. 2-8.

Ucak, A., and Tsopelas, P. (2008). "Effect of soil-structure interaction on seismic isolated bridges." Journal of Structural Engineering, Vol. 134, No. 7, pp. 1154-1164.

Veletsos, A.S. and Ventura, C.E. (1986), "Model Analysis of Non-Classically Damped Linear Systems," Earthquake Engineering and Structural Dynamics, Vol. 14, pp 217-243

Warburton, G.B. and Soni, S.R. (1977), "Errors in reponse calculations for non-classically damped structures," Earthquake Engineering and Structural Dynamics, Vol. 5, pp. 365-376.

Warn, G. P., and Whittaker, A. S. (2006). "Property modification factors for seismically isolated bridges." Journal of Bridge Engineering, Vol. 11, No. 3, pp. 371-377.

Wen, Y.-K. (1976). "Method for random vibration of hysteretic systems." Journal of Engineering Mechanics Division, Vol. 102, No. EM2. pp. 249-263.

Werner, S.D. (1976). "Engineering characteristics of earthquake ground motions." Nuclear Engineering and Design, Vol. 36, pp.367-395.

Werner, S.D. (1994), "Study of Caltrans' seismic evaluation procedure for short bridges." In Proc. 3rd Annual Seismic Research Workshop. Sacramento, Calif., California Department of Transportation.

Werner, S.D., Beck, J.L. and Levine, M. B. (1987). "Seismic response evaluation of Meloland road overpass using 1979 Imperial Valley Earthquake records." Earthquake Engineering and Structural Dynamics, Vol. 15, pp. 249-274.

Wilson, J. C., and Tan, B. S. (1990 a). "Bridge abutments: formulation of simple model for earthquake response analysis." Journal of Engineering Mechanics, Vol. 116, No. 8, pp. 1828-1837.

Wilson, J.C. and Tan, B.S. (1990 b), "Bridge abutments: Assessing their influence on earthquake response of Meloland Road Overpass" Journal of Engineering Mechanics, Vol.116, No.8, pp.1838-1856.

Wong, C. W., Ni, Y. Q., and Lau, S. L. (1994a). "Steady-state oscillation of hysteretic differential model. I : Response analysis." Journal of Engineering Mechanics, Vol. 120, No. 11, pp. 2271-2298.

Wong, C. W., Ni, Y. Q., and Lau, S. L. (1994b). "Steady-state oscillation of hysteretic differential model. II : Performance analysis." Journal of Engineering Mechanics, Vol. 120, No. 11, pp. 2299-2325.

Zhang, J. and Makris, N. (2002), "Seismic response analysis of highway overcrossing including soil-structure interaction" Earthquake Engineering and Structural Dynamics, Vol. 31, pp. 1967-1991

EFFECTS OF GROUND MOTION PARAMETERS ON SHORT-SPAN BRIDGE

A.1 Free Field Ground Motions

The historic earthquake data of free field ground motions at the PSO are shown in Figs. A.1.1 to A.1.6. The velocity and displacement responses were obtained from the original data file. The ground motions shown in this section were recorded by Channel 14 located as shown in Fig. 4.2.1. All the data are accessible at http://strongmotioncenter.org.

A.2 EMDR and Ground Motion Parameters

Figures A.2.1 to A.2.4 show the relation between the EMDR and the ground motion parameters. Abbreviations in these figures are: Avg, Average intensity; RMS, root-mean-square intensity; Arias, Arias intensity; C.I., Characteristic intensity; CAV, Cumulative absolute velocity; RSI, Response spectrum intensity; ASI, Acceleration spectrum intensity; EPA and EPV, Effective peak acceleration and velocity, respectively.
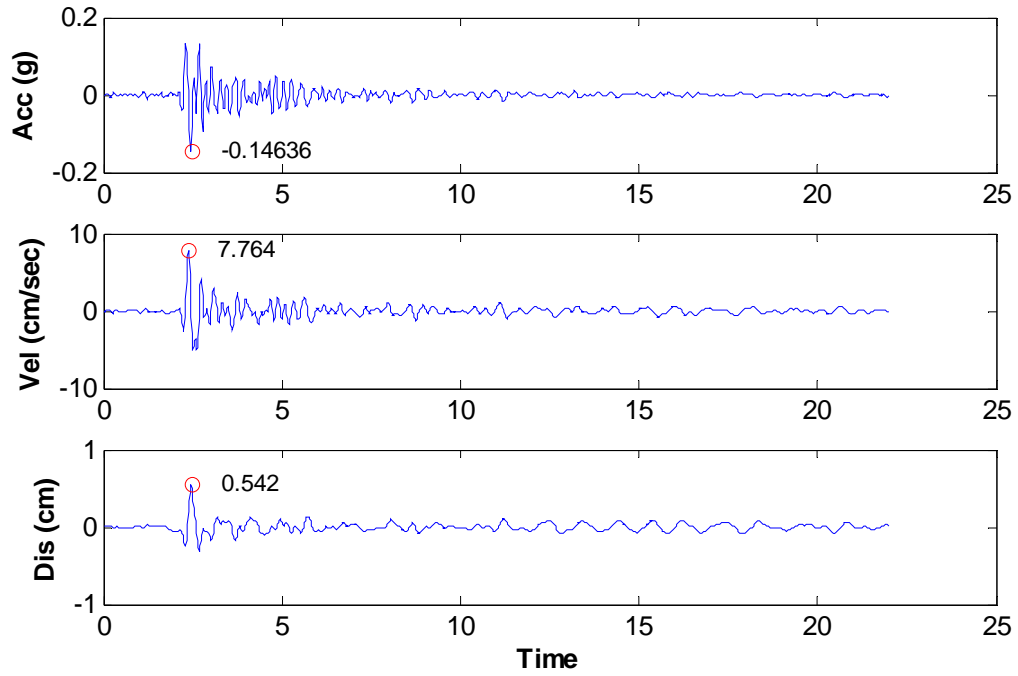
Figure A.1.1 Cape Mendocino Earthquake in 1986
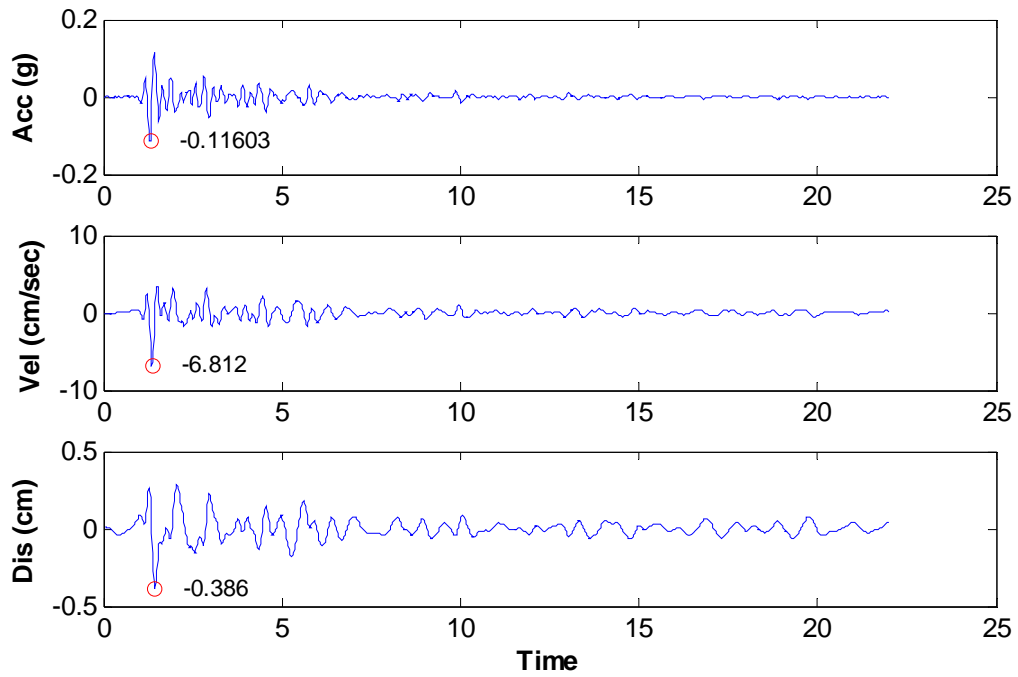
Figure A.1.2 Cape Mendocino Earthquake in 1986 (Aftershock)
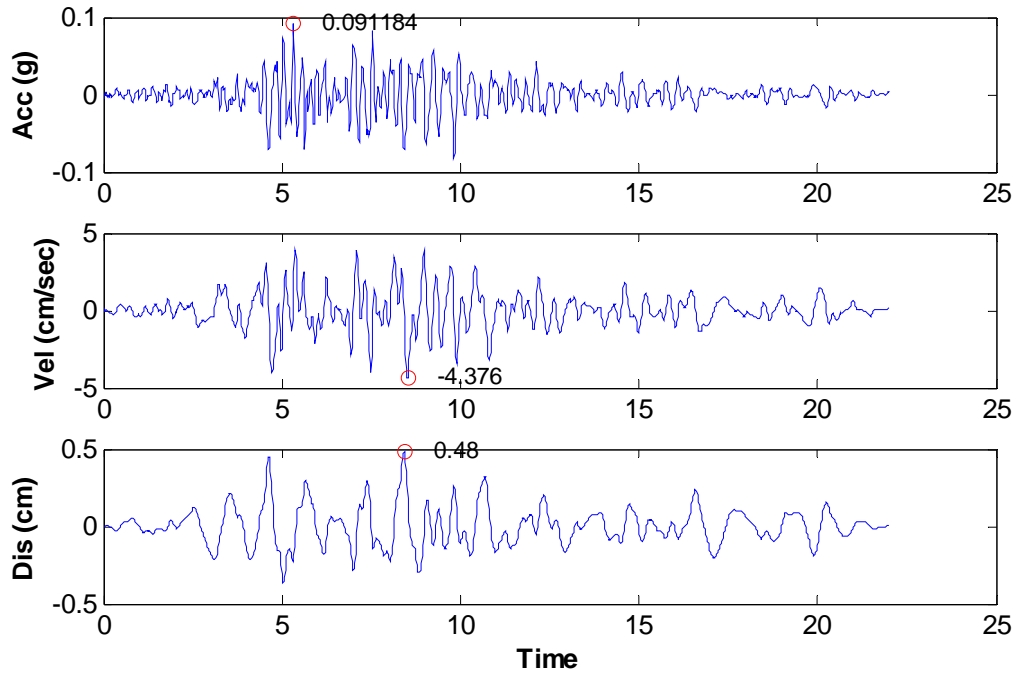
Figure A.1.3 Cape Mendocino Earthquake in 1987
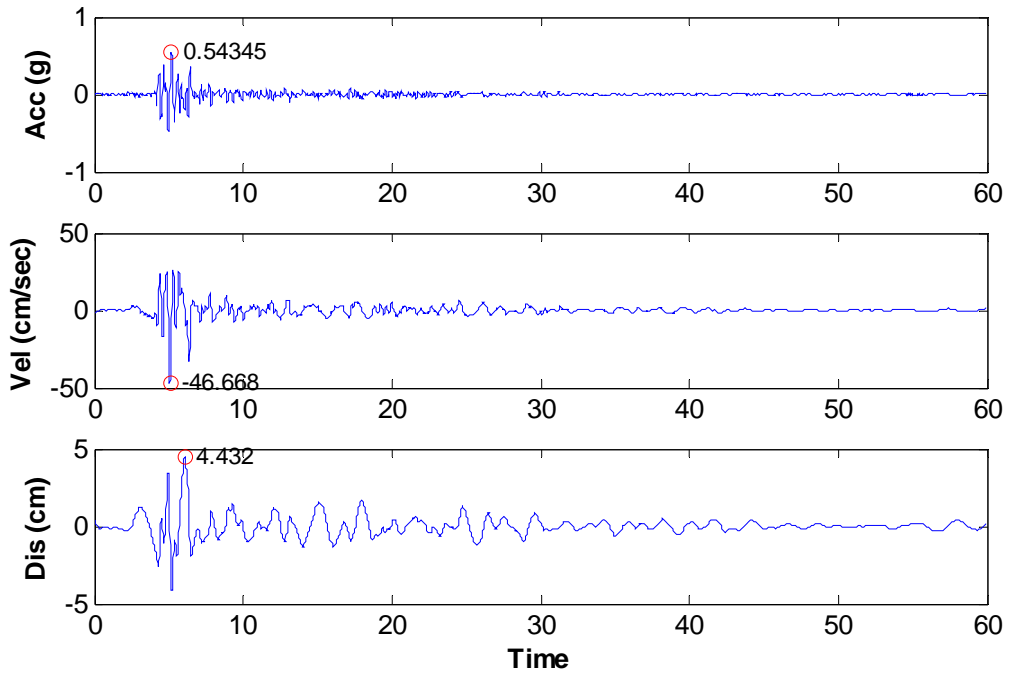
Figure A.1.4 Cape Mendocino/Petrolina Earthquake in 1992
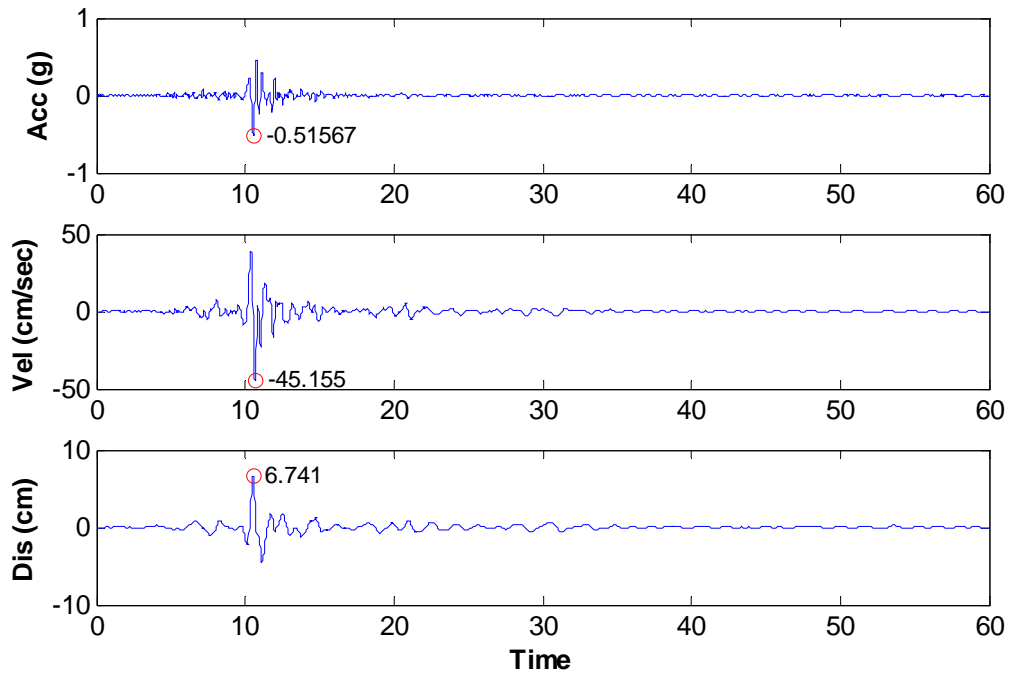
Figure A.1.5 Cape Mendocino/Petrolina Earthquake in 1992 (Aftershock 1)
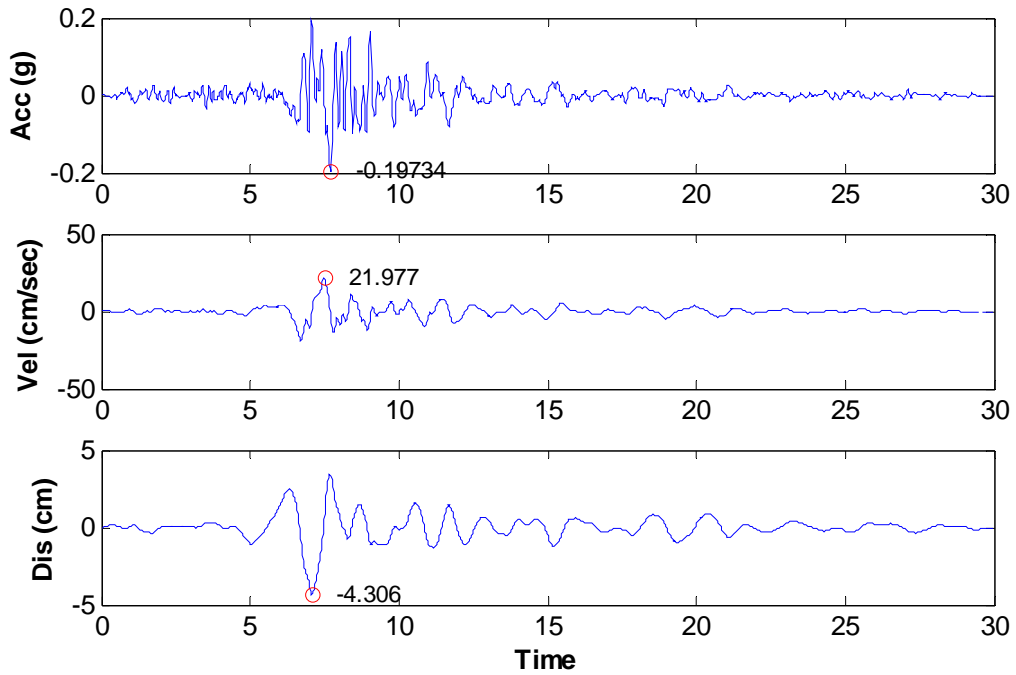
Figure A.1.6 Cape Mendocino/Petrolina Earthquake in 1992 (Aftershock 2)
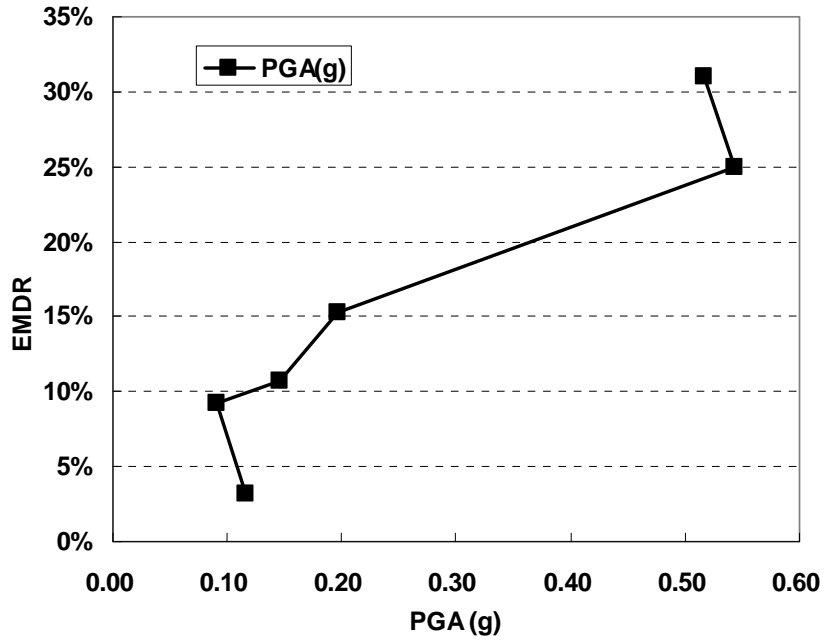
Figure A.2.1 PGA and EMDR
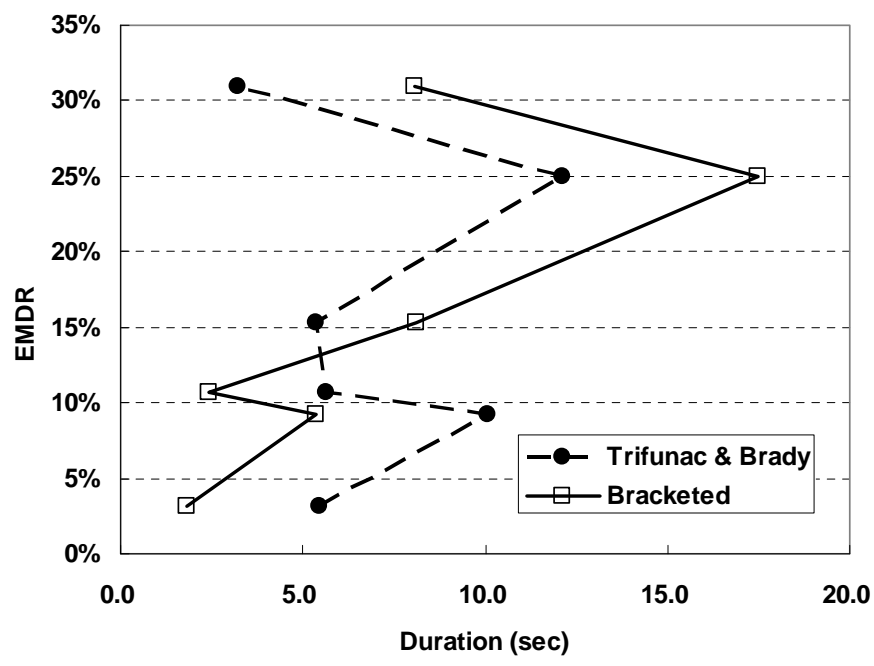
Figure A.2.2 Time duration and EMDR

178
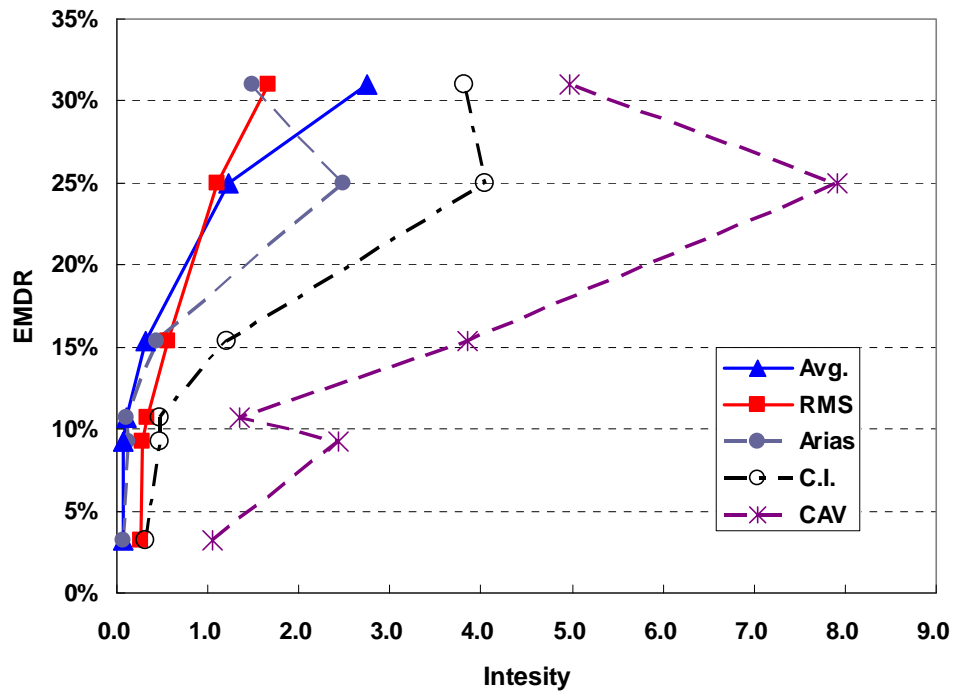
Figure A.2.3 Ground motion intensity and EMDR (1)
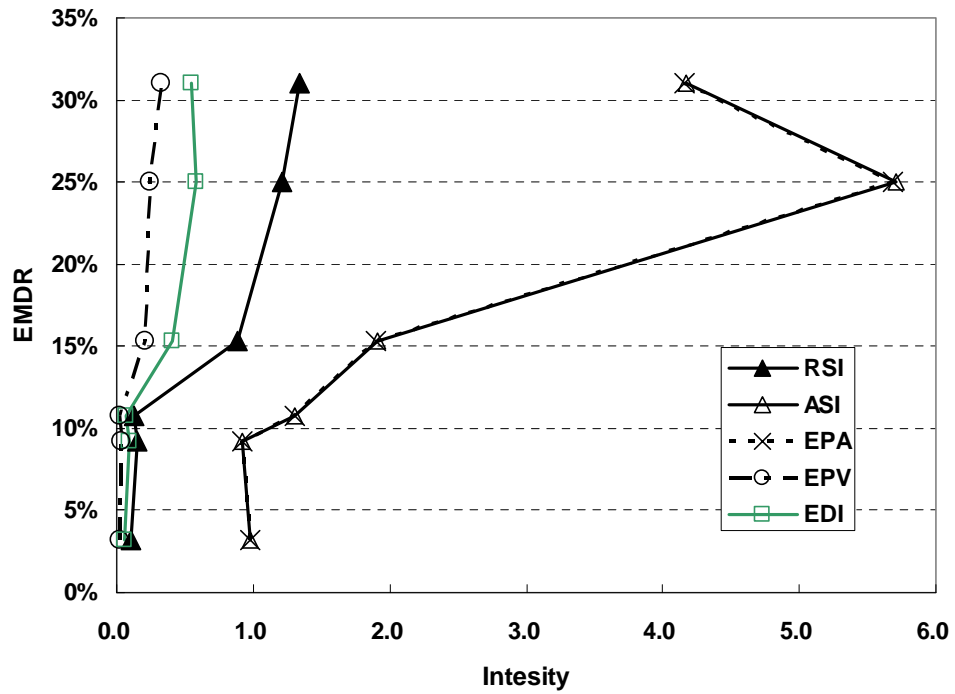
Figure A.2.4 Ground motion intensity and EMDR (2)

179

<div align="right">

Appendix B

</div>

EQUIVALENT LINEAR SYSTEM OF ISOLATION BEARINGS AND SEISMIC ANALYSIS RESULTS

B.1   Equivalent Linear System

From each linearization method, the effective stiffness and effective damping ratio are computed as shown in Table B.1.1 to B.1.3 for the different ground motions.

B.2   Seismic Analysis Results from NP-Model

Using the effective stiffness and effective damping coefficient for the isolation bearing, the equivalent linear analysis is conducted and the displacement results are summarized in Tables B.2.1 through B.2.3.

Table B.1.1 Equivalent linearization of isolation bearing by AASHTO method

Ground Motion	Spring stiffness (kN/m)			Damping ratio			Damping coef. (kNsec/m)		
	A-1	P-2	P-3	A-1	P-2	P-3	A-1	P-2	P-3
Array#6 140°	2,300	5,790	5,830	0.093	0.084	0.088	129	295	310
Array#6 230°	2,256	5,688	5,724	0.083	0.075	0.078	114	260	273
Holliste 0°	2,523	6,312	6,384	0.136	0.126	0.131	200	463	487
Holliste 90°	3,713	9,295	9,669	0.252	0.248	0.255	461	1,135	1,214
Lexingt 0°	2,480	6,201	6,262	0.128	0.118	0.122	187	428	449
Lexingt 90°	2,402	6,023	6,074	0.114	0.104	0.108	163	373	390
Petrolia 0°	3,044	7,540	7,727	0.205	0.195	0.202	335	789	841
Petrolia 90°	2,366	5,934	5,977	0.107	0.097	0.100	151	343	359
Lucerne Long.	4,641	11,885	12,388	0.276	0.276	0.278	572	1,466	1,535
Lucerne Tran.	2,449	6,134	6,189	0.123	0.113	0.117	177	407	427
Yermo 270°	2,680	6,676	6,766	0.161	0.150	0.155	244	568	597
Yermo 360°	3,538	8,826	9,086	0.243	0.238	0.244	432	1,055	1,114
Sylmarff 90°	2,416	6,057	6,108	0.116	0.107	0.111	167	383	401
Sylmarff 360°	2,226	5,617	5,645	0.076	0.068	0.071	103	235	246
Newhall 90°	2,778	6,927	7,043	0.174	0.165	0.171	270	637	672
Newhall 360°	2,349	5,894	5,936	0.103	0.093	0.097	145	330	345
Corralit 0°	3,381	8,294	8,467	0.233	0.223	0.228	407	953	995
Corralit 90°	2,895	7,196	7,329	0.189	0.179	0.185	300	706	745
S. Monica 90°	2,982	7,415	7,549	0.198	0.189	0.195	321	760	798
S. Monica 360°	4,242	10,721	11,225	0.270	0.269	0.273	532	1,338	1,423
Oak Whaf 35°	2,956	7,339	7,470	0.196	0.186	0.192	315	742	779
Oak Whaf 305°	2,952	7,341	7,493	0.195	0.186	0.193	313	742	785
Pomona 0°	6,961	19,378	21,399	0.244	0.226	0.197	633	1,627	1,570
Pomona 90°	7,236	19,986	21,542	0.236	0.217	0.195	630	1,603	1,549
Altadena 0°	4,418	11,030	11,516	0.274	0.272	0.275	554	1,374	1,451
Lacc. N 90°	4,385	11,160	11,817	0.273	0.273	0.276	546	1,388	1,489
Lacc. N 360°	3,814	9,555	9,930	0.257	0.253	0.259	476	1,177	1,253

Table B.1.2 Equivalent linearization of isolation bearing by Caltrans 94 method

Ground Motion	Spring stiffness (kN/m)			Damping ratio			Damping coef. (kNsec/m)		
	A-1	P-2	P-3	A-1	P-2	P-3	A-1	P-2	P-3
Array#6 140°	1,431	3,390	3,505	0.207	0.217	0.213	227	562	570
Array#6 230°	1,306	3,099	3,201	0.219	0.229	0.224	227	564	571
Holliste 0°	2,043	4,837	5,029	0.171	0.178	0.175	227	559	570
Holliste 90°	4,932	12,172	12,980	0.107	0.110	0.106	232	587	603
Lexingt 0°	1,926	4,534	4,698	0.176	0.185	0.181	227	559	568
Lexingt 90°	1,715	4,046	4,184	0.188	0.196	0.193	227	559	567
Petrolia 0°	3,382	8,038	8,503	0.132	0.137	0.133	231	571	587
Petrolia 90°	1,615	3,796	3,916	0.194	0.203	0.200	227	559	567
Lucerne Long.	6,727	17,234	18,080	0.088	0.088	0.085	229	588	596
Lucerne Tran.	1,842	4,350	4,502	0.181	0.189	0.185	226	559	568
Yermo 270°	2,457	5,810	6,047	0.155	0.162	0.159	228	562	573
Yermo 360°	4,548	11,121	11,710	0.113	0.116	0.112	233	584	598
Sylmarff 90°	1,752	4,140	4,281	0.186	0.194	0.190	226	559	568
Sylmarff 360°	1,219	2,888	2,974	0.228	0.238	0.234	228	567	573
Newhall 90°	2,713	6,469	6,770	0.148	0.153	0.150	228	565	578
Newhall 360°	1,567	3,685	3,802	0.197	0.207	0.203	227	560	567
Corralit 0°	4,190	9,881	10,290	0.118	0.123	0.120	235	579	591
Corralit 90°	3,012	7,165	7,504	0.140	0.145	0.142	230	568	581
S. Monica 90°	3,230	7,722	8,059	0.135	0.140	0.137	231	572	583
S. Monica 360°	6,005	15,110	16,059	0.095	0.096	0.093	232	590	603
Oak Whaf 35°	3,164	7,530	7,862	0.137	0.142	0.139	230	570	582
Oak Whaf 305°	3,153	7,534	7,918	0.137	0.142	0.138	230	570	584
Pomona 0°	9,745	26,343	27,861	0.062	0.057	0.051	202	502	475
Pomona 90°	9,998	21,542	26,831	0.059	0.055	0.050	198	492	470
Altadena 0°	6,333	15,698	16,586	0.092	0.094	0.091	232	589	599
Lacc. N 90°	6,271	15,941	17,117	0.093	0.093	0.089	231	589	602
Lacc. N 360°	5,147	12,736	13,527	0.105	0.107	0.103	233	588	603

Table B.1.3 Equivalent linearization of isolation bearing by Caltrans 96 method

Ground Motion	Spring stiffness (kN/m)			Damping ratio			Damping coefficient (kNsec/m)		
	A-1	P-2	P-3	A-1	P-2	P-3	A-1	P-2	P-3
Array#6 140°	2,410	6,035	6,090	0.152	0.148	0.150	218	531	543
Array#6 230°	2,350	5,899	5,946	0.147	0.143	0.145	208	506	517
Holliste 0°	2,721	6,757	6,858	0.167	0.165	0.166	257	629	644
Holliste 90°	4,595	11,401	12,040	0.161	0.163	0.160	335	841	870
Lexingt 0°	2,660	6,600	6,685	0.166	0.162	0.164	251	612	625
Lexingt 90°	2,551	6,354	6,423	0.161	0.157	0.159	238	581	593
Petrolia 0°	3,498	8,566	8,854	0.173	0.174	0.173	308	756	780
Petrolia 90°	2,500	6,231	6,290	0.158	0.154	0.156	232	563	574
Lucerne Long.	6,251	16,005	16,936	0.138	0.138	0.133	344	880	898
Lucerne Tran.	2,616	6,507	6,584	0.164	0.161	0.162	246	601	613
Yermo 270°	2,947	7,277	7,407	0.172	0.170	0.171	277	678	693
Yermo 360°	4,299	10,617	11,051	0.165	0.167	0.165	331	826	849
Sylmarff 90°	2,570	6,401	6,472	0.162	0.158	0.160	241	587	599
Sylmarff 360°	2,309	5,802	5,841	0.143	0.138	0.140	200	486	496
Newhall 90°	3,093	7,643	7,815	0.173	0.172	0.173	286	705	723
Newhall 360°	2,476	6,177	6,234	0.157	0.153	0.154	228	555	566
Corralit 0°	4,038	9,749	10,029	0.168	0.171	0.170	327	802	820
Corralit 90°	3,270	8,043	8,243	0.174	0.174	0.174	297	730	749
S. Monica 90°	3,403	8,374	8,579	0.173	0.174	0.174	303	748	766
S. Monica 360°	5,524	13,887	14,796	0.148	0.150	0.145	343	871	897
Oak Whaf 35°	3,362	8,259	8,458	0.174	0.174	0.174	302	742	760
Oak Whaf 305°	3,356	8,262	8,493	0.174	0.174	0.174	301	742	763
Pomona 0°	10,439	29,094	31,628	0.085	0.074	0.060	290	698	614
Pomona 90°	10,872	29,926	31,781	0.080	0.069	0.059	280	670	602
Altadena 0°	5,842	14,443	15,326	0.144	0.147	0.142	346	873	896
Lacc. N 90°	5,781	14,679	15,879	0.145	0.146	0.139	343	874	903
Lacc. N 360°	4,768	11,844	12,491	0.159	0.161	0.158	337	849	876

Table B.2.1 Displacement from NP-Model by AASHTO

Group	No.	Ground Motion	PGA (g)	Displacement (cm)				
				Deck			Pier top	
				A-1	P-2	P-3	P-2	P-3
Group 1	1	Array#6 140°	0.376	44.51	44.56	44.73	5.54	7.59
	2	Array#6 230°	0.437	38.65	38.69	38.84	4.73	6.49
	3	Holliste 0°	0.369	21.77	21.82	21.94	2.98	4.10
	4	Holliste 90°	0.178	5.82	5.82	5.85	1.26	1.73
	5	Lexingt 0°	0.442	25.56	25.61	25.74	3.41	4.68
	6	Lexingt 90°	0.410	31.63	31.67	31.80	4.08	5.59
	7	Petrolia 0°	0.590	10.91	10.93	10.99	1.91	2.64
	8	Petrolia 90°	0.663	30.30	30.35	30.49	3.84	5.27
	9	Lucerne Long.	0.704	4.60	4.64	4.72	1.23	1.67
	10	Lucerne Tran.	0.665	20.95	20.98	21.07	2.78	3.82
	11	Yermo 270°	0.245	16.13	16.16	16.25	2.36	3.24
	12	Yermo 360°	0.152	6.33	6.34	6.37	1.22	1.68
	13	Sylmarff 90°	0.605	26.48	26.52	26.63	3.43	4.70
	14	Sylmarff 360°	0.844	49.14	49.19	49.36	5.87	8.05
	15	Newhall 90°	0.583	15.72	15.76	15.86	2.40	3.31
	16	Newhall 360°	0.590	34.62	34.68	34.83	4.38	6.01
Group 2	17	Corralit 0°	0.630	7.25	7.34	7.52	1.73	2.42
	18	Corralit 90°	0.479	10.78	10.79	10.84	1.75	2.41
	19	S. Monica 90°	0.884	13.12	13.15	13.23	2.15	2.95
	20	S. Monica 360°	0.753	5.89	5.92	5.99	1.41	1.93
Group 3	21	Oak Whaf 35°	0.287	11.50	11.54	11.63	1.90	2.61
	22	Oak Whaf 305°	0.271	13.21	13.23	13.30	2.15	2.96
	23	Pomona 0°	0.186	1.84	1.88	1.96	0.67	0.91
	24	Pomona 90°	0.207	1.82	1.87	1.95	0.68	0.92
	25	Altadena 0°	0.448	4.87	5.00	5.23	1.38	1.94
	26	Lacc. North 90°	0.256	4.74	4.76	4.80	1.20	1.67
	27	Lacc. North 360°	0.222	6.46	6.50	6.59	1.46	2.01

Table B.2.2 Displacement from NP-Model by Caltrans 94

Group	No.	Ground Motion	PGA (g)	Displacement (cm)				
				Deck			Pier top	
				A-1	P-2	P-3	P-2	P-3
Group 1	1	Array#6 140°	0.376	34.76	34.77	34.81	2.88	4.04
	2	Array#6 230°	0.437	47.75	47.76	47.82	3.61	5.07
	3	Holliste 0°	0.369	22.57	22.60	22.67	2.54	3.55
	4	Holliste 90°	0.178	7.14	7.20	7.29	1.67	2.29
	5	Lexingt 0°	0.442	21.44	21.46	21.52	2.38	3.32
	6	Lexingt 90°	0.410	26.05	26.06	26.10	2.63	3.67
	7	Petrolia 0°	0.590	11.26	11.30	11.37	1.92	2.66
	8	Petrolia 90°	0.663	29.77	29.78	29.84	2.97	4.15
	9	Lucerne Long.	0.704	7.10	7.20	7.38	2.13	2.87
	10	Lucerne Tran.	0.665	23.19	23.20	23.26	2.42	3.37
	11	Yermo 270°	0.245	15.66	15.68	15.75	2.07	2.88
	12	Yermo 360°	0.152	8.77	8.83	8.94	1.91	2.63
	13	Sylmarff 90°	0.605	28.76	28.78	28.84	2.84	3.97
	14	Sylmarff 360°	0.844	40.56	40.56	40.61	3.01	4.23
	15	Newhall 90°	0.583	16.48	16.53	16.62	2.36	3.28
	16	Newhall 360°	0.590	27.62	27.64	27.69	2.62	3.65
Group 2	17	Corralit 0°	0.630	7.57	7.67	7.85	1.55	2.14
	18	Corralit 90°	0.479	11.63	11.66	11.72	1.82	2.52
	19	S. Monica 90°	0.884	14.52	14.57	14.67	2.39	3.30
	20	S. Monica 360°	0.753	8.47	8.58	8.78	2.33	3.18
Group 3	21	Oak Whaf 35°	0.287	12.38	12.42	12.50	1.99	2.75
	22	Oak Whaf 305°	0.271	15.31	15.35	15.44	2.46	3.41
	23	Pomona 0°	0.186	2.21	2.28	2.40	0.88	1.18
	24	Pomona 90°	0.207	2.29	2.37	2.49	0.92	1.23
	25	Altadena 0°	0.448	5.65	5.74	5.89	1.60	2.18
	26	Lacc. North 90°	0.256	6.70	6.79	6.94	1.90	2.60
	27	Lacc. North 360°	0.222	8.82	8.90	9.05	2.13	2.92

Table B.2.3 Displacement from NP-Model by Caltrans 96

Group	No.	Ground Motion	PGA (g)	Displacement (cm)				
				Deck			Pier top	
				A-1	P-2	P-3	P-2	P-3
Group 1	1	Array#6 140˚	0.376	35.75	35.80	35.93	4.73	6.48
	2	Array#6 230˚	0.437	35.26	35.30	35.43	4.55	6.24
	3	Holliste 0˚	0.369	18.95	19.00	19.12	2.78	3.81
	4	Holliste 90˚	0.178	6.45	6.49	6.56	1.49	2.04
	5	Lexingt 0˚	0.442	23.57	23.63	23.77	3.47	4.76
	6	Lexingt 90˚	0.410	27.97	28.02	28.16	3.91	5.36
	7	Petrolia 0˚	0.590	10.81	10.85	10.94	2.02	2.78
	8	Petrolia 90˚	0.663	27.83	27.89	28.03	3.90	5.35
	9	Lucerne Long.	0.704	6.12	6.19	6.33	1.78	2.41
	10	Lucerne Tran.	0.665	19.68	19.72	19.81	2.85	3.90
	11	Yermo 270˚	0.245	15.81	15.85	15.95	2.53	3.46
	12	Yermo 360˚	0.152	7.29	7.32	7.38	1.56	2.12
	13	Sylmarff 90˚	0.605	23.22	23.26	23.36	3.28	4.49
	14	Sylmarff 360˚	0.844	42.20	42.24	42.38	5.38	7.36
	15	Newhall 90˚	0.583	15.35	15.40	15.50	2.57	3.52
	16	Newhall 360˚	0.590	29.59	29.65	29.80	4.11	5.64
Group 2	17	Corralit 0˚	0.630	7.43	7.53	7.74	1.73	2.39
	18	Corralit 90˚	0.479	11.51	11.54	11.61	2.03	2.77
	19	S. Monica 90˚	0.884	12.95	12.99	13.09	2.31	3.16
	20	S. Monica 360˚	0.753	7.18	7.27	7.42	1.91	2.62
Group 3	21	Oak Whaf 35˚	0.287	11.64	11.67	11.75	2.04	2.79
	22	Oak Whaf 305˚	0.271	13.76	13.81	13.91	2.45	3.36
	23	Pomona 0˚	0.186	2.10	2.17	2.30	0.90	1.21
	24	Pomona 90˚	0.207	2.27	2.35	2.49	0.98	1.30
	25	Altadena 0˚	0.448	5.37	5.47	5.66	1.52	2.09
	26	Lacc. North 90˚	0.256	6.00	6.08	6.21	1.65	2.27
	27	Lacc. North 360˚	0.222	7.50	7.57	7.71	1.79	2.45

EFFECTS OF GROUND MOTION PARAMETERS ON ISOLATED BRIDGE

C.1 Effects on Ductility Ratio

The relations between the ductility ratios of the isolation bearings and the ground motion parameters are shown in Figs. C.1.1 to C.1.6. As seen from these figures, the response spectrum intensity and energy dissipation index show a good relation with the ductility ratio of the isolation bearings of the example bridge. In all figures, each ground motion parameter is normalized to the maximum value of each parameter.
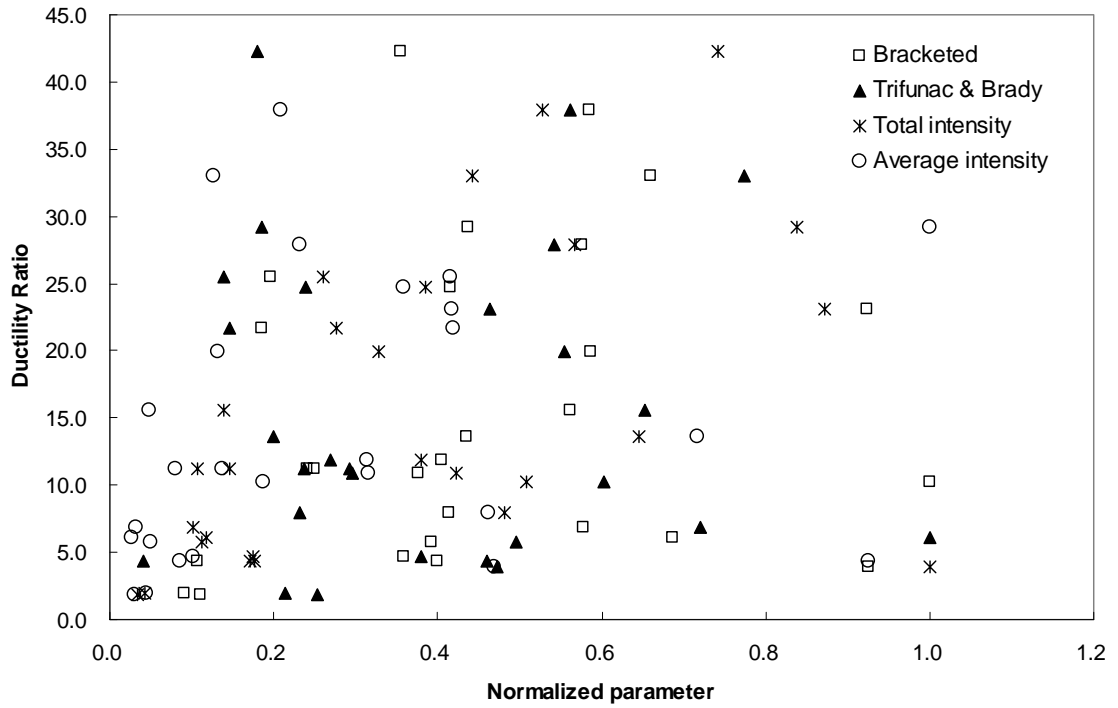
Figure C.1.1 Ductility ratio and time duration parameters
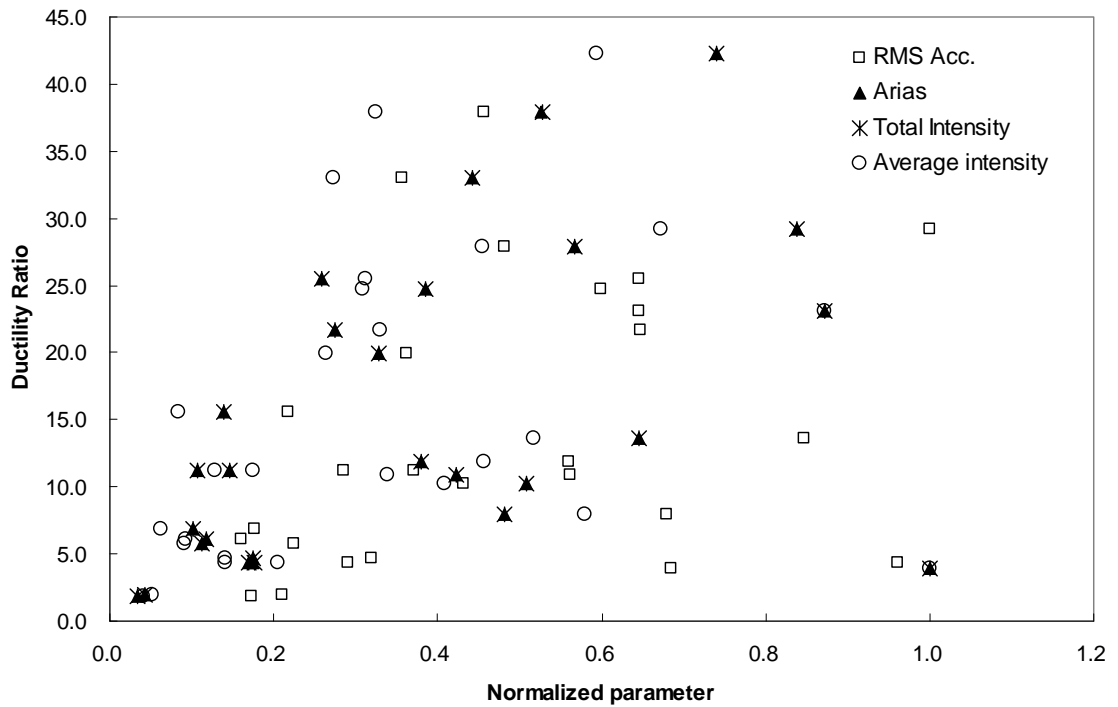
Figure C.1.2 Ductility ratio and intensity parameters
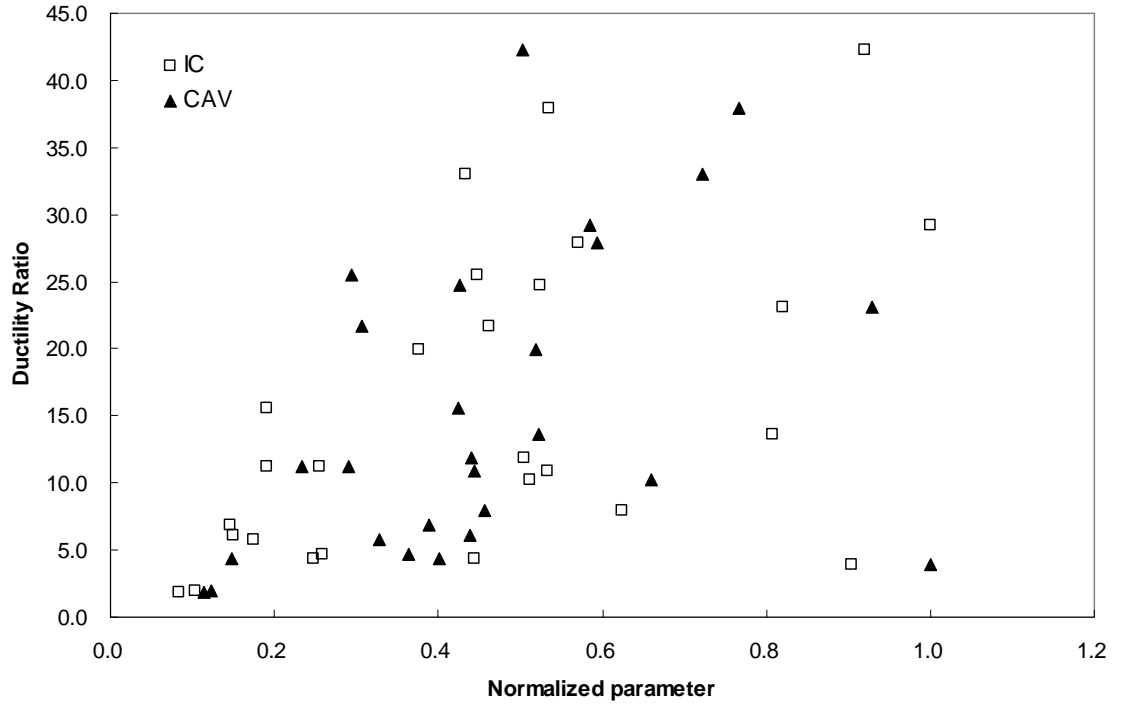
Figure C.1.3 Ductility ratio and damage parameters
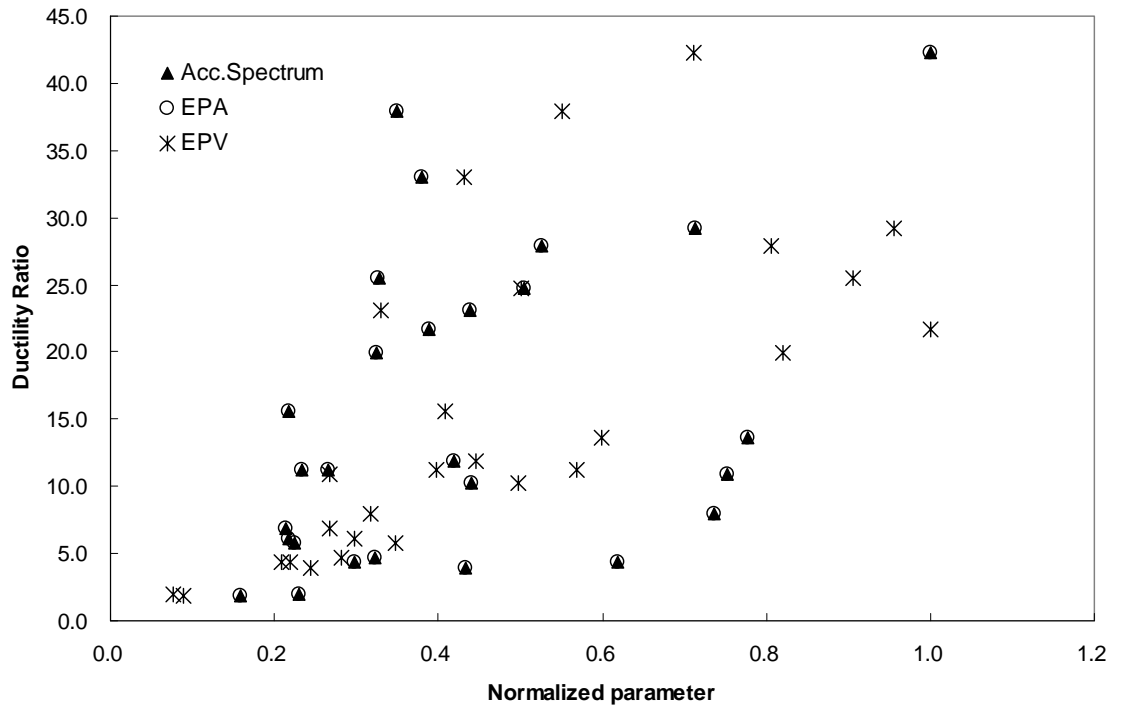
Figure C.1.4 Ductility ratio and spectrum intensity parameters
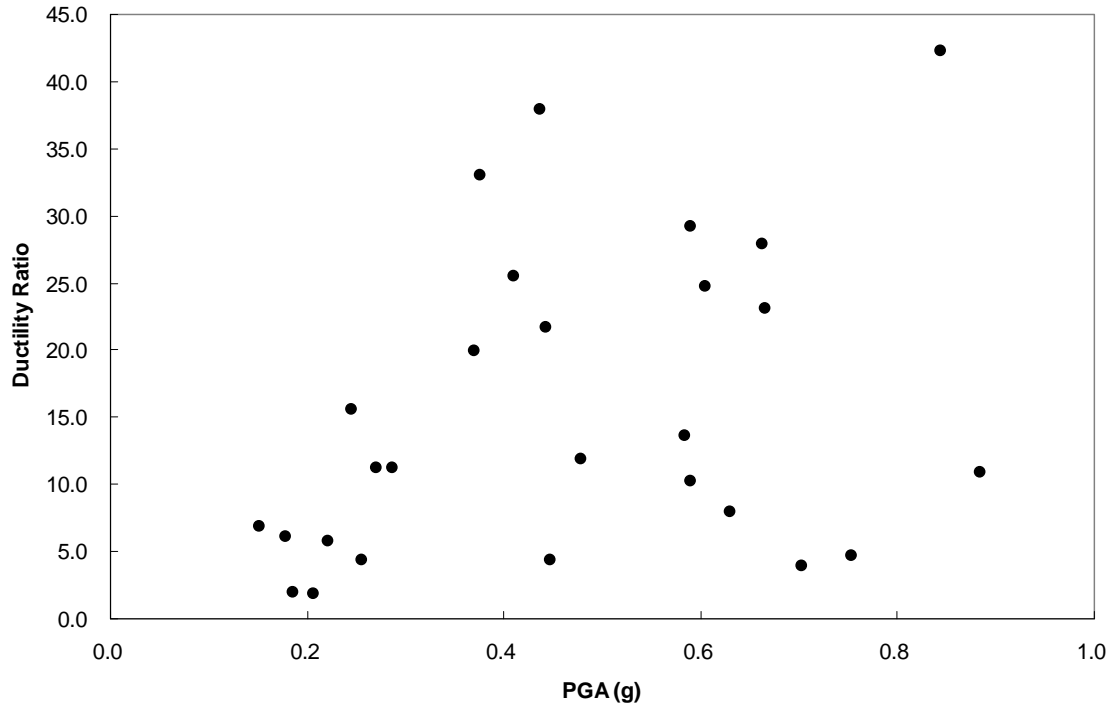
Figure C.1.5 Ductility ratio and peak ground acceleration
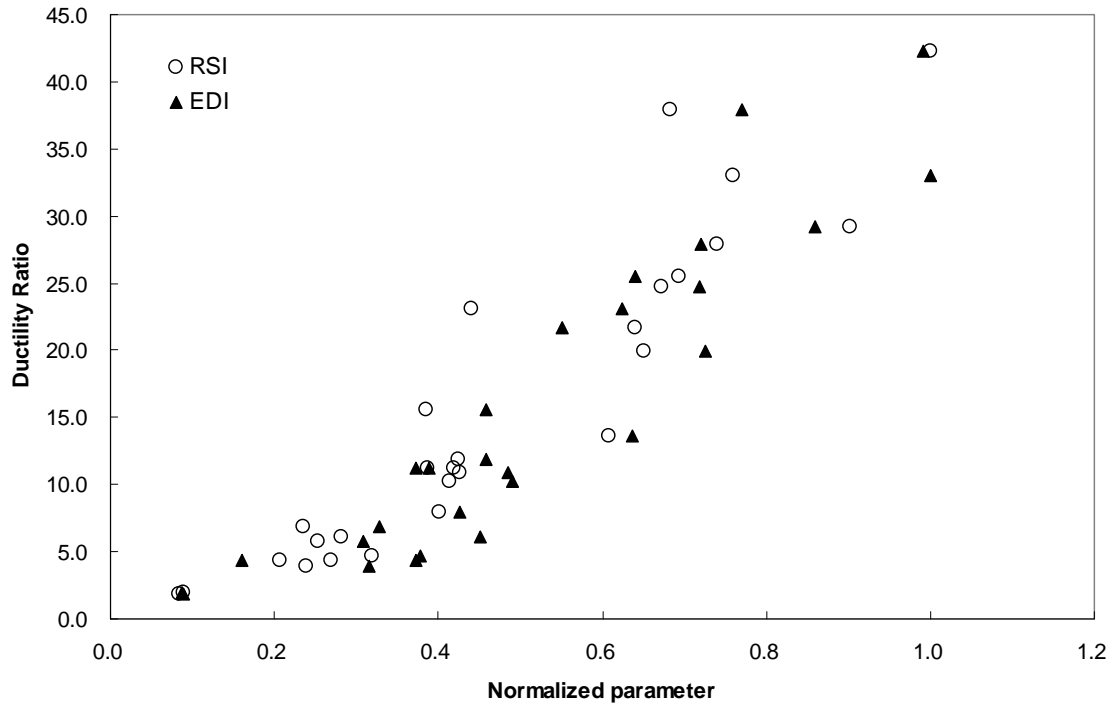
Figure C.1.6 Ductility ratio and response spectrum intensity and energy dissipation index

C.2 Effects on Equivalent Linearization of Isolation Bearings

The effects of the ground motion parameters on the equivalent linearization of the isolation bearings are shown in Figs. C.2.1 to C.2.3. The effective stiffness of the equivalent linear system is normalized by the initial elastic stiffness of the isolation bearing. Figure C.2.1 shows that the PGA does not affect the equivalent linear system of the isolation bearings; however, it can be seen that the RSI and EDI of the ground motion parameter show good correlation with the equivalent linear system of the isolation bearings in Figs. C.2.2 and C.2.3. The figures of effective stiffness and effective damping ratio shown in Figs. C.2.1 to C.2.3 are very similar to Figs. 5.3.2 and 5.3.3 which show the relations of the effective stiffness and effective damping ratio with the ductility ratio.
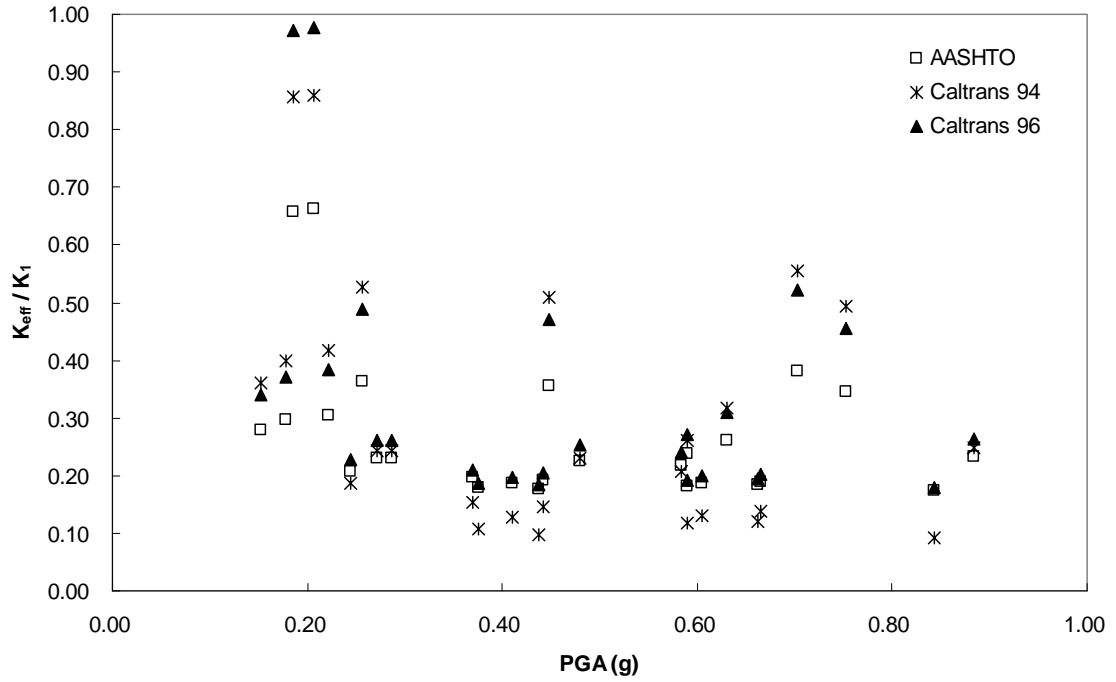
(a) Effective stiffness
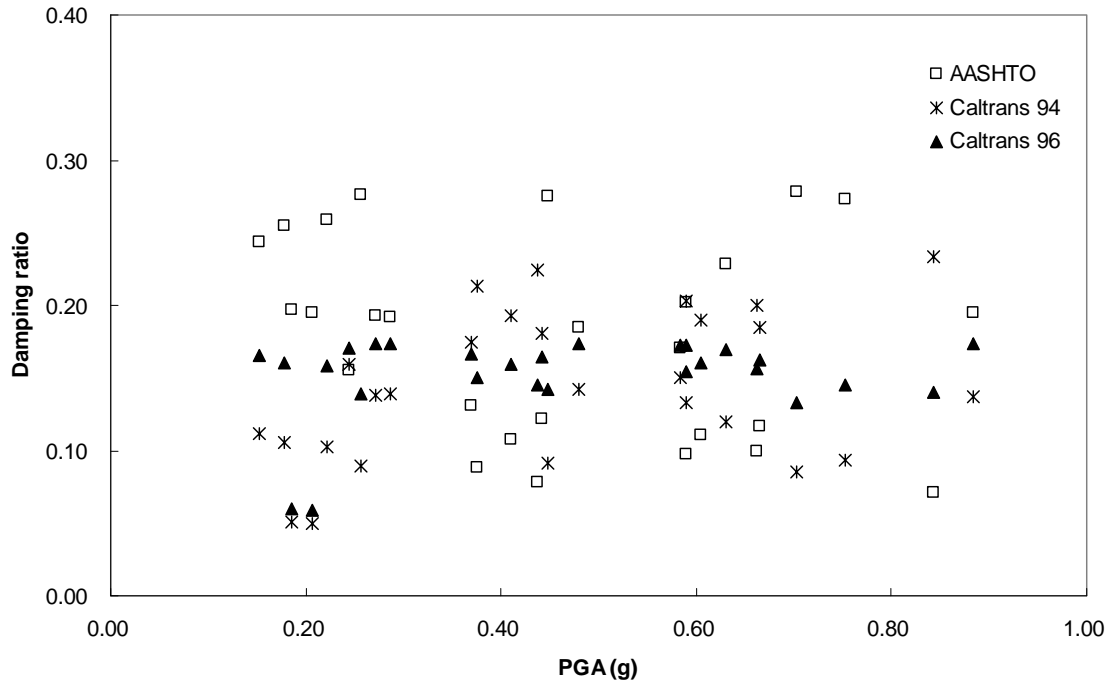
(b) Effective damping ratio

Figure C.2.1 Effects of PGA on equivalent linearization
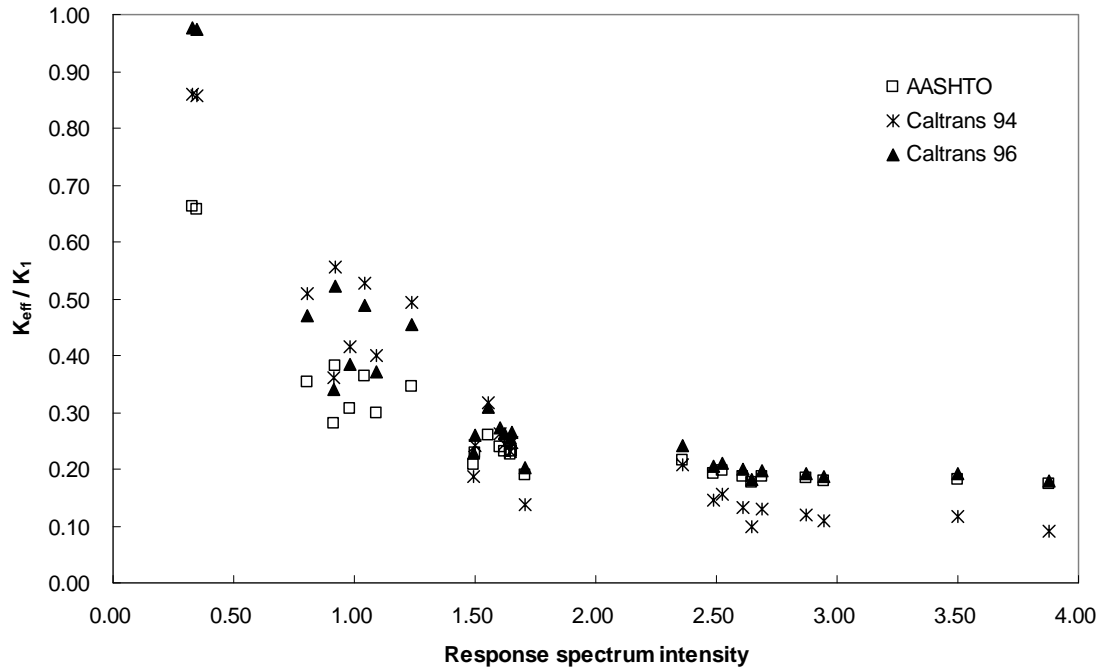
(a) Effective stiffness
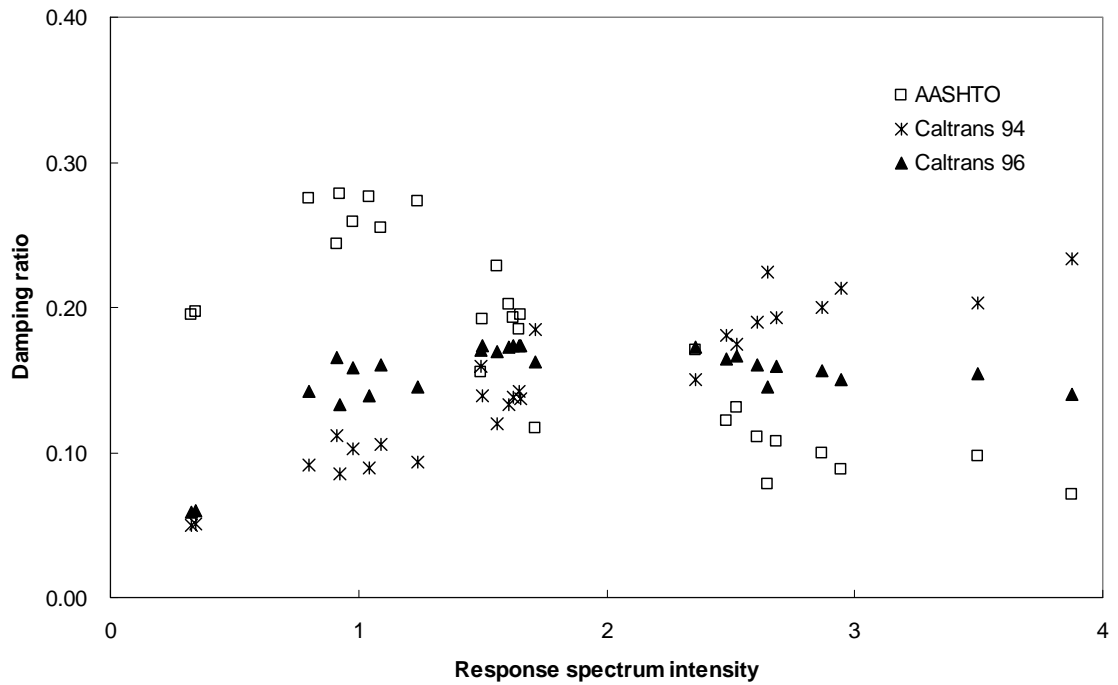
(b) Effective damping ratio

Figure C.2.2 Effects of RSI on equivalent linearization
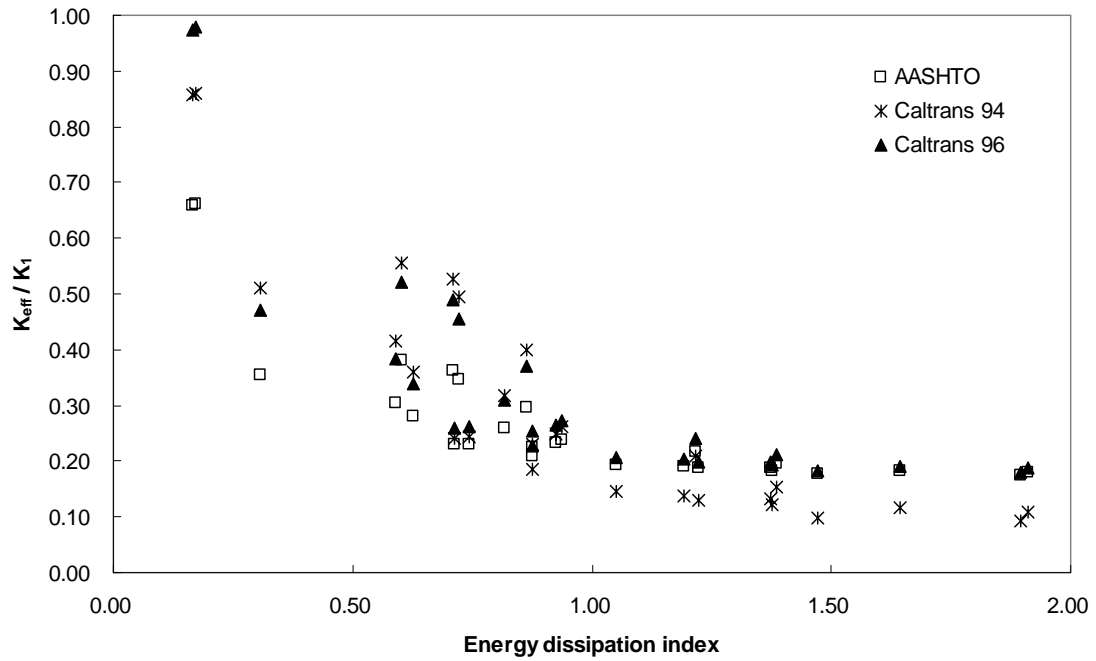
(a) Effective stiffness
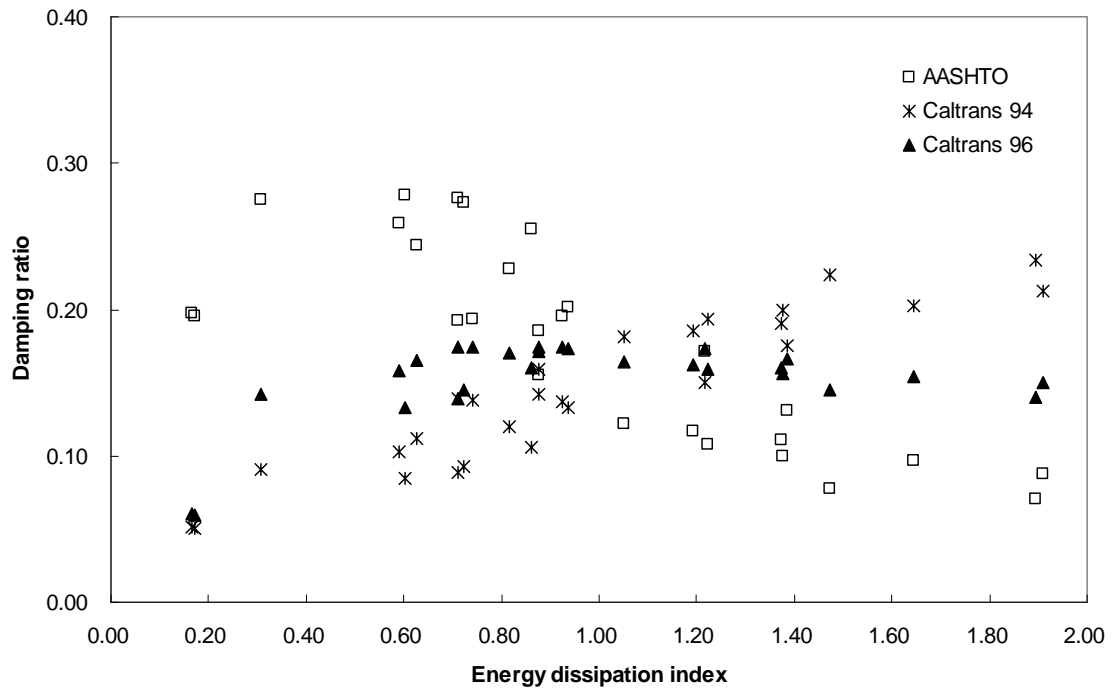
(b) Effective damping ratio

Figure C.2.3 Effects of EDI on equivalent linearization

194

C.3 Effects on EMDR

The effects of the ground motion parameters on the equivalent modal damping ratio of the example bridge are shown Figs. C.3.1 to C.3.9.
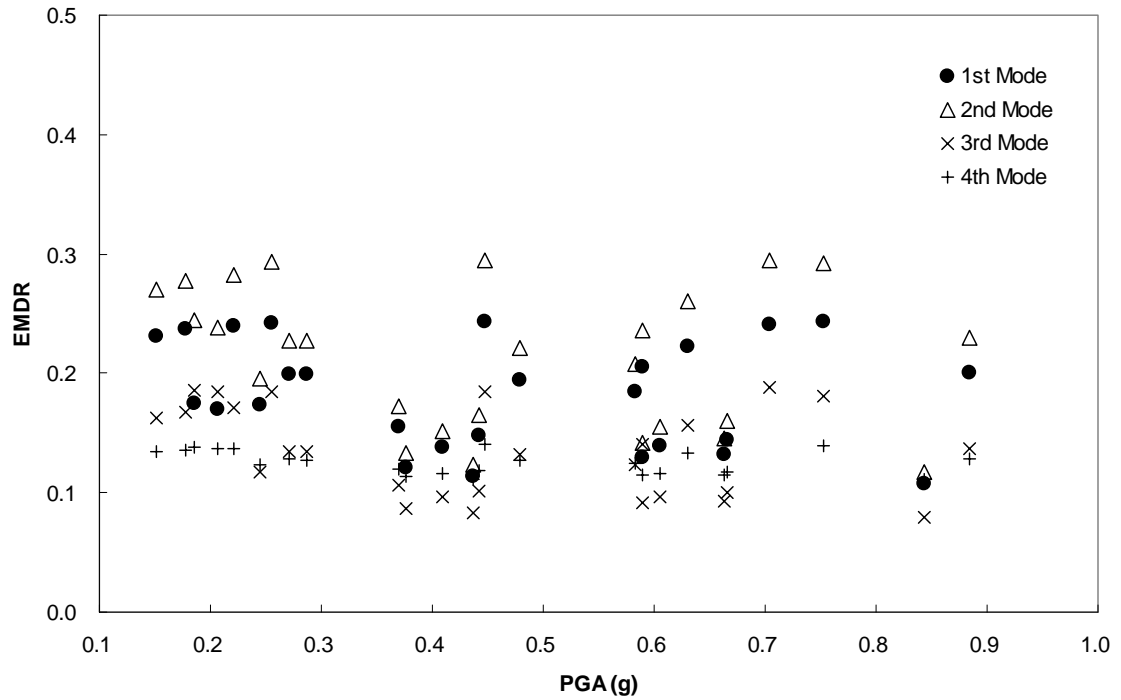
Figure C.3.1 EMDR with PGA
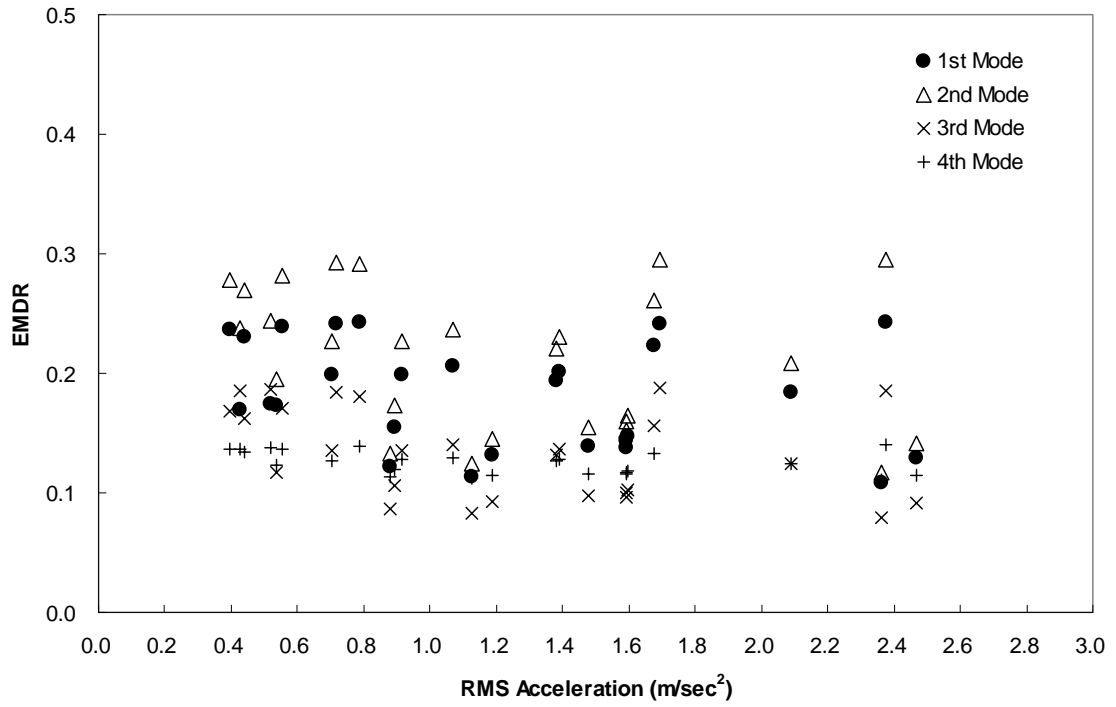
Figure C.3.2 EMDR with root mean square acceleration
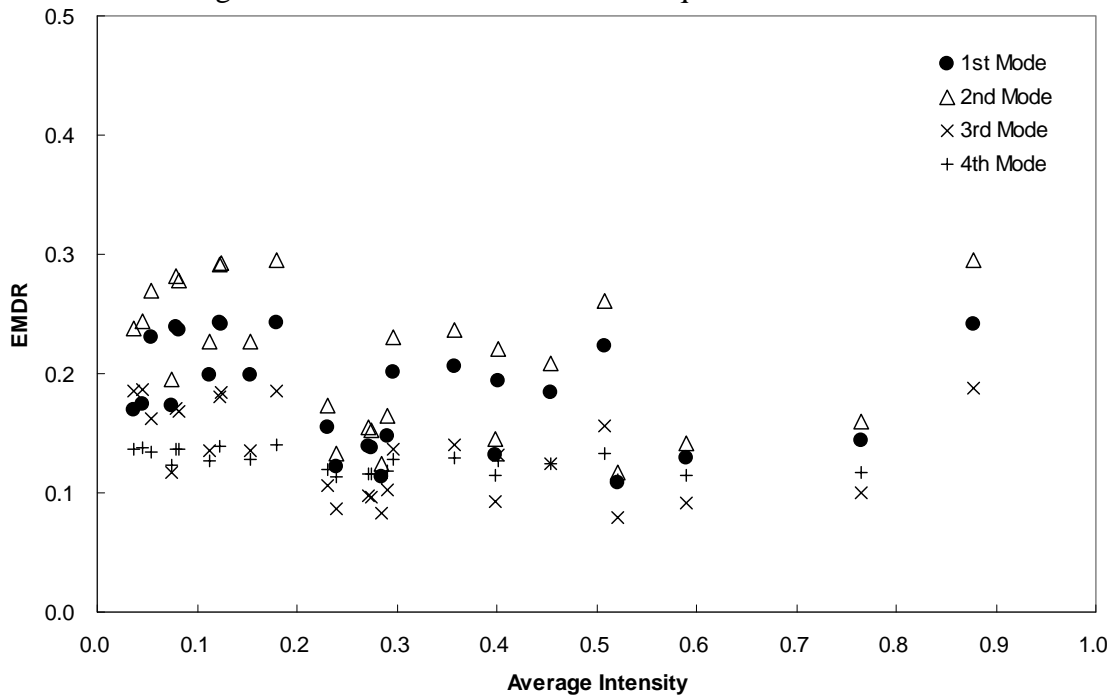
Figure C.3.3 EMDR with average intensity

196
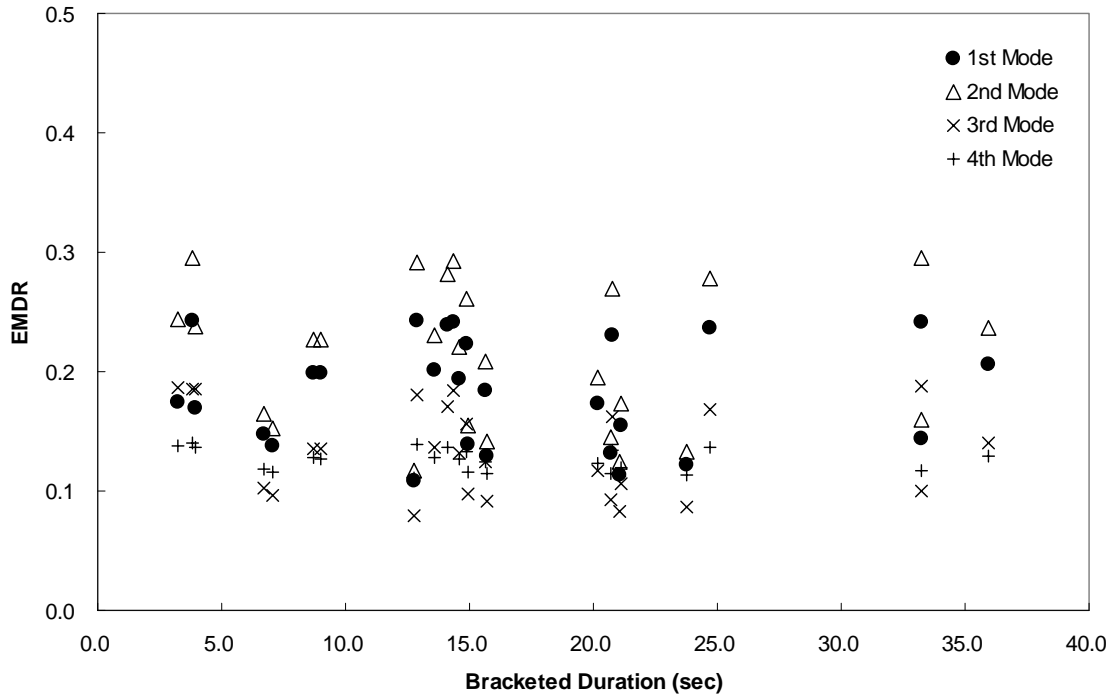
Figure C.3.4 EMDR with bracketed duration
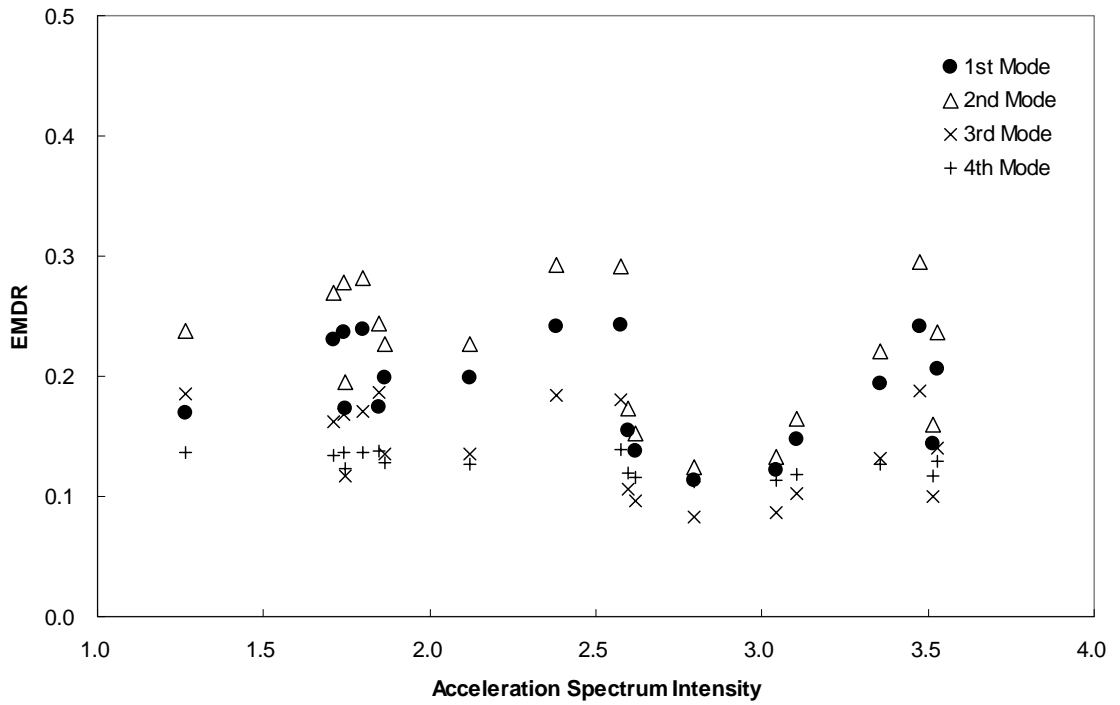
Figure C.3.5 EMDR with acceleration spectrum intensity

197
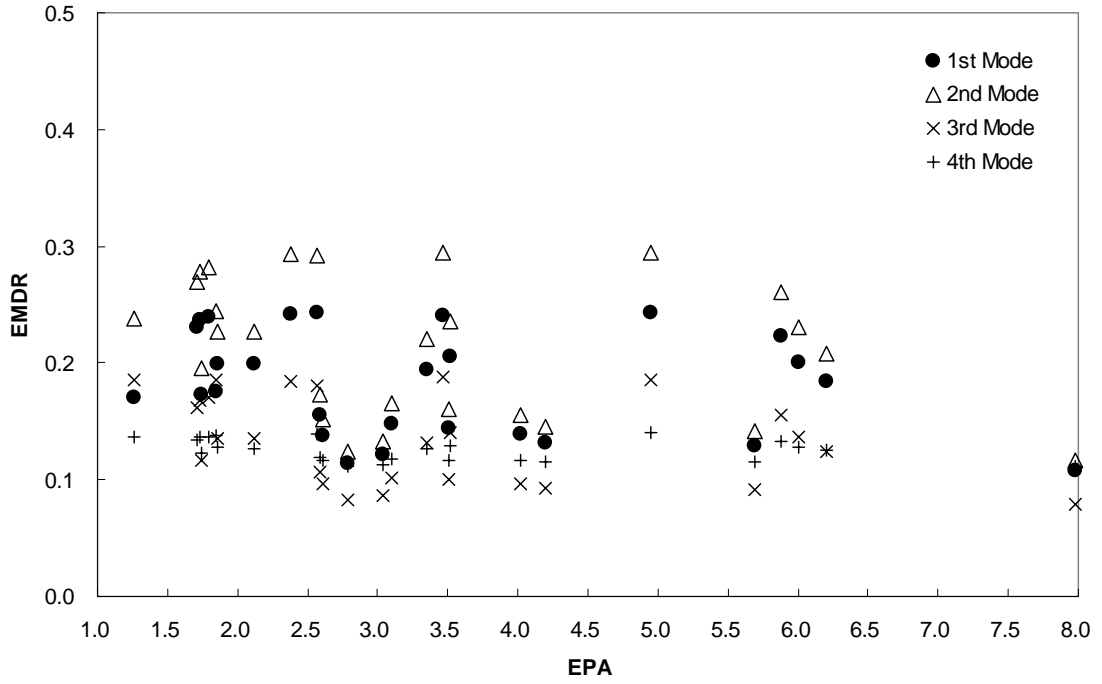
Figure C.3.6 EMDR with effective peak acceleration
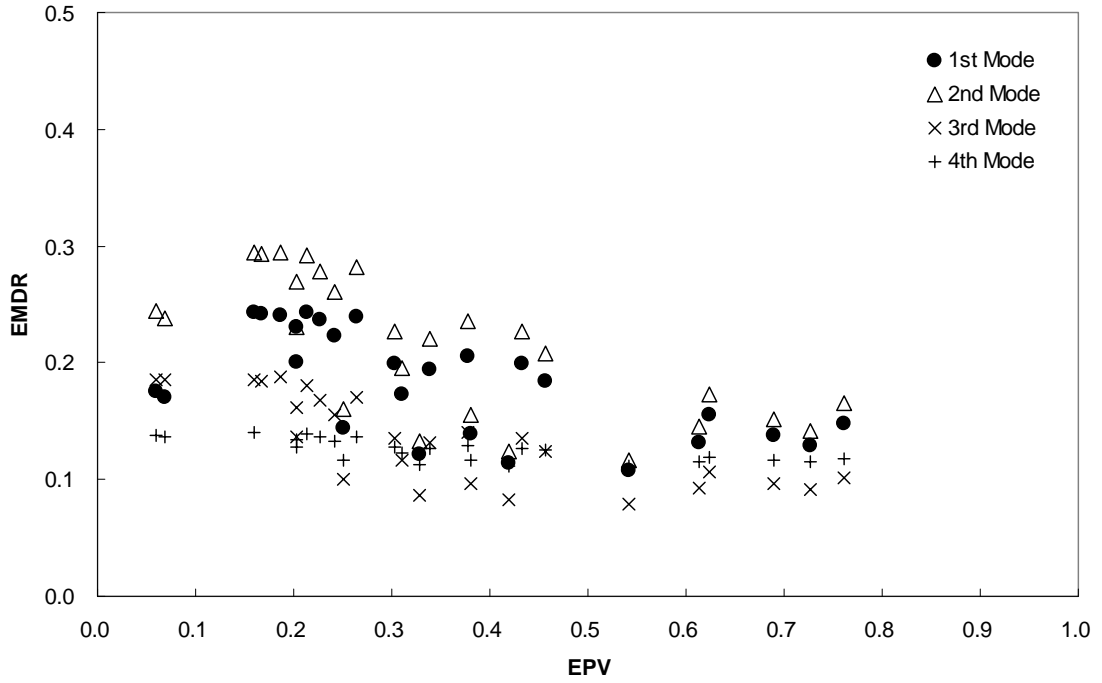
Figure C.3.7 EMDR with effective peak velocity

198
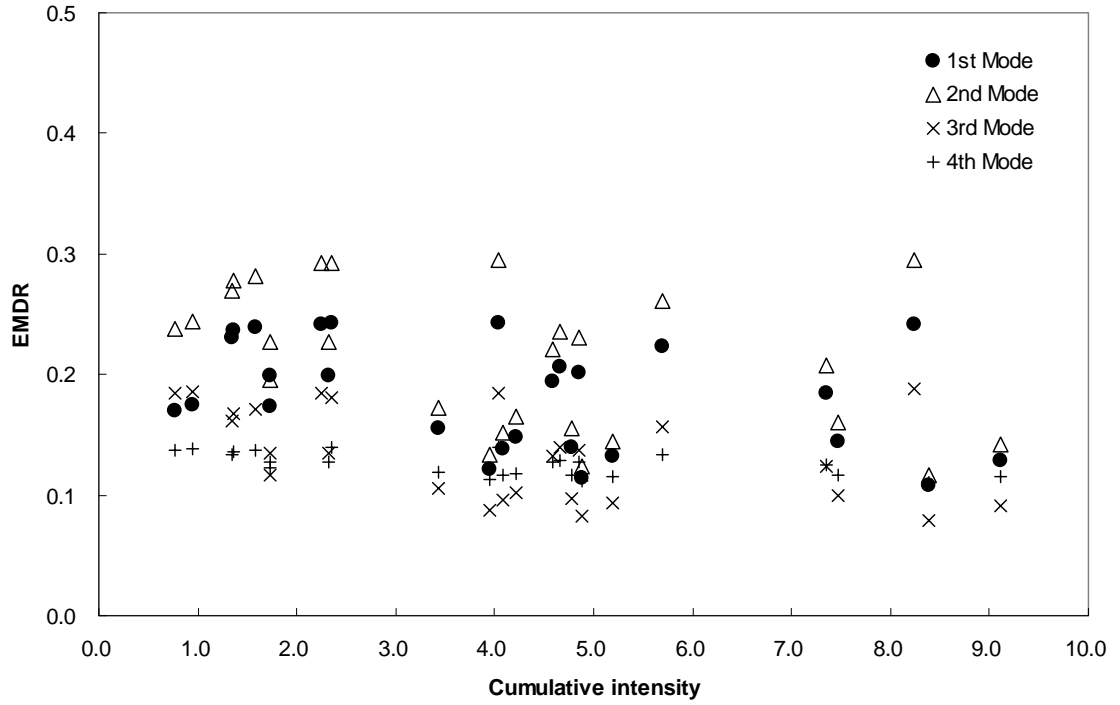
Figure C.3.8 EMDR with cumulative intensity
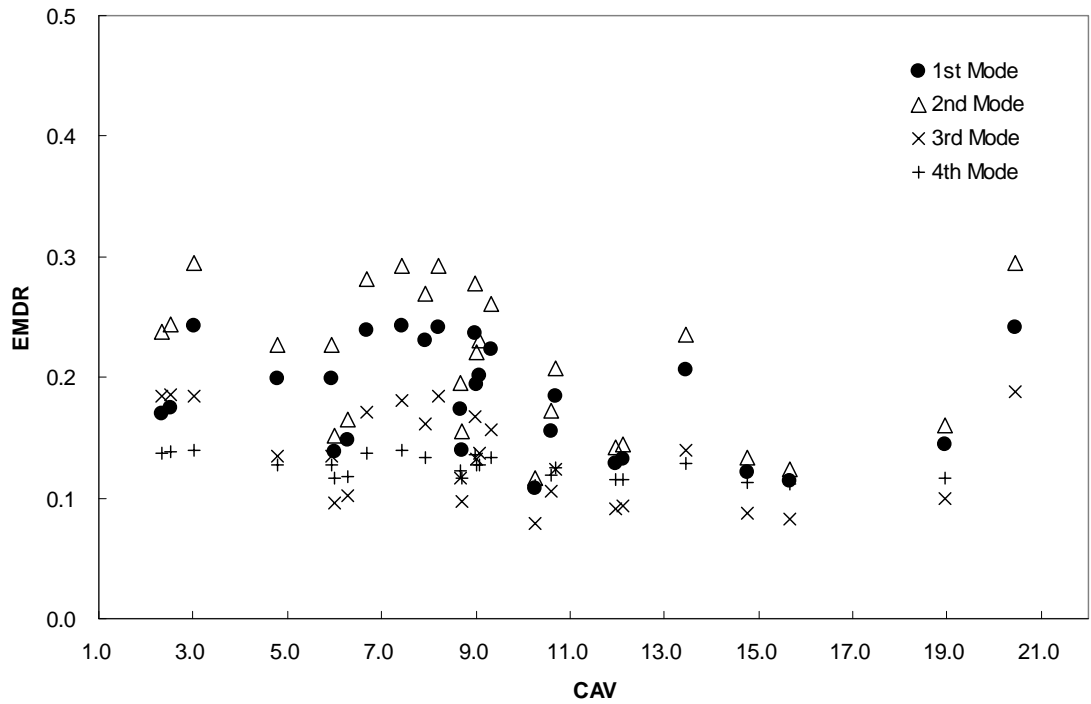
Figure C.3.9 EMDR with Cumulative absolute velocity

199

Appendix D

MECHANICALLY STABILIZED EARTH (MSE) WALLS

D.1 Mechanically Stabilized Walls

Mechanically stabilized earth (MSE) walls use either metallic (inextensible) or geosynthetic (extensible) soil reinforcement in the soil mass and vertical or near vertical discrete modular precast concrete facing elements. Various aesthetic treatments can be incorporated in the precast concrete face panels. MSE walls behave as a gravity wall, deriving their lateral resistance through the dead weight of the reinforced soil mass behind the facing.

MSE walls are typically used where conventional reinforced concrete retaining walls are considered, and are particularly well suited for sites where substantial total and differential settlements are anticipated.   MSE wall can be used in both cut and fill applications. Because their base width is greater than that of conventional reinforced concrete walls they are most cost effective in fill applications. The practical height of MSE walls is limited by the competence of the foundation material at a given site.

MSE walls shall be designed for external stability of the wall system as well as internal stability of the reinforced soil mass behind the facing. MSE wall system design requires knowledge of short and long-term properties of the materials used as soil reinforcement

as well as the soil mechanics which govern MSE wall behavior. Structural design of the wall facing may also be required.

Design of MSE wall presented in this manual is based on AASHTO LRFD section 11.10 (2007). See the following for detailed procedure.

D.1.1 MSE Wall Design

In LRFD MSE wall design, the external and internal stability of the MSE wall is evaluated at all appropriate strength limit states. The overall stability including lateral and vertical wall deformations are evaluated at the service limit state. The specific checks for the strength and service limit states required for MSE wall design are listed below.

Strength Limit States

• External Stability (Figure 12-1)

1. Limiting Eccentricity

2. Sliding

3. Bearing Resistance

• Internal Stability

1. Tensile Resistance of Reinforcement

2. Pullout Resistance of Reinforcement

3. Structural Resistance of Face Elements

4. Structural Resistance of Face Element Connections

Service Limit States for MSE walls

1. Overall Stability

2. Lateral and Vertical Wall Deformations

(a) Sliding   (b) Overturning (eccentricity)

(c) Bearing capacity   (d) Deep seated stability (rotational)
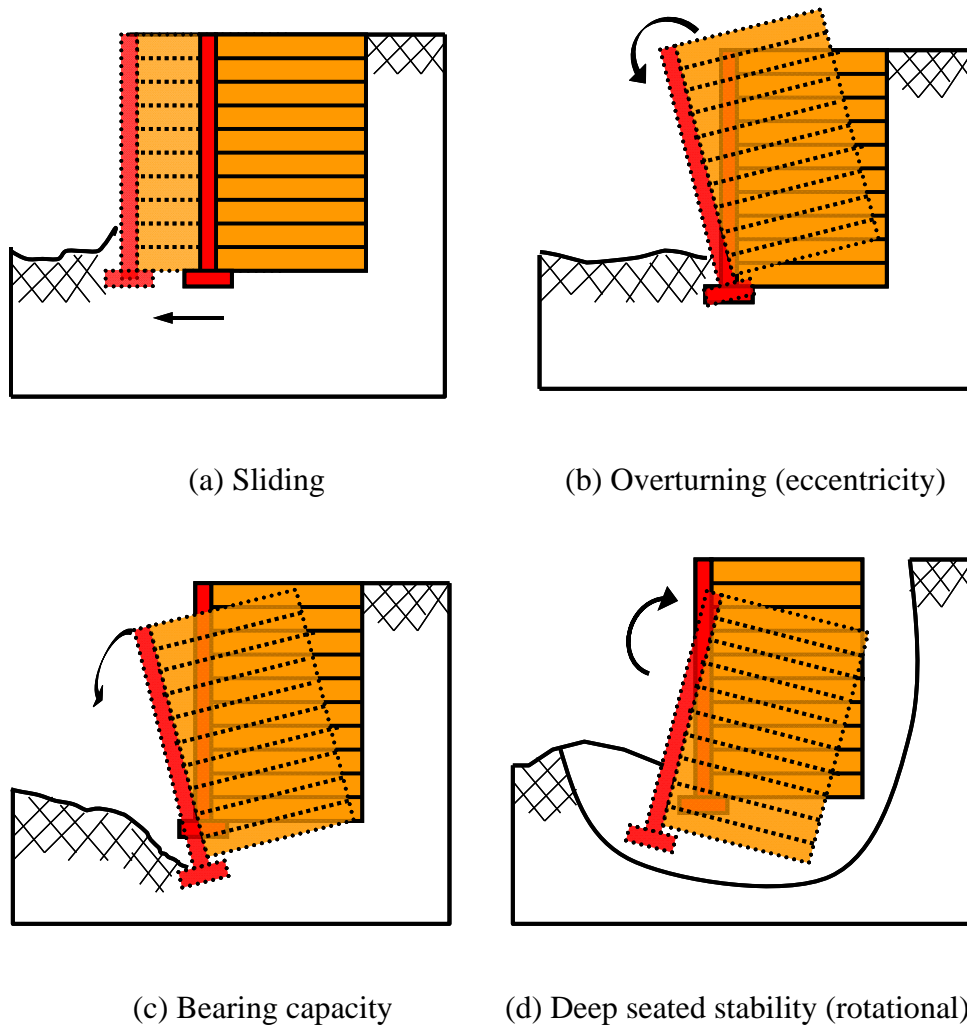
Figure D.1.1 Potential external failure mechanisms for MSE walls.

The internal stability analyses of an MSE wall shall satisfy all applicable strength, service and extreme event limit states using the following procedures.

1) Determine the maximum factored load in each reinforcement

2) Determine maximum factored pullout resistance

3) Determine maximum factored tensile resistance

The factored pullout and tensile reinforcement resistance must be larger than factored load in each reinforcement layer.

D.1.2 Initial Design Steps

Step 1 – Select Initial Wall Geometry

The design height of the MSE wall (for external stability computations) is the sum of the required embedment depth and the wall height. To prevent exceeding local bearing resistance, the minimum embedment depths shown in Table D-1-1 should be used in the design. The minimum wall embedment, in any case, should be 1.5 ft.

The minimum reinforcement length (L) should be 0.7H (or 8 ft, whichever is greater), where H is the design height of the structure as measured from the top of the leveling pad as shown in Figure D.1.2. MSE walls with sloping surcharge fills or other external loads, such as abutment footings or surcharges, generally require longer reinforcements for stability, often on the order of 0.8H to as much as 1.1H. Shorter lengths may be required for individual reinforcement levels. Shorter minimum reinforcement lengths, on the

order of 6 ft, but no less than 70 percent of the wall height, can be considered if smaller compaction equipment is used, facing panel alignment can be maintained, and minimum requirements for wall external stability are met. Additional discussion is provided in Section C11.10.2.1 (AASHTO, 2007).

Table D.1.1 Minimum embedment requirements for MSE walls

Slope in front of structures		Minimum embedment depth
Horizontal	for walls	H/20.0
	for abutments	H/10.0
3.0H:1.0V	walls	H/10.0
2.0H:1.0V	walls	H/7.0
1.5H:1.0V	walls	H/5.0

A minimum horizontal bench width of 4 ft (measured from bottom of wall horizontally to slope face) should be provided in front of walls founded on slopes. This minimum bench width is required to protect against local instability near the toe of the wall.

STRENGTH LIMIT STATES – EXTERNAL STABILITY (Steps 2 through 6)

Step 2 – Estimate Unfactored Loads

The unfactored loads for MSE walls may include loads due to horizontal earth pressure (EH), vertical earth pressure (EV), live load surcharge (LS), and earth surcharge (ES). Water, seismic, and vehicle impact loads should also be evaluated.
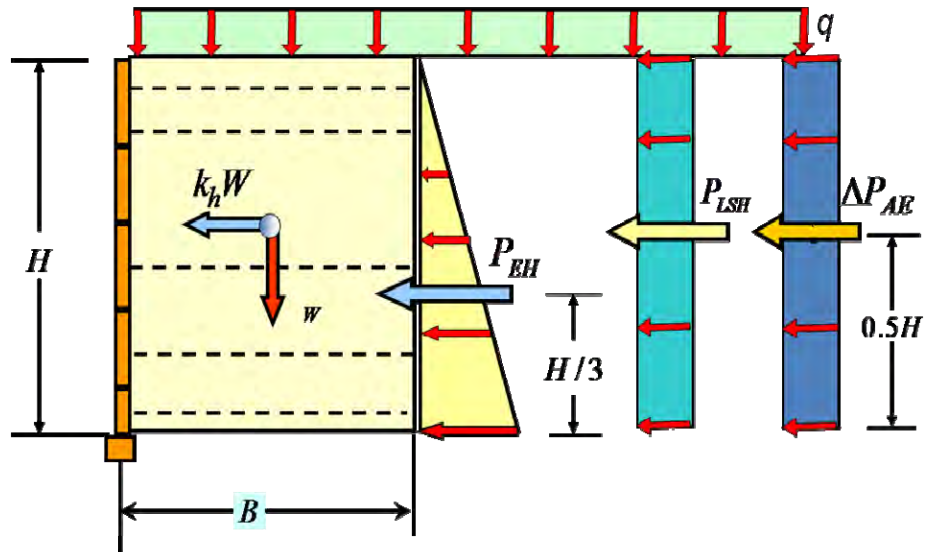
Figure D.1.2 Pressure diagram for MSE walls

Horizontal backslope with traffic surcharge

The active earth pressure coefficient (K_a) for vertical walls (i.e., walls with less than an 8 degree batter) with horizontal backslope is calculated from a simplified version of the Coulomb equation as presented in AASHTO (2007) Equation C11.10.6.2.1-1 and shown below:

$$K_a = \tan^2\left(45 - \frac{\phi'_f}{2}\right)$$

(D.1.1)

where: ϕ'_f = friction angle of retained fill.

The live load surcharge is not included over the backfill for evaluation of eccentricity, sliding, reinforcement pullout, or other failure mechanisms for which the surcharge load would increase resistance to failure. The stresses from concentrated vertical and

205

horizontal loads can be calculated using simplified approaches illustrated in Figures D.1.3 and D.1.4 respectively.
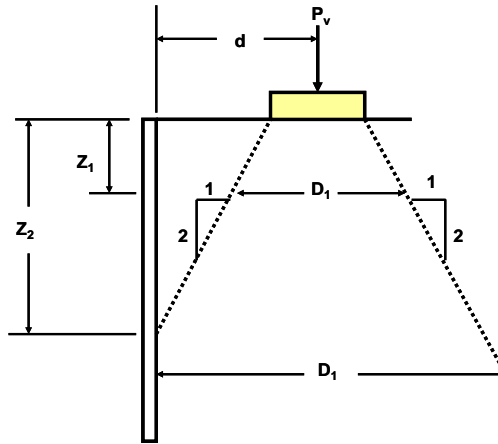
Figure D.1.3 Distribution of stress from concentrated vertical load

In Figure D.1.3, D_1= Effective width of applied load at any depth, calculated as shown above; B_f = Width of applied load. For footings which are eccentrically loaded (e.g., bridge abutment footings), set b_f equal to the equivalent footing width B' by reducing it by 2e', where e' is the eccentricity of the footing load (i.e., b_f-2e'); L_f = Length of footing; Q_v = Load per linear feet of strip footing; Q_v'= Load on isolated rectangular footing or point load; Z_f = Depth where effective width intersects back of wall face = $2d_1$-b_f
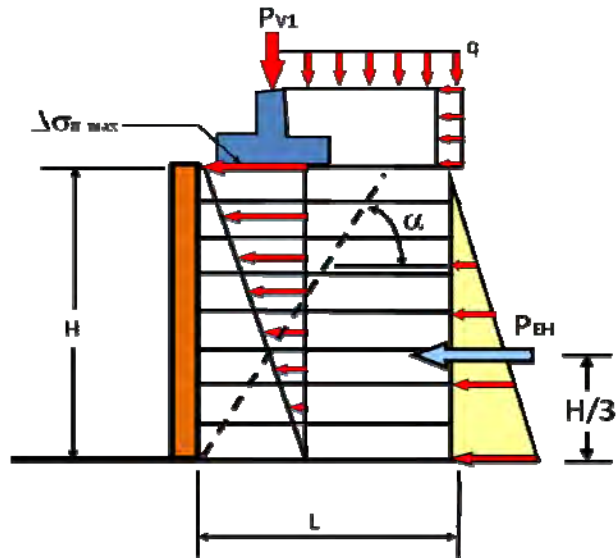
(a) Distribution of stress for internal stability calculations
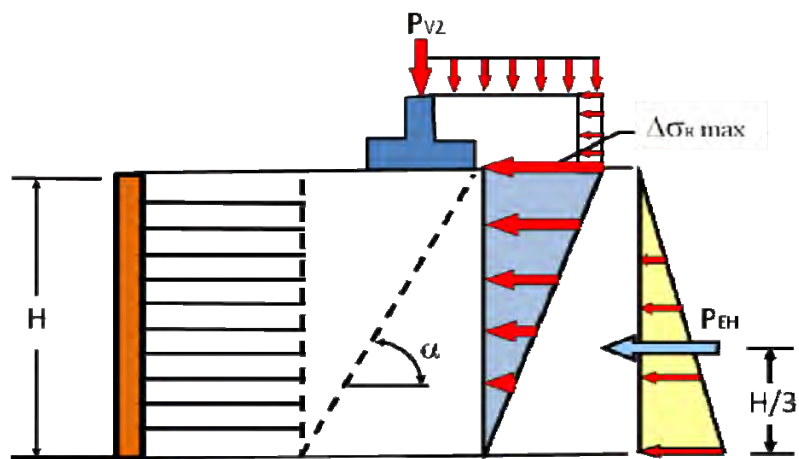
(b) Distribution of stress for external stability calculations

Figure D.1.4 Distribution of stress from concentrated horizontal loads for external and internal stability calculations

loping backslope

Figure D.1.5 shows the procedure to estimate the earth pressure acting on the back of the reinforced zone for the case of a sloping backslope. The active earth pressure coefficient (Ka) to determine the pressure on vertical walls with a surcharge slope is calculated as shown below:

$$K_a = \frac{\sin^2(\theta + \phi')}{\Gamma \sin^2 \theta \cdot \sin(\theta - \delta)} \tag{D.1.2}$$

Where: $\Gamma = \left[1 + \sqrt{\frac{\sin(\phi' + \delta) \cdot \sin(\phi' - \beta)}{\sin(\theta - \delta) \cdot \sin(\theta + \beta)}} \right]^2$; $\beta =$ Nominal slope of backfill behind wall (deg);

$\delta =$ Angle of wall friction (deg) ; $\phi' =$ friction angle of retained fill ; $\theta = 90^o$ for vertical wall
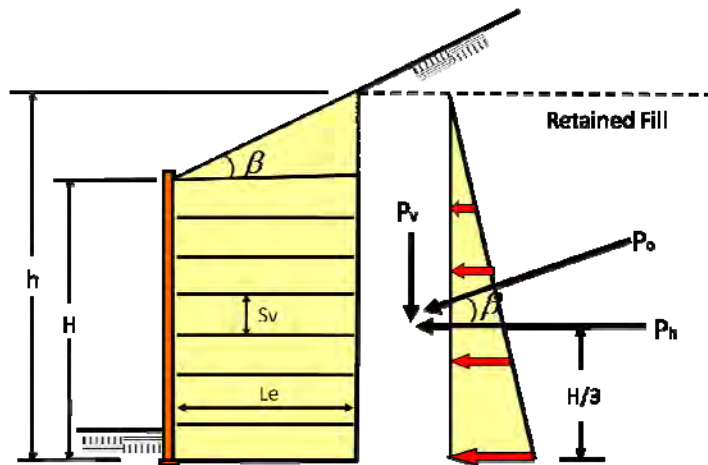
Figure D.1.5 Pressure diagram for MSE walls with sloping backslope

Broken backslope

Figure D.1.6 shows the procedure to estimate the earth pressure acting on the back of the reinforced zone for the case of a broken backslope.
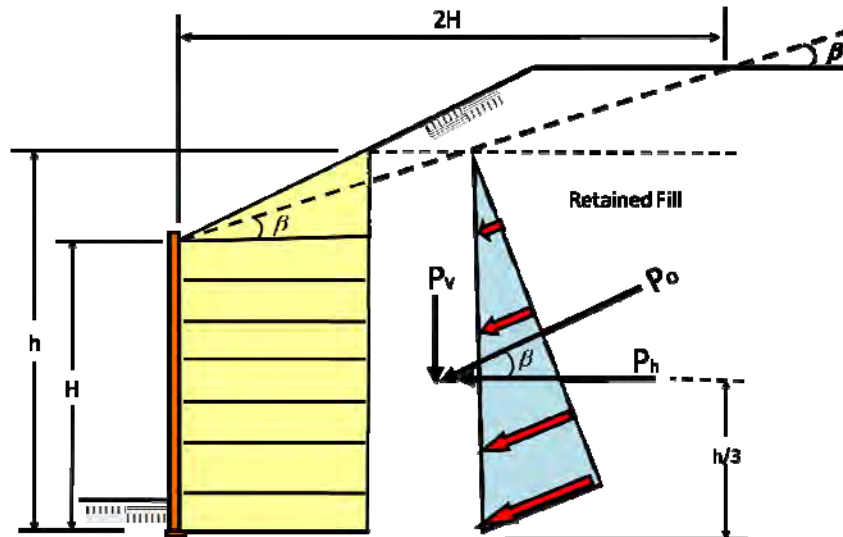
Figure D.1.6 Pressure diagram for MSE walls with broken backslope

Step 3 – Calculate Factored Loads

In this design step, the unfactored loads from Step 2 are multiplied by load factors to obtain the factored loads for each appropriate limit state. The load factors for the limit states are provided in Table D.1.2.

Table D.1.2 Load factors and load combinations

Limit State	EV	LS_V	LS_H	P_a	Probable USE
Strength I (a)	1.00	1.75	1.75	1.50	BC/EC/SL
Strength I (b)	1.35	1.75	1.75	1.50	BC (max. value)
Service I	1.00	1.00	1.00	1.00	Settlement
Extreme Event	1.00	1.00	1.00	1.00	BC/EC/SL

In Table D.1.2, EV: Dead load of Vertical Earth Backfill; LS_V: Surcharge (Vertical Component); LS_H: Horizontal Surcharge Load; P_a: Earth Pressure; BC: Bearing Capacity; EC: Eccentricity; SL: Sliding

Step 4 – Check Eccentricity

The eccentricity of the wall (e_B) can be calculated for each load group as:

$$e_B = \frac{B}{2} - X_o \qquad \text{(D.1.3)}$$

where: B = base width (length of reinforcement elements) and X_o = location of the resultant from the toe of the wall.

The parameter X_o is calculated as:

$$X_o = \frac{(M_{EV} - M_{HTOT})}{P_{EV}} \qquad \text{(D.1.4)}$$

where: M_{EV} = resisting moment due to factored vertical earth pressure calculated about the toe of the wall; M_{HTOT} = driving moment due to factored horizontal earth pressure from ground and from factored live load surcharge calculated about the toe of the wall; P_{EV} = factored resultant force from vertical earth pressure due to the weight of reinforced soil.

It should be noted that the effect of external loadings on the MSE mass, which increases sliding resistance, should only be included if the loadings are permanent. For example, live load traffic surcharges should be excluded.

210

For sloping backslope (Figure D.1.7) condition:

$$M_{EV} = P_{EV1} \frac{L}{2} + P_{EV2} \frac{2L}{3} + P_{EH} \sin \beta L$$

$$M_{HTOT} = P_{EH} \cos \beta \frac{h}{3}$$

where P_{EV2} = factored resultant force from earth pressure due to the weight of soil of sloping backslope; $P_{EH} \sin \beta$ = factored resultant force from vertical component of the earth pressure; $P_{EH} \cos \beta$ = factored resultant force from horizontal component of the earth pressure.

For eccentricity to be considered acceptable, the calculated location of the resultant vertical force (based on factored loads) should be within the middle one-half of the base width for soil foundations (i.e., e_{max} = B / 4) and middle three-fourths of the base width for rock foundations (i.e., . e_{max} = 3/8 B).
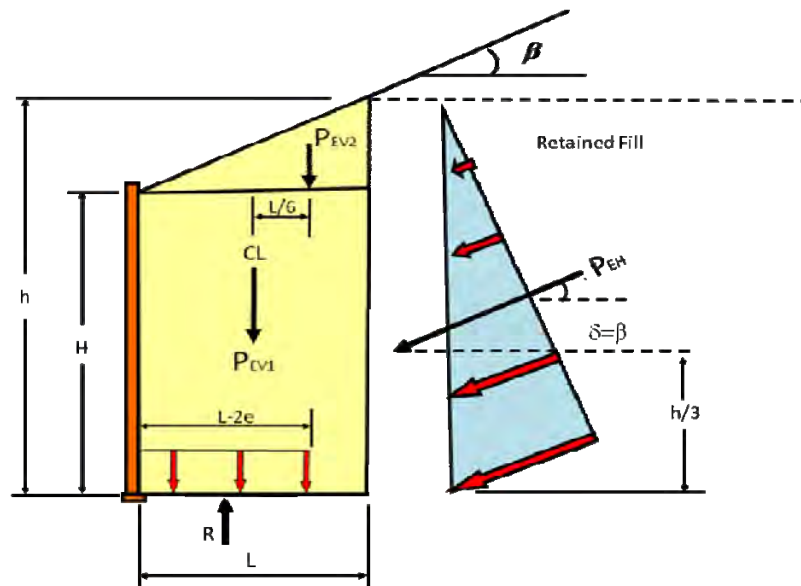
Figure D.1.7 Calculation of eccentricity for sloping backslope condition

Step 5 – Check Sliding Resistance

Sliding and overall stability usually govern the design of structures greater than about 30 ft high, structures constructed on weak foundation soils, or structures with a sloping surcharge. The live load surcharge is not considered as a stabilizing force when checking sliding. The driving forces in a sliding evaluation will generally include factored horizontal loads due to earth, water, seismic, and surcharge pressures and the resisting force is provided by the minimum shear resistance between the base of the MSE wall and foundation soil.

The factored resistance against failure by sliding (R_R) can be estimated by:

$$R_R = \phi R_n = \phi_\tau R_\tau + \phi_{ep} R_{ep} \tag{D.1.5}$$

Where, R_n = nominal sliding resistance against failure by sliding; ϕ_τ = resistance factor for shear resistance between soil and foundation; R_τ = nominal sliding resistance between soil and foundation; ϕ_{ep} = resistance factor for passive resistance (provided in Table 10.5.5.2.2-1 of AASHTO (2007)); R_{ep} = nominal passive resistance of soil available throughout design life.

It should be noted that any passive resistance provided by soil at the toe of the wall by embedment (i.e., $\varphi_{ep}\, R_{ep}$) is ignored due to the potential for the soil to be removed through natural or manmade processes during the service life of the structure. The shear strength of the facing system is also conservatively neglected in most cases.

If the soil beneath the wall is cohesionless, the nominal sliding resistance between soil and foundation is:

$$R_\tau = P_{EV} \tan \delta \qquad \text{(D.1.6)}$$

where P_{EV} = minimum factored vertical load for the strength limit state being considered and δ = coefficient of sliding friction at the base of the reinforced soil mass.

For continuous sheet reinforcement, δ is selected as the minimum of:

(1) friction angle of reinforced fill

(2) friction angle of foundation soil or

(3) interface friction angle between the reinforcement and soil

For discontinuous reinforcement (e.g., geogrid), δ is selected as the minimum value of (1) or (2).

Sliding resistance of the MSE wall is considered adequate if R_R is equal to or greater than the maximum factored horizontal earth pressure force from the ground and from the factored live load surcharge calculated in Step 3.

Step 6 – Check Bearing Resistance

Due to the flexibility of MSE walls and the inability of the flexible reinforcement to transmit moment, a uniform base pressure distribution is assumed over an equivalent footing width. Unlike the bearing resistance check for CIP walls founded on rock, the assumption of a uniform base pressure is used for MSE walls founded on rock (see Section 11.10.5.4 of AASHTO (2007)). The effect of eccentricity, load inclination, and live load surcharges must be included in this check. Effects of live load surcharges are included because they increase the loading on foundation.

The factored bearing resistance (q_R) is given as:

$$q_R = \phi q_n \tag{D.1.7}$$

where, ϕ = resistance factor (see AASHTO (2007) Table 11.5.6-1) (for walls with flexible footings such as MSE walls, this factor is 0.65 in AASHTO (2007)) and q_n = nominal bearing resistance (see AASHTO (2007) Equation 10.6.3.1.1.2a-1). The design example provided in Section 7.9 illustrates the evaluation of q_n for MSE walls.

To check whether the bearing resistance of the MSE wall is adequate, the q_R computed in Equation D.1.7 is compared against the following criterion:

$$q_R > q_{uniform}$$

Where, $q_{uniform}$ = vertical stress for walls on soil foundations, which is calculated assuming a uniform distribution of pressure over an effective base width ($B' = B - 2e$)

$$q_{uniform} = \frac{V_{TOT}}{B - 2e_B} \qquad \text{(D.1.8)}$$

Where, V_{TOT} = sum of all factored vertical forces acting at the base of the wall (e.g., weight of reinforced fill, live and dead load surcharges); B = base width (length of reinforcement strips); and e_B = eccentricity determined from Equation12-4; however for bearing resistance calculations, X_o is defined as:

$$X_o = \frac{(M_{VTOT} - M_{HTOT})}{V_{TOT}}$$

Where, M_{VTOT} = resisting moment due to factored total vertical load based on earth pressure and live load surcharge calculated about the toe of the wall and M_{HTOT} = driving moment due to factored lateral load based on earth pressure and live load surcharge calculated about the toe of the wall.

STRENGTH LIMIT STATES – INTERNAL STABILITY (Steps 7 through 11)

To be internally stable, the MSE structure must be coherent and self supporting under the action of its own weight and any externally applied forces. This is accomplished through stress transfer from the soil to the reinforcement. This interaction between the soil and reinforcement improves the tensile properties and creates a composite material with the following characteristics:

• Stress transfer between the soil and reinforcement takes place continuously along the reinforcement; and

• Reinforcements are distributed throughout the soil mass with a degree of regularity and must not be localized.

Step 7 – Select Location of Critical Failure Surface

When inextensible reinforcements are used, the soil deforms more than the reinforcement. Therefore, the soil strength in this case is measured at low strain. The critical failure surface for this reinforcement type is determined by dividing the reinforced zone into active and resistant zones with a bilinear failure surface as shown in Figure D.1.8(a).
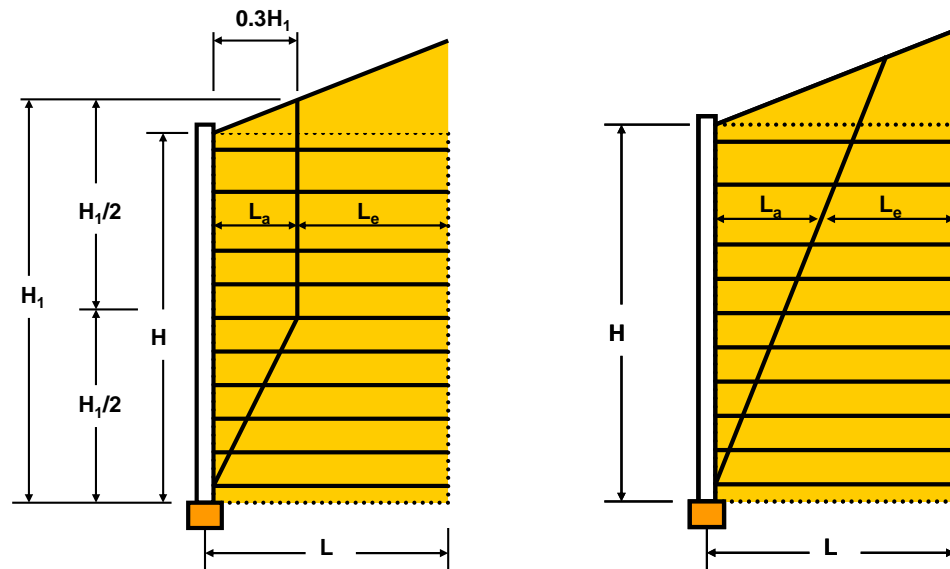
(a) Inextensible reinforcements   (b) Extensible reinforcements

Figure D.1.8 Potential failure surface for internal stability design of MSE wall

Step 8 – Calculated Factored Horizontal Stress

The purpose of this design step is to calculate the maximum factored horizontal stress. It is specifically noted that load factors are typically applied to unfactored loads, not to an unfactored stress (as it is in Eq. D.1.9) below. The AASHTO (2007) LRFD code, however, applies the "load" factor to the unfactored "stress" for this particular design calculation. The factored horizontal stress (σ_H) at each reinforcement level is based on AASHTO (2007) Equation 11.10.6.2.1-1:

$$\sigma_H = \gamma_P \left(\sigma_v k_r + \Delta \sigma_H \right) \tag{D.1.9}$$

Where, γ_P = the load factor for vertical earth pressure (*EV*), (1.35 per AASHTO (2007) Table 3.4.1-2); k_r = lateral earth pressure coefficient; σ_v = pressure due to resultant of gravity forces from soil self weight within and immediately above the reinforced wall backfill, and any surcharge loads present; $\Delta \sigma_H$ = horizontal stress at reinforcement level resulting from a concentrated horizontal surcharge load (see AASHTO (2007) Section 11.10.10.1))

Research studies have indicated that the maximum tensile force is primarily related to the type of reinforcement in the MSE mass, which, in turn, is a function of the modulus extensibility, and density of reinforcement.

Based on this research, a relationship between the type of the reinforcement and the overburden stress has been developed and is shown in (Figure D.1.9).

Figure D.1.9 was prepared by back analysis of the lateral stress ratio from available field data where stresses in the reinforcements have been measured and normalized as a function of an active earth pressure coefficient.
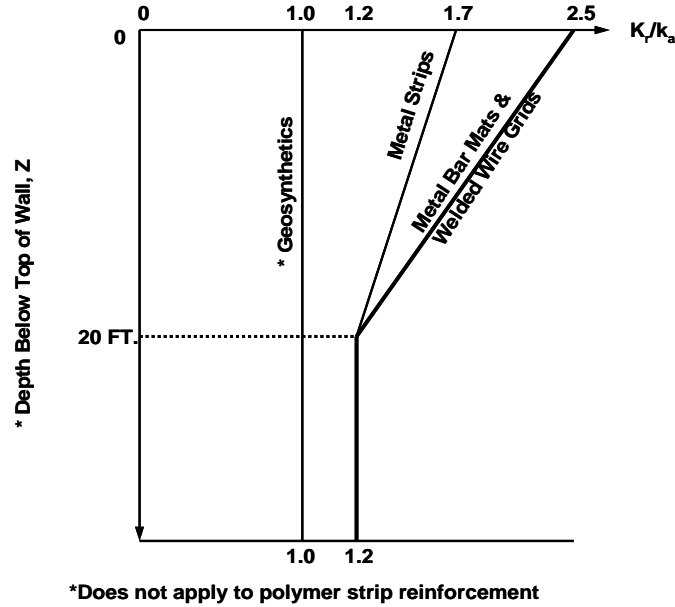
Figure D.1.9 Variation of the coefficient of lateral stress ratio with depth

For a vertical wall face (i.e., batters less than 8 degrees from vertical), the active earth pressure coefficient (K_a) is determined using Equation D.1.1. For wall face batters equal to or greater than 8 degrees from the vertical, the following simplified form of Coulomb equation as presented in AASHTO (2007) Equation C11.10.6.2.1-2 and shown below can be used:

$$K_a = \frac{\sin^2\left(\theta + \phi'\right)}{\sin^3\theta\left[1 + \dfrac{\sin\phi'}{\sin\theta}\right]^2} \tag{D.1.10}$$

Where, θ = inclination of the back of the facing as measured from the horizontal starting in front of the wall and ϕ' = friction angle of retained fill.

218

The value of K_a in the reinforced soil mass is assumed to be independent of all external loads, even sloping fills. If testing of the site-specific select backfill is not available, the value of ϕ_f used to compute the horizontal stress within the reinforced soil mass should not exceed 34°.

Once the value of K_a is known, the lateral earth pressure coefficient (k_r) (in Equation D.1.10) that is used to compute s_H at each reinforcement level is calculated as:

$$k_r = K/K_a \text{ (from Figure 12-9)} \times K_a \text{ (from Equation D.1.10)}$$

If present, surcharge load should be added into the estimation of σ_v. For sloping soil surfaces above the MSE wall section, the actual surcharge is replaced by a uniform surcharge equal to half of the height of the slope at the back of the reinforcements (Elias et al., 2001). For cases where concentrated vertical loads occur, refer to Figures D.1.3 and D.1.4 for computation of σ_v.

Step 9 – Calculate Maximum Factored Tensile Stress

The maximum tension in each reinforcement layer per unit width of wall (T_{max}) based on the reinforcement vertical spacing (S_v) is calculated as:

$$T_{max} = \sigma_H \cdot S_v \tag{D.1.11a}$$

where σ_H is the factored horizontal load calculated in step 8 using Equation D.1.9.
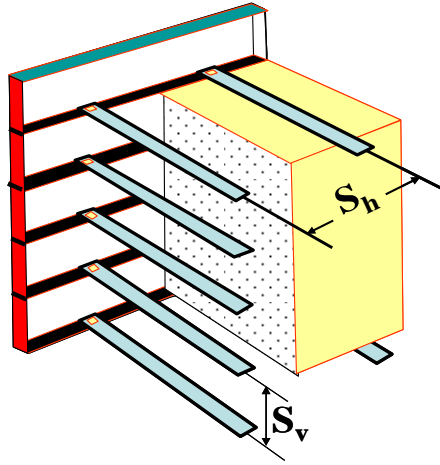
Figure D.1.10 Definition of b, S_h, and S_v

T_{max} may also be calculated at each level for discrete reinforcements (metal strips, bar mats, grids, etc.) per a defined unit width of reinforcement as:

$$T_{max-R} = \frac{\sigma_H \cdot S_v}{R_c}$$

(D.1.11b)

where, R_c = reinforcement coverage ratio = b/S_h (see Figure 12-10) (e.g., R_c = 1); b=gross width of the reinforcing element; S_h = center-to-center horizontal spacing between reinforcements .

Step 10 – Check Reinforcement Pullout Resistance

The purpose of this design step is to check the pullout resistance of the reinforcements. The resistance develops after the stress transfer between the soil and the reinforcement takes place, which occurs through two mechanisms:

(1) friction along the soil-reinforcement interface (Figure D.1.11a), and

(2) passive soil resistance or lateral bearing capacity developed along the

transverse sections of the reinforcement (Figure D.1.11b).

Stresses are transferred between soil and reinforcement by friction and/or passive resistance depending on reinforcement geometry.

Friction develops at locations where there is a relative shear displacement and corresponding shear stress between soil and reinforcement surface. Reinforcing elements where friction is important should be aligned with the direction of soil reinforcement relative movement. Examples of such reinforcing elements are steel strips, longitudinal bars in grids, geotextile, and some geogrid layers.

Passive resistance occurs through the development of bearing type stresses on "transverse" reinforcement surfaces normal to the direction of soil reinforcement relative movement. Passive resistance is generally considered to be the primary interaction for rigid geogrids, bar mat, and wire mesh reinforcements. The transverse ridges on "ribbed" strip reinforcement also provide some passive resistance.

The contribution of each transfer mechanism for a particular reinforcement will depend on the roughness of the surface (skin friction), normal effective stress, grid opening dimensions, thickness of the transverse members, and elongation characteristics of the reinforcement.

Equally important for interaction development are the soil characteristics, including grain size and grain size distribution, particle shape, density, water content, cohesion, and stiffness. The primary function of reinforcements is to restrain soil deformations. In

doing so, stresses are transferred from the soil to the reinforcement. These stresses are carried by the reinforcement in two ways: in tension or in shear and bending.
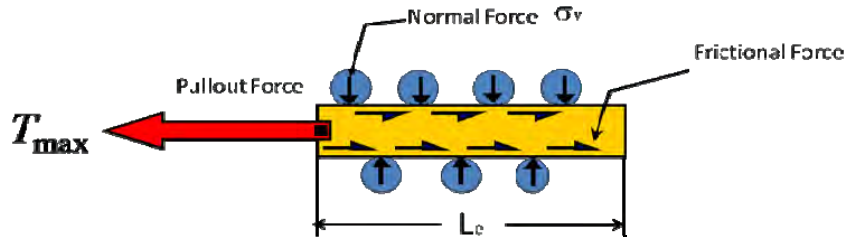
(a) By friction
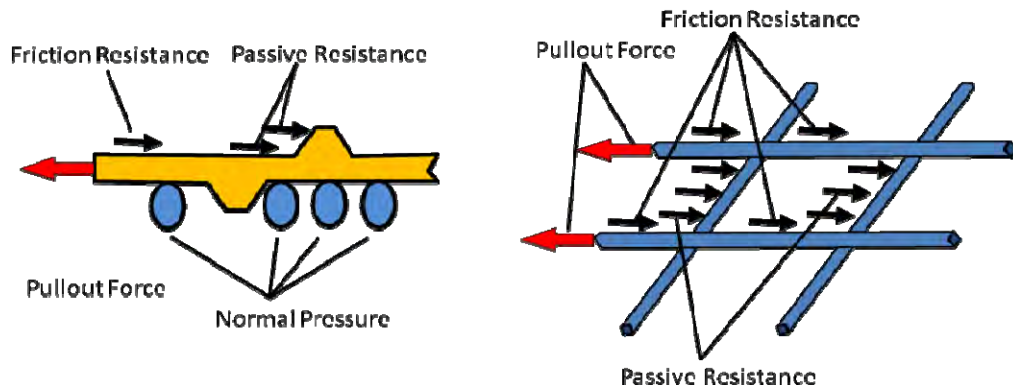
(b) By passive resistance

Figure D.1.11. Mechanisms of pullout resistance

The unfactored pullout resistance (P_r) of the reinforcement per unit width of reinforcement is estimated as:

$$P_r = F^* \alpha \sigma_v \tag{D.1.12}$$

Parameters in Equation D.1. 12 are defined in Equation D.1.14.

222

In this design step, the reinforcement pullout resistance is evaluated at each reinforcement level of the MSE wall. The required total length for reinforcement to generate appropriate pullout resistance for each level is calculated and then compared against the total reinforcement length initially estimated in design step 1. The initially estimated total reinforcement length may have to be adjusted based on the required length calculated in this step. The total length of reinforcement (L) required for internal stability is determined as:

$$L = L_e + L_a \qquad\qquad \text{(D.1.13)}$$

Where, L_e = required length of reinforcement in resisting zone (i.e., beyond the potential failure surface) and L_a = remainder length of the reinforcement.

Estimating L_e

The length of reinforcement in the resisting zone (L_e) is determined using the following equation (see AASHTO (2007) Equation 11.10.6.3.2-1):

$$L_e \geq \frac{T_{max}}{\phi F^* \alpha \sigma_v C R_c} \qquad\qquad \text{(D.1.14)}$$

Where, L_e = length of reinforcement in resisting zone (ft.); T_{max} = applied factored load (kips/ft.); ϕ = resistance factor for reinforcement pullout; F^* = pullout friction factor; α = scale effect correction factor (see Table D.1.3); σ_v= unfactored vertical stress at the reinforcement level in the resistant zone (ksf); C = overall reinforcement surface area geometry factor based on the gross perimeter of the reinforcement and is equal to 2 for

strip, grid and sheet-type reinforcements, i.e., two sides; R_c = reinforcement coverage ratio

Correction Factor (α)

The correction factor (α) depends primarily upon the strain softening of the compacted granular backfill material, the extensibility, and the length of the reinforcement. For inextensible reinforcement, α is approximately 1, but it can be substantially smaller than 1 for extensible reinforcements. The α factor can be obtained from pullout tests on reinforcements with different lengths or derived using analytical or numerical load transfer models which have been "calibrated" through numerical test simulations. In the absence of test data, $\alpha = 0.8$ for geogrids and $\alpha = 0.6$ for geotextiles (extensible sheets) is recommended (Elias et al., 2001).

Table D.1.3 Typical values for α

Reinforcement type	Default value for α
All Steel Reinforcements	1.0
Geogrids	0.8
Geotextiles	0.6

Pullout Friction Factor (F^*)

The pullout friction factor can be obtained most accurately from laboratory or field pullout tests performed with the specific material to be used on the project (i.e., select backfill and reinforcement). Alternatively, F^* can be derived from empirical or

theoretical relationships developed for each soil-reinforcement interaction mechanism and provided by the reinforcement supplier. For any reinforcement, F^* can be estimated using the general equation:

$F^* =$ Passive Resistance + Frictional Resistance, or

$$F^* = F_q \times \alpha_\beta + tan\, \rho \qquad \text{(D.1.15)}$$

Where, F_q = the embedment (or surcharge) bearing capacity factor; $;\alpha_\beta$ = a bearing factor for passive resistance which is based on the thickness per unit width of the bearing member; and ρ = the soil-reinforcement interaction friction angle.

Equation D.1.15 represents systems that have both the frictional and passive resistance components of the pullout resistance. In certain systems, however, one component is much smaller than the other and can be neglected for practical purposes.

In absence of site-specific pullout testing data, it is reasonable to use these semi-empirical relationships in conjunction with the standard specifications for backfill to provide a conservative evaluation of pullout resistance.

For steel ribbed reinforcement, F^* is commonly estimated as:

$$F^* = tan\, \rho = 1.2 + log\, C_u \text{ at the top of the structure} = 2.0 \text{ maximum} \qquad \text{(D.1.16)}$$

$$F^* = tan\, \varphi \text{ at a depth of 20 ft. and below} \qquad \text{(D.1.17)}$$

Where, ρ = interface friction angle mobilized along the reinforcement; f = wall fill peak friction angle; and C_u = uniformity coefficient of the backfill (D_{60}/D_{10}).

If the specific C_u for the wall backfill is unknown during design, a C_u of 4 should be assumed (i.e., $F^* = 1.8$ at the top of the wall), for backfills.

For steel grid reinforcements with transverse spacing $(S_t) > 6$ in., F^* is a function of a bearing or embedment factor (F_q), applied over the contributing bearing factor (α_β), as follows:

$$F^* = F_q \, \alpha_\beta = 40 \, \alpha_\beta = 40 \, (t/2S_t) = 20 \, (t/S_t) \text{ at the top of the structure} \qquad (D.1.18)$$

$$F^* = F_q \, \alpha_\beta = 20 \, \alpha_\beta = 20 \, (t/2S_t) = 10 \, (t/S_t) \text{ at a depth of 20 ft and below} \qquad (D.1.19)$$

where t is the thickness of the transverse bar. St shall be uniform throughout the length of the reinforcement, rather than having transverse grid members concentrated only in the resistant zone.

For geosynthetic (i.e., geogrid and geotextile) sheet reinforcement, the pullout resistance is based on a reduction in the available soil friction with the reduction factor often referred to as an interaction factor (C_i). In the absence of test data, the F^* value for geosynthetic reinforcement should conservatively be estimated as:

$$F^* = 0.67 \, tan \, \varpi' \qquad (D.1.20)$$

When used in the above relationships, f is the peak friction angle of the soil which, for MSE walls using select granular backfill, is taken as 34 degrees unless project specific test data substantiates higher values. The relationship between F^* and depth below the top of wall for different reinforcement types is summarized in Figure D.1.12.
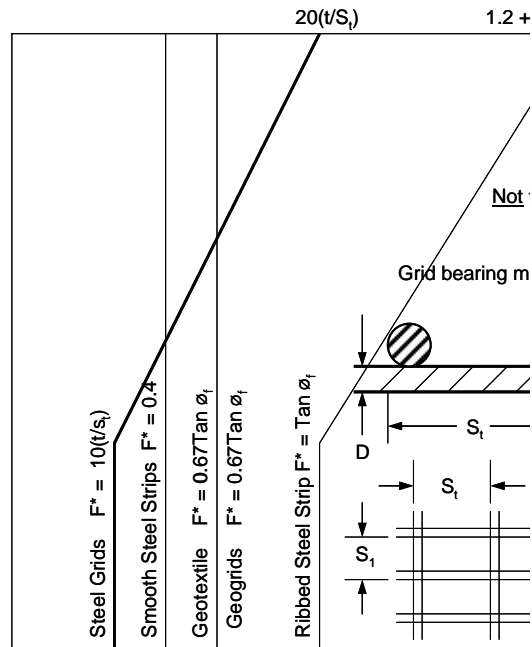
Figure D.1.12 Typical values for F^*

Estimating L_a

The La is obtained from Figure D.1.8 for simple structures not supporting concentrated external loads such as bridge abutments. Based on this figure, the following relationships can be obtained for La:

• For MSE walls with extensible reinforcement, vertical face, and horizontal backfill:

$$L_a = (H - Z) \ tan \ (4 - \varphi'/2) \tag{D.1.21}$$

where Z is the depth to the reinforcement level.

• For walls with inextensible reinforcement from the base up to H/2:

$$L_a = 0.6 \ (H\text{-}Z) \tag{D.1.22}$$

• For the upper half of a wall with inextensible reinforcements:

$$L_a = 0.3H \tag{D.1.23}$$

For ease of construction, based on the maximum total length required, a final uniform reinforcement length is commonly chosen. However, if internal stability controls the length, it could be varied from the base, increasing with the height of the wall to the maximum length requirement based on a combination of internal and maximum external stability requirements. See Chapter 5 of Elias et al. (2001) for additional guidance.

Step 11 – Calculate Long-Term Reinforcement Design Strength

In this design step, the maximum factored tensile stress in each reinforcement layer (T_{max}, which is calculated in design step 9) is compared to the nominal long-term reinforcement design strength (see AASHTO (2007) Equation 11.10.6.4.1-1) as presented in Equation 7-24 below.

$$T_{max} \leq \phi T_{al} R_c \tag{D.1.24}$$

Where, ϕ = resistance factor for tensile rupture (see Table D.1.4)

Table D.1.4. Resistance factors for tensile resistance

	Strip Reinforcement	
Metallic Reinforcement and Connectors	Static Loading	0.75
	Combined Static/Earthquake Loading	1.00
	Grid Reinforcement[1]	
	Static Loading	0.65
	Combined Static/Earthquake Loading	0.85
Geosynthetic Reinforcement and Connectors	Static Loading	0.90
	Combined Static/Earthquake Loading	1.20

Note: [1]Applies to grid reinforcements connected to a rigid facing element, e.g., a concrete panel or block.

R_c = reinforcement coverage ratio as defined in Equation 12-11b and T_{al} = nominal long-term reinforcement design strength.

The nominal long-term reinforcement design strength (T_{al}) for LRFD is computed for inextensible and extensible reinforcements as presented below.

T_{al} for Inextensible Reinforcements – AASHTO (2007) Equation 11.10.6.4.3a-1:

$$T_{al} = \frac{A_c F_y}{b}$$
(D.1.25)

Where, F_y = minimum yield strength of steel; b = unit width of sheet, grid, bar, or mat; and A_c = design cross sectional area corrected for corrosion loss (A_c for strips and bars are defined below)

The lower resistance factor of 0.65 for grid reinforcement (as compared to a resistance factor of 0.75 for strip reinforcement) accounts for the greater potential for local overstress due to load nonuniformities for steel grids than for steel strips or bars.

A_c for strips is determined as:

$$A_c = b \, t_c = b \, (t_n - t_s) \tag{D.1.26}$$

Where, b = unit width of sheet, grid, bar, or mat; t_c = thickness at end of design life (See Figure D.1.13); t_n = thickness at end of construction; and t_s = sacrificial thickness of metal expected to be lost by uniform corrosion during the service life of the structure (see discussion on corrosion rates below).
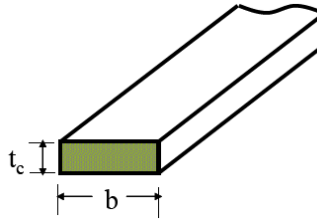
Figure D.1.13. Cross section area for strip

When estimating ts, it may be assumed that equal loss occurs from the top and bottom of the strip.

A_c for bars is determined as:

$$A_c = N_b \, (\pi D^{*2}/4) \tag{D.1.27}$$

Where, N_b = No. of bars per unit width b and D^* = Bar diameter after corrosion loss (Figure D.1.14).

When estimating D^*, it may be assumed that corrosion losses occur uniformly over the area of the bar.
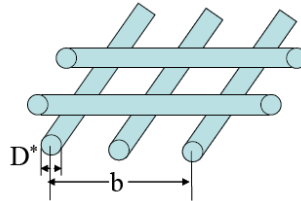
Figure D.1.14 Cross section area for bars

Corrosion Rates

The corrosion rates presented below are suitable for conservative design. These rates assume a mildly corrosive backfill material having the controlled electrochemical property limits that are discussed under electrochemical properties for reinforced fills.

   Corrosion Rates - mildly corrosive backfill

      For corrosion of galvanization on each side

      • 0.58 mil./yr/side (first 2 years) and

      • 0.16 mil./yr/side (thereafter)

      For corrosion of residual carbon steel on each side

      • 0.47 mil./yr/side (after zinc depletion)

Based on these rates, complete corrosion of galvanization with the minimum required thickness of 3.4 mil. (AASHTO M 111) is estimated to occur during the first 16 years and a carbon steel thickness or diameter loss of 0.055 in. to 0.08 in. would be anticipated over the remaining years of a 75 to 100 year design life, respectively. The designer of an MSE structure should also consider the potential for changes in the reinforced backfill

environment during the structure's service life. In certain parts of the United States, it can be expected that deicing salts might cause such an environment change. For this problem, the depth of chloride infiltration and concentration are of concern.

For permanent structures directly supporting roadways exposed to deicing salts, limited data indicate that the upper 8 ft of the reinforced backfill (as measured from the roadway surface) are affected by higher corrosion rates not presently defined. Under these conditions, it is recommended that a 30 mil (minimum) geomembrane be placed below the road base and tied into a drainage system to mitigate the penetration of the deicing salts in lieu of higher corrosion rates. Tal for Extensible Reinforcements – AASHTO (2007) Equation 11.10.6.4.3b-1:

$$T_{al} = \frac{T_{ult}}{RF} \tag{D.1.28}$$

where, T_{ult} = minimum average roll value ultimate tensile strength. T_{ult} may be obtained from ultimate (or yield) tensile strength wide strip test (ASTM D4595) for geotextiles and wide strip (ASTM D4595) or single rib test (GRI:GG1) for geogrids based on minimum average roll value (MARV) for the product; and RF = combined strength reduction factor to account for potential long-term degradation due to installation damage, creep and chemical aging. Determined as $RF = RF_{ID} \times RF_{CR} \times RF_D$ where, RF_{ID} = strength reduction factor to account for installation damage to reinforcement; RF_{CR} = strength reduction factor to prevent long-term creep rupture of reinforcement; and RF_D = strength reduction factor to prevent rupture of reinforcement due to chemical and biological degradation.

According to AASHTO (2007) Section 11.10.6.4.2b, values for RF_{ID}, RF_{CR}, and RF_D shall be determined from product specific test results.

Reduction Factor RF_{ID}

RF_{ID} can range from 1.05 to 3.0, depending on backfill gradation and product mass per unit weight. Even with product specific test results, the minimum reduction factor shall be 1.1 to account for testing uncertainties. The placement and compaction of the backfill material against the geosynthetic reinforcement may reduce its tensile strength. The level of damage for each geosynthetic reinforcement is variable and is a function of the weight and type of the construction equipment and the type of geosynthetic material. The installation damage is also influenced by the lift thickness and type of soil present on either side of the reinforcement. Where granular and angular soils are used for backfill, the damage is more severe than where softer, finer, soils are used. For a more detailed explanation on the RF_{ID} factor, see FHWA-NHI-00-044 "Corrosion/Degradation of Soil Reinforcements for Mechanically Stabilized Earth Walls and Reinforced Soil Slopes," (Elias, 2000).

To account for installation damage losses of strength where full-scale product-specific testing is not available, Table D.1.5 may be used with consideration of the project specified backfill characteristics. In absence of project specific data the largest indicated reduction factor for each geosynthetic type should be used.

Table D.1.5 Installation damage reduction factors

		Reduction Factor (RF$_{ID}$)	
No.	Geosynthetic	Type 1 Backfill Max. Size 4 in. D50 about 1.2 in	Type 2 Backfill Max. Size 0.75 in. D50 about 0.03 in
1	HDPE uniaxial geogrid	1.20-1.45	1.10-1.20
2	PP biaxial geogrid	1.20-1.45	1.10-1.20
3	PVC coated PET geogrid	1.30-1.85	1.10-1.30
4	Acrylic coated PET geogrid	1.30-2.05	1.20-1.40
5	Woven geotexiles (PP&PET) [1]	1.40-2.20	1.10-1.40
6	Non woven geotexiles (PP&PET) [1]	1.40-2.50	1.10-1.40
7	Slit film woven PP geotextile [1]	1.60-3.00	1.10-2.00

(1) Minimum weight 7.9 oz/yd^2

Reduction Factor RF$_{CR}$

RF_{CR} is obtained from long-term laboratory creep testing as detailed in Elias et al. (2001). This reduction factor is required to limit the load in the reinforcement to a level known as the creep limit that will preclude creep rupture over the life of the structure. Creep in itself does not degrade the strength of the polymer. Creep testing is essentially a constant load test on multiple product samples, loaded to various percentages of the ultimate product load, for periods of up to 10,000 hours. The creep reduction factor is the ratio of the ultimate load to the extrapolated maximum sustainable load (i.e., creep limit) within the design life of the structure (e.g., several years for temporary structures, 75 to 100 years for permanent structures). Typical reduction factors as a function of polymer type are indicated in Table D.1.6.

Table D.1.6. Creep reduction factors (RF_{CR})

Polymer Type	RF_{CR}
Polyster	1.6 to 2.5
Polypropylene	4.0 to 5.0
Polyethylene	2.6 to 5.0

Reduction Factor RF_D

RF_D is dependent on the susceptibility of the geosynthetic to be attacked by microorganisms, chemicals, thermal oxidation, hydrolysis and stress cracking and can vary typically from 1.1 to 2.0. Even with product specific test results, the minimum reduction factor shall be 1.1. A protocol for testing to obtain this reduction factor has been described in Elias and Christopher (1997). Current research suggests the following information regarding RF_D for polyster and polyolefin geosynthetics.

• Polyster (PET) geosynthetics are recommended for use in environments characterized by $3 < pH < 9$, only. The following reduction factors for PET aging (RFD) are presently indicated for a 100-year design life in the absence of product specific testing as presented in Table D.1.7.

• Polyolefin geosynthetics have a unique and proprietary blend of antioxidants; product specific testing is required to determine the effective life span of protection at the in-ground oxygen content. Limited data suggests that certain antioxidants are effective for up to 100 years in maintaining strength for in-ground use.

Table D.1.7 Aging reduction factors (RF_D)

No.	Product	Reduction factor (RFD)	
		$5 \le pH \le 8$	$5 \le pH \le 8$ $5 \le pH \le 8$
1	Geotextiles $M_n<20,000$, $40<CEG<50$	1.6	2.0
2	Coated geogrids, Geotextiles $M_n>25,000$, $CEG<30$	1.15	1.3

M_n=number average molecular weight   CEG=carboxyl end group

*Use of materials outside the indicated pH or molecular property range required specific product testing

SERVICE LIMIT STATES (Steps 12)

Step 12 – Check Overall Stability

This design step is performed to check the overall stability of the wall. Overall stability is determined using rotational or wedge analyses, as appropriate, which can be performed using a classical slope stability analysis method. Computer programs that directly incorporate reinforcement elements (e.g., ReSSA) are available for these analyses. Generally, the reinforced soil wall is considered as a rigid body and only failure surfaces completely outside a reinforced mass (e.g., global failure planes) are considered. For simple structures with rectangular geometry, relatively uniform reinforcement spacing, and a near vertical face, compound failure planes (e.g., passing both through the unreinforced and reinforced zones) will not generally be critical. However, if complex conditions exist such as changes in reinforced soil types or reinforcement lengths, high

surcharge loads, sloping faced structures, significant slopes at the toe or above the wall, or stacked structures, compound failures must be considered.

The evaluation of overall stability of earth slopes with or without a foundation unit should be investigated at the Service 1 Load Combination and an appropriate resistance factor.

Commonly used slope stability programs can be used to conduct this evaluation. In lieu of better information, the resistance factor (φ) is defined in AASHTO (2007) Section 11.6.2.3 as:

- $\varphi = 0.75$; where the geotechnical parameters are well defined, and the slope does

   not support or contain a structural element; and

- $\varphi = 0.65$; where the geotechnical parameters are based on limited information,

   or the slope contains or supports a structural element

The evaluation of overall stability should be performed with reasonable estimates of long-term water pressures acting on the wall. If the evaluation of overall stability does not indicate a satisfactory result then the reinforcement length may have to be increased or the foundation soil may have to be improved. The design must be revised according to these changes. It should be noted that wall designs that are performed by MSE wall suppliers typically will not include the overall stability check.

D.2 MSE Wall Example Problem 1

Step 1: Initial Wall Geometry

Design wall height (H)

In this design, the wall height is selected as 27.5 ft including a 2.5 ft embedment depth. The minimum required embedment depth for a 25 ft high wall is 1.25 ft. For a complete design, the selected design wall height would also be evaluated based on overall stability, bearing resistance, and scour potential.

Minimum reinforcement length (L)

The minimum reinforcement length should be greater of 0.7H or 6 ft. Therefore, as a preliminary estimate, L is selected to be:

$$L = 0.7 \times 27.5 \text{ ft} = 19.25 \text{ ft (use 20.0 ft)}$$
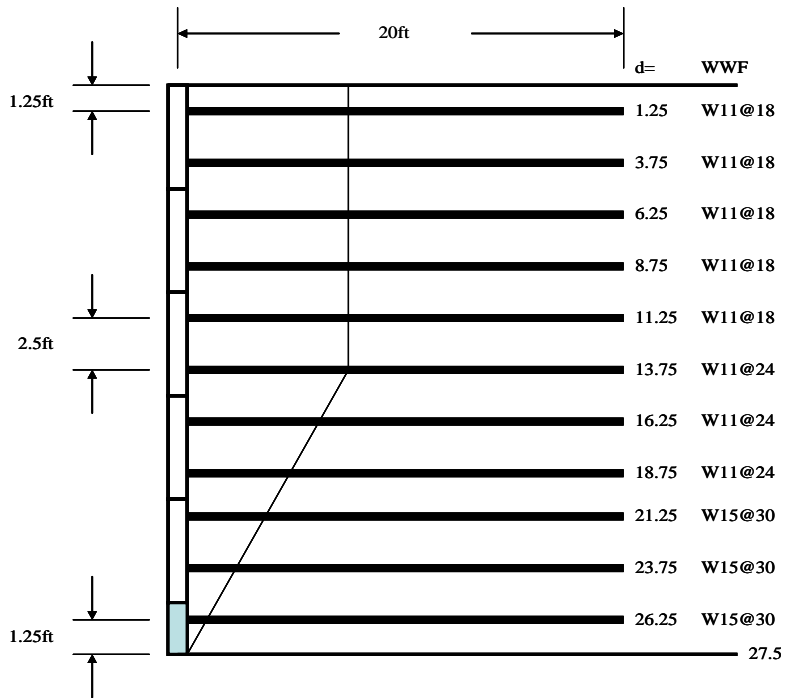
Figure D.2.1 Wall section with embedded rebar.

d=	WWF
1.25	W11@18
3.75	W11@18
6.25	W11@18
8.75	W11@18
11.25	W11@18
13.75	W11@24
16.25	W11@24
18.75	W11@24
21.25	W15@30
23.75	W15@30
26.25	W15@30
27.5	
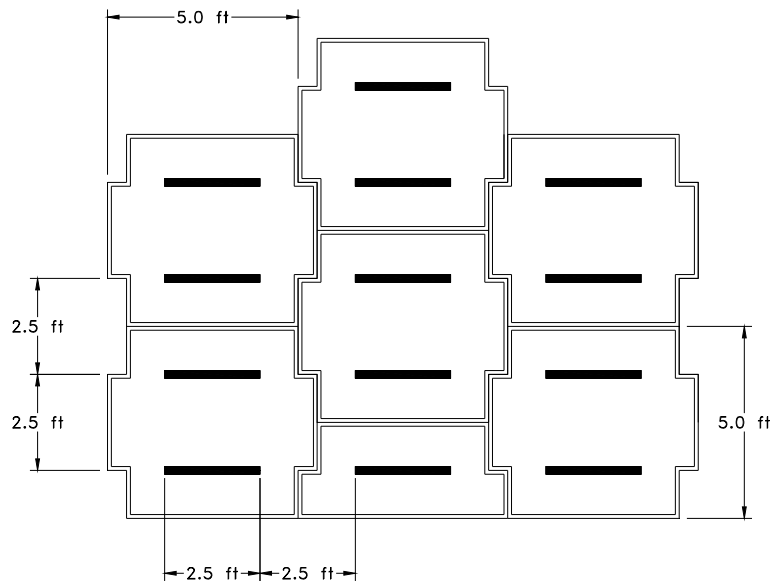
Figure D.2.2 Wall face panels and spacing between reinforcements

239

Step 2: Estimate Unfactored Loads

Vertical Loads

Vertical Earth Pressure (EV)

The weight of the reinforced soil backfill is:

$$P_{EV} = H\,L\gamma_r = (27.5\,ft)(20.0\,ft)(120\,pcf)$$
$$P_{EV} = 66.0\,kips\,/\,ft\;length\,of\;wall$$

Surcharge Load (LS)

The vehicular surcharge load on the wall is calculated using an equivalent

height of soil (h_{eq}). AASHTO (2007) provides a table summarizing h_{eq}

based on the wall height (Table E-1).

Table D.2.1 Equivalent height of soil for vehicular loading (after AASHTO, 2007)

Wall Height (ft)	h_{eq}
5	5
10	3.5
≥ 20	2

Based on Table 1 above, h_{eq} for 27.5 ft high wall is 2 ft. Therefore the vertical load due to

vehicular loading can be estimated as:

$$P_{LSV} = (\gamma_r)(h_{eq})(L) = 120\,pcf \times 2\,ft \times 20.0\,ft = 4.8\,kips\,/\,length\,of\;wall$$

It should be noted that the traffic load surcharge over the reinforced zone is not considered for checks on sliding, eccentricity, or reinforcement pullout, but is considered in evaluation of bearing resistance, overall stability, and reinforcement tensile resistance.

Horizontal Loads

The active earth pressure coefficient K_a is:

$$K_a = \tan^2 \left(45 - \frac{\phi_f^{'}}{2} \right)$$

Where $\phi_f^{'} = 34^{\circ}$, therefore $K_a = 0.283$

Horizontal Earth Pressure (EH)

$$P_{EH} = 0.5\,(\gamma_r)(H^2)\,K_a = (0.5)(120\,pcf)(27.5\,ft)^2(0.283)$$
$$P_{EH} = 12.84\,kips\,/\,ft\,length\,of\,wall$$

Surcharge Load (LS)

The horizontal load due to surcharge is computed based on the uniform increase in horizontal earth pressure due to traffic load surcharge (Δp) as:

$$\Delta p = (k_a)(\gamma_r)(h_{eq})$$
$$\Delta p = (0.283)(120\,pcf)(2\,ft) = 0.068\,ksf$$

For a 27.5 ft high wall, the resultant of the live load surcharge horizontal earth pressure (P_{LSH}), acting on the reinforced soil mass becomes:

$$P_{LSH} = (\Delta p)(H)$$
$$P_{LSH} = 0.068\,ksf \times 27.5\,ft = 1.87\,kips\,/\,ft\;length\,of\,wall$$

Tables D.2.2 and D.2.3 summarize the unfactored vertical and horizontal loads, respectively. The moment arms about the toe of the wall for each of these loads are also summarized.

Table D.2.2 Unfactored vertical loads and moment arm for design example

Load	V (kips/ft)	Moment arm about toe (ft)
P_{EV}	66.0	10.0
P_{LSV}	4.8	10.0
Total	60.8	

Table D.2.3 Unfactored horizontal loads and moment arm for design Example

Load	H (kips/ft)	Moment Arm About Toe (ft)
$P_{EH} = P_{aH}$	12.84	9.17
P_{LSH}	1.87	13.75
Total	14.06	

Step 3: Calculate Factored Loads

The load combinations and load factors used in this example are summarized below and in Table D.2.2 Factored vertical and horizontal loads can be determined based on multiplying unfactored loads (summarized in Tables D.2.2 and D.2.3) with load factors in Table D.2.4. The factored loads are provided in Tables D.2.4 and D.2.5.

Table D.2.4 Factored vertical loads and moments

Group	P_{EV} (kips/ft)	P_{LSV} (kips-ft/ft)	V_{TOT} $= P_{EV} + P_{LSV}$ (kips-ft/ft)	Moment Arm about Toe (ft)	M_{EV} (kips-ft/ft)	M_{VTOT} (kips-ft/ft)
Unfactored	66.0	4.8	70.8	10.0	660.0	708.0
Strength I (a)	66.0	8.4	74.4	10.0	660.0	744.0
Strength I (b)	89.1	8.4	97.5	10.0	891.0	975.0
Service I	66.0	4.8	70.8	10.0	660.0	708.0

Table D.2.5 Factored horizontal loads and moments

Group	P_{EH} (kips/ft)	Moment Arm About Toe for P_{EH} (ft)	P_{LHS} (kips/ft)	Moment Arm About Toe for PLSH (ft)	H_{TOT} $= P_{EH} +$ P_{LSH} (kips/ft)	M_{HTOT} (kips-ft/ft)
Unfactored	12.84	9.17	1.87	13.75	14.71	143.46
Stength I (a)	19.26	9.17	3.27	13.75	22.53	219.94
Stength I (b)	19.26	9.17	3.27	13.75	22.53	219.94
Service I	12.84	9.17	1.87	13.75	14.71	143.46

Step 4: Check Eccentricity

The eccentricity check is summarized in Table D.2.6.

Table D.2.6 Summary for eccentricity check

Group	P_{EV} (kips/ft)	M_{EV} (kips-ft/ft)	M_{HTOT} (kips-ft/ft)	X_o (ft)	e_B(ft)	Eccentricity check $(e_B < e_{max})$
Strength I (a)	66.0	660.0	219.94	6.67	3.33	O.K.
Strength I (b)	89.1	891.0	219.94	7.53	2.47	O.K.
Service I	66.0	660.0	143.46	7.83	2.17	O.K.

Where, X_o = Location of the resultant from toe of wall = $(M_{EV} - M_{HTOT})/P_{EV}$; B = Base width = Length of reinforcement strips = 20.0 ft; e_B = Eccentricity = B/2 - X_o

The location of the resultant must be in the middle half of the base.

$$e_{max} = B/4 = 20.0 \text{ ft}/4 = 5.0 \text{ ft}$$

For all cases, $e_B < e_{max}$; therefore, the design is adequate with respect to eccentricity.

Step 5: Check Sliding Resistance

The passive resistance of the foundation material is neglected when checking the sliding resistance of MSE walls. Therefore, the factored resistance against failure by sliding (R_R) is computed as:

$$R_R = \phi_r \, R_r$$

where: $\phi_r = 1.0$ and $R_r = V \tan \delta$ where $V = P_{EV}$ and $\tan \delta = \tan \phi_f$

Therefore: $R_n = P_{EV} \tan \phi_f$

P_{EV} is obtained from Table D.2. 5 as the minimum vertical factored load for the strength limit state (i.e., using $\gamma_{EV} = 1.00$)

$\phi_f = 30^o$ (It is assumed in this example that the friction angle of reinforced fill is less than the friction angle of the foundation and the interface friction angle between reinforcement and soil)

$$R_n = (66.0 \text{ kips/ft }) (\tan 30) = (66.0 \text{ kips/ft }) (0.58)$$

$$R_n = 38.1 \text{ kips/ft length of wall}$$

Applying the resistance factor ϕ to R_n, the factored sliding resistance is:

$$R_R = (1.0) \, (38.1 \text{ kips/ft}) = 38.1 \text{ kips/ft length of wall}$$

For the wall to have adequate sliding resistance:

$$R_R \text{ must be} > H_{TOT} \text{ (maximum)}$$

(H_{TOT} is obtained from Table D.2.6 as the maximum total horizontal factored load for the strength limit state (i.e., 22.53 kips/ft))

In this design example: CDR Static = (R_R = 38.1kips/ft) / (H_{TOT} = 22.53 kips/ft) = 1.69, therefore, sliding resistance is adequate.

Table D.2.7 Program results – direct sliding for given layout

(Along reinforced and foundation soils interface: CDR Static = 1.69)

#	Metal Mats Elevation [ft]	Metal Mat Length [ft]	CDR Static	Product Name
1	1.25	20	2.058	W15@30
2	3.75	20	2.239	W15@30
3	6.25	20	2.455	W15@30
4	8.75	20	2.717	W11@24
5	11.25	20	3.042	W11@24
6	13.75	20	3.455	W11@24
7	16.25	20	3.997	W11@18
8	18.75	20	4.742	W11@18
9	21.25	20	5.828	W11@18
10	23.75	20	7.559	W11@18
11	26.25	20	10.753	W11@18

Step 6: Check Bearing Resistance

The factored bearing resistance is computed as:

$$q_R = \phi \, q_n$$

Where, $\phi=0.65$ (see Table 10.5.5.2.2-1 in AASHTO (2007)) and

$$q_n = c\, N_{cm} + \gamma\, D_f\, V_{qm}\, C_{\varpi q} + 0.5\gamma\, B N_{\gamma m} C_{\varpi \gamma} \quad \text{(see AASHTO (2007) Equation 10.6.3.1.2a-1)}$$

In this design example: $c=0,\ D_f =0$ (because embedment depth is neglected)

$$q_n = 0.5\gamma\, B N_{\gamma m} C_{\varpi \gamma}$$

$N_{\gamma m} = N_\gamma s_\gamma i_\gamma$ (see AASHTO (2007) Equation 10.6.3.1.2a-4); $N_\gamma =22.4$ (see AASHTO Table 10.6.3.1.2a-1); $s_\gamma = 1 - 0.4 \cdot \left(\dfrac{B}{L}\right) = 1.0$ (Assumed long wall); $i_\gamma = 1.0$ (see AASHTO Table 10.6.3.1.2a-8); $C_{\varpi \gamma} = 1.0$ (Assumed that the groundwater depth is > $1.5\text{B} + D_f$)

$$q_n = 0.5 \cdot (120\ pcf\,) \cdot (20\,ft - 2\cdot e_B) \cdot (22.4) \cdot (1.0) \cdot (1.0) \cdot (1.0)$$
$$= 1.344 \cdot (20 - 2\cdot e_B\,(ft))\,ksf$$

$$q_R = \phi\, q_n = 0.874\,(20 - 2\,e_B\,(ft))\ ksf$$

To check whether the bearing resistance of the MSE wall is adequate, q_R computed above must be compared against the following criteria:

where: $q_{uniform} = \dfrac{V_{TOT}}{B - 2e_B}$ and e_B is computed as $(M_{VTOT} - M_{HTO}T)/V_{TOT}$. In this check the effects of live load surcharges are included because they increase the loading on the foundation.

Table D.2.8 Summary for checking bearing resistance

Group	V_{TOT} (kips/ft)	M_{VTOT} (kips-ft/ft)	M_{HTOT} (kips-ft/ft)	X_o (ft)	e_B (ft)	$q_{uniform}$ (ksf)	q_R (ksf)
Strength I (a)	74.4	744.0	219.94	7.04	2.96	5.3	12.3
Strength I (b)	97.5	975.0	219.94	7.74	2.26	6.3	13.5
Service I	70.8	708.0	143.46	7.97	2.03	4.5	13.9

Maximum value of $q_{uniform}$ = 6.3 ksf

q_R > $q_{uniform}$ (13.5 ksf > 6.3 ksf)

Therefore bearing resistance is adequate.

Step 7: Location of Critical Failure Surface

The critical failure surface for the inextensible reinforcement is determined by dividing the reinforced zone into active and resistant zone with a bilinear failure surface as shown in Figure E-2. For the top half of the wall $L_a = 0.3 H$.

Step 8: Calculate Factored Horizontal Stress

The factored horizontal stress (σ_H) at each reinforcement level is determined as:

$$\sigma_H = \gamma_P (\sigma_v k_r + \Delta \sigma_H)$$

where: γ_p = the maximum load factor for vertical earth pressure (=1.35); k_r = horizontal pressure coefficient; σ_v = unfactored vertical stress at the reinforcement level due to resultant of gravity forces (i.e., $\gamma_r H_i$) and any surcharge loads (i.e., $\gamma_r h_{eq}$); γ_r = unit

weight of reinforced fill; H_i= backfill thickness over the reinforcement within layer i;
h_{eq} = equivalent height of soil for vehicular loading; $\Delta\sigma_H$ = horizontal stress at
reinforcement level resulting from a concentrated surcharge load. For this example, no
concentrated surcharge loads are present.

Step 9: Calculate Maximum Factored Tensile Force

The maximum factored tensile force in the Top Layer is computed as

$$T_{max} = \sigma_H S_v$$

Therefore, T_{max} = 1064 lb/ft, and in the bottom layer, T_{max} = 3966 lb/ft

Step 10: Check Reinforcement Pullout Resistance

The effective pullout length (L_e) should be computed for each reinforcement layer as:

$$L_e \geq \frac{T_{max}}{\phi F^* \alpha C R_c}$$

Where, T_{max} = maximum tensile force determined in step 9; ϕ = 0.9 based on AASHTO
(2007) Table 11.5.6-1; F^*= pullout friction factor determined from Figure 4; α = scale
effect correction factor, 1; σ_v = unfactored vertical stress at the reinforcement level; C =
2; and R_c = coverage ration = 0.5

For the top layer, the required length of reinforcement in the resistance zone is calculated as follows:

$$L_e = \frac{1064\,lb/ft}{0.9 \times 0.308 \times 1 \times 150\,psf \times 2 \times 0.5} = 25.6\,ft$$

The total length of reinforcement (L) required for the top layer for internal stability is,

$$L = L_a + L_e$$

For top layer, L_a is determined from step 7 as 0.3 H = 0.3 × 27 ft = 8.1 ft

$$L = 8.1 + 25.6 = 33.7 \text{ ft (use 34 ft)}$$

Length of reinforcement estimated in step 1 was 20.0 ft. Therefore, the total length of reinforcement is unacceptable. In this example, use 20 ft of reinforcement length, and then increase L value to 34 ft later.

Step 11: Calculate Long-term Reinforcement Design Strength

Long-term strength $= \dfrac{0.65 F_y A_c R_c}{b}$

Ex) For the first layer with W11@18, $A_c = 0.385$, $F_y = 65000$, $R_c = 0.5$, $b = 2.5$

$$\therefore \text{ Long-term strength} = \frac{0.65 \cdot 65000 \cdot 0.385 \cdot 0.5}{2.5} = 3253 [lb/ft]$$

For the last layer with W15@30, $A_c = 0.5$, $F_y = 65000$, $R_c = 0.5$, $b = 2.5$

$$\therefore \text{ Long-term strength} = \frac{0.65 \cdot 65000 \cdot 0.6 \cdot 0.5}{2.5} = 5070 \, [lb/ft]$$

* Avail. Static Pullout $(P_r) = L_e \cdot \phi \cdot F^* \cdot \alpha \cdot \sigma_v \cdot C \cdot R_c$

Ex) For the first layer with W11@18,

$\phi = 0.9$

F^* = interpolated number, see Figure 12-12 = 0.308 (also see graph below),

$\alpha = 1, \quad \sigma_v = 1.25 \times 120 = 150, \quad C = 2, \quad R_c = 0.5$

$\therefore P_r = 11.75 \times 0.9 \times 0.308 \times 1 \times 150 \times 2 \times 0.5 = 488.3$

For the last layer with W15@30,

$F^* = 0.119$

$\sigma_v = 26.25 \times 120 = 3150$

$\therefore P_r = 19.25 \times 0.9 \times 0.119 \times 1 \times 3150 \times 2 \times 0.5 = 6494.3$

d=0 F*=0.318

d=1.2 F*=0.308

d=20

d=26.25 F*=0.119
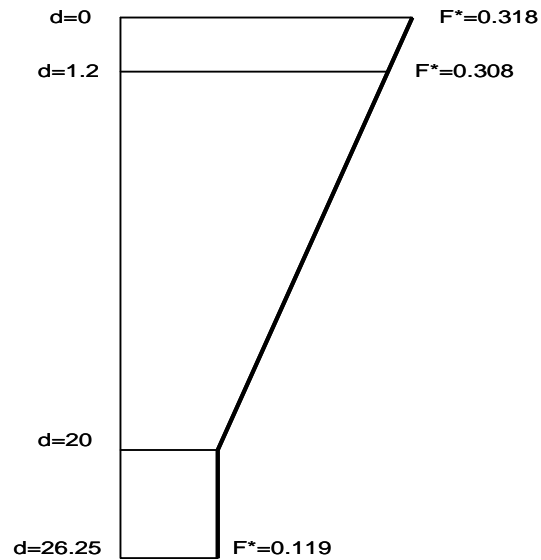
Figure D.2.3 Determining F^* using interpolation

Table D.2.9 Program results – strength with L=20 ft

#	Metal Mats Elevation [ft]	Horizontal Spacing [ft]	Long-term strength $(F_v)(A_c)(R_c)/b$ [lb/ft]	T_{max} [lb/ft]	Actual CDR static
1	1.25	5.0	5070	3962.95	1.279
2	3.75	5.0	5070	3619.46	1.401
3	6.25	5.0	3253	3275.96	1.548
4	8.75	5.0	3253	3085.68	1.054
5	11.25	5.0	3253	3051.38	1.066
6	13.75	5.0	3253	2976.32	1.093
7	16.25	5.0	3253	2785.30	1.168
8	18.75	5.0	3253	2478.22	1.313
9	21.25	5.0	3253	2094.24	1.553
10	23.75	5.0	3253	1627.25	1.999
11	26.25	5.0	3253	1055.51	3.082

* $T_{max} = \sigma_H \cdot S_v, \quad \sigma_H = \gamma_P(\sigma_v k_r + \Delta\sigma_H)$

Ex) For the first layer with W11@18,

γ_P=1.35, for soil mass, γ_P=1.75 for surcharge, σ_v= 120

$$K_r = \frac{K_r}{K_a} \cdot K_a = 2.418 \times 0.283 = 0.684$$

$\Delta\sigma_H = 0$ (no concentrated surcharge), $S_v = 2.5$ ft

$\therefore T_{max} = [1.35 \times 120 \times 1.25 + 1.75 \times 120 \times 2] \times 0.684 \times 2.5 = 1064 \ (\cong 1056)$

Ex) For the bottom layer with W15@30,

$$K_r = \frac{K_r}{K_a} \cdot K_a = 1.2 \times 0.283 = 0.3396$$

$\therefore T_{max} = [1.35 \times 120 \times 26.25 + 1.75 \times 120 \times 2] \times 0.3396 \times 2.5 = 3966 \ (\cong 3963)$

Step 12: Check Overall Stability

Table D.2.10 Program results – pullout with L=20 ft

#	Metal Mats Elevation [ft]	T_{max} [lb/ft]	L_e [ft]	L_a [ft]	Avail. Static Pullout, P_r [lb/ft]	Actual CDR static
1	1.25	3962.95	19.25	0.75	6494.3	1.639
2	3.75	3619.46	17.75	2.25	5416.7	1.497
3	6.25	3275.96	16.25	3.75	4435.8	1.354
4	8.75	3085.68	14.75	5.25	4824.7	1.564
5	11.25	3051.38	13.25	6.75	3914.4	1.283
6	13.75	2976.32	11.75	8.25	3057.8	1.027
7	16.25	2785.30	11.75	8.25	3241.9	1.164
8	18.75	2478.22	11.75	8.25	2745.7	1.108
9	21.25	2094.24	11.75	8.25	2121.3	1.013
10	23.75	1627.25	11.75	8.25	1368.9	0.841
11	26.25	1055.51	11.75	8.25	488.3	0.463

* Actual Static CDR = (Avail. Static Pullout, P_r) / (T_{max})

Ex) Pullout CDR of the last layer with

$$W15@30 = \frac{6494.3}{3963.0} = 1.639 \qquad ...………...O.K.$$

Ex) Pullout CDR of the first layer with $W11@18 = \dfrac{488.3}{1055.5} = 0.463 \;………..N.G.$

$\therefore$ Increase L = 34 ft as recommended in Step 10.

Table D.2.11 Program results – pullout with L=34 ft

#	Metal Mats Elevation [ft]	T_{max} [lb/ft]	L_e [ft]	L_a [ft]	Avail. Static Pullout, P_r [lb/ft]	Actual CDR static
1	1.25	3962.95	33.25	0.75	11217.1	2.830
2	3.75	3619.46	31.75	2.25	9689.8	2.677
3	6.25	3275.96	30.25	3.75	8259.1	2.521
4	8.75	3085.68	28.75	5.25	9404.8	3.048
5	11.25	3051.38	27.25	6.75	8052.3	2.639
6	13.75	2976.32	25.75	8.25	6701.7	2.252
7	16.25	2785.30	25.75	8.25	7105.2	2.551
8	18.75	2478.22	25.75	8.25	6017.6	2.428
9	21.25	2094.24	25.75	8.25	4649.2	2.220
10	23.75	1627.25	25.75	8.25	3000.1	1.844
11	26.25	1055.51	25.75	8.25	1070.2	1.014

By increasing L, capacity-demands ratios is greater than 1.0 and **the design is O.K.**

Appendix E

ABUTMENT DESIGN EXAMPLE

E.1 Given Conditions

This example illustrates the design of high parapet abutment. After determination of dead, earth and live load components, a load combination with factor 1 is assembled. After which, the capacity of an assumed pile group is evaluated. Subsequently, the flexural design of the footing, stem, and backwall is presented. The shear capacity of the footing is also checked.

The design parameters for the example are:

The superstructure consists of a 9 ½" deck on 5 steel girders with a beam spacing of 11'-4" and a skew of 20°. The abutment is supported on cast-in-place piling (12-inch diameter). The abutment supports a 20-feet long, 1-foot thick approach panel that is partially supported by the top of the backwall and partially supported by subgrade material.

The Bridge Construction Unit's Recommendations for the foundations are referenced at the start of final design. The recommendations identify the appropriate design capacity and resistance factor to be used.

Bearing Resistance, $Q_r = \emptyset Q_n = 0.45 \times 225 = 101$ tons/pile $= 202$ kips/pile

Pile Rows I contains 11 piles, II contain six piles, and Row III contains nine piles. Avoid pile layouts that permit individual piles to go into tension.

Table E.1.1 Material and design parameters

Unit Weights	Soil	0.120 kcf
	Reinforced Concrete	0.150 kcf
Concrete	Compressive Strength, f'c	4.0 ksi
	Crack Control, Z	170 kip/in
Reinforcement	Modulus of Elasticity, Es	29,000 ksi
	Yield Strength, Fy	60 ksi
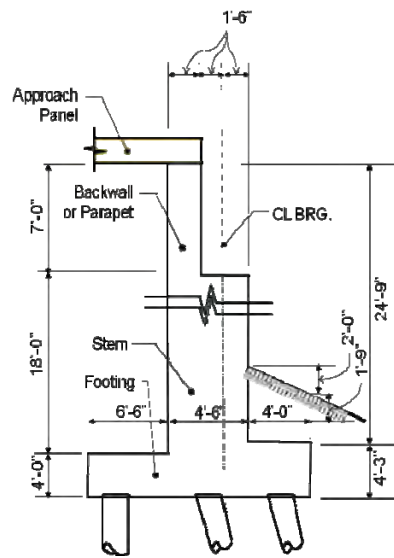
Figure E.1.1 Example cross-section for the abutment

255

E.2 Permanent Loads (DC & EV)

Calculate the dead loads:

Backwall:

$$P_{bw} = 0.150 \times 1.5 \times 7.0 \times 54.27 = 85.5 \text{ kips}$$

Stem:

$$P_{st} = 0.15 \times 4.5 \times 18 \times 54.27 = 659.4 \text{ kips}$$

Footing:

$$P_f = 0.15 \times (4 \times 11.0 + 4.25 \times 4) \times 55.33 = 506.3 \text{ kips}$$

Approach Panel (Assume half carried by the abutment):

$$P_{ap} = 0.15 \times 1 \times 20/2 \times 48/\cos20o = 76.6 \text{ kips}$$

Superstructure Dead Load (Given here):

$$P_{super} = (95 + 22) \times (5 \text{ girders}) = 585.0 \text{ kips}$$

Wingwall DL (Assume 5 feet of the wing walls beyond the footing are carried by the abutment. Also assume the corner fillet weight is balanced by the taper in the wing wall.):

$$P_{wing} = 0.15 \times 2 \times 1.5 \times (6.5/\cos20o + 5) \times (15.25 + 6.75 + 1.25) = 124.7 \text{ kips}$$

Summing the dead loads:

$$P_{DC} = 85.5 + 659.4 + 506.3 + 76.6 + 585.0 + 124.7 = 2037.5 \text{ kips}$$

Calculate vertical earth pressure (EV) of fill above the footing:

On the Heel:

$$P_{EV} = 0.12 \times (18 + 7) \times 6.5 \times 48.0/\cos20^o = 996.1 \text{ kips}$$

On the Toe:

$$P_{EV} = 0.12 \times \{(3.75 + 1.75)/2\} \times 4 \times 55.33 = 73.0 \text{ kips}$$

E.3 Earthquake Load (AE)

The active earthquake pressure coefficient, $K_{AE} = 0.45$

$$\therefore P_{AE} = (1/2)(0.12)(29.02)(0.45)(48/\cos20o) = 1159.9 \text{ kips}$$

The force acts at the middle of the wall:

$$0.5 \times 29.0 = 14.5 \text{ ft}$$

Passive earth pressure in front of the abutment is neglected in the design.

E.4 Live Load Surcharge (LS)

The live load surcharge is applied to the abutment during construction. It represents construction activity on the fill behind the abutment prior to construction of the approach panel.

Use a surcharge height of 2.0 feet:

$$p = \gamma_{eq} \times h_{eq} = 0.033 \times 2.0 = 0.066 \text{ kips /ft}^2$$

Horizontal resultant of LS:

$$P_{LS} = 0.066 \times 29.0 \times (48/\cos 20^o) = 97.8 \text{ kips}$$

Table E.4.1 Vertical load components and moments about toe of footing

	Load	Label	P(kips)	Distance to Toe (ft)	Moment about Toe (kip-ft)
DC	Backwall	P_{bw}	85.5	-7.75	-662.6
	Stem	P_{st}	659.4	-6.25	-4121.3
	Footing	P_f	506.3	-7.41	-3751.7
	Approach Panel	P_{ap}	76.6	-8.17	-625.8
	Superstructure DL	P_{super}	585.0	-5.50	-3217.5
	Wingwall	P_{wing}	124.7	-14.10	-1758.3
	Total		2037.5		-14137.2
EV	Backfill on Heel	$P_{EV(HEEL)}$	996.1	-11.75	-11704.2
	Fill on Toe	$P_{EV(TOE)}$	73.0	-2.24	-163.5
	Total		1069.1		-11867.7

Table E.4.2 Horizontal load components and moments about bottom of footing

Load			H (kips)	Distance to Bottom (ft)	Moment about Bottom (kip-ft)
Type	Description	Label			
AE	Earthquake Load	P_{AE}	1159.9	14.5	16818.6
LS	Live Load Surcharge	P_{LS}	97.8	14.5	1418.1

E.5 Design Piles

Table E.5.1 summarizes the vertical, horizontal, and moment forces that are applied to the pile group.

Table E.5.1 Force resultants

	Vertical Load P (kips)	Horizontal Load H (kips)	Moment about Toe M_{toe} (kip-ft)
Total	3106.6	1257.7	-7768.2

Table E.5.2 Pile group properties

Pile Group Properties	Row Number			Sum
	I	II	III	
Pile per Row (N)	12	6	9	27
Distance to Toe (d_{toe})	1.25	6	13.75	
$N \times d_{toe}$	15.0	36.0	123.75	174.75
Neutral Axis of Pile Group to Toe (X_{NA})	$(\sum N \cdot d_{toe})/\sum N$			6.47
Distance from Neutral Axis to Pile Row (d)	5.22	0.47	-7.28	
$I = N \cdot d^2$	327.26	1.34	476.69	805.29

Vertical Capacity of Pile Group

Based on above results, determine the properties of the pile group. These properties include the number of piles, the location of the centroid or neutral axis with respect to the toe, and the moment of inertia of each pile row.
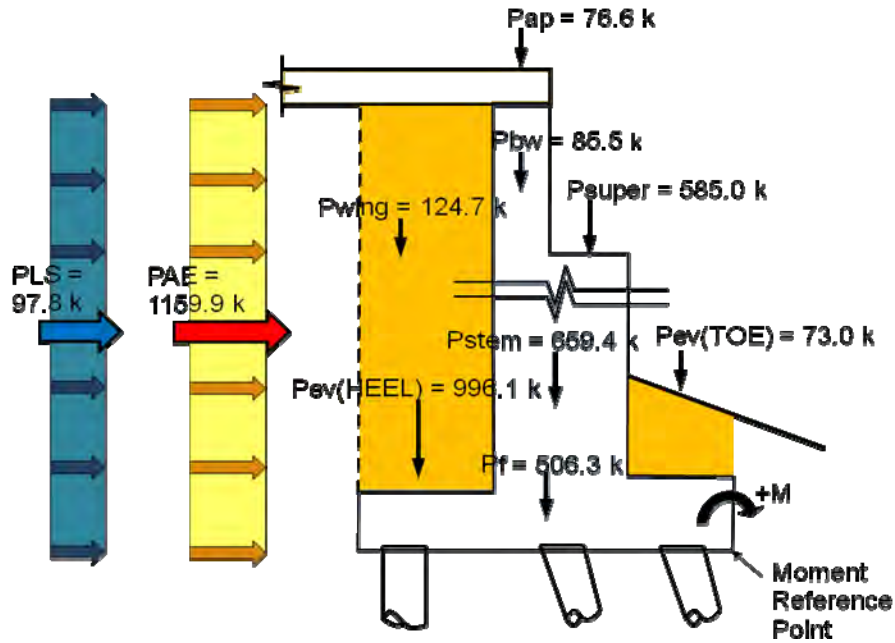
Figure E.5.1 Summary of permanent loads

Using solid mechanics equations adapted for discrete elements, the forces in the pile rows for different load combinations are determined.

The force in each pile row is found using:

$$\text{Pile load} = P/N + (M_{NA} \cdot d)/I$$

First, the moment about the toe must be translated to get the moment about the neutral axis of the pile group. The eccentricity about the toe is

$$e_{toe} = \frac{M_{toe}}{p} = \text{-}7768.2/3106.6 = \text{-}2.5 \text{ ft}$$

The eccentricity about the neutral axis of the pile group is

$$e_{NA} = X_{NA} + e_{toe} = 6.47 \text{ -}2.5 = 3.97 \text{ ft}$$

The moment about the neutral axis of the pile group becomes

$$M_{NA} = P \cdot e_{NA} = 3106.6(3.97) = 12340.1 \text{ kip-ft}$$

The pile load on each row:

Pile load of Row I = 3106.6/27 + 12340.1 × 5.22/805.29 = 195.08 kips/pile

Pile load of Row II = 3106.6/27 + 12340.1 × 0.47/ 805.29 = 122.30 kips/pile

Pile load of Row III = 3106.6/27 + 12340.1 × (-7.28)/ 805.29 = 3.54 kips/pile

The largest pile load is 195.04 kips, which is less than the bearing resistance of 202 kips. There is no tension pile. Therefore, the pile layout is considered satisfactory for bearing.

Lateral Capacity of Pile Group

Assume a lateral resistance of 18 kips/pile plus the resistance due to the two rows of battered piles.

$$R_H = 27 \times 18 + 18 \times 202 \times 3 / \sqrt{3^2 + 12^2} = 1367.9 \text{ kips} > 1257.7 \text{ kips} \qquad \text{OK}$$

E.6 Check Shear in Footing

General practice is to size the thickness of footings such that shear steel is not required. Try 48 inch thick footing with 3 inch step at the toe.

Determine d_v

Based on past design experience assume the bottom mat of steel is #9 bars spaced at 12 inches (A_s = 1.0 in²/ft). Begin by determining the depth of flexural reinforcement:

$$d_{toe} = \text{(thickness) - (pile embedment)} - (\text{Ø}/2) = 51 - 12 - 1.128/2 = 38.44 \text{ in}$$

$$d_{heel} = 48 - 12 - 1.128/2 = 35.44 \text{ in}$$

The depth of the compression block is:

$$a = A_s \times f_y/(0.85 \text{ f'}_c \times b) = (1.00 \times 60)/(0.85 \times 4 \times 12) = 1.47 \text{ in}$$

The effective shear depth is:

$$d_{vtoe} = d - a/2 = 38.44 - 1.47/2 = 37.71 \text{ in}$$

$$d_{vheel} = 35.44 - 1.47/2 = 34.71 \text{ in}$$

It needs to be no less than 0.9 d_e:

For toe, 0.9 d_e = 0.9 d_{toe} = 0.9×38.44 = 34.9 in

For heel, 0.9 d_e = 0.9 d_{heel} = 0.9 × 35.44 = 31.90 in

Use d_{vtoe} = 37.71 in and d_{vheel} = 34.71 in

One-Way Shear in Footing

The critical section is located d_v from the face of the abutment. The center line of the Row III piles is 63 inches from the back face of abutment. Therefore, the entire load from the Row III piles contributes to shear on the critical section. Ignore the beneficial effects of the vertical earth loads and footing self weight:

$$V_{UROW\ III} = (Pile\ Reaction)/(Pile\ Spacing) = 3.54/6.56 = 0.54\ kips/ft\ width$$

The center line of the Row I piles is 33 inches from the front face of abutment. Therefore, only a portion of the load from the Row I piles contributes to shear on the critical section.

$$V_{UROW\ I} = (Pile\ Fraction\ Outside\ Critical\ Section)\ (Pile\ Reaction)/(Pile\ Spacing)$$

$$= (1.29/12)(195.08/4.77) = 4.4\ kips/ft\ width$$

The shear due to the Row I piles governs.

There is no shear reinforcement, so the nominal shear capacity of the footing is:

$$V_n = V_c$$

An upper limit is placed on the maximum nominal shear capacity a section can carry. The maximum design shear for the footing heel is:

$$V_n = 0.25 \times f'_c \times b_v \times d_v = 0.25 \times 4.0 \times 12.0 \times 34.71 = 416.5\ kips$$

The concrete shear capacity of a section is:

$$V_c = 0.0316\ \beta \times \sqrt{f'_c} \times b_v \times d_v$$

In order to determine β, start by calculating the strain ε_x. For sections without shear reinforcement,

$$\varepsilon_x = \frac{\dfrac{M_u}{d_v} + 0.5N_u + 0.5\left(V_u - V_p\right)\cos\theta - A_{ps}f_{po}}{E_s A_s + E_p A_{ps}}$$

The critical section for moment is the face of the abutment, so

$M_u = V_u \times$(Moment Arm) $= 4.4 \times (5.25) = 23.1$ kip-ft/ft

$N_u = V_p = A_{ps} = f_{po} = E_p = 0$

Assume $\theta = 53.0$ degrees

Then

$$\varepsilon_x = \frac{\dfrac{118.7(12)}{34.71} + 0.5(22.6)(\cos 53.0)}{29,000 \times 1.0} = 1.71 \times 10^{-3}$$

Next, determine crack spacing parameter sxe

$a_g = 1.5$ inches

$sx = d_v = 34.71$ inches

Then

$$sxe = sx\left(\frac{1.38}{a_g + 0.63}\right) = 34.71\left(\frac{1.38}{1.50 + 0.63}\right) = 22.49 \text{ in} < 80 \text{ in} \quad \text{OK}$$

With ε_x and sxe determined, interpolated to find   and   in AASHTO (2007) Table 5.8.3.4.2-2.

$\theta = 53.3$ degrees, which is close to the assumed angle $\beta = 1.38$

For a 1 ft wide section, substituting values into V_c equation produces:

$$V_c = 0.0316 \times 1.38 \sqrt{4} \times 12 \times 34.71 = 36.3 \text{ kips}$$

This results in:

$$V_n = V_c = 36.3 \text{ kips} < 416.5 \text{ kips} \quad \text{OK}$$

Including the shear resistance factor, the shear capacity is found to be:

$$V_r = \emptyset V_n = 0.90 \times 36.3 = 32.7 \text{ kips} > 22.6 \text{ kips} \quad \text{OK}$$

Check Two-Way Shear in Footing

Punching of an individual pile through the abutment footing is checked next. The critical section for two-way shear is located at 0.5 dv from the perimeter of the pile. The Row I pile at the acute corner is governing case because it has the shortest length of critical section.

Measured from a CAD drawing, the length of the critical section

$b_o = 61.4 \text{ in}$

$$\emptyset V_n = \emptyset(0.126 \times \sqrt{f_c'} \times b_o \times d_v) = (0.9)(0.126)(\sqrt{4})(61.4)(34.71) = 483.4 \text{ kips}$$

$V_u = \text{Row I Factored Pile Load} = 195.08 \text{ kips} < 483.4 \text{ kips}$

E.7 Design Footing Reinforcement

The critical section for flexure in the footing is located at the face of the stem for both the top and bottom transverse reinforcement.

E.7.1 Top Transverse Reinforcement Design for Strength Limit State

The design moment for the top transverse bars is found by assuming the heel acts as a cantilever supporting its self weight and the weight of the earth resting on it. In cases where the required reinforcement to resist these loads seems excessive, the moment due to the minimum back pile reaction may be included to decrease the top mat design moment. Use the maximum load factors for DC and EV.

The distributed load associated with the self weight of the footing heel is:

$$W_{ftg} = Y \times (thickness)(width) = 0.150 \times 4.0 \times 1.0 = 0.60 \text{ kips/ft}$$

A heel length of 6.5 feet produces a moment of:

$$M_{DC} = W_{ftg} \times L \times \frac{L}{2} = 0.60 \times \frac{6.5^2}{2} = 12.7 \text{ kip-ft}$$

The distributed load associated with fill on top of the footing heel is:

$$W_{EV} = 0.120(15.25 + 6.75) \times 1.0 = 3.64 \text{ kips/ft}$$

The associated moment in the footing at the stem is:

$$M_{EV} = 2.64 \times \frac{6.5^2}{2} = 55.8 \text{ kip-ft}$$

Combining loads to determine the design moment produces:

$$M_u = 1.25\ M_{DC} + 1.35\ M_{EV} = 1.25 \times 12.7 + 1.35 \times 55.8 = 91.2 \text{ kip-ft}$$

Determining the depth of the flexural reinforcement:

$$d = (\text{thickness}) - (\text{cover}) - \frac{d_b}{2} = 48 - 3 - \frac{1.128}{2} = 44.44 \text{ in}$$

Solve for the required area of reinforcing steel:

$$M_r = \emptyset M_n = \emptyset A_s \times f_y \times \left[d - \frac{A_s \times f_y}{2 \times 0.85 \times f_c' \times b} \right] \geq M_u$$

Then for $f_c' = 4.0$ ksi and $\emptyset = 0.90$,

$$M_u = 0.9 M_n = \emptyset A_s \times 60 \times \left[d - \frac{A_s \times 60}{1.7 \times 4 \times 12} \right] \frac{1}{12}$$

Which can be rearranged to:

$$3.309\ A_s^2 - 4.5\ d \times A_s + M_u = 0$$

The required area of steel can be found by solving for the smaller root in the quadratic equation.

$$A_s = \frac{4.5d - \sqrt{20.25d^2 - 13.236 M_u}}{6.618}$$

The required area of steel is 0.46 in^2/ft. Try #22 bars at 12 inches ($A_s = 0.60$ in^2/ft)

Check Maximum Reinforcement

No more than 42 percent of the flexural cross section can be in compression at the strength limit state.

For #22 bars, d= 48-3-$\dfrac{0.875}{2}$= 44.56 in

$$c = \dfrac{A_s \times f_y}{0.85 f_c' \beta_1 b} = \dfrac{0.6 \times 60}{0.85 \times 4 \times 0.85 \times 12} = 1.04 \text{ in}$$

The fraction of the section in compression is:

$$\dfrac{c}{d_e} = \dfrac{1.04}{44.56} = 0.023 < 0.42$$

Check Minimum Reinforcement

The minimum reinforcement check has two parts. The flexural reinforcement needs to be able to carry a moment 20 percent larger than the cracking moment of the cross section. If this criteria is not satisfied, the amount of reinforcement needs to be increased to carry the lesser of 1.20 times the cracking moment or 1.33 times the original design moment.

The rupture stress of concrete in flexure is:

$$f_r = 0.24 \sqrt{f_c'} = 0.24 \sqrt{4} = 0.48 \text{ ksi}$$

The gross moment of inertia is:

$$I_g = \dfrac{1}{12} b \times t^3 = \dfrac{1}{12} \times 12 \times (48)^3 = 110{,}600 \text{ in}^4$$

The distance from the centroidal axis to the tension face is:

$$y_t = 24.0 \text{ in}$$

Combining these parameters leads to a cracking moment of:

$$M_{cr} = \frac{f_r I_g}{y_t} = \frac{0.48 \times 110.600}{24.0 \times 12} = 184.3 \text{ kip-ft}$$

With a 20 percent increase, the required capacity is:

$$1.2 \, M_{cr} = 221.2 \text{ kip-ft}$$

The capacity of the #22 bars at a 12 inch spacing is:

$$M_r = \emptyset A_s \times f_y \left(d - \frac{a}{2} \right)$$

$$M_r = 0.9 \times 0.6 \times 60 \times \left(44.56 - \frac{1.04 \times 0.85}{2} \right) \left(\frac{1}{12} \right) = 119.1 \text{ kip-ft}$$

This is less than 221.2 kip-ft.

The strength design moment of 91.2 kip-ft is less than half of the 1.2 M_{cr} moment. Provide reinforcement capable of resisting:

$$1.33 \, M_u = 1.33 \times 91.2 = 121.8 \text{ kip-ft}$$

The #22 bars at 12 inches, with a capacity of 119.1 kip-ft, are within 3% of the required capacity. Consider the design adequate.

E.7.2 Bottom Transverse Reinforcement Design for Strength Limit State

Although the toe has a greater thickness than the heel, for simplicity assume a constant thickness of 48 inches. Then the design moment for the bottom mat is the largest of the moments due to the maximum pile reactions for the Row I or Row III piles.

For the Row I piles:

$$M_{uRowI} = \left(\frac{Pile\ reaction}{Pile\ spacing}\right)(Moment\ arm)$$

$$= \left(\frac{195.08}{4.77}\right)(4.0 - 1.25) = 112.5\ \text{kip-ft/ft width}$$

For the Row III piles, subtract off the moment due to earth on the heel when calculating the factored moment:

$$M_{uRowIII} = \left(\frac{Pile\ reaction}{Pile\ spacing}\right)(Moment\ arm) - \phi M_{ev}$$

$$= \left(\frac{3.54}{6.56}\right)(6.5 - 1.25) - 0.9(55.8) = -47.4\ \text{kip-ft/ft width}$$

The Row I moment governs. $M_{udes} = 112.5$ kip-ft/ft width

Assuming #29 bars, the depth of the bottom flexural reinforcement is:

$$d = (thickness) - (pile\ embedment) - \left(\frac{d_b}{2}\right) = 48\text{-}12 - \frac{1.128}{2} = 35.44\ \text{in}$$

Solve once again with:

$$A_s = \frac{4.5d - \sqrt{20.25d^2 - 13.236M_u}}{6.618}$$

The required area of steel is 0.72 in^2/ft. Try #8 bars at 12 inches with standard hooks (A_s =0.79 in^2/ft)

$$c = \frac{0.79 \times 60}{0.85 \times 4 \times 0.85 \times 12} = 1.37 \text{ in}$$

Check Minimum Reinforcement

The minimum reinforcement check for the bottom of the footing has the same steps as the other elements. The gross moment of inertia is:

$$I_g = \frac{1}{12} b \times t^3 = \frac{1}{12} \times 12 \times (48)^3 = 110,600 \text{ in}^4$$

The distance from the centroidal axis to the tension face is:

$$y_t = 24.00 \text{ in}$$

Combining these parameters and using the rupture stress computed earlier leads to a cracking moment of:

$$M_{cr} = \frac{f_r I_g}{y_t} = \frac{0.48 \times 110.600}{24.0 \times 12} = 184.3 \text{ kip-ft}$$

With a 20 percent increase, the required capacity is:

$$1.2 \, M_{cr} = 221.2 \text{ kip-ft}$$

For #8 bars, d=48-12-$\frac{1}{2}$ = 35.5 in

The capacity of the #8 bars at a 12 inch spacing is:

$$M_r = \emptyset A_s\, f_y \left(d - \frac{a}{2} \right)$$

$$M_r = 0.9 \times 0.79 \times 60 \times \left(35.5 - \frac{1.37 \times 0.85}{2} \right)\left(\frac{1}{12} \right)$$

$= 124.1$ kip-ft < 221.2 kip-ft   NO GOOD

Therefore, we must provide reinforcement capable of resisting:

1.33 M_u = 1.33$\times$ 112.5

$= 149.6$ kip-ft > 94.8 kip-ft   NO GOOD

Revise reinforcement to #8 bars at 12 inches ($A_s = 0.79$ in^2/ft). Then

$M_r = 124.1$ kip-ft > 98.8 kip-ft   OK

Check Maximum Reinforcement

For #8bars, d = 48-12 - $\frac{1}{2}$ = 35.5 in

$$c = \frac{A_s \times f_y}{0.85 f_c' \beta_1 b} = \frac{0.79 \times 60}{0.85 \times 4 \times 0.85 \times 12} = 1.37 \text{ in}$$

The fraction of the section in compression is:

$$\frac{c}{d_e} = \frac{1.37}{35.5} = 0.039 < 0.42$$

Provide #25 bars at 12 inches ($A_s = 0.79$ in^2/ft).

E.7.3 Longitudinal Reinforcement Design for Strength Limit State

For longitudinal bars, design for uniform load due to all vertical loads spread equally over the length of the footing. Assume the footing acts as a continuous beam over pile supports. Use the longest pile spacing for design span.

Based on the maximum vertical load:

$$W_u = \frac{4252}{55.33} = 76.8 \text{ kips/ft}$$

$$M_u = \frac{w_u L^2}{10} = \frac{76.8 \times 8.75^2}{10} = 588.0 \text{ kip-ft}$$

Assume #19 bars, which is the smallest size used by Mn/DOT in footings:

$$d = 48\text{-}12\text{-}1.0 - \frac{0.75}{2} = 34.63 \text{ in}$$

Solve for required area of reinforcement:

$$M_r = \emptyset M_n = \emptyset A_s \times f_y \times \left[d - \frac{A_s \times f_y}{2 \times 0.85 \times f_c' \times b} \right] \geq M_u$$

Then

$$588.0 = 0.9A_s \times 60 \times \left(34.63 - \frac{A_s \times 60}{2 \times 0.85 \times 4 \times 180}\right)\left(\frac{1}{12}\right)$$

Rearrange and get

$$0.2206\ A_s^2 - 155.84\ A_s + 588.0 = 0$$

Solving, minimum $A_s = 3.79\ \text{in}^2$

The 15-#19 bars at a 12 inch spacing. ($A_s = 6.60\ \text{in}^2$)

Check Minimum Reinforcement

By inspection, $M_r > 1.33\ M_u$

Check Maximum Reinforcement

$$c = \frac{A_s \times f_y}{0.85 f_c' \beta_1 b} = \frac{6.60 \times 60}{0.85 \times 4 \times 0.85 \times 180} = 0.76\ \text{in}$$

$$\frac{c}{d_e} = \frac{0.76}{34.63} = 0.0219 < 0.42$$

Provide 15-#19 bars at 12 inches (As = 6.6 in2) for the footing longitudinal reinforcement.

The fraction of the section in compression is:

$$= 0.039 < 0.42$$

274

E.8 Flexural Design of the Stem

The moments associated with the eccentricity of vertical loads are minimal and are therefore ignored. Use a one-foot wide design strip. The stem design is governed by the horizontal earth pressure and live load surcharge loading during construction.

Horizontal Earth Pressure

$P_{top} = 0.0$ ksf

$P_{bottom} = 0.033 \times 22.25 = 0.734$ ksf

The resultant force applied to the stem is:

$P_{EH} = 0.5 \times 0.734 \times 22.25 \times 1.0 = 8.17$ kips

The height of the resultant above the footing is:

$X_{EH} = 0.33 \times 22.25 = 7.34$ ft

The moment at the base of the stem is:

$M_{EH} = P_{EH} \times X_{EH} = 8.17 \times 7.34 = 60.0$ kip-ft

Live Load Surcharge

For walls over 20 feet in height, h_{eq} is 2 feet. The resultant force applied to the stem is:

$P_{LS} = 0.033 \times 2.0 \times 22.25 \times 1.0 = 1.47$ kips

The height of the resultant force above the footing is:

$$X_{LS} = \frac{22.25}{2} = 11.13 \text{ ft}$$

The moment at the base of the stem is:

$$M_{LS} = P_{LS} \times X_{LS} = 1.47 \times 11.13 = 16.4 \text{ kip-ft}$$

Design Moments

The design factored moment is:

$$M_u = 1.5 \, M_{EH} + 1.75 \, M_{LS} = 1.5 \times 60.0 + 1.75 \times 16.4 = 118.7 \text{ kip-ft}$$

The design service moment is:

$$M_{service} = 1.0 \, M_{EH} + 1.0 \, M_{LS} = 1.0 \times 60.0 + 1.0 \times 16.4 = 76.4 \text{ kip-ft}$$

Investigate the Strength Limit State

Determine the area of back-face flexural reinforcement necessary to satisfy the "d" dimension:

$$M_u = 118.7 \text{ kip-ft}$$
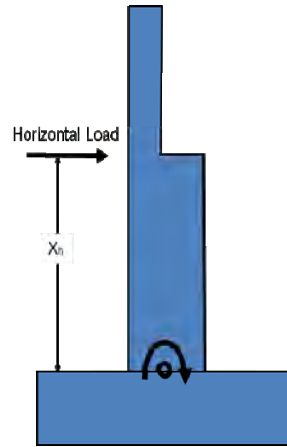
Figure E.8.1 Load diagram for stem design

Initially, assume that #19 bars are used for flexural reinforcement to compute the "d" dimension:

$$d = \text{(thickness)} - \text{(cover)} - \left(\frac{d_b}{2}\right) = 54 - \frac{0.75}{2} = 51.63 \text{ in}$$

Using

$$A_s = \frac{4.5d - \sqrt{20.25d^2 - 13.236M_u}}{6.618}$$

Solve once again with:

The required area of steel is 0.51 un2/ft. Try #16 bars at 6 inches ($A_s = 0.62$ in^2/ft, d=51.69 in).

Crack Control

Check crack control equations to ensure that the primary reinforcement is well distributed.

The transformed area of the reinforcement is:

$nA_s = 8 \times 0.62 = 4.96$ in^2

Determine the location of the neutral axis:

$$\frac{1}{2} b \times x^2 = n \, As \, (d\text{-}x)$$

$$\frac{1}{2} (12) \times x^2 = 4.96 \times (51.69\text{-}x) \quad \text{solving, } x = 6.14 \text{ inches}$$

$$j \times d = d - \frac{x}{3} = 51.69 - \frac{6.14}{3} = 49.64 \text{ in}$$

$$\text{Actual } f_s = \frac{M}{A_s \, j \times d} = \frac{76.4 \times 12}{0.62 \times 49.64} = 29.8 \text{ ksi}$$
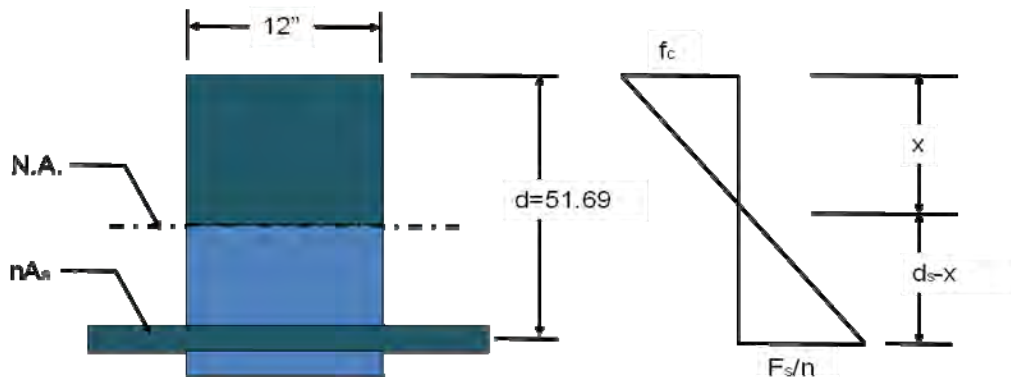

Figure E.8.2 Location of neutral axis

For z=170 kips/in, d_c = 2.313 inches, #16 bars at 16 inches:

$$A= \frac{2d_c b}{N} = \frac{2 \times 2.313 \times 12}{2} = 27.8 \text{ in}^2$$

$$\text{Permitted } f_s = \frac{z}{\sqrt[3]{d_c \times A}} = \frac{170}{\sqrt[3]{2.313 \times 27.8}} = 42.4 > 0.6 \, f_y = 36 \text{ ksi}$$

Actual f_s = 29.8 ksi < permitted f_s = 36.0 ksi

Check Maximum Reinforcement

No more than 42 percent of the flexural cross section can be in compression at the strength limit state. With A_s= 0.62 in^2/ft and d= 51.69 inches, the depth of the section in compression is:

$$c = \frac{A_s \times f_y}{0.85 f_c' \beta_1 b} = \frac{0.62 \times 60}{0.85 \times 4 \times 0.85 \times 12} = 1.07 \text{ in}$$

the fraction of the section in compression is:

$$\frac{c}{d} = \frac{1.07}{51.69} = 0.021 < 0.42$$

Check Minimum Reinforcement

The gross moment of inertia is:

$$I_g = \frac{1}{12} \, b \times t^3 = \frac{1}{12} \times 12 \times (54)^3 = 157{,}500 \text{ in}^4$$

The distance from the centroidal axis to the tension face is:

$$y_t = 27.00 \text{ in}$$

Combining these parameters and using the rupture stress computed earlier leads to a cracking moment of:

$$M_{cr} = \frac{f_r I_g}{y_t} = \frac{0.48 \times 157{,}500}{27.0 \times 12} = 233.3 \text{ kip-ft}$$

With a 20 percent increase, the required capacity is:

$$1.2 \, M_{cr} = 280.0 \text{ kip-ft}$$

The capacity of the #16 bars at a 6 inch spacing is:

$$M_r = \emptyset A_s \times f_y \times \left(d - \frac{a}{2} \right)$$

$$M_r = 0.9 \times 0.62 \times 60 \times \left(51.69 - \frac{1.07 \times 1.85}{2} \right) \left(\frac{1}{12} \right) = 142.9 \text{ kip-ft}$$

$$142.9 \text{ kip-ft} < 280.0 \text{ kip-ft} \qquad \text{OK}$$

The strength design moment of 118.7 kip-ft is less than half of the $1.2 M_{cr}$ moment. Provide reinforcement capable of resisting:

$$1.33 \, M_u = 1.33 \times 118.7 = 157.9 \text{ kip-ft}$$

With #19 bars (d= 51.63) the required area of steel is 0.69 in^2/ft.

Provide #19 bars at 6 inches (A$_s$ = 0.88 in^2/ft) for vertical back face reinforcement.

Shrinkage and Temperature Reinforcement

Mn/DOT practice for members over 48 inches thick is to use #19 bars spaced at 12 inches.

Use #19 bars at 12 inches (A$_s$ = 0.44 in^2/ft) on each face, for horizontal reinforcement and #19 bars at 12 inches for vertical front face reinforcement.

E.9 Splice Length

Calculate the tension lap length for the stem reinforcing. For epoxy coated #19 bars the basic development length l$_{db}$ is the greater of:

$$l_{db} = \frac{1.25 A_b f_y}{\sqrt{f_c'}} = \frac{1.25 \times 0.44 \times 60 A_b f_y}{\sqrt{40}} = 16.5 \text{ in}$$

or

$$l_{db} = 0.4 \, d_b \times f_y = 0.4 \times 0.75 \times 60 = 18.0 \text{ in}$$

The modification factors to the development length are:

1.5 for epoxy coated bars with cover less than three bar diameters (2.25 in)

0.8 for bars with spacing ≥ 6 inches and cover ≥ 3 inches in direction of spacing. (Note that cover for the end bars is < 3 inches, but the wall is long, so cover will have negligible effect)

Then the development length l_d is:

$$l_d = 18.0 \times 1.5 \times 0.8 = 21.6 \text{ in}$$

Referring to AASHTO (2007) Table 5.11.5.3.1-1, with 100 percent of the steel spliced and less than twice the necessary amount of steel provided, a Class C splice should be provided.

The required lap length l_{spl} is:

$$l_{spl} = 1.70 \ l_d = 1.70 \times 21.6 = 36.7 \text{ in}$$

Use a tension lap length of 37 inches.

E.10 Flexural Design of the Backwall (parapet)

The required vertical reinforcement in the backwall (parapet) is sized to carry the moment at the bottom of the backwall. The design is performed on a one-foot wide strip of wall. The backwall design is governed by the horizontal earth pressure and live load surcharge loading during construction.

Horizontal Earth Pressure

$$P_{top} = 0.0 \text{ ksf}$$

$$P_{bottom} = 0.033 \times 6.75 = 0.223 \text{ ksf}$$

The resultant force applied to the backwall is:

$$P_{EH} = 0.5 \times 0.223 \times 6.75 \times 1.0 = 0.75 \text{ kips}$$

The height of the resultant above the bottom of the backwall is:

$$X_{EH} = 0.33 \times 6.75 = 2.25 \text{ ft}$$

The moment at the bottom of the backwall is:

$$M_{EH} = P_{EH} \times X_{EH} = 0.75 \times 2.25 = 1.69 \text{ kip-ft}$$

Live Load Surcharge

Interpolate between the values provided in the table to arrive at the required equivalent height of surcharge to use for the design of the backwall.

$$h_{eq} = \left(\frac{6.75 - 5}{10.0 - 5} \right)(3 - 4) + 4 = 3.65 \text{ ft}$$

The resultant force applied to the backwall is:

$$P_{LS} = 0.033 \times 3.65 \times 6.75 \times 1.0 = 0.81 \text{ kips}$$

The height of the resultant force above the bottom of the backwall is:

$$X_{LS} = \frac{6.75}{2} = 3.38 \text{ ft}$$

Moment at the bottom of the backwall is:

$$M_{LS} = P_{LS} \times X_{LS} = 0.81 \times 3.38 = 2.74 \text{ kip-ft}$$
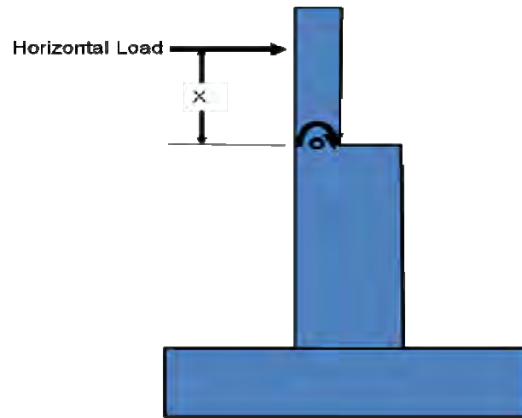

Figure E.10.1 Load diagram for backwall design

Design Moments

Combining the load factors for the EH and LS load components with the flexural design forces at the bottom of the backwall produces the following design forces.

$$M_u = 1.5\ M_{EH} + 1.75\ M_{LS} = 1.5 \times 1.69 + 1.75 \times 2.74 = 7.33 \text{ kip-ft}$$

$$M_{SERVICE} = M_{EH} + M_{LS} = 1.69 + 2.74 = 4.43 \text{ kip-ft}$$

Investigate the Strength Limit State

Determine the area of back-face flexural reinforcement necessary to satisfy the design moment. Once again, use

$$A_s = \frac{4.5d - \sqrt{20.25d^2 - 13.236M_u}}{6.618}$$

Initially, assume that #19 bars are used for flexural reinforcement to compute the "d" dimension:

$$d = \text{(thickness) - (clear cover)} - \frac{d_b}{2} = 18 - 2 - \frac{0.75}{2} = 15.63 \text{ in}$$

Solving the equation, the required area of steel is 0.10 in^2/ft.

In no case should reinforcement be less than #16 bars at a 12 inch spacing. The area of steel for #16 bars at 12 inches is 0.31 in^2/ft.

Continue the backwall flexural checks using #16 bars at 12 inches. The actual "d" for this reinforcement layout is:

$$d = 18 - 2 - \frac{0.625}{2} = 15.69 \text{ in}$$

Check Crack Control

Check crack control equations to ensure that the primary reinforcement is well distributed. Design for a z value of 170 kip/in.

To check if steel stresses are acceptable, determine the cracked section properties with the trial reinforcement. Compute the modular ratio for 4.0 ksi concrete:

$$n = \frac{E_s}{E_c} = \frac{29{,}000}{33{,}000 \times 0.145^{1.5} \times \sqrt{4}} = 7.96$$

The transformed area of the reinforcement is:

$$n \cdot A_s = 8 \times 0.31 = 2.48 \text{ in}^2$$

Determine the location of the neutral axis:

$$\frac{1}{2} bx^2 = n \cdot A_s \, (d_s - x)$$

$$\frac{1}{2} 12x^2 = 2.48 \, (15.69 - x) \quad \text{solving, } x = 2.35 \text{ inches}$$

$$j \cdot d = d - x/3 = 15.69 - 2.35/3 = 14.91 \text{ in}$$

$$\text{Actual } f_s = \frac{M}{A_s \, j \times d} = \frac{4.43 \times 12}{0.31 \times 14.91} = 11.5 \text{ ksi}$$

For z = 170 kips/in, d_c = 2.31 inches, #16 bars at 12 inches:

$$A = \frac{2d_c b}{N} = \frac{2 \times 2.313 \times 12}{1} = 55.4 \text{ in}^2$$

$$\text{Permitted } f_s = \frac{z}{\sqrt[3]{d_c \times A}} = \frac{170}{\sqrt[3]{2.313 \times 55.4}} = 33.7 > 0.6 \, f_y = 36 \text{ ksi}$$

Actual f_s = 11.5 ksi < permitted f_s = 33.7 ksi   OK

Check Maximum Reinforcement

No more than 42 percent of the flexural cross section can be in compression at the strength limit state. With $A_s = 0.31$ in^2/ft and $d = 15.69$ inches, the depth of the section in compression is:

$$c = \frac{A_s \times f_y}{0.85 f_c' \beta_1 b} = \frac{0.31 \times 60}{0.85 \times 4 \times 0.85 \times 12} = 0.54 \text{ in}$$

the fraction of the section in compression is:

$$\frac{c}{d} = \frac{0.54}{15.69} = 0.034 < 0.42$$

Check Minimum Reinforcement

The gross moment of inertia is:

$$I_g = \frac{1}{12} \, b \cdot t^3 = \frac{1}{12} 12 \times 18^3 = 5{,}832 \text{ in}^4$$

The distance from the centroidal axis to the tension face is:

$$y_t = 9.0 \text{ in}$$

Combining these parameters leads to a cracking moment of:

$$M_{cr} = \frac{f_r I_g}{y_t} = \frac{0.48 \times 5832}{9 \times 12} = 25.9 \text{ kip-ft}$$

and with the 20 percent increase, the required capacity is:

$1.2\ M_{cr} = 31.1$ kip-ft

The capacity of the #16 bars at a 12 inch spacing is:

$$M_r = \mathcal{O} \cdot A_s \cdot f_y \cdot \left(d - \frac{a}{2} \right)$$

$$M_r = 0.9 \cdot 0.31 \cdot 60 \cdot \left(15.69 - \frac{0.54 \times 0.85}{2} \right)\left(\frac{1}{12} \right) = 21.6 < 31.1 \text{ kip-ft}$$

The required steel area due to flexure is 0.10 in2/ft. The minimum steel permitted (#16 bars at 12 inches) has an area of $0.31\ \text{in}^2$/ft.

Consequently, the minimum steel provides more than 1.33 of the required steel.

Use #16 bars at 12 inches for vertical back face reinforcement.

Shrinkage and Temperature Reinforcement

To distribute and limit the size of cracks associated with concrete shrinkage and with temperature changes, a modest amount of reinforcement is provided transverse to the primary reinforcement. The total area of required transverse reinforcement to be distributed to both faces is:

$$A_s \geq 0.11 \times \left(\frac{A_g}{f_y} \right) = 0.11 \times \left(\frac{18 \times 12}{60} \right) = 0.4 \text{ in}^2/\text{ft}$$

Provide horizontal #16 bars at 12 inches to both faces, $A_s = 0.31\ \text{in}^2$/ft